NUREG/CR-6119, Vol. 3, Rev. 0
SAND2001-0929P

MELCOR Computer Code Manuals

Vol. 3: Demonstration Problems

Version 1.8.5 May 2001

Revised October 2000
Printed May 2001

Prepared by
R. O. Gauntt, R. K. Cole,
C. M. Erickson, R. G. Gido, R. D. Gasser,
S. B. Rodriguez, and M. F. Young
Scott Ashbaugh, Mark Leonard, and Adam Hill

Sandia National Laboratories
Albuquerque, NM 87185-0739

Prepared for
Division of Systems Analysis and Regulatory Effectiveness
Office of Nuclear Regulatory Research
U.S. Nuclear Regulatory Commission
Washington, DC 20555-0001
NRC Job Code W6203

Abstract

MELCOR is a fully integrated, engineering-level computer code that models the progression of severe accidents in light-water reactor nuclear power plants. MELCOR is being developed at Sandia National Laboratories (Sandia) for the U.S. Nuclear Regulatory Commission (NRC) as a second-generation plant risk assessment tool and the successor to the Source Term Code package. A broad spectrum of severe accident phenomena in both boiling and pressurized water reactors is treated in MELCOR in a unified framework. These include thermal-hydraulic response in the reactor coolant system (RCS), reactor cavity, containment, and confinement buildings; core heatup, degradation, and relocation; core-concrete attack; hydrogen production, transport, and combustion; fission product release and transport behavior. Current uses of MELCOR include estimation of severe accident source terms and their sensitivities and uncertainties in a variety of applications.

This publication of the MELCOR computer code manuals corresponds to MELCOR 1.8.5, released to users in July 2000. Volume 1 contains a primer that describes MELCOR's phenomenological scope, organization (by package), and documentation. The remainder of Volume 1 contains the MELCOR User's Guides, which provide the input instructions and guidelines for each package. Volume 2 contains the MELCOR Reference Manuals, which describe the phenomenological models that have been implemented in each package. A new volume, Volume 3 of this publication, presents a portfolio of test and sample problems consisting of both analyses of experiments and of full plant problems. These analyses will be repeated with future releases of MELCOR in order to provide a metric on code predictions as new versions are released.

Contents

Figures

Tables

Acronyms

ADS	Automatic Depressurization System
B&W	Babcock and Wilcox
BMC	Battelle Model Containment
BWR	boiling water reactor
CF	Control function
CFD	computational fluid dynamics
CONTAIN	Contain code
COR	Core package
CRGTs	Control rod guide tubes
CSP	core support plate
CSTF	Containment Systems Test Facility
CV	control volume
CVH	Control Volume Hydrodynamics package
DEC	Digital Equipment Corporation
ECCS	Emergency Core Cooling System
EDF	external data file
FL	flow path
HEDL	Hanford Engineering and Development Laboratory
HPCS	high-pressure core spray system
HPI	high-pressure injection
HS	heat structure
IPSN	Nuclear Safety and Protection Institute
ISP	International Standard Problem
LB	large-break
LOCA	Loss-of-coolant accident
LPCI	low-pressure coolant injection system
LPCS	low-pressure core spray system
LPSI	Low Pressure Safety Injection
LWR	light water reactor
MP	materials properties
MSIV	main steam isolation valve
NRC	Nuclear Regulatory Commission
NS	non-supporting structure
NUPEC	Nuclear Power Engineering Corporation
ORNL	Oak Ridge National Laboratory
OS	other structures
PORV	power-operated relief valve
PWR	pressurized water reactor
RCP	reactor coolant pump
RCS	reactor coolant system
RN	radionuclide
RWST	Refueling water storage tank
SNL	Sandia National Laboratories
SPR	containment sprays
SRVs	safety relief valves
SS	supporting structures
TAF	top of active fuel

1. Analysis of the Nuclear Power Engineering Corporation (NUPEC) M-8-1 Mixing Test

1.1 Background

The NUPEC mixing tests were conducted in a large, 1/4-scale simulated containment [1]. (See Figure 1-1.) The tests explored the containment response to steam injection and containment spray actuation. Helium gas was introduced into the containment as a surrogate for hydrogen. Test M-8-1 introduced a combined source of helium and steam into the lower portion of one of the steam generator compartments [1]. This particular test is modeled to examine MELCOR's performance in three broad areas: (1) pressure response; (2) temperature distribution and stratification; and (3) hydrogen mixing. Note that this test is similar to the M-8-2 test, except that M-8-2 includes effects of spray operation while M-8-1 does not model sprays.

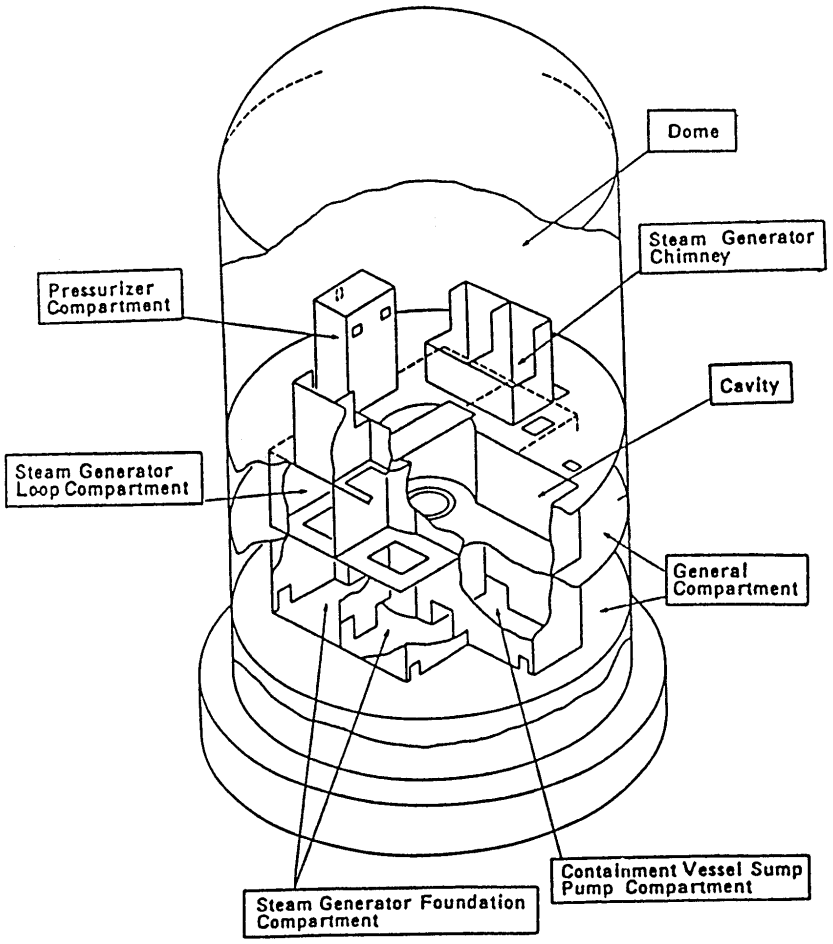

Figure 1-1. NUPEC 1/4-Scale Containment Mixing Facility [1]

The NUPEC facility is a domed cylinder, approximately 10.8 m in diameter, 17.4 m high, and 1310 m^3 in volume [1]. The facility contains 28 compartments, of which only 25 are interconnected. The dome volume constitutes approximately 71% of the total containment volume. The containment is constructed entirely of carbon steel. The containment shell and floors are 12 mm thick, except for the first floor, which is 16 mm thick. The compartment walls are 4.5 mm thick. The outside of the containment is covered with a layer of insulation, which is covered by a thin metal sheet to protect from weather damage. The insulation around the cylinder and hemisphere is 125 mm and 150 mm thick, respectively. A water storage tank is located below the first floor of the containment to collect draining condensate and spray water. The tank is separated from the rest of the containment by 100 mm of insulation. Water is pumped from the tank to 21 spray nozzles in the dome. The facility is equipped with a remote boiler for co-injecting steam and helium. The facility includes instrumentation for helium gas concentration at various locations, pressure, gas temperature, and wall temperatures.

1.2 Nodalization

The MELCOR nodalization of the NUPEC Mixing Facility is presented in Figure 1-2. The nodalization contains 35 control volumes (CVs), with a single control volume modeling each room, except for the dome and the upper pressurizer compartment. The dome and the pressurizer compartment were further subdivided into seven and two volumes, respectively. The dome was subdivided into central volumes (CVs 30, 32, and 34), annular volumes (CVs 29, 31, and 33), and the top of the dome (CV 25). This nodalization allowed convection loops to form during the calculation. The upper pressurizer compartment was also subdivided (CVs 22 and 35) to allow circulation of gases from the upper pressurizer compartment to the lower pressurizer compartment (CV 16), which is a dead-end room. A detailed layout of the containment rooms and connectivity is given in Figure 1-3.

The reactor vessel and primary shield cells (CVs 27 and 28) were also explicitly included in the MELCOR model. Rather than modeling the drain tank explicitly, condensate and spray water were removed via CVH package mass and energy sinks. Two additional CVs were added (CVs 998 and 999) to represent ambient heat transfer boundary conditions. CV 998 represents the thermal conditions below the bottom of the primary shield, and CV 999 represents the outside environment.

A total of 124 MELCOR heat structures are included in the NUPEC model.

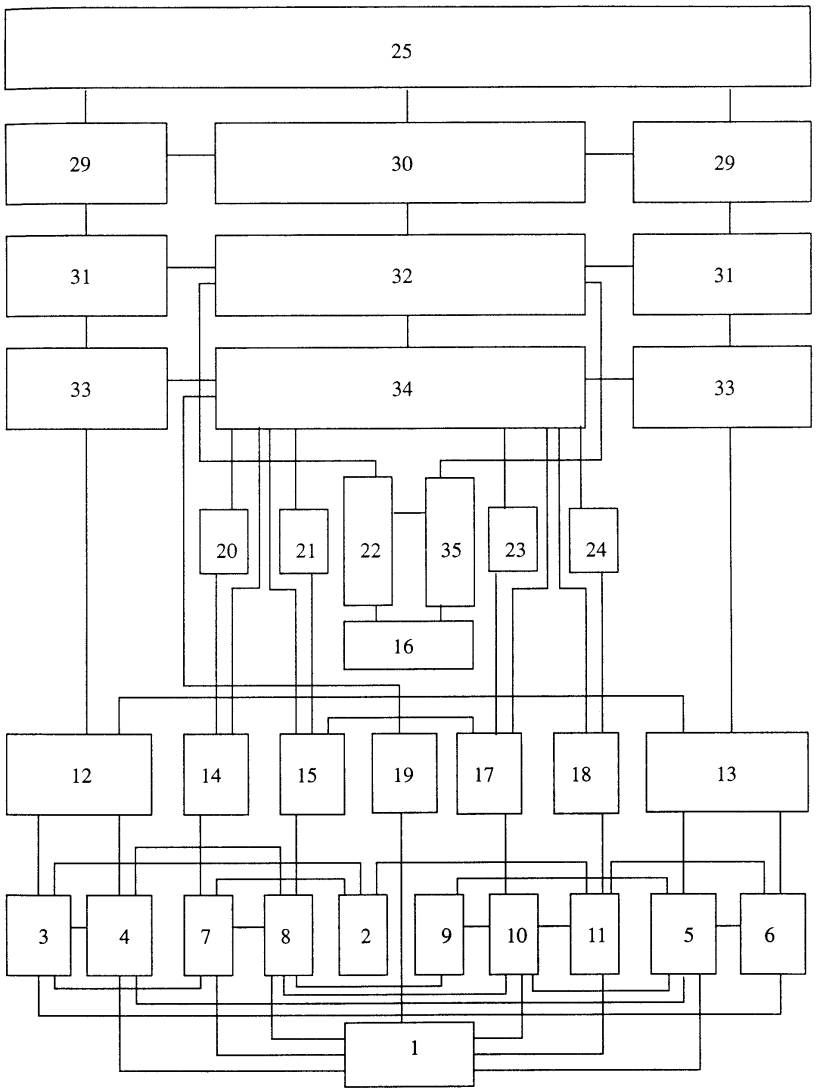

Figure 1-2. MELCOR NUPEC Nodalization

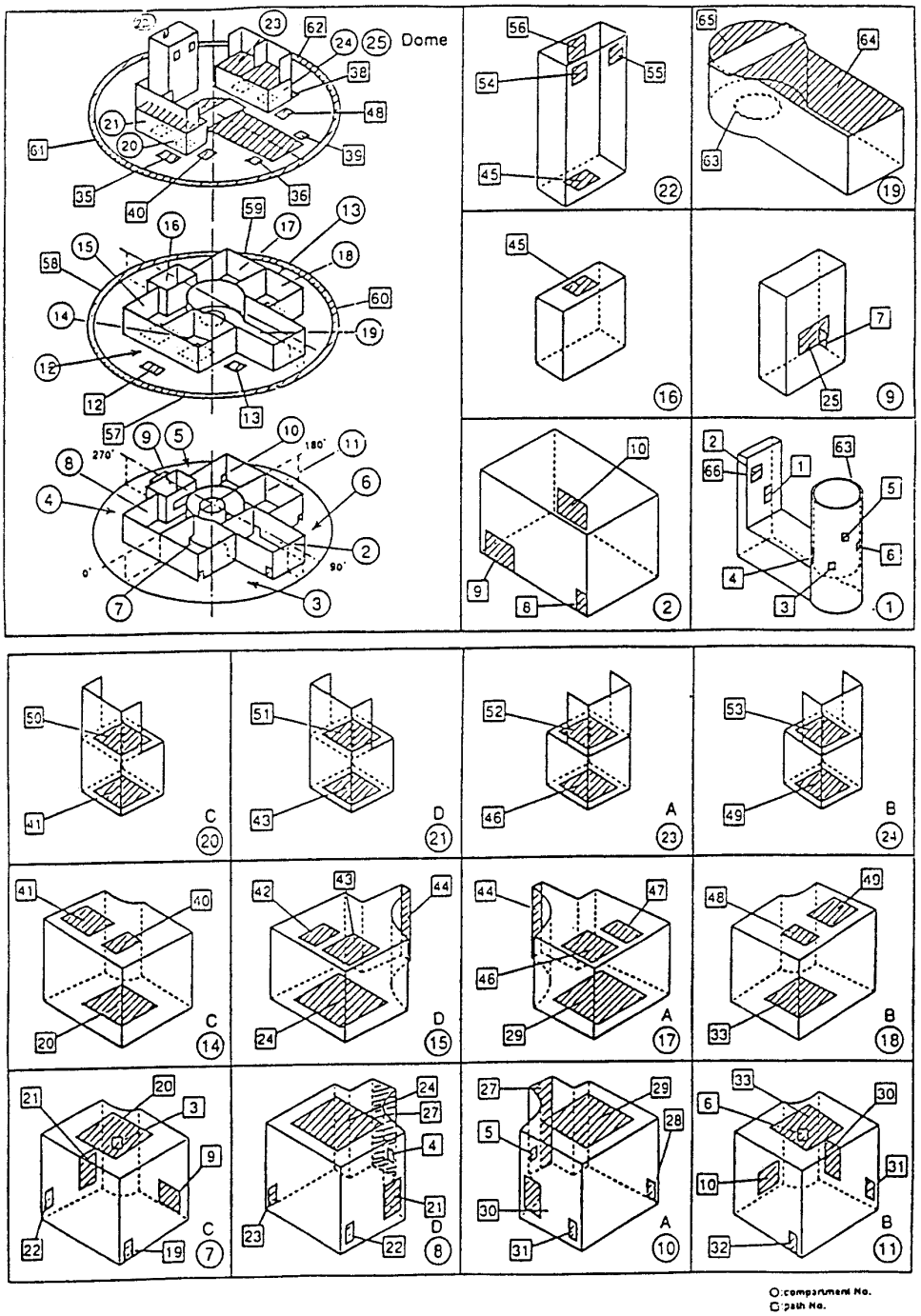

Figure 1-3. Detailed NUPEC Facility Layout [1]

1.3 MELCOR Input Specifications

The MELGEN input files for this calculation are listed below. The “m81.gen” is the primary MELGEN file. The other files are automatically read in during MELGEN processing because they are identified by the “r*I*f” command in the “m81.gen” input file.

- m81.gen
- mp.gen
- nupec.gen
- film.gen
- m81_bc.gen
- cf_he.gen

The MELCOR input file for this calculation is “m81.cor.”

In general, the NUPEC model was developed using standard, default MELCOR modeling parameters. A few exceptions are noted below. Also, since this calculation was performed strictly as an assessment of containment thermal-hydraulic modeling capabilities, the Radionuclide (RN) and Core (COR) packages were not activated.

Heat Structures

Heat Structures were modeled with the band radiation model activated. At containment temperatures during NUPEC Test M-8-1, radiative exchange is not expected to be important. However, for completeness, the models were activated.

Several heat transfer coefficients were augmented to reflect local conditions not directly simulated by the thermal-hydraulic models in MELCOR. These heat transfer coefficients were based on CONTAIN calculations of the M-8-1 test [2, 3]. The modified heat transfer coefficient for structures exposed to the environment were augmented to 6.02 W/m^2–K with a 284 K outside temperature. The locations of the augmented heat transfer coefficients are summarized in Table 1-1.

Table 1-1. Locations of Augmented Heat Transfers

Location	Purpose	Value
Outer Wall	To simulate external environment conditions.	Similar to the CONTAIN deck, a specified value of heat transfer coefficient of 6.02 W/m^2–K was used.
Floor of Primary Shield	Room underneath the primary shield was not modeled.	T = 313 K

1.4 Results of Analysis

Figure 1-4 through Figure 1-8 show containment temperature and helium concentration results for the NUPEC M-8-1 MELCOR 1.8.5 (QX) simulation. Results are compared both to measured test data and to MELCOR 1.8.4 simulation results. General trends show adequate comparison to test data. There are no discernible differences between MELCOR 1.8.4 and MELCOR 1.8.5 calculated results. MELCOR 1.8.4 results are identified as MELCOR-QQ in the plot legends, while MELCOR 1.8.5 results are identified as MELCOR-QX.

1.5 Discussion

The highlights from the MELCOR base case calculation are summarized below.

Pressure response

The prediction of pressure response by MELCOR was good. MELCOR slightly overpredicted facility pressure, but the prediction was within 10% of the data measurements.

Gas Temperature Response

The final temperature was slightly overpredicted by MELCOR for all of the compartments; however, the MELCOR-predicted temperature change in the dome, the pressurizer compartments, and the majority of the lower compartments was within 10% of the data. Although the MELCOR results show considerable stratification, more mixing was predicted in the lower portion of the containment and the temperature response than was measured.

Helium Concentrations

The dome and most of the lower rooms followed the measured trends. Although the helium concentrations in the pressurizer compartments were overpredicted by MELCOR, the calculated trend was in good agreement with the data. Both the MELCOR calculation and the data show extreme stratification of helium to the dome.

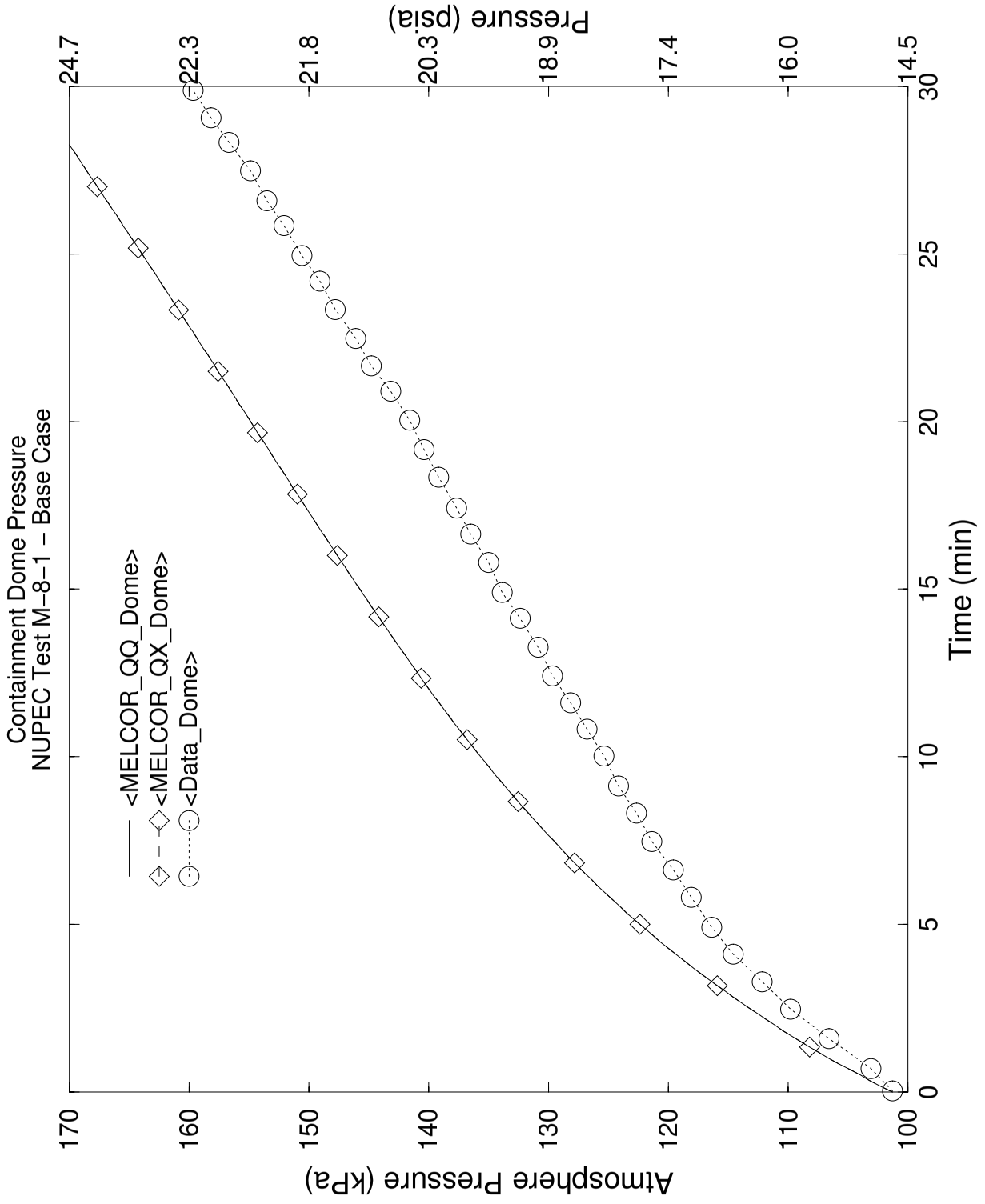

Figure 1-4. Containment Pressure Response

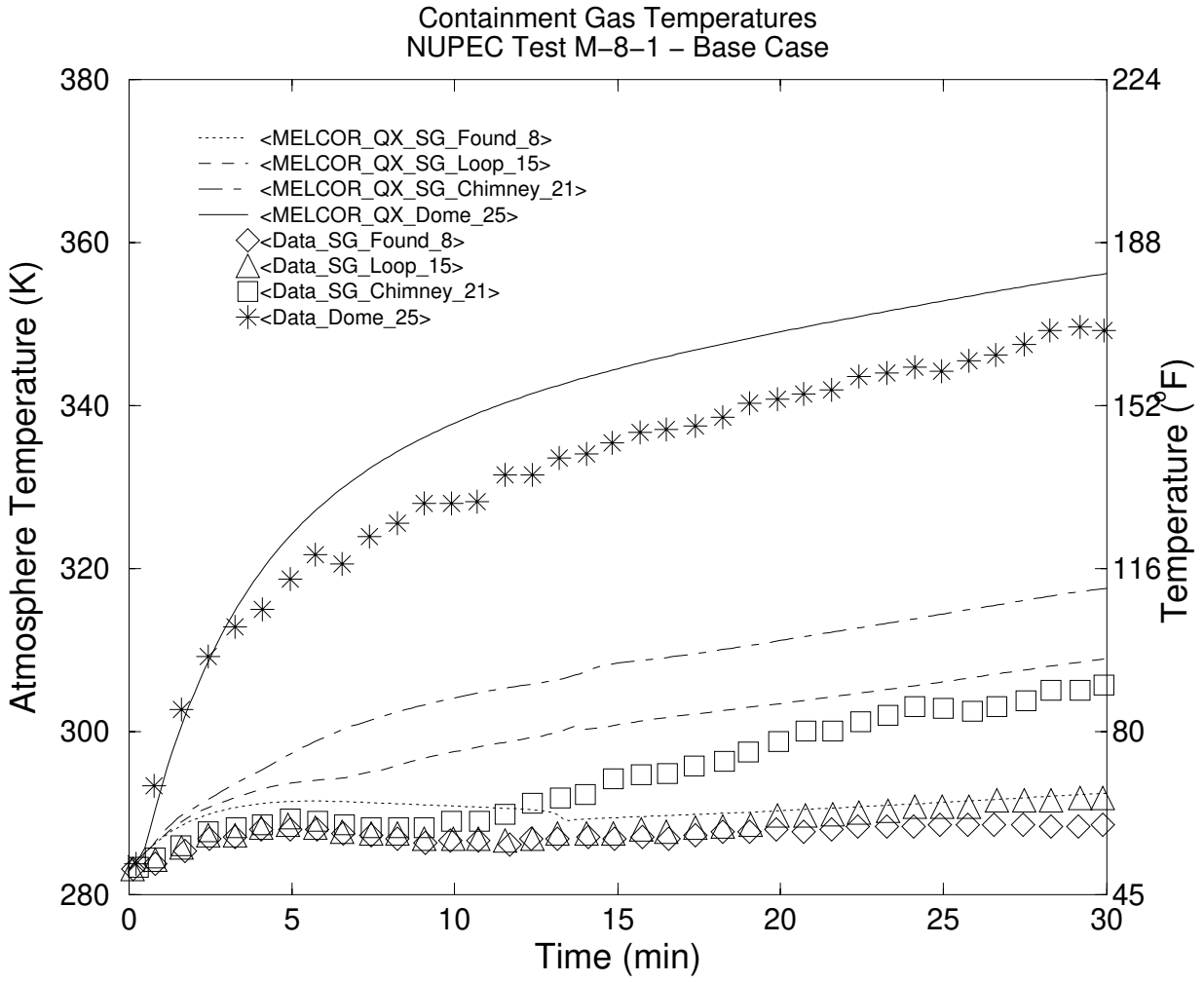

Figure 1-5. Selected Containment Gas Temperatures (comparison to test data)

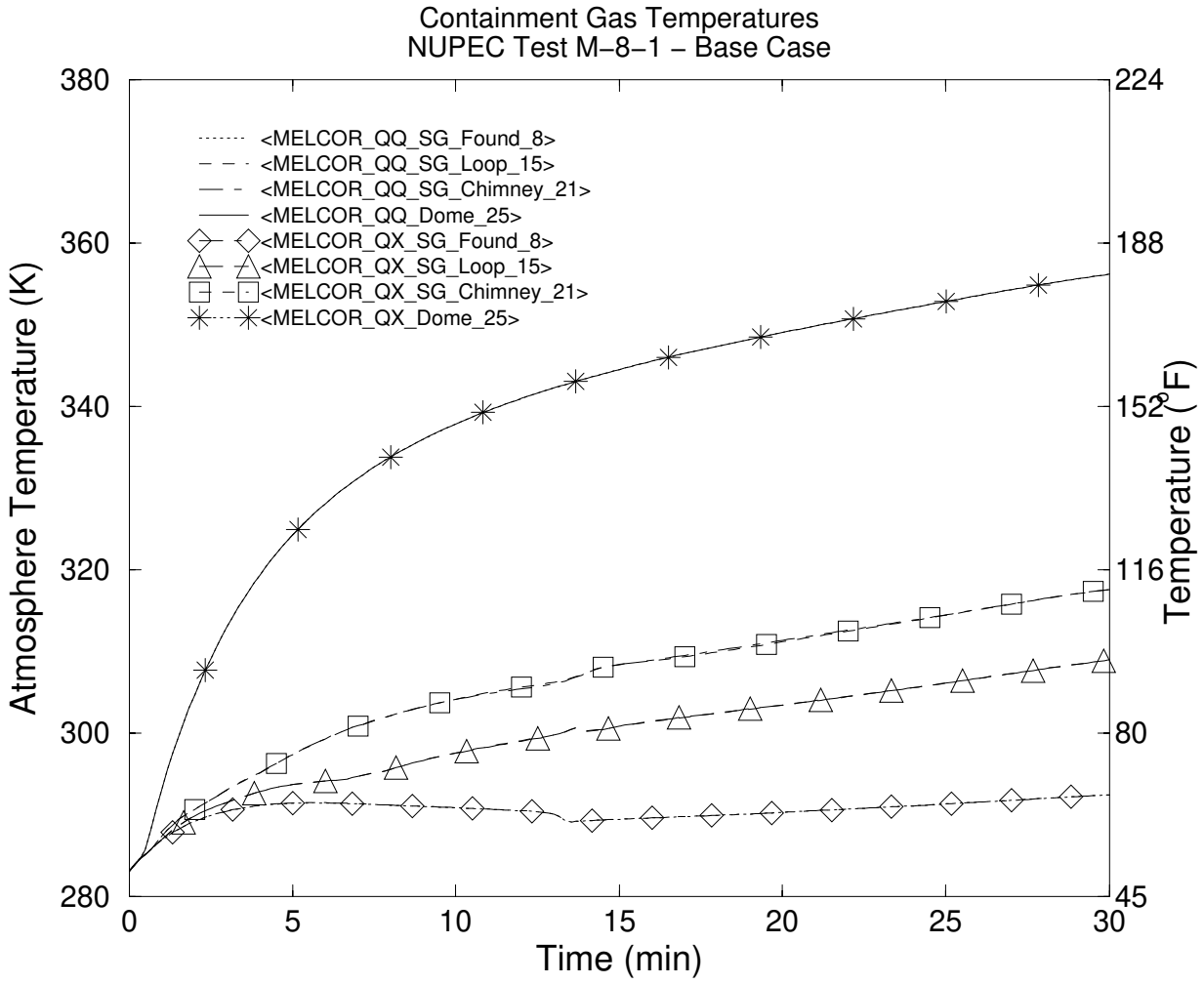

Figure 1-6. Selected Containment Gas Temperatures (comparison to MELCOR 1.8.4)

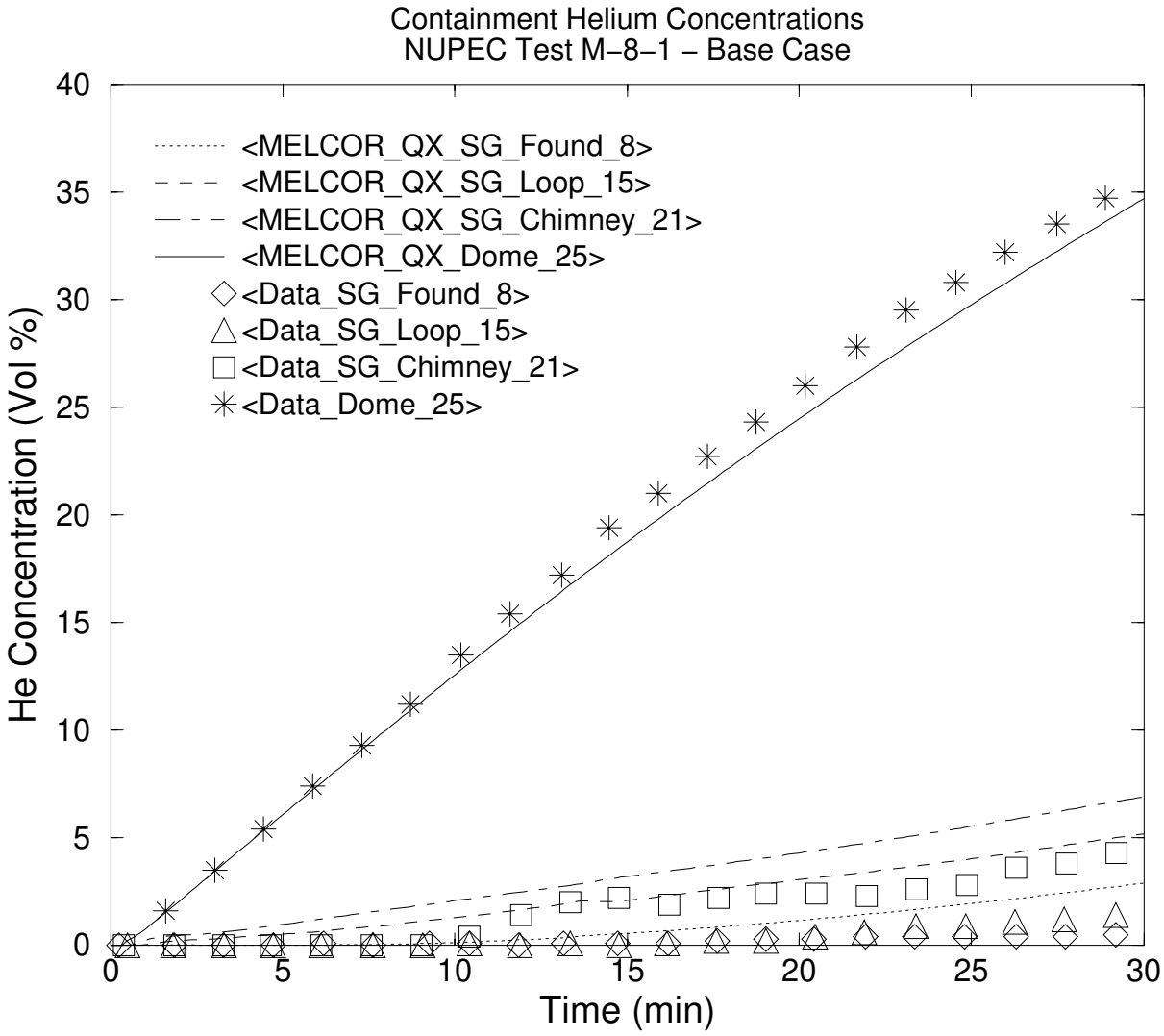

Figure 1-7. Containment He Concentrations (comparison to test data).

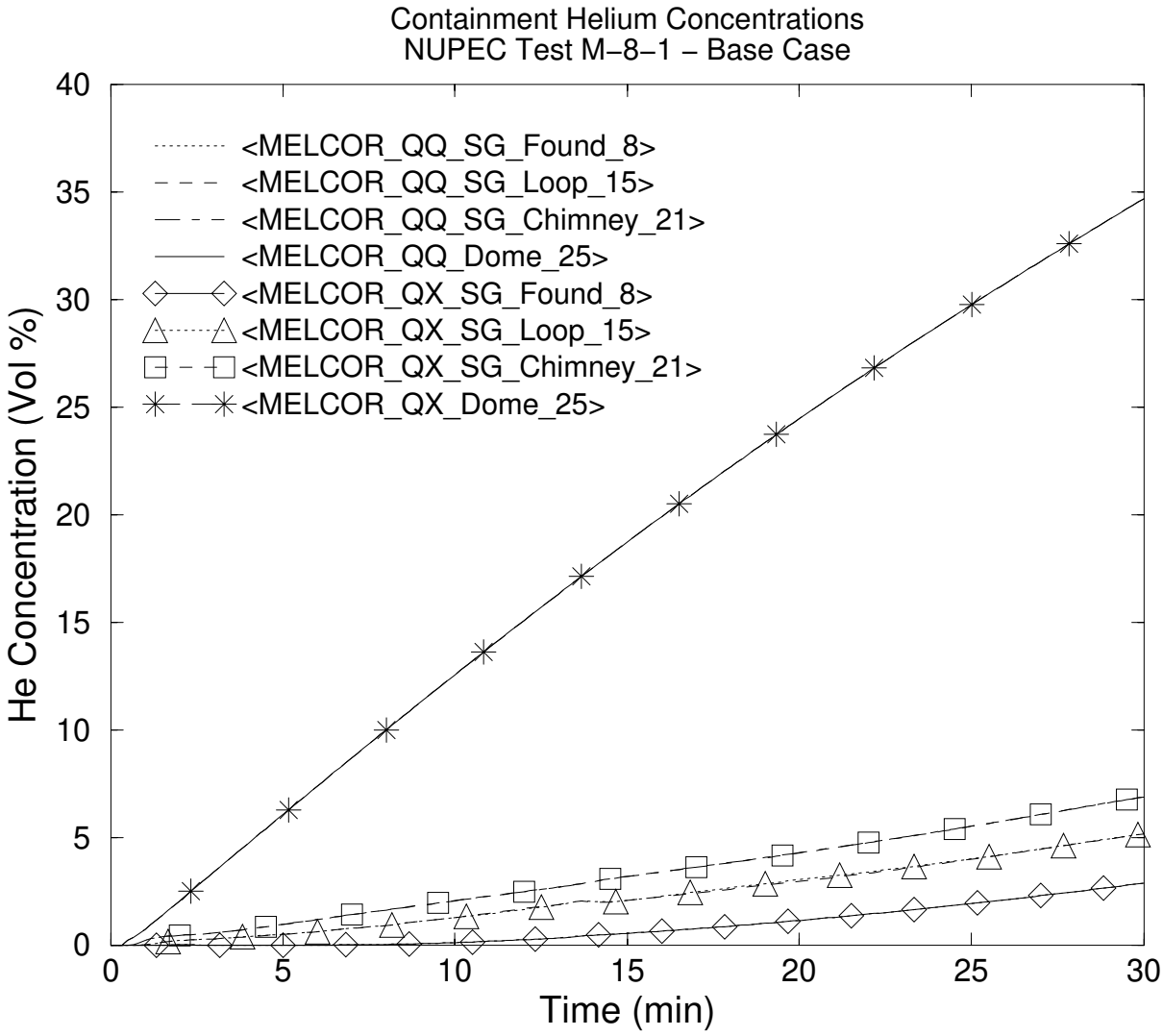

Figure 1-8. Containment He Concentrations (comparison to MELCOR 1.8.4)

1.6 References

1. Nuclear Power Engineering Corporation (NUPEC), System Safety Department, “Specification of ISP-35—NUPEC’s Hydrogen Mixing and Distribution Test—Test M-5-5”, ISP35-027, Revision 1, NUPEC, November 3-4, 1993.

2. Stamps, D. W., “CONTAIN Assessment of the NUPEC Mixing Experiments,” SAND94-2880, August 1995.

3. Stamps, D. W., Murata, K. K., “CONTAIN Assessment of the NUPEC Mixing Experiments—Supplement 1,” SAND94-2880, August 1995.

2. MELCOR 1.8.5 Analysis of NUPEC Test M-8-2

2.1 Background

This report documents an assessment of test M-8-2 from the NUPEC mixing tests. The NUPEC mixing tests were conducted in a large, 1/4-scale simulated containment [1] (see Figure 2-1 [1]). The tests explored the containment response to steam injection and containment spray actuation. Helium gas was introduced into the containment as a surrogate for hydrogen. Test M-8-2 included steam injection, which was injected into the lower steam generator foundation compartment along with the helium (Cell 8, Figure 2-2). The containment sprays also operated for the duration of the test [1]. The spray water was cooler than the initial gas and structure temperatures, and despite the addition of hot steam, was the primary cause of the temperature changes in the test. This particular test was identified as testing three broad areas: (1) hydrogen mixing; (2) the temperature distribution and stratification; and (3) the containment spray performance.

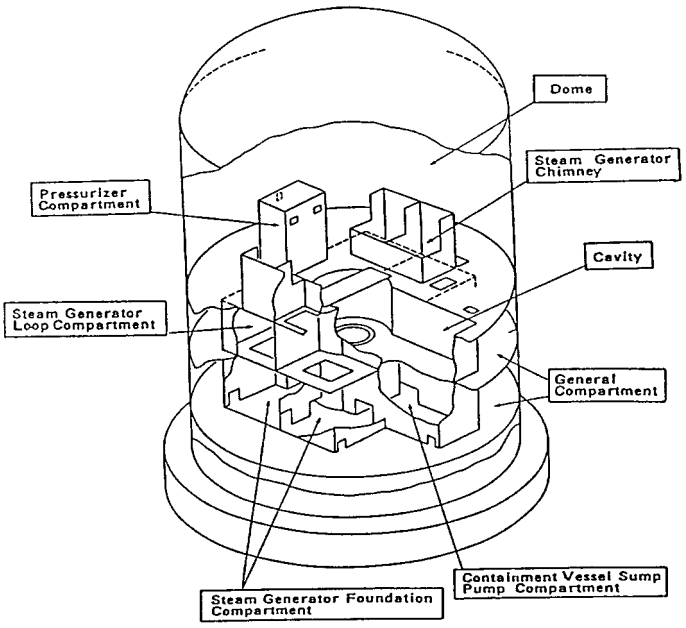

Figure 2-1. NUPEC 1/4-Scale Containment Mixing Facility [1]

The NUPEC facility is a domed cylinder approximately 10.8 m in diameter, 17.4 m high, and 1310 m^3 in volume [1]. The facility contains 28 compartments, of which only 25 are interconnected. The dome volume constitutes approximately 71% of the total containment volume. The containment is constructed entirely of carbon steel. The containment shell and floors are 12 mm thick except for the first floor, which is 16 mm thick. The compartment walls are 4.5 mm thick. The outside of the containment is covered with a layer of insulation, which is covered by a thin metal sheet to protect from weather damage. The insulation

around the cylinder and hemisphere is 125 mm and 150 mm thick, respectively. A water storage tank is located below the first floor of the containment so that condensate and spray water can drain. The tank is separated from the rest of the containment by 100 mm of insulation. Water is pumped from the tank to 21 spray nozzles in the dome. The facility is equipped with a remote boiler for co-injecting steam and helium. The facility includes instrumentation for helium gas concentrations, pressure, gas temperature, and wall temperatures.

A CONTAIN code assessment of NUPEC Test M-7-1 was performed at Sandia as part of the NRC's participation in International Standard Problem (ISP) 35 [2]. In that effort, a CONTAIN Version 1.12 model of the NUPEC facility was constructed. The CONTAIN model was used to simulate Test M-7-1 as well as four other NUPEC mixing tests, including Test M-8-2. After the NUPEC assessment report was completed, it was discovered that the NUPEC measurement for helium concentration was better described by a dry measurement versus a wet measurement. Sandia subsequently revised the calculated predictions of helium concentrations and documented the results in a supplement to the original report [3]. These two Sandia reports were used as the basis for the CONTAIN assessment of NUPEC Test M-8-2.

In a separate study, several assessments were performed using the NUPEC data. Table 2-1 summarizes the key initial and boundary conditions in the tests. As shown in the table, the tests include many variations on the helium and steam sources, the injection location (e.g., high or low in the containment), and containment spray operation. Test M-8-2 started from elevated temperature and pressure conditions and included variable helium and steam sources as well as containment sprays. Test M-7-1 is identical to Test M-8-2 except for the location of the steam and helium sources.

Table 2-1. Summary of Selected NUPEC Tests.

Test	Injection Location	Initial Conditions	Helium Source	Steam Source	Containment Sprays
M-4-3	Bottom of SG Comp D (8)	303 K, 101 kPa	0.027 kg/s	0.33 kg/s, 115 K	*None*
M-5-5	Bottom of SG Comp D (8)	303 K, 101 kPa	0.027 kg/s	*None*	19.4 m^3/s 292 K
M-7-1	Bottom of SG Comp D (8)	343 K, 146 kPa	0→0.03 kg/s→0	0.08 kg/s→0.03 kg/s 110 K	19.4 m^3/s 313 K
M-8-1	Upper Pressurizer Comp (22)	303 K, 101 kPa	0.027 kg/s	0.33 kg/s, 115 K	*None*
M-8-2	Upper Pressurizer Comp (22)	343 K, 146 kPa	0→0.03 kg/s→0	0.08 kg/s→0.03 kg/s 90 K	19.4 m^3/s 313 K

2.2 MELCOR Calculational Approach

This section describes the model nodalization as well as code parameter specifications and sensitivities. A MELCOR model of the NUPEC facility was prepared based on a previously existing CONTAIN model [2,3]. The CONTAIN NUPEC containment model included some modeling features not directly available in MELCOR. The approach used to convert these features is discussed. The resultant nodalization and modeling features are documented in Section 2.2.1. MELCOR includes provisions to specify sensitivity parameters to the physics models as well as to specify alternate physics models. Descriptions of the nondefault or specific sensitivity variables are described in Section 2.2.2. To implement some of the parameters in the CONTAIN NUPEC model, MELCOR code modifications were required. These code modifications are also described in Section 2.2.2.

2.2.1 MELCOR Nodalization

A MELCOR model of the NUPEC facility was created during this study for Test M-7-1. To expedite the development of the MELCOR model and facilitate the parity comparison with CONTAIN, the MELCOR model was developed directly from the CONTAIN deck for M-7-1, and the MELCOR model for M-7-1. The resulting MELCOR model is described in the remainder of this section.

In the effort that supported the CONTAIN analysis of the NUPEC mixing tests, several nodalization and modeling permutations were performed. In particular, the following variations were studied:

(1) Two nodalizations, 35-cell and 28-cell;

(2) Two types of flow solvers;

(3) Several containment spray nodalizations;

(4) Variations in the specification of the initial and boundary conditions to account for measurement uncertainties; and

(5) Variations in MELCOR options for wall heat transfer.

The motivation for the different modeling and nodalization schemes was to improve the computational simulation of the tests. A significant part of the effort was devoted to simulating the thermal-hydraulic effects from the convective currents during spray operation. Based on the results of the nodalization and modeling studies, a base CONTAIN model was defined. It was beyond the scope of the present effort to duplicate all these modeling and nodalization variations. Consequently, the base CONTAIN, the input model that gave the best comparisons to the data from Test M-7-1, was selected as the starting point for the MELCOR model. A description of the base CONTAIN model follows.

The CONTAIN nodalization that was converted to a MELCOR representation is presented in Figure 2-2. The nodalization included a 35-cell representation of the facility. Each room

was represented by a computational cell, except for the dome and the upper pressurizer compartment. The dome and the pressurizer compartment were further subdivided into seven and two cells, respectively. The dome was subdivided into central cells (Cells 30, 32, and 34), annular cells (Cells 29, 31, and 33), and the top of the dome (Cell 25). This nodalization allowed convection loops to form during the calculation. The upper pressurizer compartment was also subdivided (Cells 22 and 35) to allow circulation of gases from the upper pressurizer compartment to the lower pressurizer compartment (Cell 16), which is a dead-end room. A detailed layout of the containment rooms and connectivity is given in Figure 2-3. The CONTAIN and MELCOR cell numbering is consistent with Figure 2-2, except as noted above.

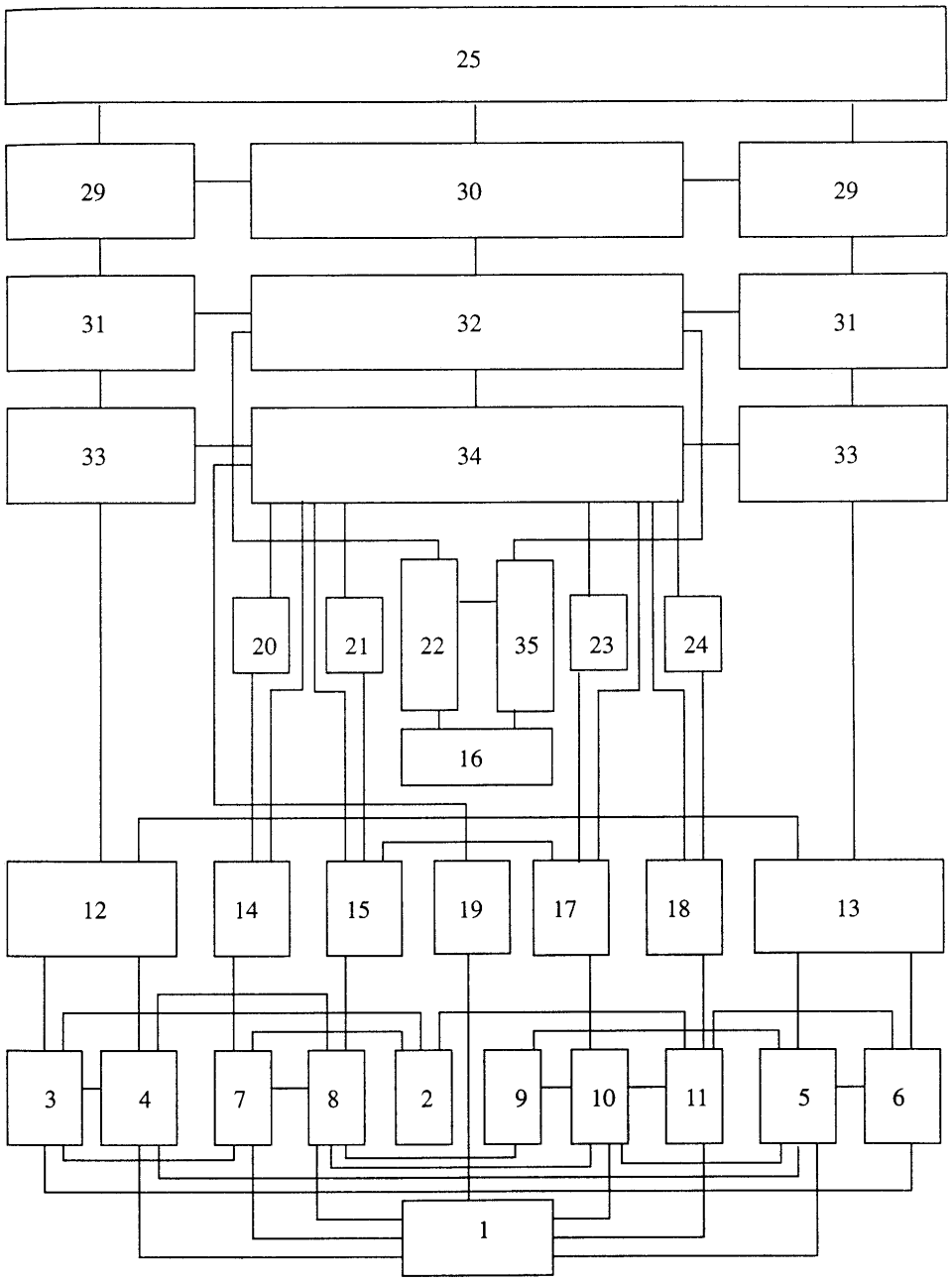

Figure 2-2. Nodalization Used in CONTAIN and MELCOR Analyses of M-8-2

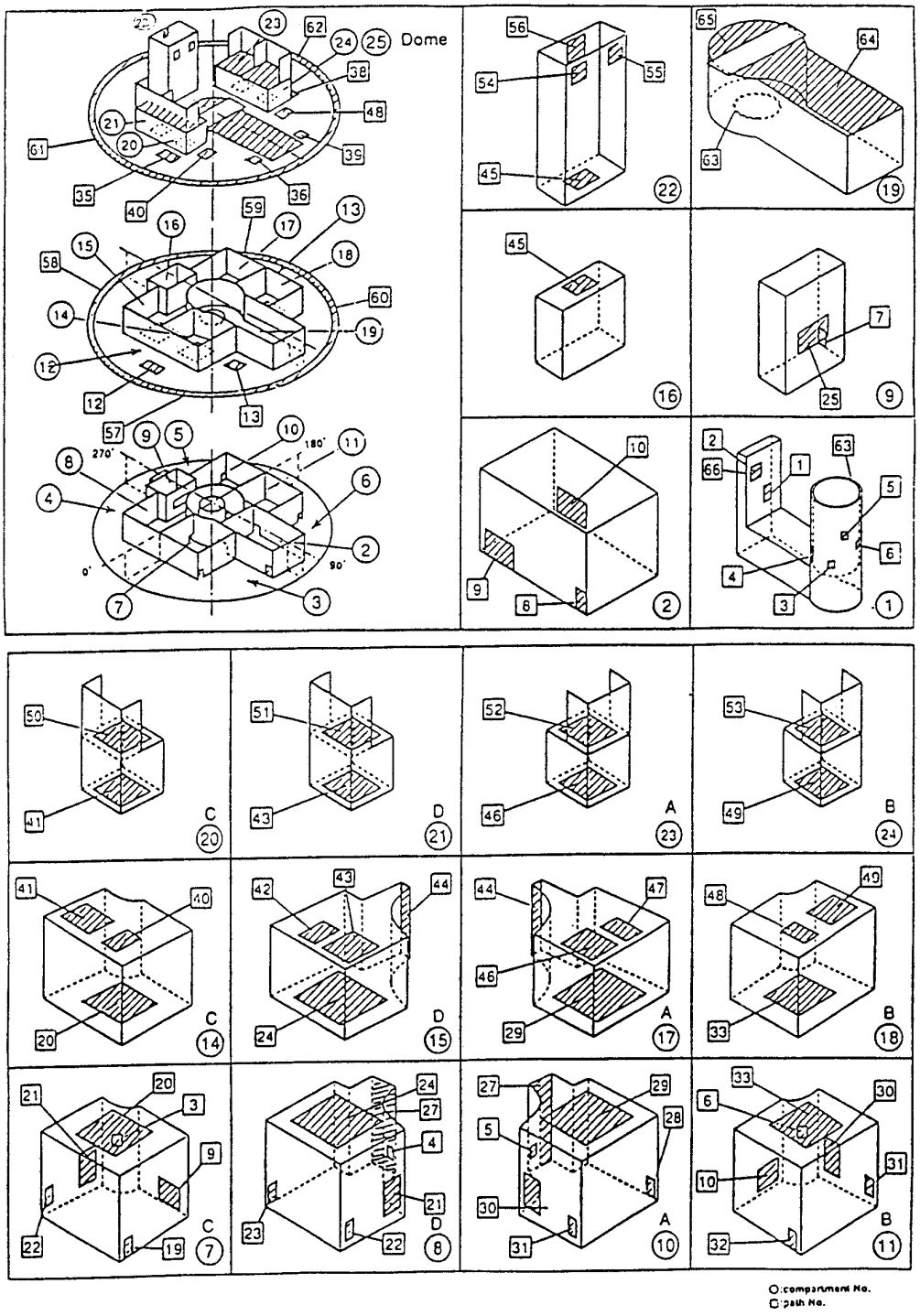

Figure 2-3. Detailed NUPEC Facility Layout [NUPEC, 93]

Several cells are not shown in Figure 2-2. The CONTAIN model included explicit representation of the drain tank (Cell 26), the reactor vessel (Cell 27), and the primary shield (Cell 28) for heat transfer purposes. None of these cells were explicitly coupled to the containment momentum solution via interconnecting flow paths. The drain tank was coupled to the sump volumes of the containment (Cells 1 and 6) via special engineering safety system flow paths. Since the drain tank was well insulated, no heat transfer coupling to the drain tank was modeled. The reactor vessel and primary shield were represented as airtight vessels. These cells and the associated heat structures for the vessel walls served as a heat transfer boundary for adjacent cells.

The MELCOR conversion of the CONTAIN model preserved the nodalization of the containment. The reactor vessel and primary shield cells (e.g., Cells 27 and 28) were also explicitly included. Rather than modeling the drain tank explicitly, condensate and spray water were removed via Control Volume Hydrodynamics (CVH) package mass and energy sinks. Two additional control volumes were added (CVs 998 and 999) to represent ambient heat transfer boundary conditions explicitly specified in the CONTAIN heat slab input. CV 998 represents the thermal conditions below the bottom of the primary shield and CV 999 represents the outside environment.

A total of 124 MELCOR heat structures were created from the CONTAIN model input. The structures in the CONTAIN model came from two sources, heat slabs and lower cell models. Both were converted to MELCOR heat structures. Most of the CONTAIN heat slabs were coupled between two adjacent fluid cells via ICELL and STRNUM directives. Typically, half the structure was associated with a slab in one cell and the other half was associated with a slab in another cell. The ICELL and STRNUM directives thermally connected the outer surfaces of the two heat slabs. When the heat slabs were implemented into MELCOR, the whole width of the slab was used and the appropriate boundary cells were specified. The CONTAIN lower cell model was used to model some of the floors in the CONTAIN cells. The lower cell input was also converted into MELCOR heat structures. As was done in the CONTAIN model, the heat transfer coefficient for structures exposed to the environment were augmented to 26.62 W/m^2–K with a 284 K outside temperature.

The CONTAIN structure-to-gas radiative heat transfer models were also activated in the NUPEC deck. The structure surface emissivities and geometric mean beam length were translated into the equivalent band radiation model in MELCOR. At containment temperatures during NUPEC Test M-8-2, radiative exchange is not expected to be important. However, for completeness, the models were activated.

Containment Spray Models

As discussed previously, several alternate methods were used to model the containment sprays. Heat and mass transfer from the containment sprays dominate the system thermal-hydraulics. The CONTAIN study cites analytic studies that show the very high velocities, vortices, and other circulatory flow patterns created by spray operation [2]. One key limitation in both the MELCOR and CONTAIN containment spray models is the omission of the complex hydraulic flow patterns created by the sprays. (See Figure 2-4 [2].) In particular, the fluid drag on the air, the spray and recirculation flow patterns, and the impaction of the drops on surfaces is very complicated and omitted from the MELCOR and CONTAIN spray models. The best agreement between the CONTAIN model and the NUPEC data was achieved with the following modeling options:

(1) The containment dome was subdivided into seven cells to permit natural circulation flow patterns. The flow areas were specified to infer a contraction of the spray towards the center of the containment. The outer annular cells represented the region not covered by the sprays where an upflow of vapor was expected. The spray sources were introduced into the dome and specified to only fall through the center region. This was a significant modeling assumption since the region of spray coverage was specified through the partition between the inner and annular regions of the dome.

(2) The containment spray drops were pumped downward from one cell to another using the engineering safety feature models. All of the containment spray was first injected into Cell 25. All of the spray droplets then fell through Cells 30, 32, and 34; and portions fell into Cells 19, 20, 21, 23, and 24. Some of the spray subsequently fell into Cells 7 and 14, Cells 8 and 15, Cells 10 and 17, and Cells 11 and 18. Spray droplets that collected at the bottom of these cells and did not fall to a lower cell were transferred directly to the bottom of the containment.

(3) The heat transfer coefficient on all structures exposed to the dome was augmented assuming a specified fluid velocity of 14 m/s on the outer surface. The flow velocity specification was derived from a full containment CONCHAS spray computational fluid dynamics (CFD) study that showed very high fluid velocities in the dome during spray operation [2] (Figure 2-4).

(4) The CONTAIN film flow model was activated for several structures from the dome into the lower containment. The film models were interconnected to allow downward film flow from structure to structure.

(5) The spray water that collected at the bottom of the containment was spread across the containment floor via engineering safety feature overflow paths. The water resided in the lower cell models associated with these cells. In Cells 1 and 6, the water was pumped to a drain tank when the fluid height was above 1.29 m and 0.05 m, respectively.

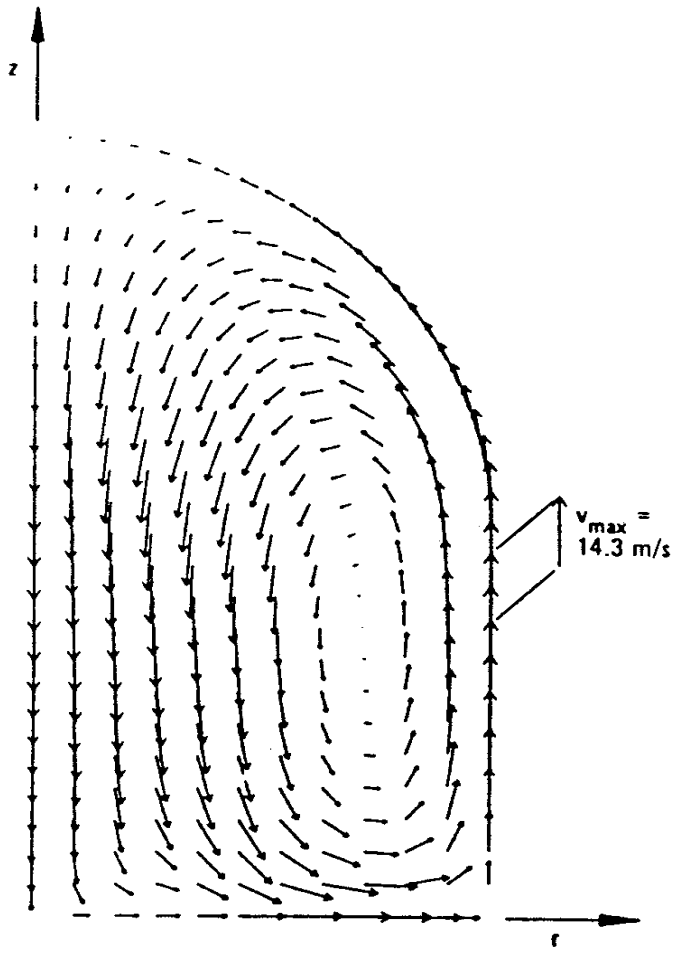

Figure 2-4. Flow Patterns in Containment During Spray Operation [2]

Some of the proceeding spray modeling options could be directly implemented in MELCOR. However, some of the models required alternative approaches. The implementation of these options into the MELCOR input deck is discussed below.

(1) The 7-cell upper dome nodalization from the best CONTAIN simulation was identically represented in MELCOR.

(2) The MELCOR containment spray model can track the fraction of droplets that carry over into lower control volumes directly without having to use pumps to move the fluid. The CONTAIN model also had four instances of parallel spray flow paths joining at a lower cell. Adjoining carry-over paths were not allowed in MELCOR. Consequently, the reconnection of spray streams was not included and the additional carry-over spray was added to the dominant path. Similar to the CONTAIN model, sump directives were added to control volumes where spray water would collect. Like CONTAIN, the sump directives transfer the water droplets

that are not carried over to a lower cell directly to the sump (e.g., bottom of the containment in the NUPEC model).

(3) MELCOR does not include a modeling option to augment the heat transfer coefficient for a user-specified forced flow condition. During preliminary calculations, the calculated heat transfer coefficients from MELCOR were reviewed. The dome heat transfer coefficients were calculated to be a natural convective coefficient of ~3–5 W/m^2–K. Spreadsheet calculations were performed assuming forced convection at 14 m/s using a Dittus-Boelter relationship. The spreadsheet calculations suggested the forced flow condition would be ~25 W/m^2–K, or approximately five times the maximum natural convective value. Assuming heat and mass transfer were equally affected, scale multipliers that increased the heat and mass transfer coefficient by a factor of five were added to the dome heat structures.

(4) The CONTAIN heat slabs with film flow were translated into equivalent MELCOR heat structure film tracking inputs including the interconnection between heat structures.

(5) Mass and energy sinks were added to the MELCOR model to remove sump water from CVs 1 and 6.

2.2.2 MELCOR Parameter Specifications and Sensitivities

The default values on all MELCOR physical models were used (i.e., no sensitivity coefficients). As described in Section 2.2.1, several heat transfer coefficients were augmented to reflect local conditions not directly simulated by the thermal-hydraulic models in CONTAIN (or MELCOR). The locations of the augmented heat transfer coefficients are summarized in Table 2-2. The augmented heat transfer conditions in the CONTAIN model were also implemented in the MELCOR model.

Table 2-2. Locations of Augmented Heat Transfer

Location	Purpose	Value
Upper Dome	To simulate the high local updraft flow adjacent to the containment walls	Simulate forced heat transfer coefficient with 14 m/s airflow with a 5X increase in natural circulation heat transfer coefficient and mass transfer coefficient
Outer Surface	To simulate the external wind and weather conditions during the test	h = 25.62 W/m^2–K T = 284 K
Floor of Primary Shield	Room underneath the primary shield was not modeled	T = 313 K

Several sensitivity calculations were performed with MELCOR that are not specifically reported in this document to help understand the importance of some modeling features on the results of this test and the other NUPEC tests. The base case was defined as the closest possible translation of the 35-cell CONTAIN input deck to MELCOR format. Sensitivity Cases 2 through 6 in Table 2-3 were run primarily to investigate sensitivities in the atmosphere and wall heat transfer during containment spray operation. No sensitivity

efforts significantly improved the comparison to the test results. Only the last sensitivity case, <Spray_Film>, is reported.

Table 2-3. List of Sensitivity Calculations

Case	Name	Description
1	Base_Case	Base translation of CONTAIN input deck.
2	Normal Dome_HT	Turn off augmented heat transfer to dome walls.
3	Rel_Humidity	Change initial relative humidity from 88% to 100%.
4	Simple_Spray	Turn off spray carry-over to subcompartments. All spray water was transferred to the sump at the bottom of CV 34.
5	No_Sump	Allow excess spray droplets that are not carried over into lower control volumes to drain downward to the sump (i.e., via flow path [FL]/CVH connections versus the spray package sump directive). The base model directly transfers any extra spray water at the bottom of the control volume to the sump via sump directives.
6	Forced_Flow	Specify spray flow momentum in the dome to simulate drag from spray droplets. This causes ~6 m/s control volume-centered gas velocity by the bottom of the dome.
7	Spray_Film	Some of the spray water is diverted onto seven separate film flow networks to allow MELCOR's film flow model to transfer water to each of heat structures. Film flow systems are created to allow flow down each of the four steam generator compartments: (a) onto the refueling floor; (b) down into the refueling pool; (c) into the lower peripheral regions of the containment; and (d) onto the dome walls and downward on the outside wall.

It was observed from the experimental data that the gas and wall temperatures dropped uniformly during the test. Despite augmenting the wall heat transfer coefficients in the dome, there was inadequate heat transfer to cool the wall structures. Even if the wall heat transfer was increased, there was inadequate heat capacity in the gas to reduce the wall temperature as much as measured. Consequently, it was concluded that the spray droplets were the primary mechanism for removing energy from the structures.

The conceptual picture for the <Spray_Film> sensitivity case assumed the containment sprays first interacted with the dome atmosphere and then impacted the dome wall, the refueling floor, the refueling pool, and the steam generator compartment walls above the refueling floor. Seven film flow networks were developed to allow the spray droplets to interact with the structures and drain downward. In addition, some of the droplets fell downward through the gas space to lower control volumes as previously described. Since the heat structure film temperature and the spray temperature were close, it was expected that this model would better represent the uniform cooling of both structures and gases observed in the test. There were 124 heat structures in the model, many of which would be expected to have film flow. Consequently, it was very awkward to specify the film networks and spray diversion to the wall. Finally, a code modification was performed to increase the number of spray control volumes available for carry-over from a spray source. The MXSPJN parameter in subroutine SPRIPT was increased from 10 to 20 and the code was recompiled.

2.3 CALCULATIONAL RESULTS

Summaries of the calculational results are presented in this section. First, Section 2.4 presents a discussion of the dominant phenomena and quantities of interest. Next,

Sections 2.5 and 2.6 present summary results of both earlier CONTAIN analyses and current MELCOR comparisons, respectively.

2.4 Dominant Phenomena and Quantities of Interest

The NUPEC facility and Test M-8-2 provided a well-instrumented and valuable contribution for the understanding of mixing phenomena in containments. The layout of the NUPEC containment is prototypical for a large, dry pressurized water reactor containment. The 1/4 scale lies between other containment testing facilities. NUPEC is larger than Battelle Frankfurt and HEDL but smaller than HDR. NUPEC has several advantages over the larger HEDL facility including a better representation of the dome and lower room partitioning [1].

The key quantities of interest obtained from Test M-8-2 include:

(1) Helium (e.g., simulated hydrogen) mixing;

(2) Spray effectiveness; and

(3) Pressure and temperature response.

The previous CONTAIN assessment concentrated on these phenomena. These key quantities are also the focus of this individual parity assessment report.

2.5 CONTAIN Results

The highlights from the CONTAIN assessment are paraphrased from [2,3] in the following bullets, and are illustrated in Figure 2-5 through Figure 2-12.

Pressure response

- As shown in Figure 2-5, the prediction of the pressure response was poor. The pressure drops rapidly, stops, and slightly recovers during the test. The measured gas temperature also dropped immediately and did not recover, which implies that the gentle rise in pressure late in the test was solely due to the addition of helium. The CONTAIN prediction greatly overestimated the late pressure increase, which may have been due to an underprediction in the amount of steam condensation.

Temperature Response

- The results for the gas temperatures are shown in Figure 2-6 through Figure 2-8. For most compartments, the difference between the predicted and measured gas temperatures was less than 5% on an absolute basis, although the discrepancy was much larger, based on the change in gas temperature. The trend was the same in all of the rooms, with temperatures decreasing considerably within the first 5 minutes of the test and then gradually leveling off. The CONTAIN results captured this trend well with the exception of the peripheral compartments. The calculated temperature response in

peripheral Compartments 4 and 12 (Figure 2-7) was underpredicted due to inadequate mixing with the dome.

Wall Temperatures

- Figure 2-9 shows a comparison of the wall temperatures for a number of rooms. The wall temperatures dropped more slowly than the gas temperatures. Similar to the calculated gas temperature comparisons, the calculated wall temperatures were good in the upper cells but underpredicted the cool-down in the lowest level compartments (Cells 6 and 8). This suggests excessive cooling and mixing in the dome and upper levels, good agreement on the middle level, and inadequate cooling and mixing at the lowest level.

Helium Concentrations

- Figure 2-10 shows the results for the steam generator foundation room and all the rooms vertically above it. Figure 2-11 shows the results for a vertical column of outer rooms (e.g., the lower general compartment and the rooms directly above it). Figure 2-12 shows a number of rooms in the center of the containment including the source room and pressurizer compartment.

- In general, the trends of the predicted results agreed with the data. Typically, the difference between the predicted and measured concentrations was less than 10% and, as shown in Figure 2-10 through Figure 2-12, was generally much better than that. The final concentration in the dome was in excellent agreement with the data.

- The comparison of the calculated and measured helium concentrations in the upper pressurizer compartment was poor, although the calculated trend was in good agreement with the measured results. This poor comparison is directly attributed to the difficulties in modeling mixing in the injection compartment.

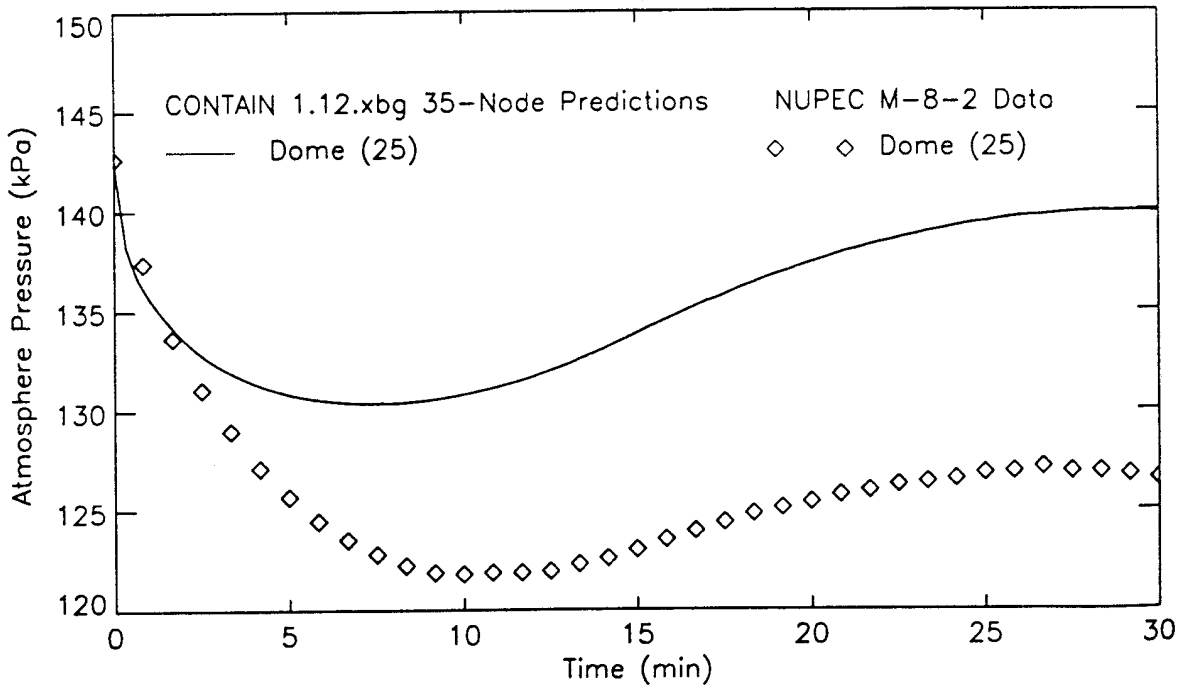

Figure 2-5. Pressure Response: CONTAIN Versus Experiment [2]

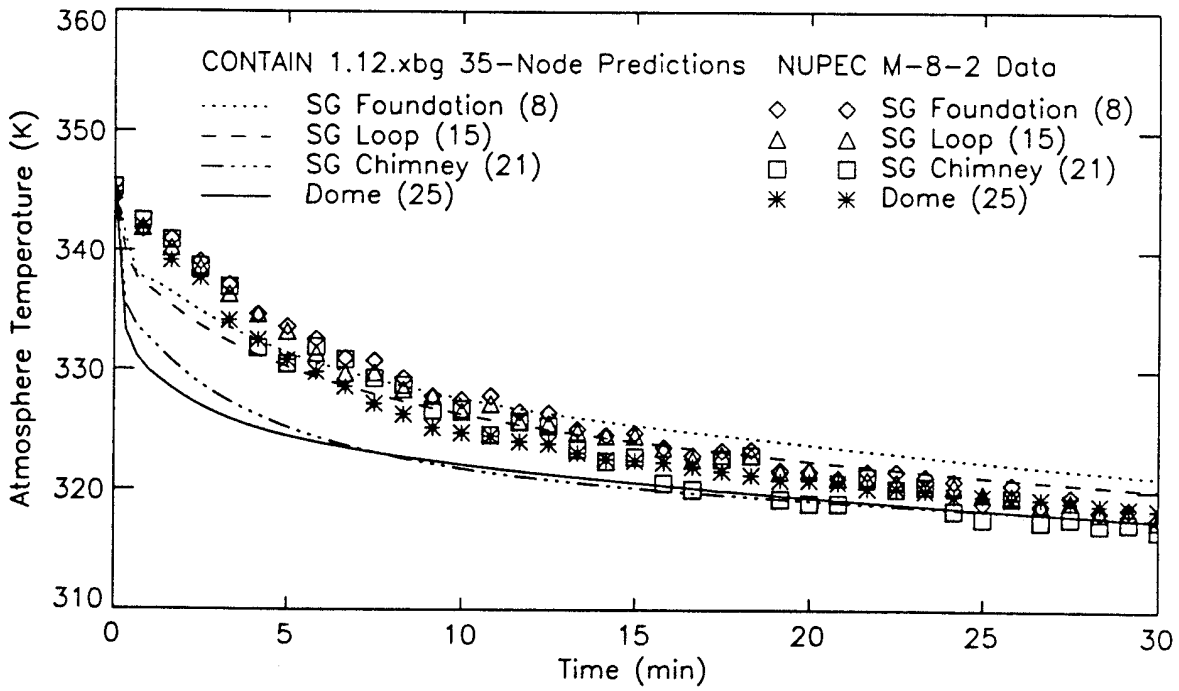

Figure 2-6. Gas Temperature Response in Cells 8, 15, 21, and 25: CONTAIN Versus Experiment [2]

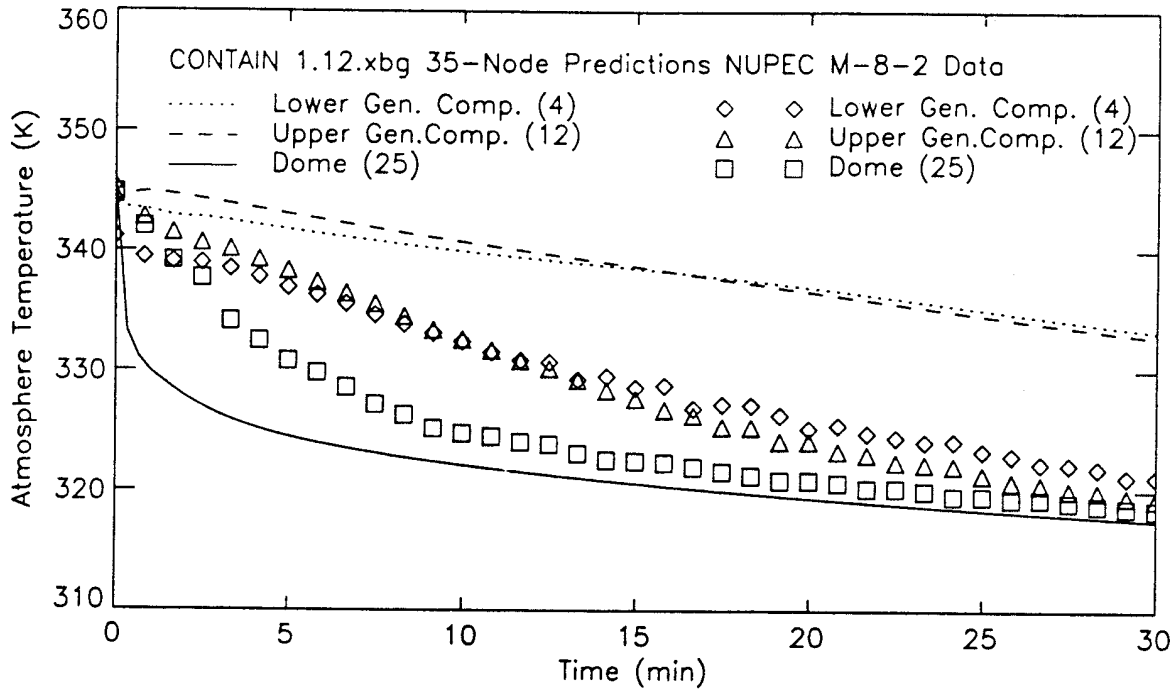

Figure 2-7. Gas Temperature Response in Cells 4, 12, and 25: CONTAIN Versus Experiment [2]

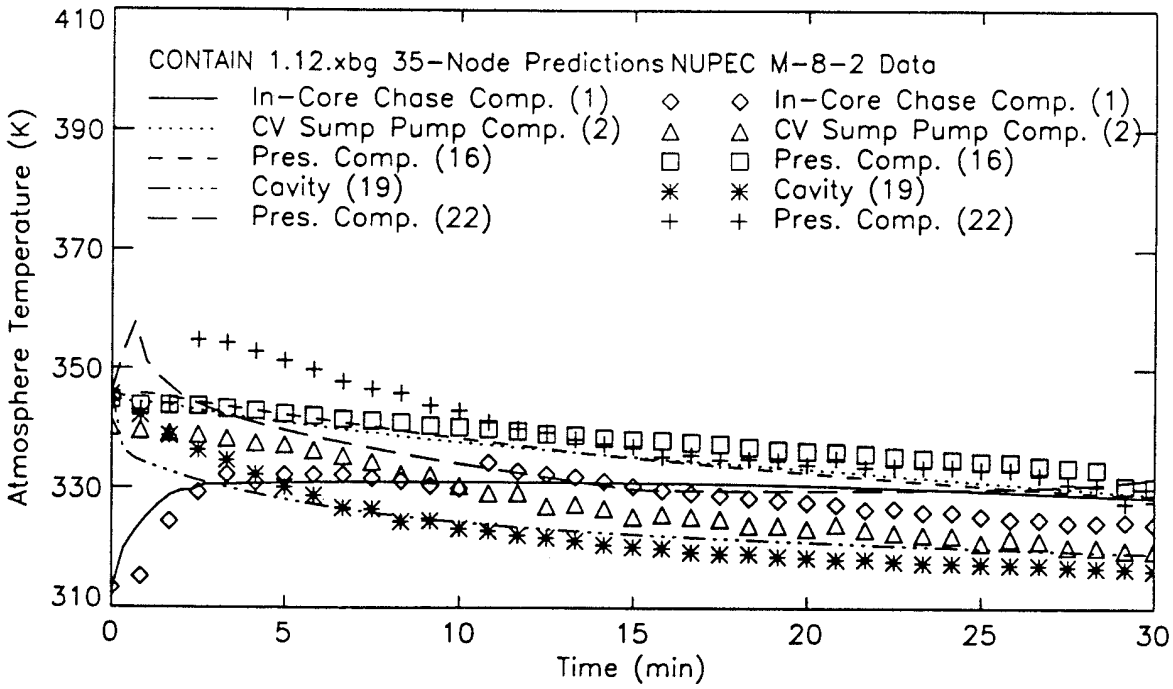

Figure 2-8. Temperature Response in Cells 1, 2, 16, 19, and 22: CONTAIN Versus Experiment [1]

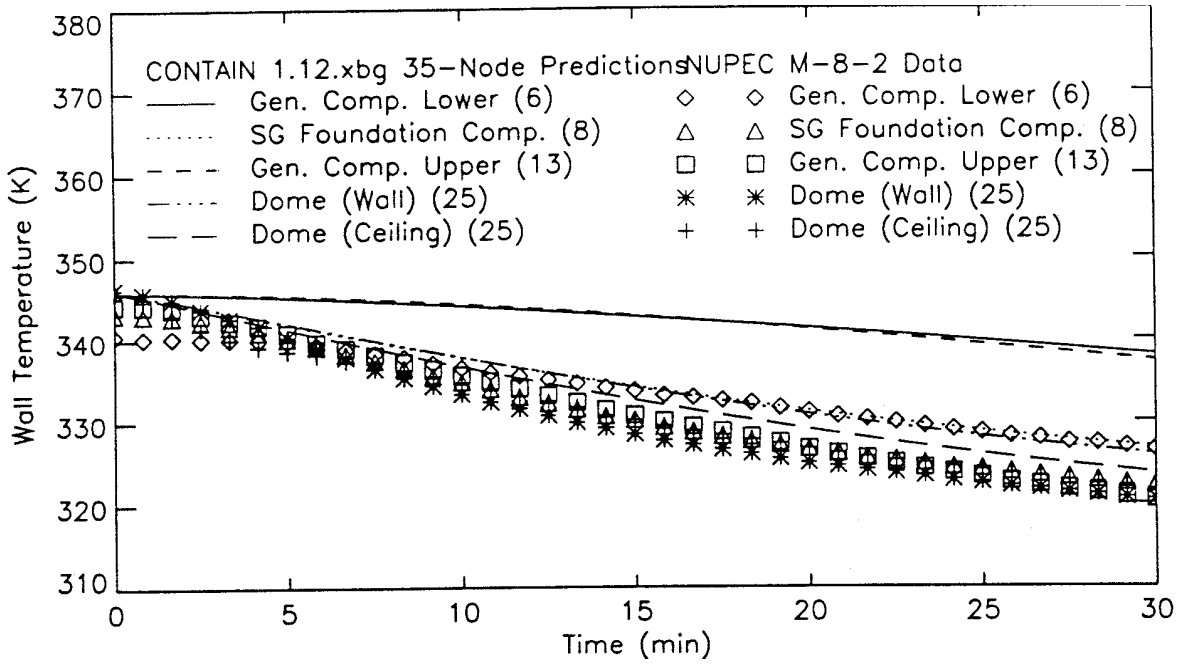

Figure 2-9. Wall Temperature Response in Cells 6, 8, 13, and 25: CONTAIN Versus Experiment [1]

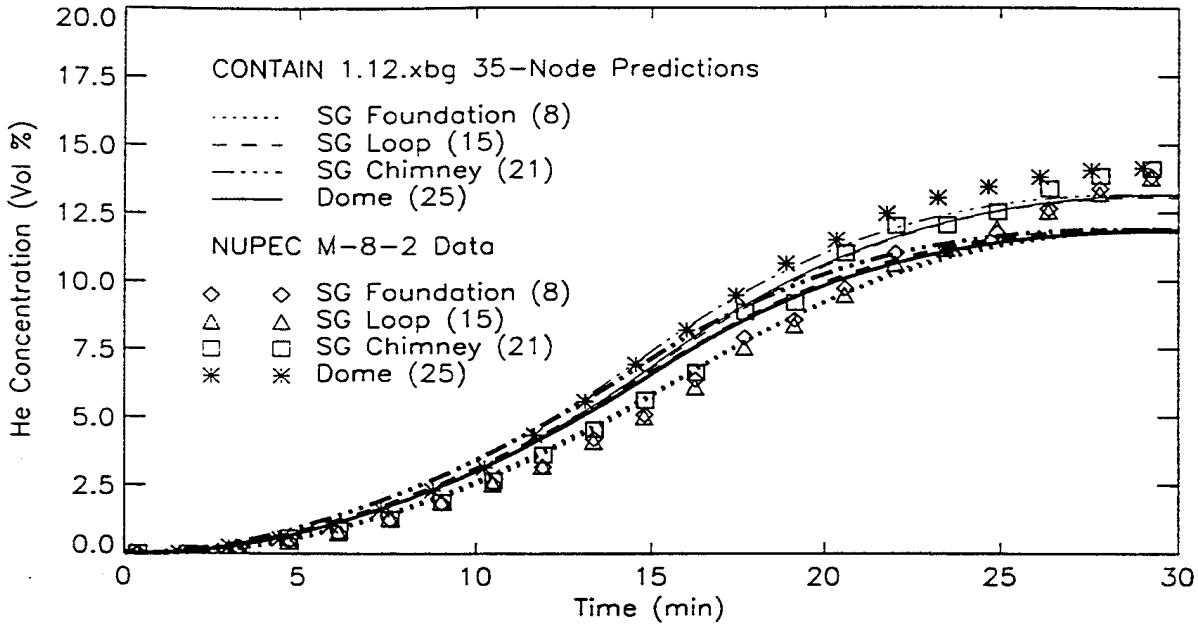

Figure 2-10. Helium Concentrations in Cells 8, 15, 21, and 25: CONTAIN Versus Experiment [2]

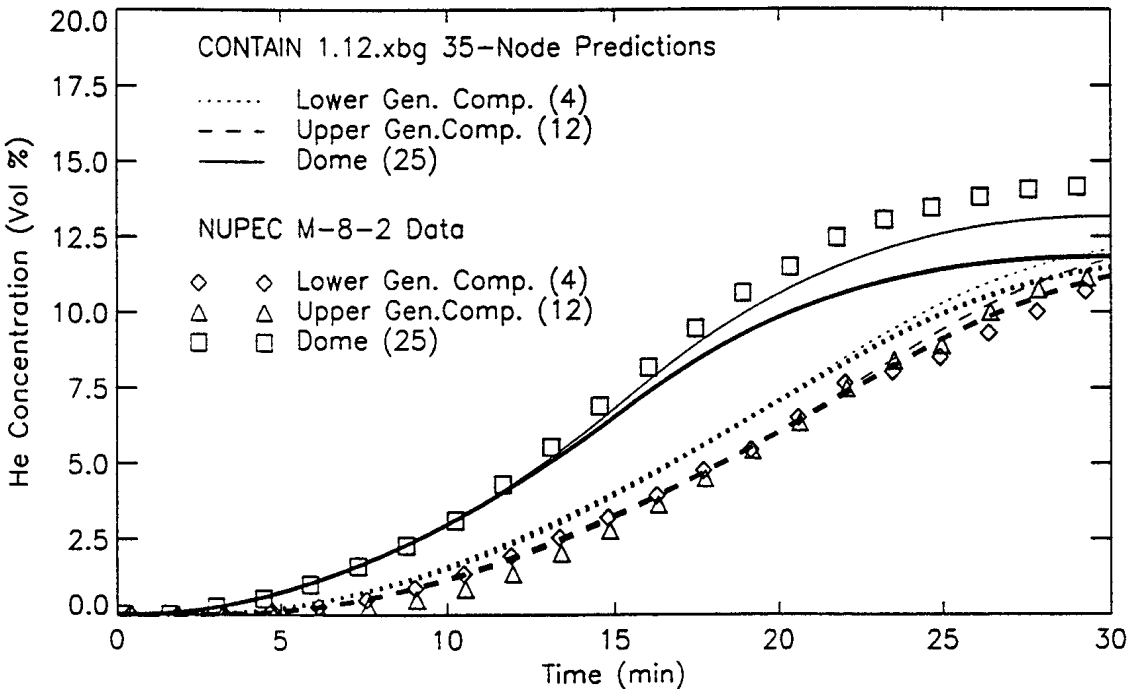

Figure 2-11. Helium Concentrations in Cells 4, 12, and 25: CONTAIN Versus Experiment [2]

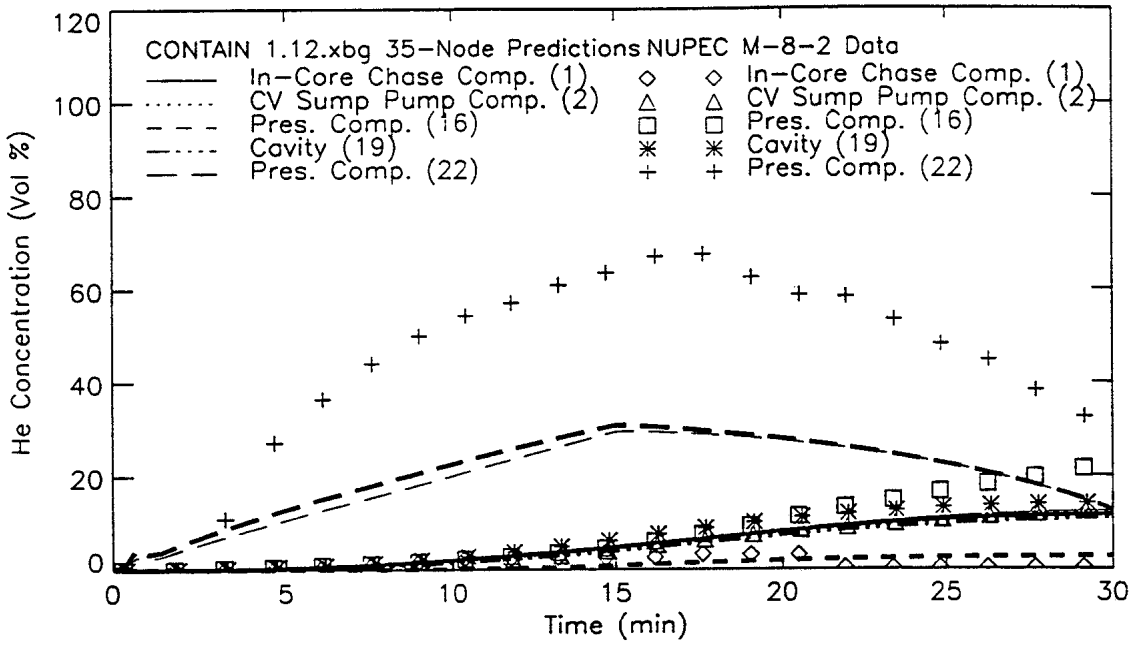

Figure 2-12. Helium Concentrations in Cells 1, 2, 16, 19, and 22: CONTAIN Versus Experiment [2]

2.6 MELCOR Results

As described earlier, a base case and a sensitivity MELCOR calculation were performed. In Section 2.5, the system pressure, 11 control volume gas temperatures, 5 wall temperatures, and 11 helium concentration comparisons were made for the CONTAIN simulation. An identical set of plots was made for the MELCOR calculations. First, the base case will be discussed. The base case represented the base conversion of the CONTAIN input to MELCOR input. Following the base case discussion, the key results from the sensitivity study will be presented.

2.6.1 MELCOR Base Case

The highlights from the MELCOR base case calculation are summarized in the following bullets and illustrated in Figure 2-13 through Figure 2-20.

Pressure response

- Similar to the CONTAIN analysis, the pressure response was not accurately predicted by the MELCOR base case calculation (Figure 2-13). Initially, the calculation followed the data trend; however, the recovery in pressure was greatly overpredicted by MELCOR. Similar to CONTAIN, the MELCOR prediction error was likely due to an underestimation of the condensation of steam.

Temperature Response

- The MELCOR-calculated results for the room gas temperature responses are shown in Figure 2-14 through Figure 2-16. In general, the MELCOR gas temperatures initially dropped more quickly than the measured response. The majority of the MELCOR data followed the temperature trend very well. Like CONTAIN, however, MELCOR underpredicted the temperature drop in the peripheral compartments.

Wall Temperatures

- As shown in Figure 2-17, MELCOR showed very little temperature change in any of the walls. The data showed a significant drop in the wall temperatures that followed behind the gas temperature. The drop in the wall temperature was not as well predicted by MELCOR as by CONTAIN. The sluggishness of the wall response is attributed to not modeling the spray droplet contact with the structures, as noted earlier. The <Spray_Film> sensitivity case presented next will investigate the influence of the spray contact on the structures.

Helium Concentrations

- Figure 2-18 shows the results for the steam generator foundation room and all the rooms vertically above it. Figure 2-19 shows the results for a vertical column of outer rooms (e.g., the lower general compartment and the rooms directly above it). Figure

2-20 shows a number of rooms in the center of the containment, including the source room and pressurizer compartment.

- The general trend in helium concentration for some control volumes was closely modeled by MELCOR; while in others the trend was followed for about 20 minutes into the experiment before the MELCOR prediction leveled off and lost the data trend. For that reason, the CONTAIN calculations produced slightly better results for helium concentrations than did the MELCOR calculations for a few of the lower and peripheral control volumes.

- The pressurizer compartment response was in better agreement with the data than the CONTAIN model; however, MELCOR overestimated the mixing between the pressurizer compartment and the dead-end compartment below it (CVs 22 and 16, respectively). Consequently, the helium concentration response of dead-end Compartment 16 followed CV 22. In the test, very little helium propagated into Compartment 16.

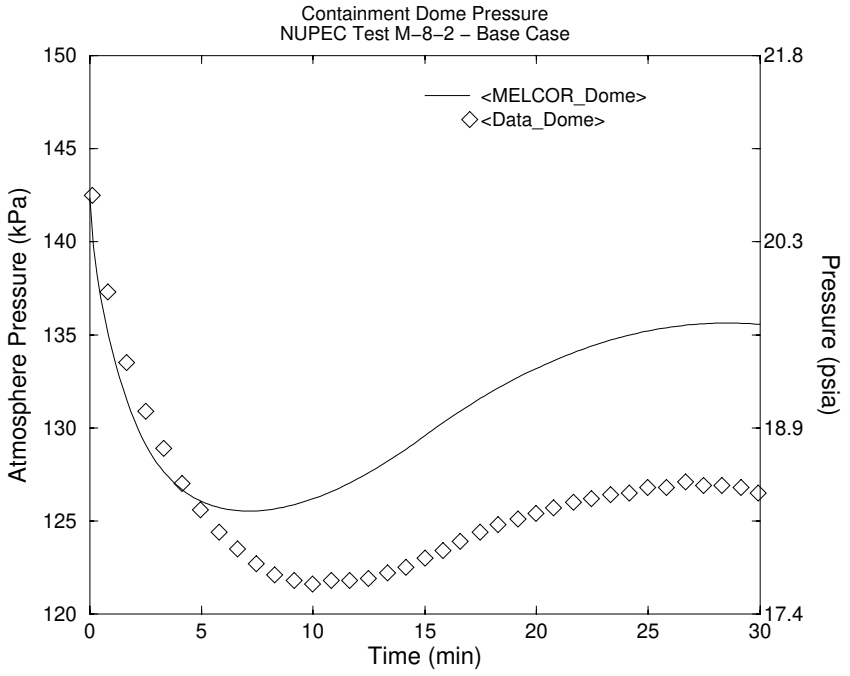

Figure 2-13. Pressure Response: MELCOR Versus Experiment

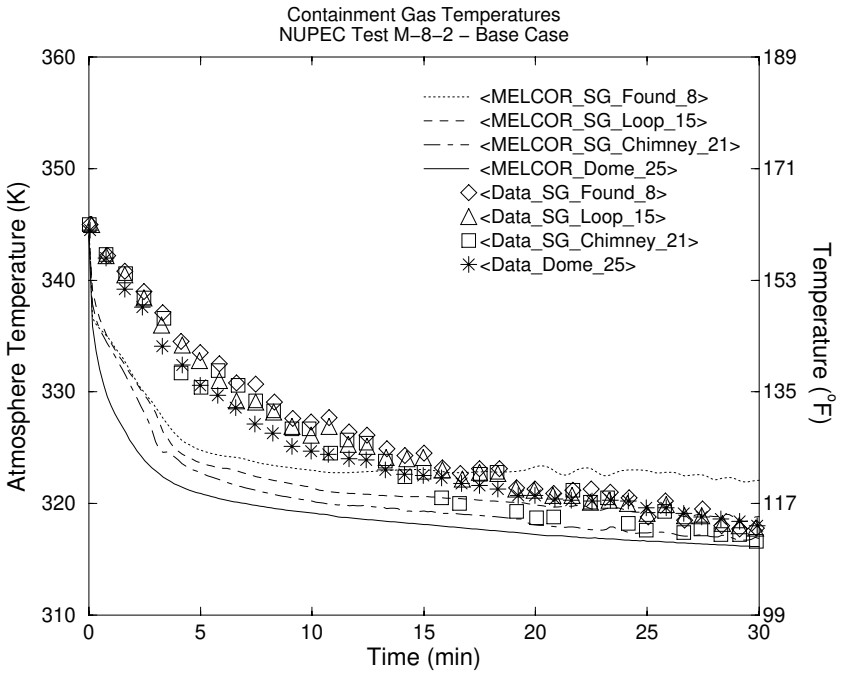

Figure 2-14. Gas Temperature Response in CVs 8, 15, 21, and 25: MELCOR Versus Experiment

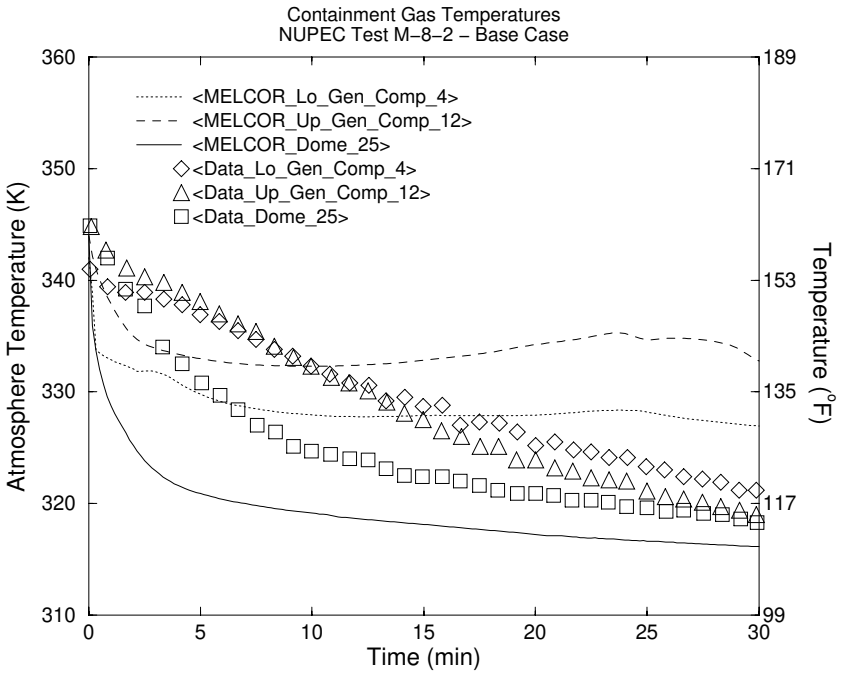

Figure 2-15. Gas Temperature Response in CVs 4, 12, and 25: MELCOR Versus Experiment

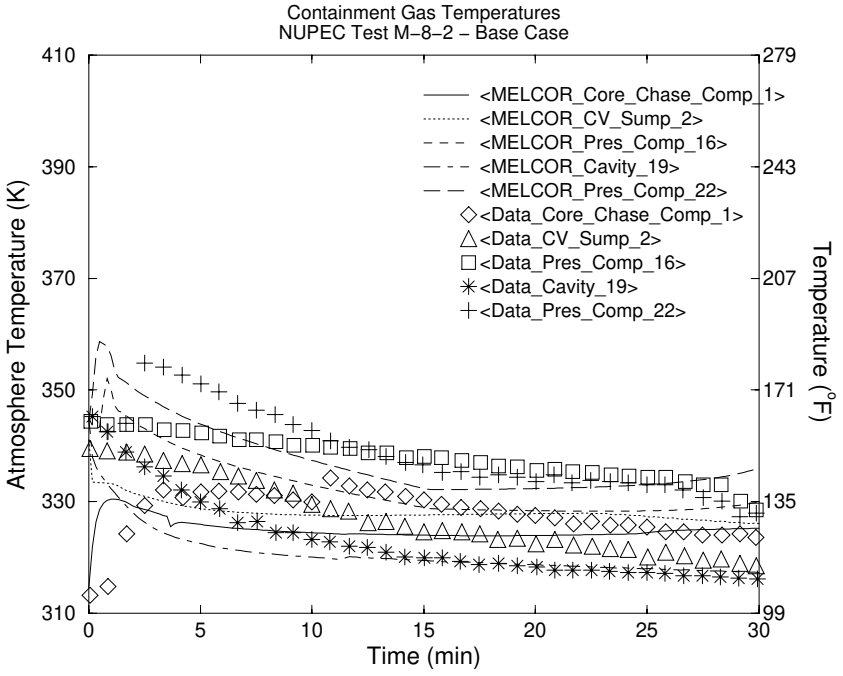

Figure 2-16. Gas Temperature Response in CVs 1, 2, 16, 19, and 22: MELCOR Versus Experiment

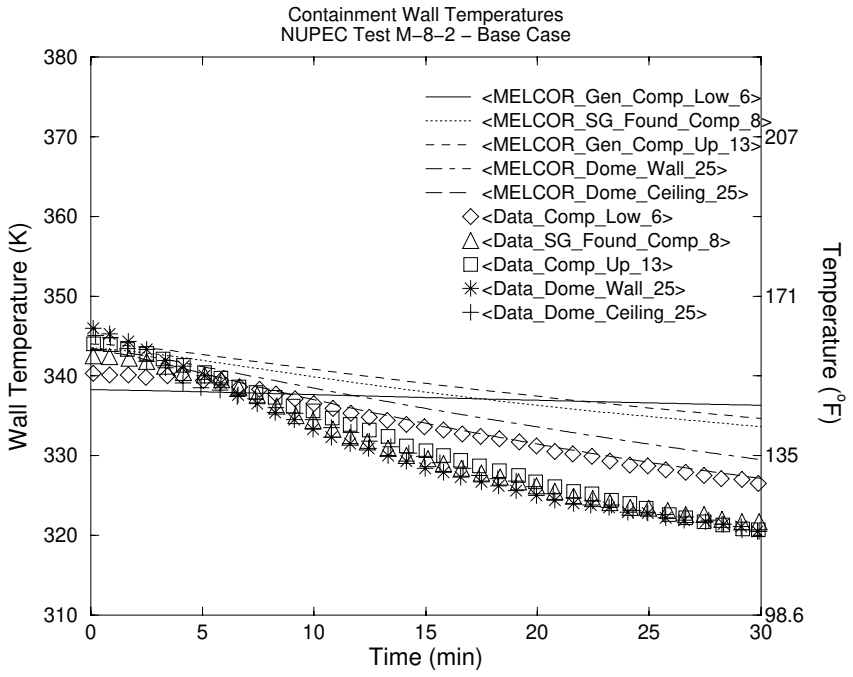

Figure 2-17. Wall Temperature Response in CVs 6, 8, 13, and 25: MELCOR Versus Experiment

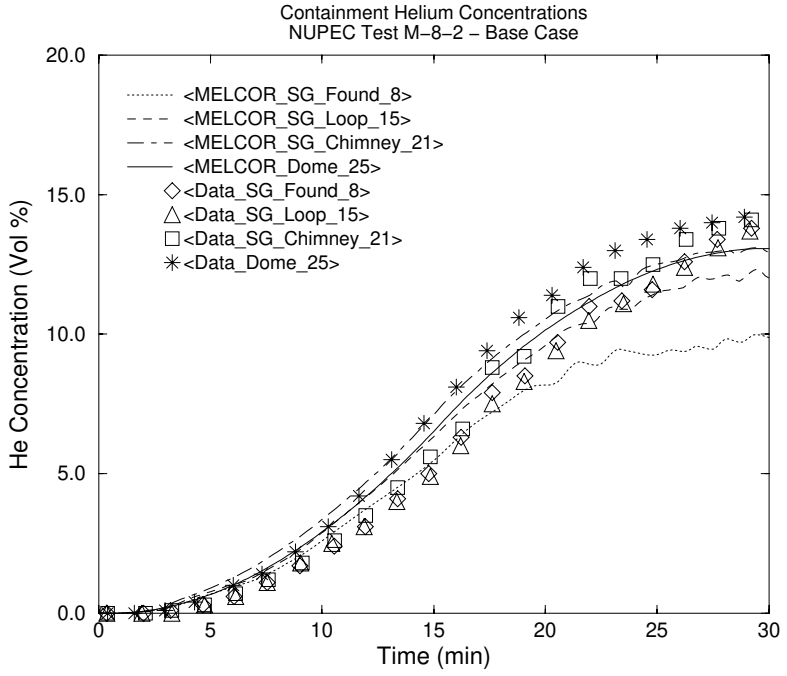

Figure 2-18. Helium Concentrations in CVs 8, 15, 21, and 25: MELCOR Versus Experiment

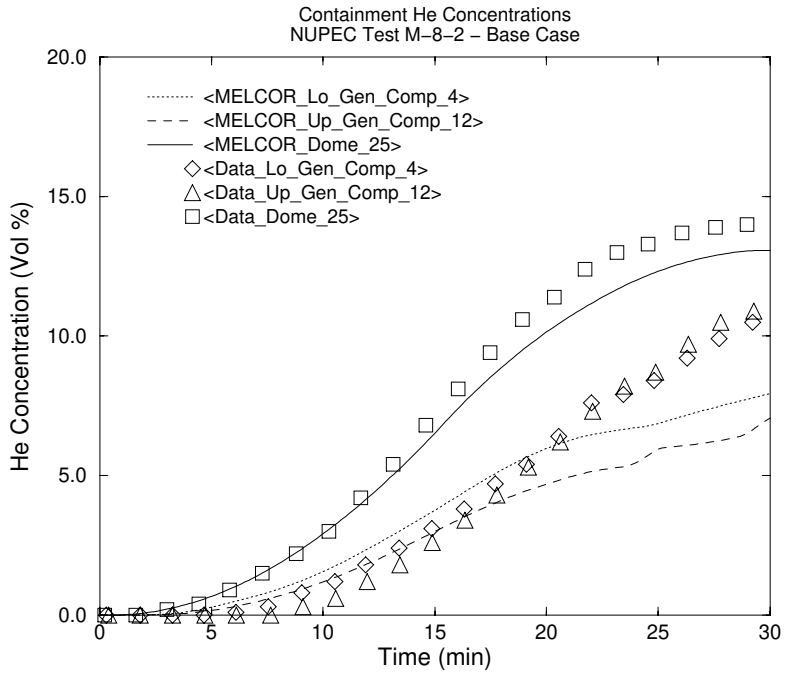

Figure 2-19. Helium Concentrations in CVs 4, 12, and 25: MELCOR Versus Experiment

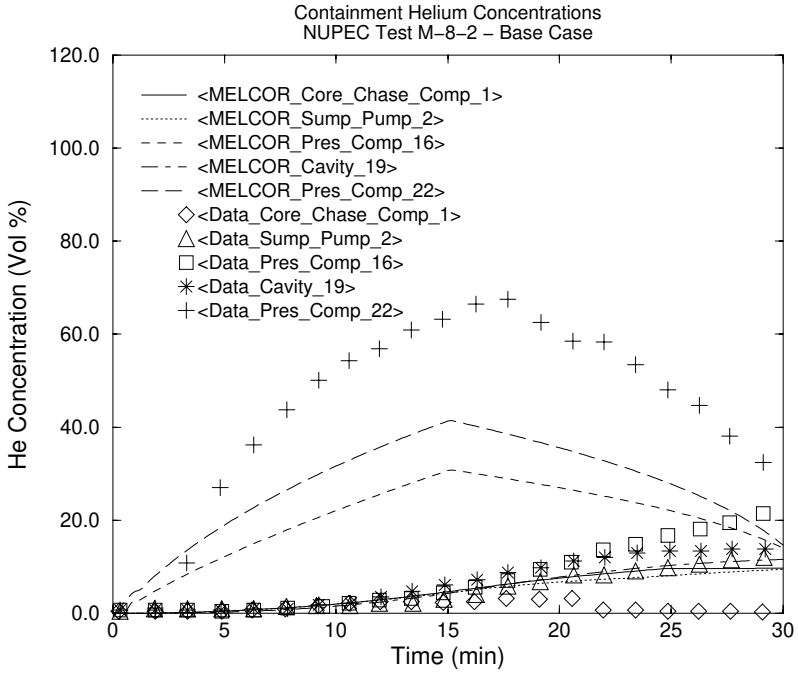

Figure 2-20. Helium Concentrations in CVs 1, 2, 16, 19, and 22: MELCOR Versus Experiment

2.6.2 MELCOR Sensitivity Case

As described earlier, a sensitivity calculation was performed that allowed the spray droplets to first interact with the dome atmosphere and then to impact the dome wall, the refueling floor, the refueling pool, and the steam generator compartment walls above the refueling floor. A set of seven film networks was developed to permit interaction of the spray droplets with the heat structures.

Pressure response

- The <Spray_Film> pressure response was substantially improved by the addition of the film network. The drop in pressure and recovery is in good agreement with the data. This suggests that the impact of the films on structure cooling and condensation of steam is very important.

Temperature Response

- The sensitivity results for the room gas temperature responses still overpredicted the decrease in temperature in the upper dome. However, the prediction of nearly every other gas temperature improved. In particular, the calculated temperature trends in the peripheral regions (CVs 4 and 12), the Steam Generator D Compartments (CVs 8, 15, 21), and the cavity (CV 21) were all in better agreement with the data. Trends calculated in the other central compartments (CVs 1, 2, 16, and 22) were smoother than the base case. The calculated wall temperatures overpredicted the measured decrease in temperature. However, the warmer trend of the General Compartment 6 was correctly predicted. It appears that the spray networks would need more balancing to better predict the measured temperature decrease.

Helium Concentrations

- In general, the helium concentration response in the base case and the <Spray_Film> sensitivity case were similar. The largest difference came in the lower two levels of Steam Generator Compartment D (CVs 8 and 15). The presence of the film network reduced the overall mixing to the lower locations of the containment. When the helium source rate decreased after 15 minutes,[1] the calculated amount of mixing to the lower cells decreased. In contrast, the data shows steady mixing throughout the calculation. As noted in the CONTAIN reports, an underprediction in the mixing during the containment spray tests was attributed to the lack of any momentum transfer between the spray droplets and the vapor in the containment spray model.

[1] As noted in Table 2-1, the helium source ramped from 0 to 0.03 kg/s and then decreased back to 0 kg/s. The peak injection rate, 0.03 kg/s, occurred at the halfway point in the test, or 15 minutes.

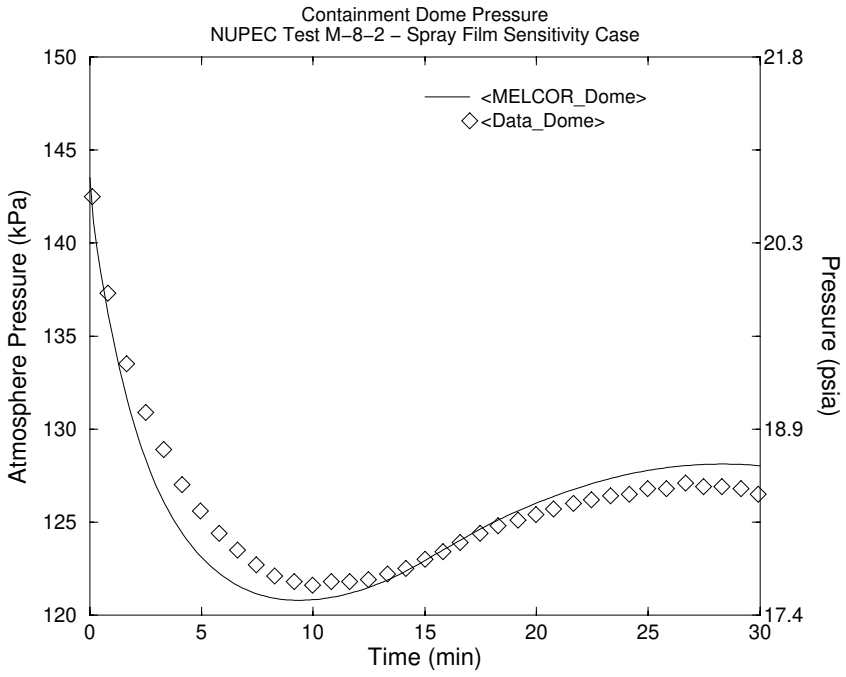

Figure 2-21. Pressure Response in Test Facility: MELCOR <Spray_Film Sensitivity Case> Versus Experiment

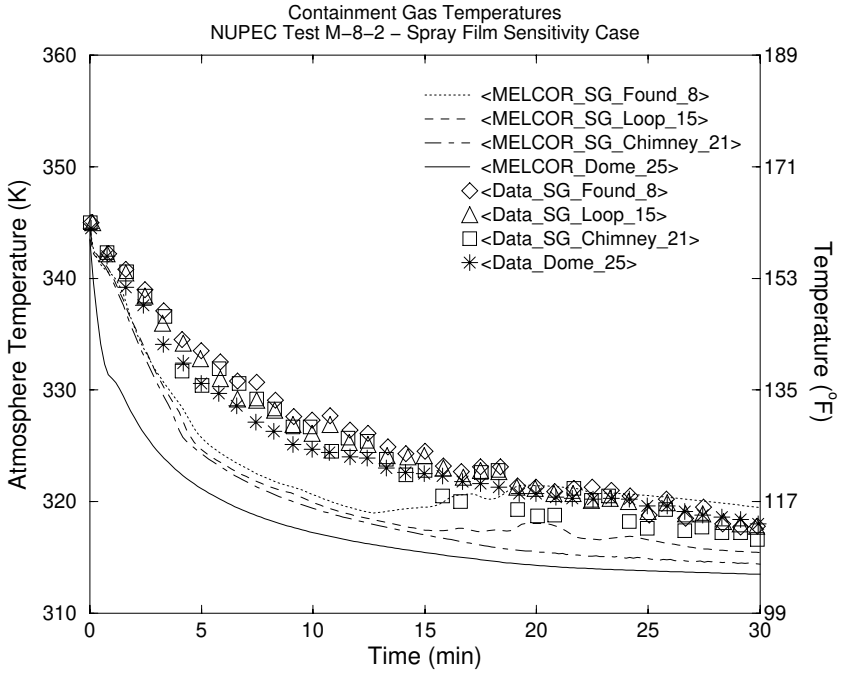

Figure 2-22. Gas Temperature Response in CVs 8, 15, 21, and 25: MELCOR <Spray_Film Sensitivity Case> Versus Experiment

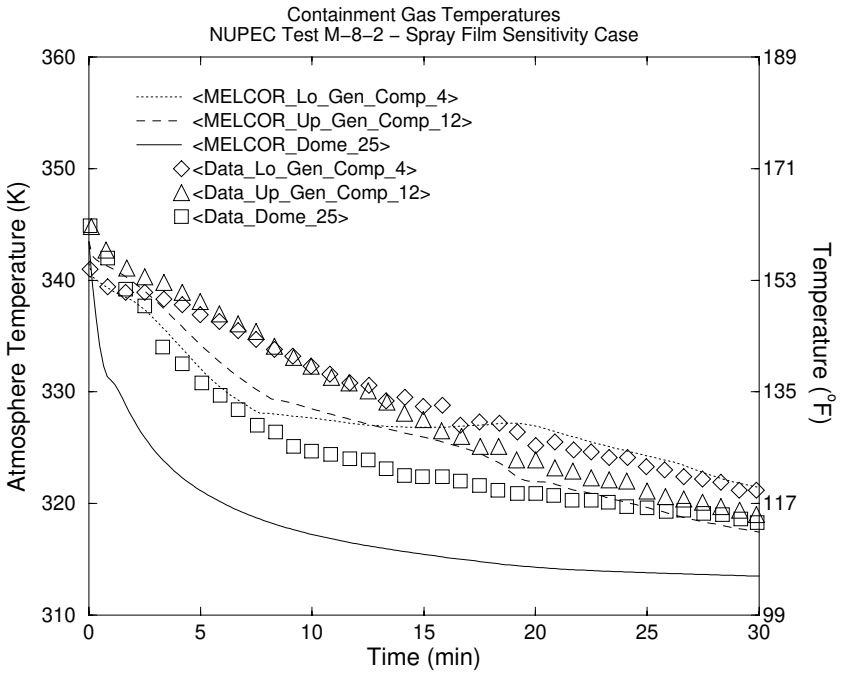

Figure 2-23. Gas Temperature Response in CVs 4, 12, and 25: MELCOR <Spray_Film Sensitivity Case> Versus Experiment

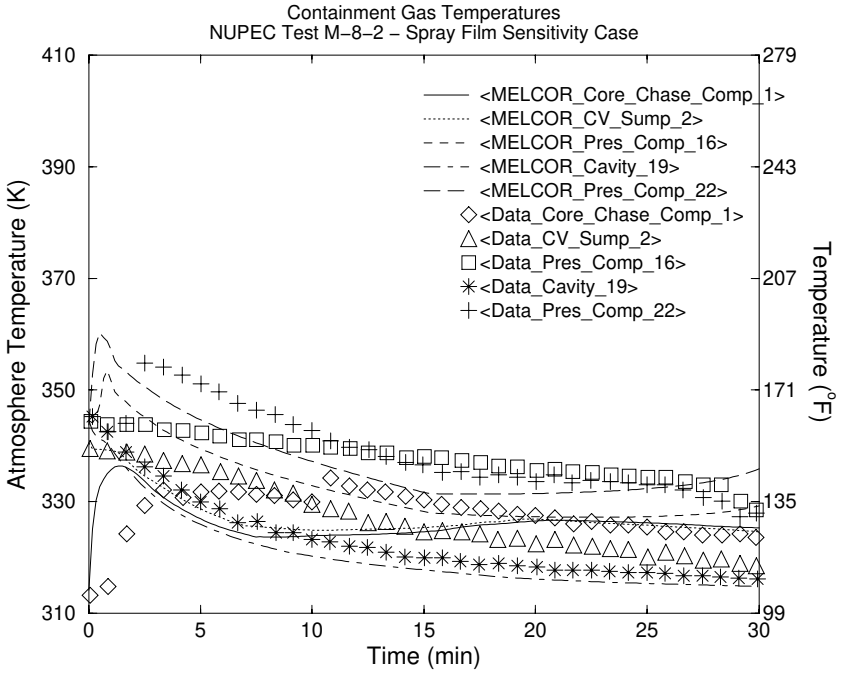

Figure 2-24. Gas Temperature Response in CVs 1, 2, 16, 19, and 22: MELCOR <Spray_Film Sensitivity Case> Versus Experiment

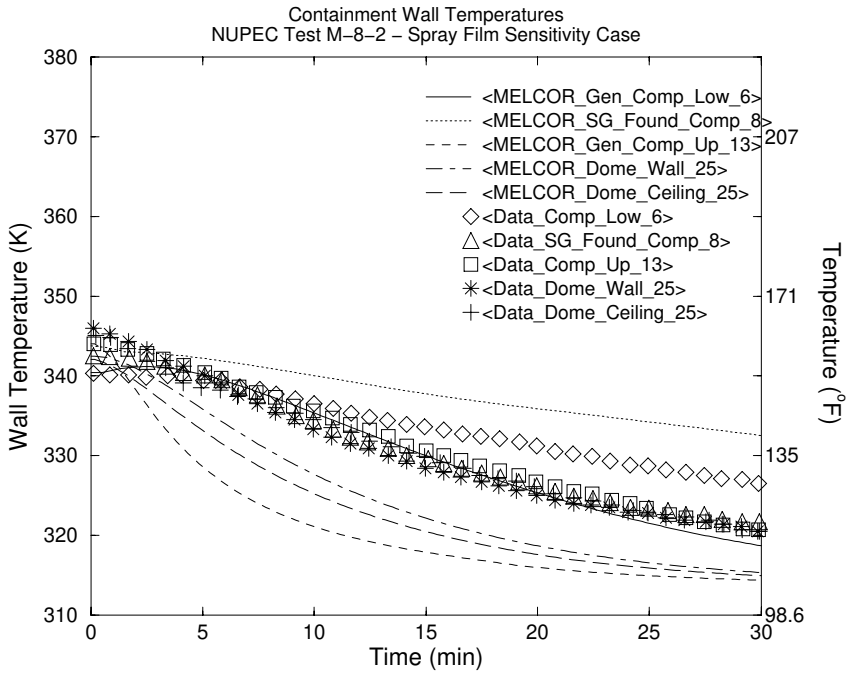

Figure 2-25. Wall Temperature Response in CVs 6, 8, 13, and 25: MELCOR <Spray_Film Sensitivity Case> Versus Experiment

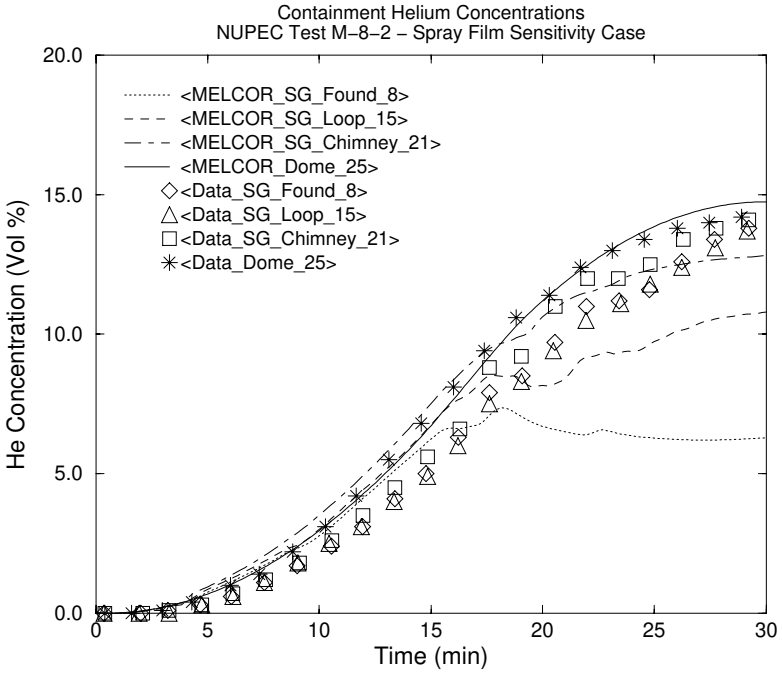

Figure 2-26. Helium Concentrations in CVs 8, 15, 21, and 25: MELCOR <Spray_Film Sensitivity Case> Versus Experiment

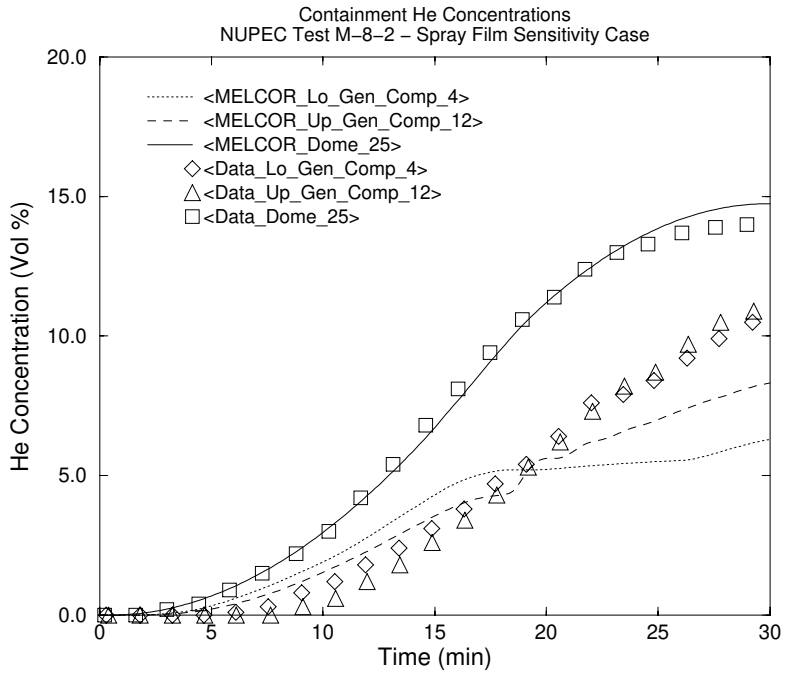

Figure 2-27. Helium Concentrations in CVs 4, 12, and 25: MELCOR <Spray_Film Sensitivity Case> Versus Experiment

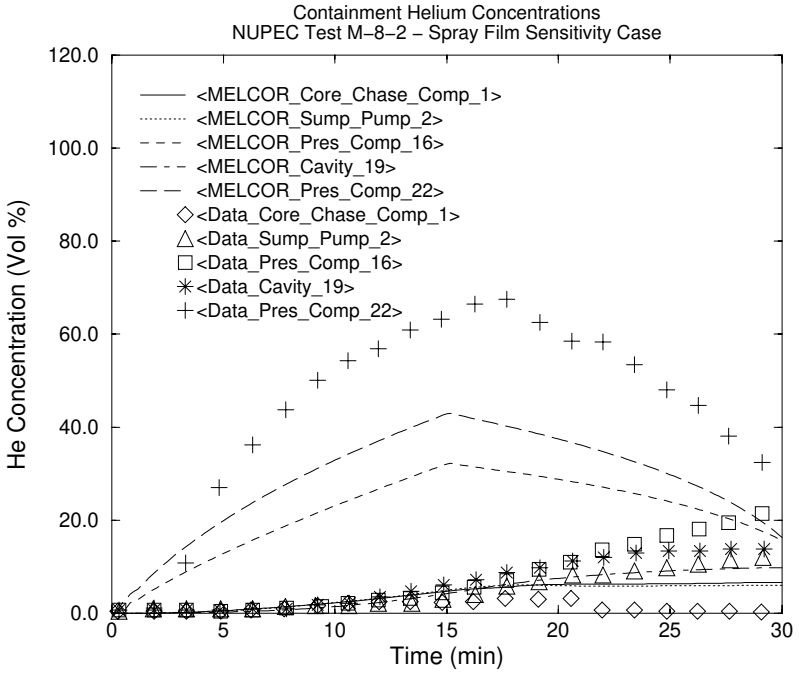

Figure 2-28. Helium Concentrations in CVs 1, 2, 16, 19, and 22: MELCOR <Spray_Film Sensitivity Case> Versus Experiment

2.7 Discussion of Results

A MELCOR model of the 1/4-scale NUPEC facility was developed from an existing CONTAIN model. The new MELCOR model was assessed against test data from Test M-8-2. Comparisons from a previous CONTAIN assessment of Test M-8-2 are presented and discussed below.

2.8 CONTAIN Results

The CONTAIN comparison to the test data was good, with the exception of pressure. The predictions of the gas temperature and helium distributions were both individually good. It should be noted that significant augmentation of several heat transfer coefficients and numerous sensitivity studies were performed before there was a good code prediction of the test. The following assessments were made:

Hydrogen Mixing

- Most of the compartments tracked the test results very closely with the exception of the pressurizer compartments (Cells 16 and 22). The larger discrepancy here was attributed to the difficulty in modeling injection compartments and dead-end compartments.

Temperature Distribution

- Most of the gas temperature responses tracked the data trends very closely. Some larger differences were noted in the peripheral compartments and in the wall temperature response.

Spray Performance

- The pressure response was not well predicted; however, the dome temperature response and induced mixing were well calculated. The poor pressure response and inadequate mixing were attributed to the lack of coupled hydraulic effects from the spray operation [2].

2.9 MELCOR Results

The MELCOR base case comparison to the test data was generally good, with the exception of pressure, and generally replicated the same trends predicted by the CONTAIN code analysis.

Hydrogen Mixing

- The MELCOR simulation generally tracked the measured helium concentrations in the dome and the upper compartments well. In the lower regions of the containment, the

degree of mixing decreased once the helium source decreased (e.g., after 15 minutes). In contrast, the data showed strong mixing and a uniform build of helium during the whole test.

Temperature Distribution

- The dome temperature and the temperature of most of the rooms was well predicted by MELCOR. The trends were followed for the duration of the test, and the final temperatures were typically within a few K of the measured data. Certain compartments were not as well predicted, and some lower and peripheral compartments showed temperature errors of up to 20 K.

Spray Performance

- As in the CONTAIN analysis, the MELCOR-predicted pressure response compared relatively poorly with the experiment. The mixing was underpredicted by MELCOR in this test (especially after the helium source decreased), and the predicted gas and helium concentrations showed more variation than the measured data. The spray sensitivity case produced markedly improved pressure predictions by allowing the sprays to cool the heated structures in the test vessel, which subsequently permitted continued steam condensation and lower atmosphere pressure.

2.10 Recommendations

The present MELCOR spray models do not directly account for the hydraulic and structural interaction effects from the droplet field. One potential area for future code development and user convenience is to add/improve spray package coupling to the momentum solution, local heat transfer rates, and the heat structure film-tracking model. Any momentum effects from the spray operation are not included in the MELCOR heat transfer package unless directly specified by the user. In addition, it is very time-consuming and awkward to set up the film flow networks and direct sprays to the heat structures. It is recommended that this input be improved to facilitate spray contact with heat structures. Without complicated heat structure film networks and redirection of spray water into the network, the water from the containment sprays does not interact with the structures.

These problems are characteristic of the limitations associated with the control volume methodology. For some sequences, momentum is induced and stored locally in a control volume by such features as spray systems or turbulent conditions generated by blowdown events. Both CONTAIN and MELCOR treatments of forced convection require that stand-alone calculations be made and the results factored into the code to supply heat transfer rates that are appropriate for these conditions. Currently, CONTAIN is more flexible in its approach to adding the characteristics of induced convective flows as input for use in calculating heat transfer rates to containment structures. As a first approach, it is recommended (short of detailed modeling of forced convection and spray/structures interaction effects) that the MELCOR code be provided with the level of flexibility currently residing in the CONTAIN code with respect to this capability. MELCOR's highly flexible

control function capability could be used to good effect in implementing a more general scheme for providing a time dependent local flow velocity for application to forced convection heat transfer.

2.11 References

1. Nuclear Power Engineering Corporation (NUPEC), System Safety Department, “Specification of ISP-35 – NUPEC’s Hydrogen Mixing and Distribution Test—Test M-5-5”, ISP35-027, Revision 1, NUPEC, November 3-4, 1993.
2. Stamps, D. W., “CONTAIN Assessment of the NUPEC Mixing Experiments,” SAND94-2880, August 1995.
3. Stamps, D. W., Murata, K. K., “CONTAIN Assessment of the NUPEC Mixing Experiments—Supplement 1,” SAND94-2880, August 1995.

3. Analysis of the LACE LA-4 Experiment

3.1 Background

An important element in the assessment of MELCOR 1.8.5 involves the baselining of the code against the previous version (1.8.4). The matrix of calculations for implementing this procedure includes both analyses of experiments, which may look at a limited number of phenomena, and analyses of plant calculations, which may run the entire range of phenomena associated with reactor accidents. This assessment will evaluate the new version with respect to its application for the analysis of the LACE LA-4 experiment.

The new models that most strongly affect the results for the LA-4 analysis are those associated with the aerosol calculations. In particular, the modeling for hygroscopic effects has been modified in the 1.8.5 code version. In MELCOR 1.8.4 hygroscopic effects were treated such that all of the aerosol material components were treated as soluble even though some components were insoluble. The revised model in MELCOR 1.8.5, although not treating two totally distinct aerosol fields, includes modifications in the RN1 package that provide for the calculation of an *average* set of hygroscopic parameters based on the solubility and ionization potential for each species present in the aerosol. The LA-4 experiment presents an ideal case to run with the 1.8.5 modification to the aerosol dynamics models, because it was specifically designed to address hygroscopic effects in aerosol with varying solubility.

The LACE LA-4 experiment was conducted by the Westinghouse Hanford Company in the Containment Systems Test Facility (CSTF) [1]. The test, performed on August 21, 1986, was designed to simulate containment conditions in an LWR severe accident with late containment failure. The purpose of the experiment was to determine the disposition of aerosols in the containment building under conditions of high steam concentrations. Of particular interest was the difference in aerosol disposition between hygroscopic (water-soluble) aerosols such as CsOH and nonhygroscopic aerosols in a high steam concentration. CsOH is a highly hygroscopic material, while MnO is nonsoluble and essential nonhygroscopic.

The experiment involved six separate phases. The initial phase was characterized by the introduction of steam into the CSTF vessel to preheat the atmosphere by about 70 K above ambient conditions and to establish the desired steam concentration. This period lasted about 3000 seconds. Following the heatup phase were three periods lasting 1830, 1200, and 1782 seconds, in which aerosols were injected: first CsOH only; then, CsOH and MnO; and finally, MnO only. The last two phases consisted of a long steady-state period that lasted about 12,000 seconds, and a venting and cooling phase lasting about 19,200 seconds.

Figure 3-1 shows a rough sketch of the CSTF containment vessel. The figure shows the locations of the vent and aerosol injection lines as well as the locations where heat and

mass transfer rates were measured. Steam was injected through the steam line near the bottom of the vessel during the heatup phase and continued at a reduced rate during the experiment phase to maintain a steady-state condition. The aerosol injection line was located at about the mid-plane of the vessel. Nitrogen gas and steam were used as the carrier medium for the aerosol injection through this line.

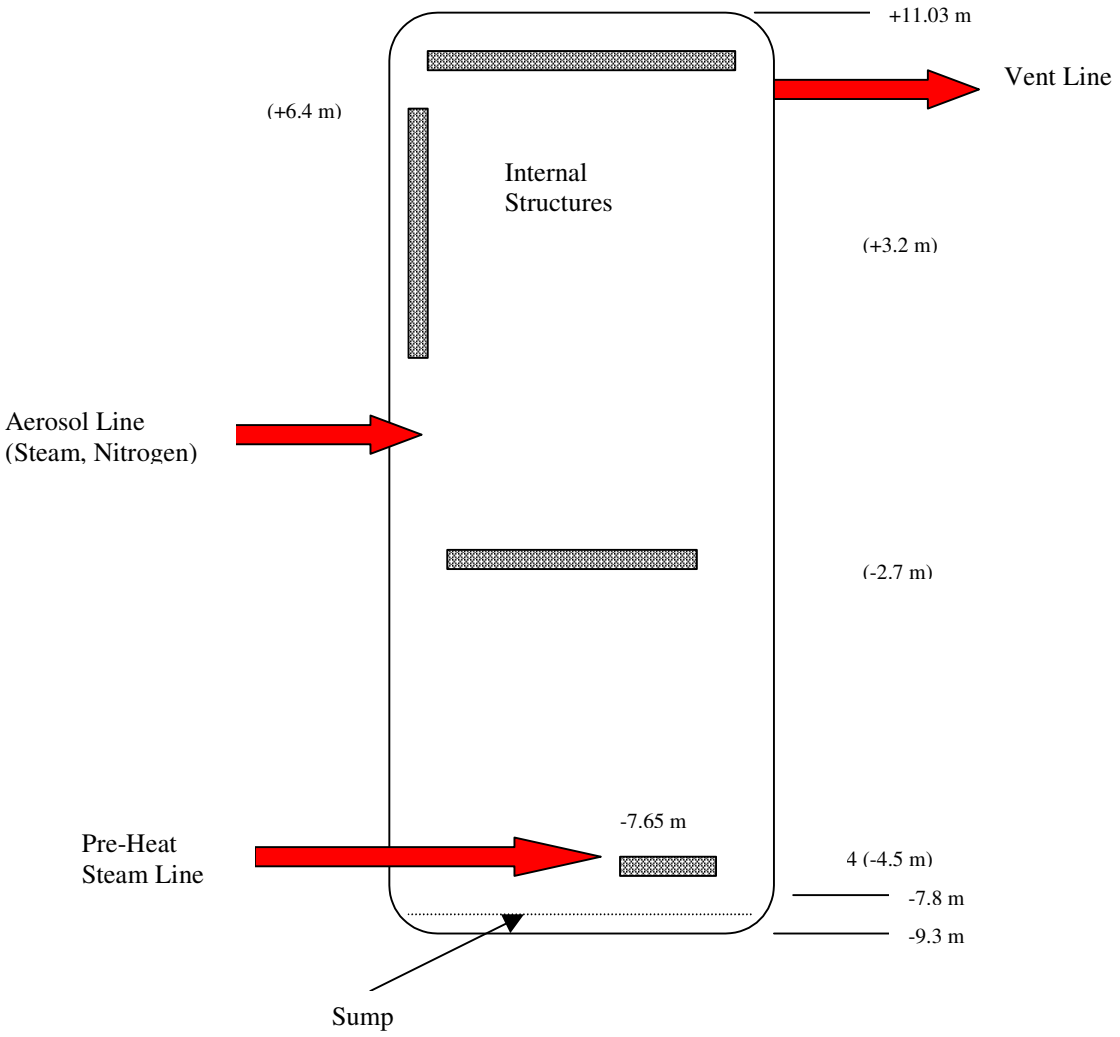

Figure 3-1. Diagram of the LACE LA-4 Experiment Test Vessel

The atmospheric aerosol concentration was determined by taking filter samples at intervals during the test. These samples were later subjected to chemical analysis to determine quantity and composition. The samples were taken both by through-the-wall samplers and by samplers suspended at various locations within the vessel atmosphere.

3.2 Nodalization

The LA-4 experimental configuration was modeled with the MELCOR code using a single control volume for the vessel and two environment volumes, one to receive the vent discharge during the vent-down phase and the other to act as the sink for leakage. A previous MELCOR analysis of this experiment was used as a starting point for this analysis [2]. (See Figure 3-2 for a diagram of the MELCOR nodalization.) Saturated steam sources were injected into the vessel at the lower steam line elevation in accordance with the measured data. The carrier gases (nitrogen and steam) were injected into the vessel at the elevation of the aerosol injection line as per the measured rates. Appropriate enthalpy sources associated with the mass sources are applied as well as the enthalpy (energy) source associated with the lighting in the vessel. Aerosol sources were input in the RNASnn card at the times and rates given in Table 3-1. The CsOH was sourced into Class 2 and the MnO was sourced into Class 7. Both the hygroscopic and nonhygroscopic aerosol classes and the water aerosol class were modeled as separate aerosol components. The important vessel structures (heat sinks) were modeled using 6 heat structures.

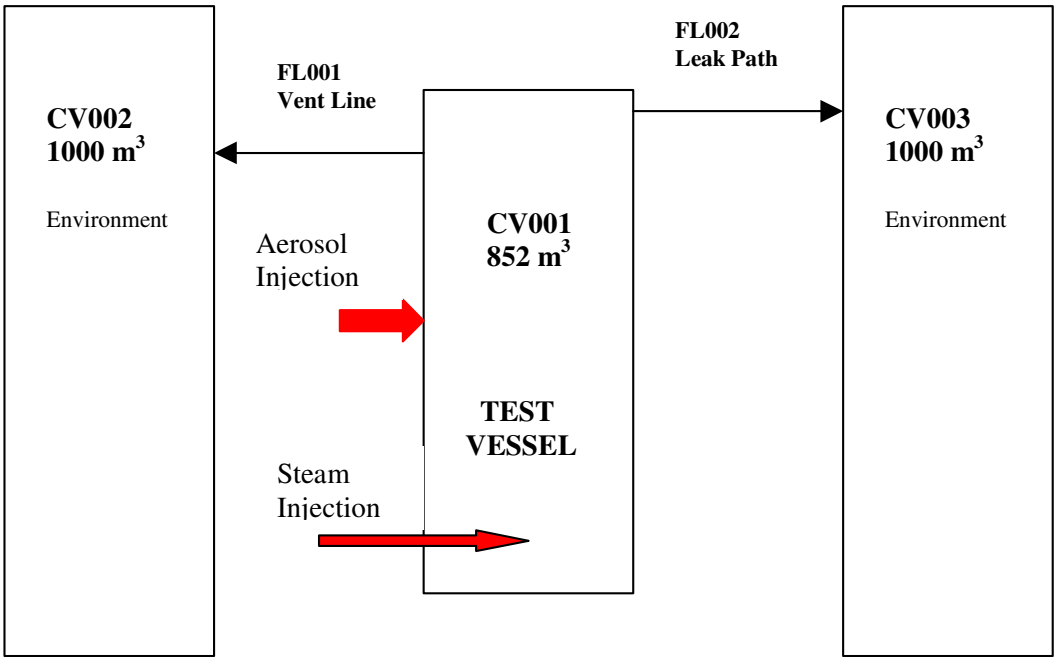

Figure 3-2. LACE LA-4 MELCOR Model Nodalization

Table 3-1. Average Aerosol Injection Input Parameters for LACE LA-4.

Period	Start (s)	End (s)	Aerosol	Rate (g/s)	AMMD** (μm)	GSD**
2–CsOH Only	0	1830	CsOH	0.949	1.35	1.81
3–CsOH + MnO	1830	3030	CsOH MnO	0.949 0.757	2.22 2.43	1.80 1.70
4–MnO Only	3030	4812	MnO	0.757	1.82	2.56

** AMMD – aerodynamic mass mean diameter, GSD – geometric standard deviation

3.3 MELCOR Input Specifications

Results of an earlier MELCOR assessment of the LA-4 experiment using code version 1.8.1 were published in 1991. The MELCOR 1.8.1 version did not have a model for the hygroscopic process. However, the basic input model for that assessment was used here with the appropriate modifications for 1.8.4 and 1.8.5 compliance. With respect to the aerosol specific input specification, no changes were required to the regular input parameters; but the 1.8.5 version required changes to the aerosol solubilities on the 7170 sensitivity coefficients for the two aerosol components (water and solid materials).

3.4 Results of Analysis

3.4.1 Thermal-Hydraulic Response

Although the thermal-hydraulic response of the test vessel is not the primary purpose of the LA-4 experiment, an adequate calculation of the pressure, temperature, and steam mole fraction are nevertheless very important elements of the aerosol dynamics calculations. To get these conditions right, it was necessary to model the steam and gas sources, the aerosol sources, and the heat structures associated with the walls and internals of the test vessel in considerable detail.

No changes were made between the input deck descriptions of the control volumes, flow paths, or heat structures for the MELCOR 1.8.4 and the 1.8.5 calculations. The pressure response of the test vessel is shown in Figure 3-3 and Figure 3-4 for the 1.8.5 and the 1.8.4 calculations, respectively. As expected, there are essentially no differences seen in the pressure responses for the two code versions. The comparisons of total and steam partial pressures with measured data also agree well for these calculations. Similarly, the vessel atmospheric temperatures agree very well between the two calculations and with the measured data as seen in Figure 3-5 and Figure 3-6. These two figures also show the measured and calculated pool temperatures, which agree well for the two code versions, but do not agree quite so well with the measured pool temperature. Here, the code appears to slightly overestimate the pool temperature during injection phase for both versions. The aerosol calculations, however, are not strongly influenced by these small differences in pool temperature.

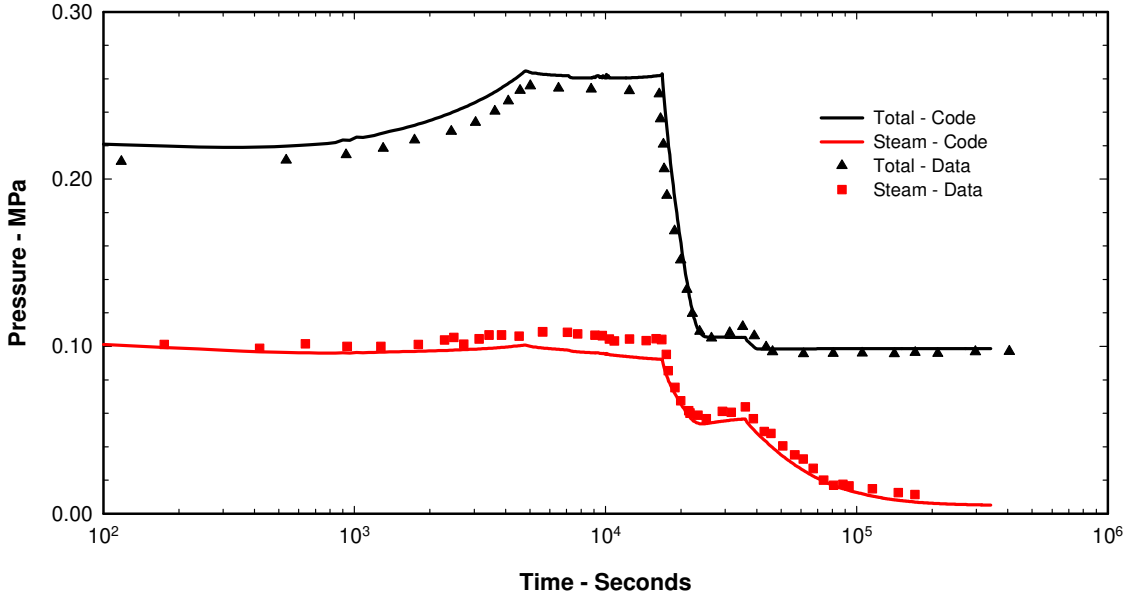

Figure 3-3. Test Vessel Pressures for Version 1.8.5 Calculation

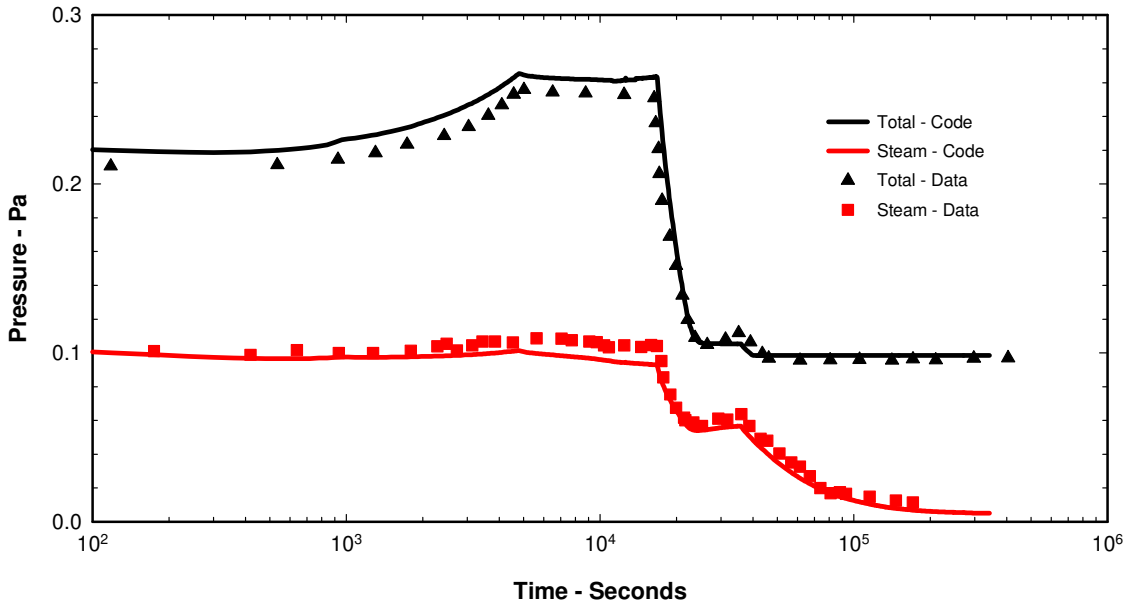

Figure 3-4. Test Vessel Pressures for Version 1.8.4 Calculation

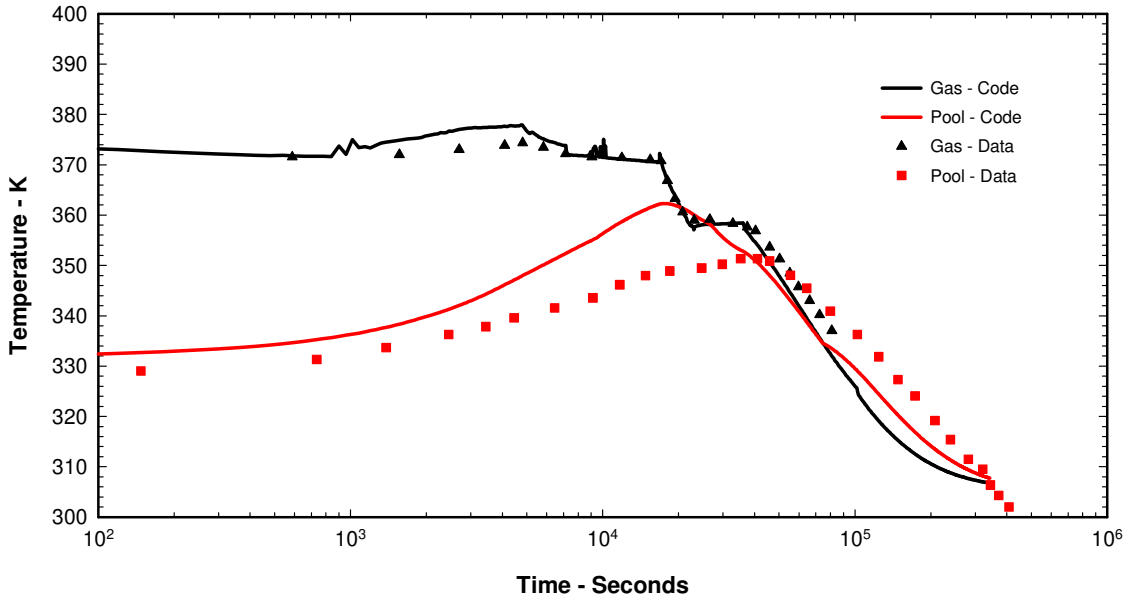

Figure 3-5. Test Vessel Gas and Pool Temperatures for Version 1.8.5 Calculation

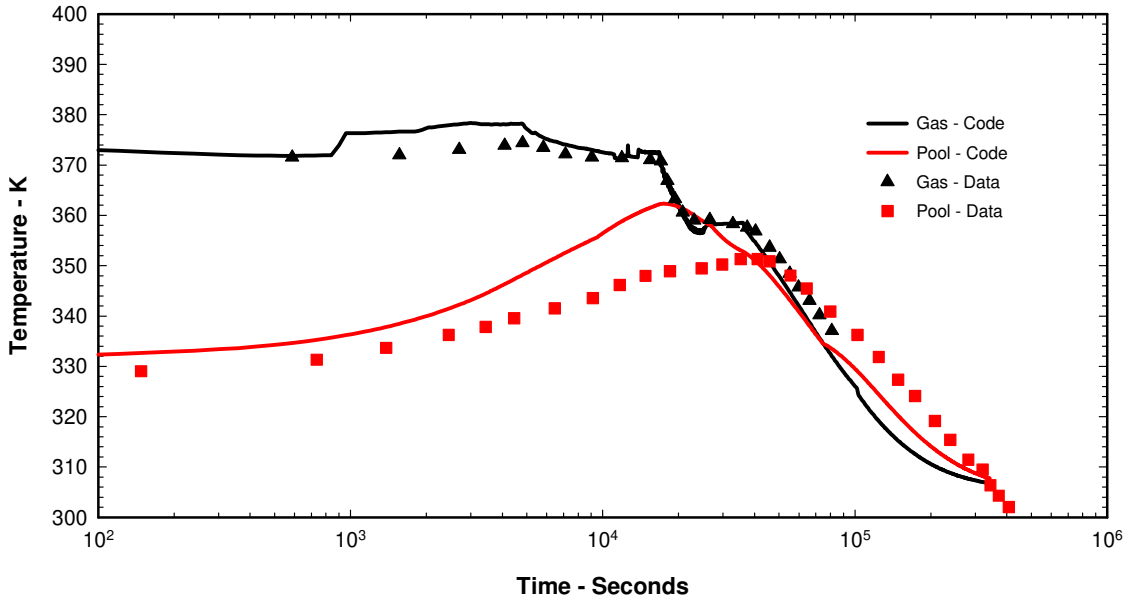

Figure 3-6. Test Vessel Gas and Pool Temperatures for Version 1.8.4 Calculation

Of greater significance is the relative humidity or steam saturation ratio ($P_{steam}/P_{saturation}$) in the test vessel. The humidity was not available as a measured parameter, but Figure 3-7 shows the calculated relative humidity. Here, the effects of the new aerosol dynamics

model begin to show some divergence with the 1.8.4 results. It is noted that the 1.8.4 calculation reveals some numerical instability that causes the relative humidity to oscillate. Atmospheric saturation of 100% is predicted during the first 1000 seconds, followed by large swings in the steam partial pressure in the 1.8.4 calculation. This was caused by an overprediction of the steam condensation rate on one timestep, which reduced the humidity and inhibited condensation or actually resulted in vaporization on the next timestep. These numerical convergence problems were addressed and removed in the 1.8.5 version. They involved tightening some criteria for the end-of-timestep temperature convergence and changing the algorithm used to project the end-of-timestep temperature. The 1.8.5 version reveals a smooth curve for the saturation ratio that shows some of the same general trends as the 1.8.4 results but lacks the oscillations associated with the numerical instabilities.

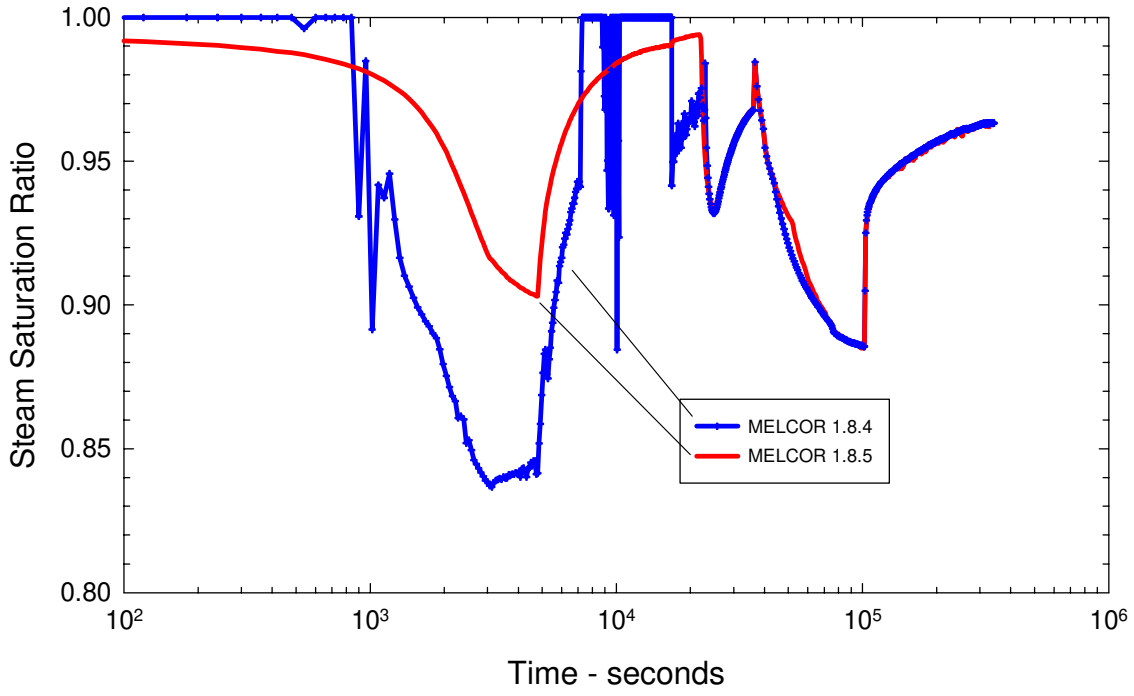

Figure 3-7. Test Vessel Relative Humidity

To demonstrate the mass balance on the steam and water sources in the test vessel, Figure 3-8 presents the calculated pool mass over the duration of the experiment as predicted by both code versions compared to actual measured water mass. Note that the original pool mass appears to be about 1600 kg in these plots. This is misleading because the log scale here does not show the negative 3000 seconds associated with the heatup and conditioning phase. That phase had quite high steam flow rates and was responsible for the initial 1600 kg of pool water. Again, there is quite good agreement with the measurements.

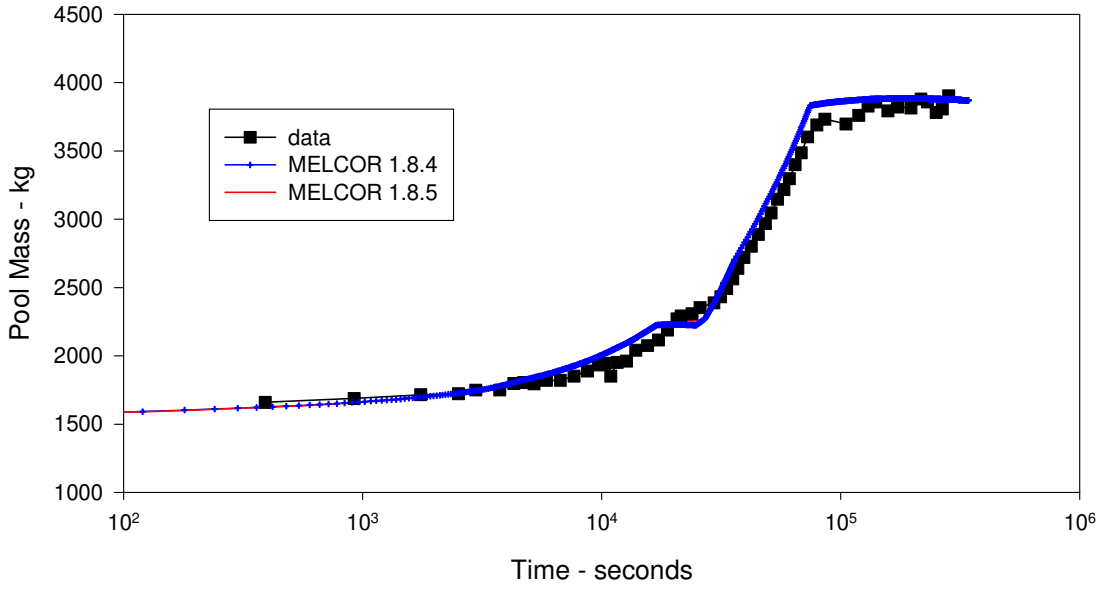

Figure 3-8. Test Vessel Pool Mass

3.4.2 Aerosol Dynamics

It has been established that the thermal-hydraulic calculations produce predictions sufficiently accurate to warrant confidence in their application to the aerosol dynamics calculations. It remains to be demonstrated that the modifications to the hygroscopic model produce the appropriate improvements in its predictive capabilities.

It should be noted here that the two basic cases that are used to compare between the version 1.8.4 and the version 1.8.5 calculations in this report differ in the maximum timesteps specified in the MELCOR input decks. The reason for this is that the numerical instability mentioned above had the effect of producing results that became progressively more degraded as the timestep was decreased in the 1.8.4 code version. This will be seen in the results presented below. Thus, the timesteps that were used in the 1.8.4 version calculations were larger than those used in the 1.8.5 calculations. The version 1.8.4 calculation used the following timestep structure:

–3000 to 16,800 seconds: Δt = 10 seconds,

16,800 to 36,000 seconds: Δt = 15 seconds,

36,000 seconds to end of calculation: Δt = 60 seconds.

A constant timestep of 2 seconds from beginning to end was used in the 1.8.5 calculations. The effects of timestep size will be discussed for both versions in what follows.

Figure 3-9 shows the predicted airborne or suspended mass of the soluble aerosol (hygroscopically active component), which in this experiment was composed of CsOH. Both version 1.8.4 and 1.8.5 results are quite good compared to the measured airborne mass until about 20,000 seconds when both calculations begin to under predict somewhat the aerosol removal rate, resulting in a slightly over predicted suspended mass. The 1.8.5 results, however, are clearly better during the first 20,000 seconds matching both the slopes and the inflection points in the measured data. The 1.8.4 results appear to be somewhat closer to that measured after 20,000 seconds, but only marginally better.

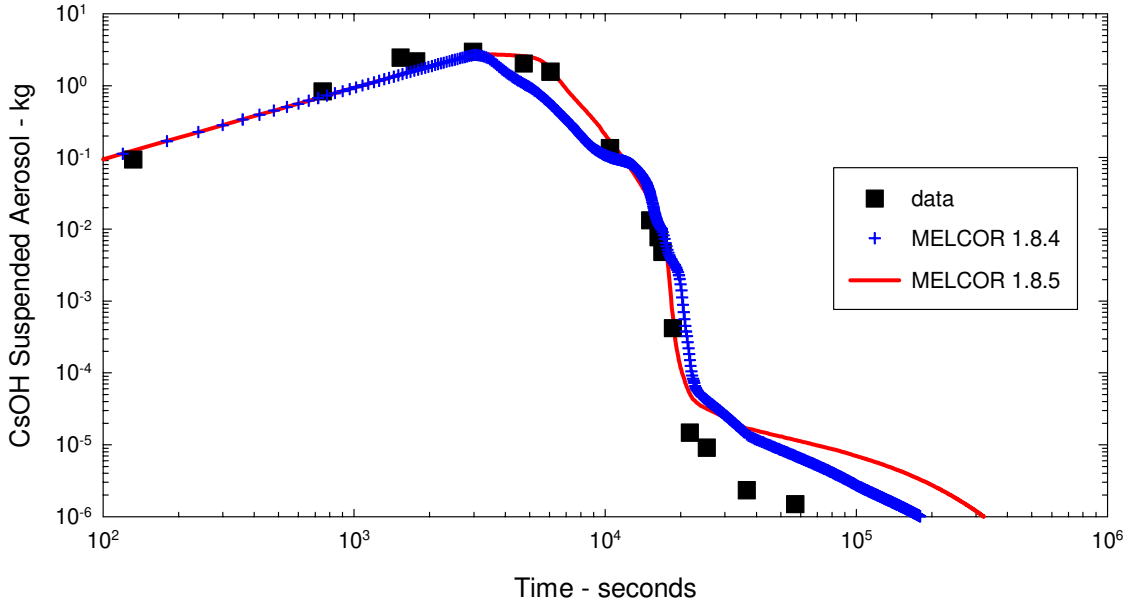

Figure 3-9. Suspended CsOH Aerosol for Version 1.8.5 Calculation

To assess the effects of differences in timesteps between the two cases, the 1.8.4 calculation was rerun with a constant 2-second timestep, which should have improved the results. The airborne mass of CsOH for this calculation is shown in Figure 3-11. Comparing this to Figure 3-9, it is evident that a decrease in timestep produced degraded results compared to the 10-second timestep case for 1.8.4.

Corresponding results for the nonsoluble aerosols (MnO) are shown in Figure 3-10 for both version 1.8.5 and 1.8.4 analyses. The version 1.8.5 calculation produced clearly superior results prior to the vent-down event at 16,800 seconds. Neither version reproduced the more gradual aerosol removal rate after venting, which is seen in the measured MnO concentrations. The venting process produced a strong effect on the soluble aerosol removal rate for measured and calculated data as clearly seen in Figure 3-9, but those effects are not as pronounced in the measured nonsoluble aerosol suspended masses. Note that part of the removal rate during venting is simply aerosols being swept out of the test vessel along with the vented gases. Because the aerosol hygroscopic parameters are weighted averages of the individual aerosol component parameters, the nonsoluble

aerosols retain some characteristics of the soluble aerosols. Thus the conditions that increased the soluble aerosol removal rate during the depressurization event at 16,800 seconds also affect the calculated nonsoluble aerosol removal rate. This effect is not seen in the measured nonsoluble aerosol concentration and the result is that the code somewhat underpredicts the MnO concentration, i.e., overpredicts the removal rate, which for this test is primarily by particle growth due to steam condensation on aerosols that in turn promotes gravitational settling.

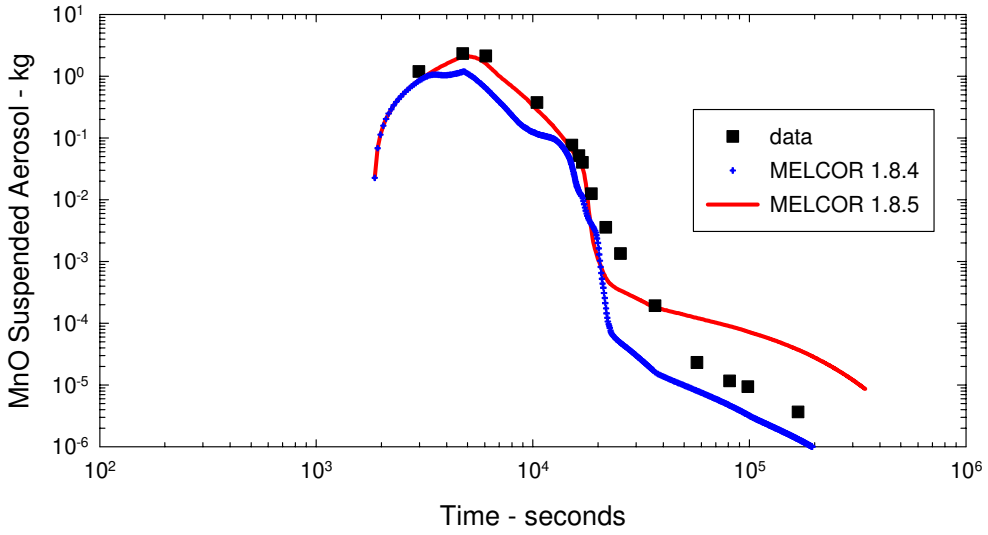

Figure 3-10. Suspended MnO Aerosol for the Version 1.8.5 Calculation

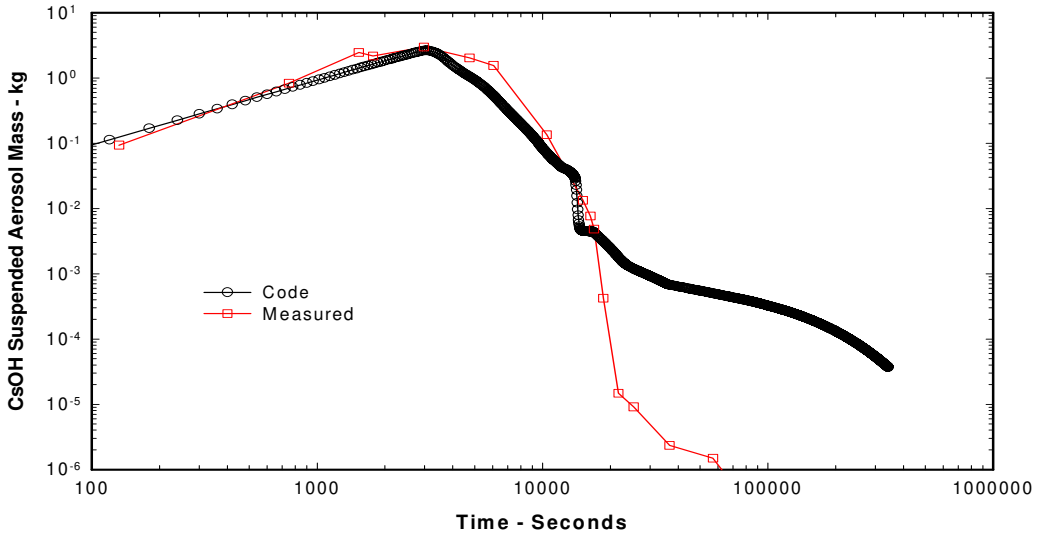

Figure 3-11. Timestep Sensitivity of Aerosol Mass (Δt = 2 s)–Version 1.8.4

The timestep issues discussed in the preceding section prompt the following rhetorical question: "What timesteps are recommended for producing adequate results for application of the improved hygroscopic model to aerosol dynamics calculations?" To answer this question, some additional timestep sensitivity calculations were run with the 1.8.5 version. The effects on the suspended aerosol concentrations are given in Figure 3-12 and Figure 3-13 for CsOH and MnO. A timestep of 10 seconds seems adequate under these conditions until the soluble aerosol concentration has been reduced to 10^{-7} kg/m^3, at which time the calculation becomes conservative (i.e., overestimates the residual albeit small aerosol concentrations) with respect to suspended mass. A considerable improvement in model performance at much lower concentrations can be obtained by decreasing the timestep down to 1 second (as seen in the soluble aerosol calculations, Figure 3-12), which produces good results at concentrations as low as 10^{-9} kg/m^3. It should be pointed out that timesteps in the range of 0.1 to 2 seconds are typical, particularly in plant calculations, while for small-scale experiment calculations, even lower timesteps are often utilized. Thus, a 1-second timestep appropriate for accommodating the aerosol dynamics calculation is not atypical of a normal MELCOR plant application and would probably not be the controlling factor for a calculation.

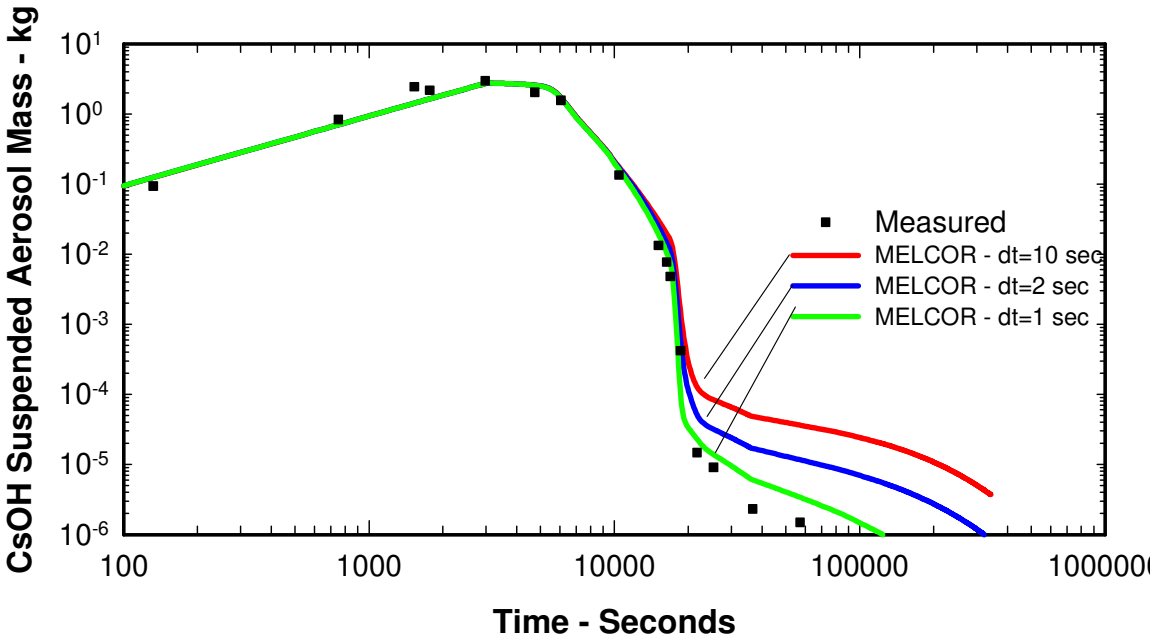

Figure 3-12. Timestep Sensitivity for CsOH Aerosol Mass–Version 1.8.5

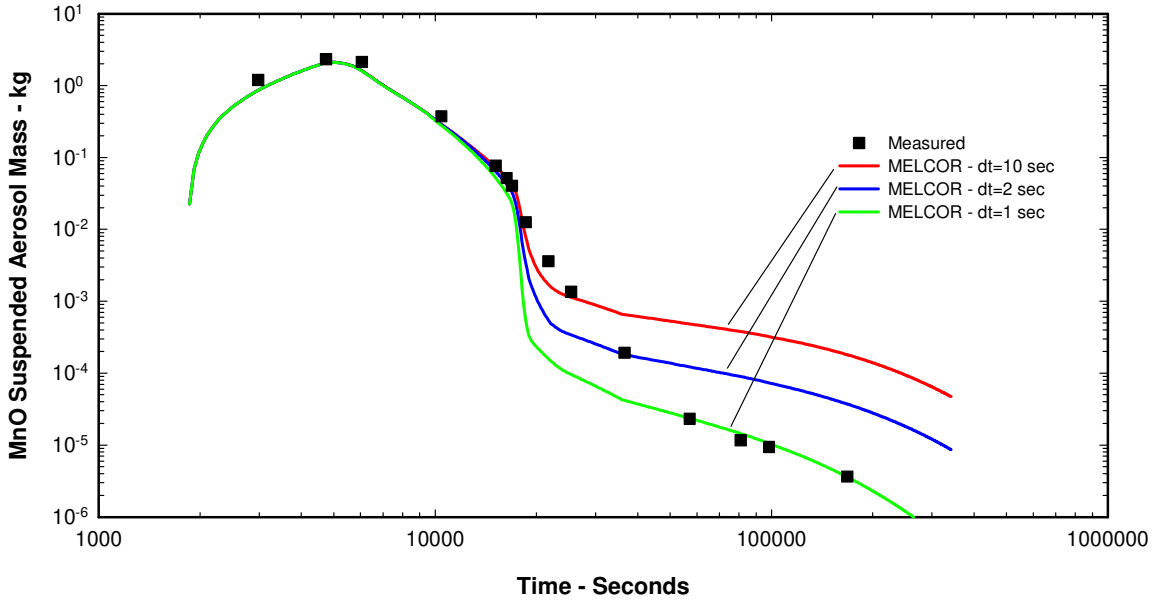

Figure 3-13. Timestep Sensitivity for MnO Aerosol Mass–Version 1.8.5

The soluble aerosol characteristics that unavoidably impact the results for nonsoluble aerosols appear to be exacerbated by a reduction in timestep (Figure 3-13). This seems to be the case in the LA-4 experiment, but also seems to be chiefly associated with the rapid change in test vessel conditions during the vent-down sequence and for some period thereafter. The dynamics of this effect are not entirely understood. However, note that the reduced timesteps produce better comparisons with measured data at later times when the effects of the depressurization have died out. The calculated aerosol mass in the case with a 1-second timestep, for example, appears to be nearly on top of the measured data by 40,000 seconds when the concentration has been reduced to about 2.5×10^{-7} kg/m^3 (2.5×10^{-4} kg/1000 m^3).

3.5 Discussion

A comparison of the version 1.8.5 modified hygroscopic/aerosol-dynamics models against the LACE LA-4 experiment showed an improvement over the previous 1.8.4 version, both with respect to comparison to experimental data and with respect to numerical robustness. The results of both calculations are qualitatively similar, although the new version produces analytical predictions that are quantitatively improved over the older version.

In general, it was not expected that the new aerosol dynamics models would produce significant effects on the thermal-hydraulic response. This was verified by nearly identical pressure and temperature responses for the 1.8.4 and 1.8.5 calculations. There were, however, improvements in the limited domain in which the hygroscopic modeling does

impact thermal-hydraulic responses, namely, its direct effect on the steam partial pressure and consequently on the relative humidity. The previous version produced oscillations in the relative humidity, and efforts to damp them by tighter timestep controls exacerbated the problem. These numerical and modeling problems have been removed in the present version of MELCOR.

3.6 References

1. McCormack, et al., “Final Report of Experimental Results of LACE Test LA-4,” LACE TR-025, Westinghouse Hanford Co., October 1987.

2. Kmetyk, L.N., MELCOR 1.8.1 Assessment of LACE Aerosol Experiment LA-4, SAND91-1532, September 1991.

4. Analysis of the VANAM-M3 Experiment–ISP 37

4.1 Introduction

The VANAM-M3 test, like the NUPEC mixing tests, constitutes an integral test of MELCOR's ability to model complicated building geometry, emphasizing phenomena associated with:

- Multi-compartment geometry,
- Stratified atmosphere,
- Atmosphere mixing by forced convection loops,
- Thermal energy balance,
- Structural heat transfer,
- Steam condensation effects, and
- Aerosol behavior.

The VANAM-M3 test was performed in the Battelle Model Containment (BMC) facility in Frankfurt, Germany, for the purpose of providing data on containment-building response to severe accident conditions with particular emphasis on characterizing the depletion rate of hygroscopic aerosol under varying humidity and thermal-hydraulic conditions. Details on the facility and the M-3 experiment are found in reference [1]. The VANAM-M3 experiment has been widely studied by various containment analysis codes in the context of the ISP exercise, ISP-37. The results of the ISP-37 multi-code comparison are found in a report by Firnharber [2].

Both the MELCOR and CONTAIN codes were represented in the ISP exercise, and the results of the exercise illustrate the application of these codes to a blind problem by a variety of different users having varying levels of expertise. At the time of the ISP exercise, the current MELCOR code version (version 1.8.3) did not have models for treating hygroscopic aerosol behavior, and as a result, ISP participants using this version of the code failed to capture the aerosol depletion rates observed in the experiment. However, the Sandia participant in this exercise used a developmental version of MELCOR, which did include a model for treating the hygroscopic effect. This model, which was being prototyped at the time of the ISP, was subsequently included in version 1.8.4 of the MELCOR code. The hygroscopic model was originally limited to treat aerosol particles as being either highly soluble (when the model was active) as being nonsoluble (when the model was inactive). In MELCOR 1.8.5 the model has been generalized to allow consideration of a mean aerosol solubility based on a mixture of aerosol materials of varying degrees of solubility. The present report presents the reapplication of MELCOR version 1.8.5 to the VANAM-M3 experiment. In this report, comparisons are made to earlier versions of MELCOR and to several different CONTAIN analyses of the problem. The report also highlights the importance of adequate control volume hydrodynamics (CVH) nodalization in capturing circulation and stratification effects.

A schematic of the test facility is shown in Figure 4-1. The containment building was largely of concrete construction with multiple connected rooms. The internal volume was 626 m^3. The test was conducted over a period of more than 30 hours, during which time steam, air, and hygroscopic (NaOH) aerosol were injected into specified rooms in the facility. During the first 17 hours, steam was injected into room R5 in order to heat the building walls and structures. After preheating the building, at 17.2 hours, both aerosol and steam were injected into the same room for a period of about an hour. Following this, the steam and aerosol injection was suspended for roughly 2 hours. During this time, the aerosol depletion was measured under what were described as dry conditions (i.e., steam was not being supplied during this time and the relative humidity fell below saturation, RH<1). After this period, at 22.7 hours, aerosol and steam were again injected into room R5 for about one hour. Following this, steam was injected into room R3 in the bottom of the building, causing a widely dispersed circulation pattern to develop throughout the facility. At 25 hours into the test, steam injection was switched back to room R5 and aerosol depletion during this period took place under wet steam-rich conditions. Figure 4-2 shows the steam injection history for the test, and Figure 4-3 shows the air leakage rate from the facility. The air leakage rate was described in the ISP report as being “well known”. Somewhat inconsistent with this claim, however, is the rather crude temporal description of the leak rate shown in Figure 4-3. Additionally, the leak was shown to be caused by a multitude of cracks in the seams of the external structural walls. Given this description, it seems doubtful that the leak characterization actually was well known and was certainly not directly measurable. This point is being made because the predicted facility pressures are somewhat sensitive to this leak rate, and improved comparisons to measured pressure would likely result if a constant leak rate were used over the duration of the test in contrast with the profile given in Figure 4-3.

Throughout the test, temperatures and aerosol concentrations were measured in the various rooms. Relative humidity was also measured in several rooms, although the measurements appear to be a bit in error, since the maximum RH is reported to be 1.2, which is not likely. These data are taken to be qualitative.

4.2 MELCOR Nodalization

The original nodalization used in the ISP-37 exercise is shown below in Figure 4-4. (This nodalization was proposed by the ISP organizers and used by most participants. Some participants, however, used a refined nodalization and obtained improved results.) The diagram illustrates approximate elevations and volumes of the rooms in the facility as well as the flow paths between the rooms. Heat structures, although modeled in the MELCOR input deck, are not shown in the nodalization diagram.

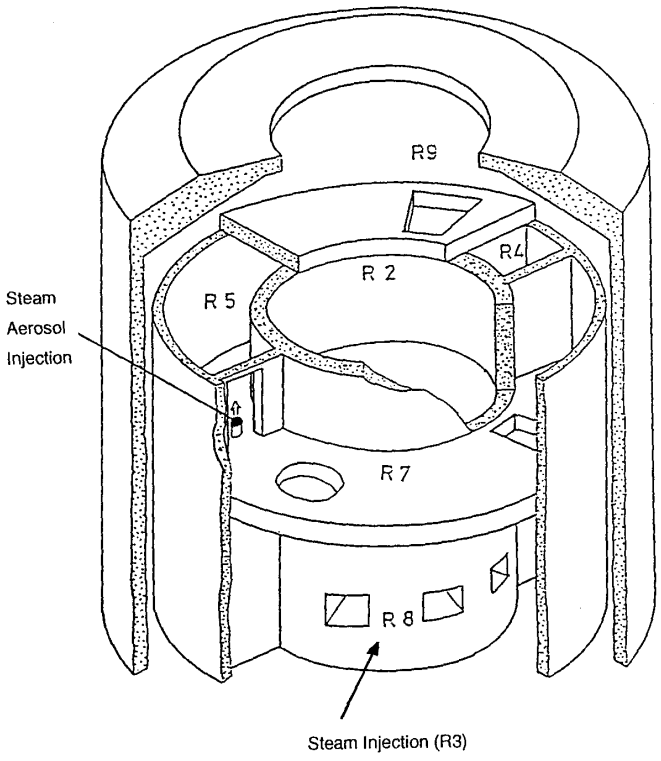

Figure 4-1. Schematic of the BMC Facility

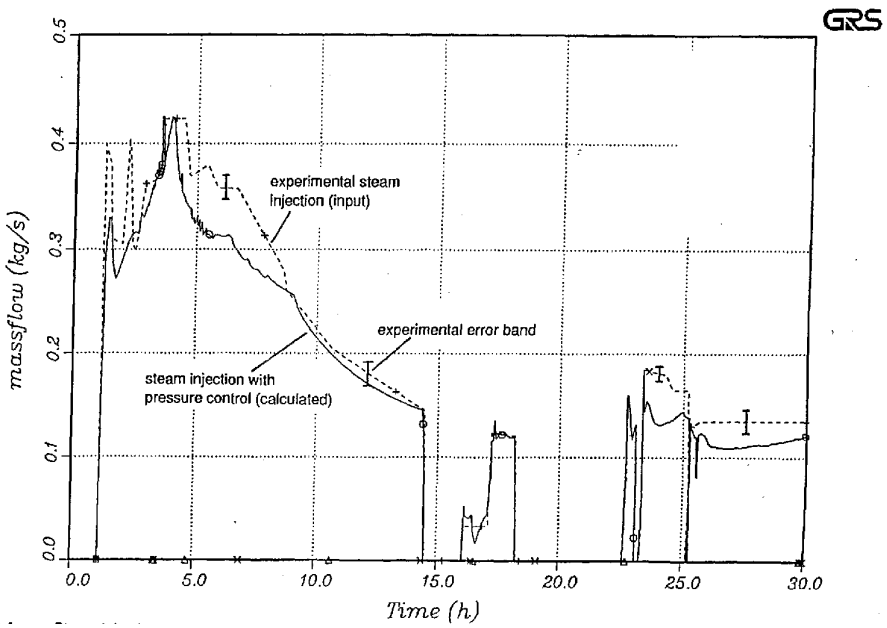

Figure 4-2. Steam Injection History for the VANAM M3 Test

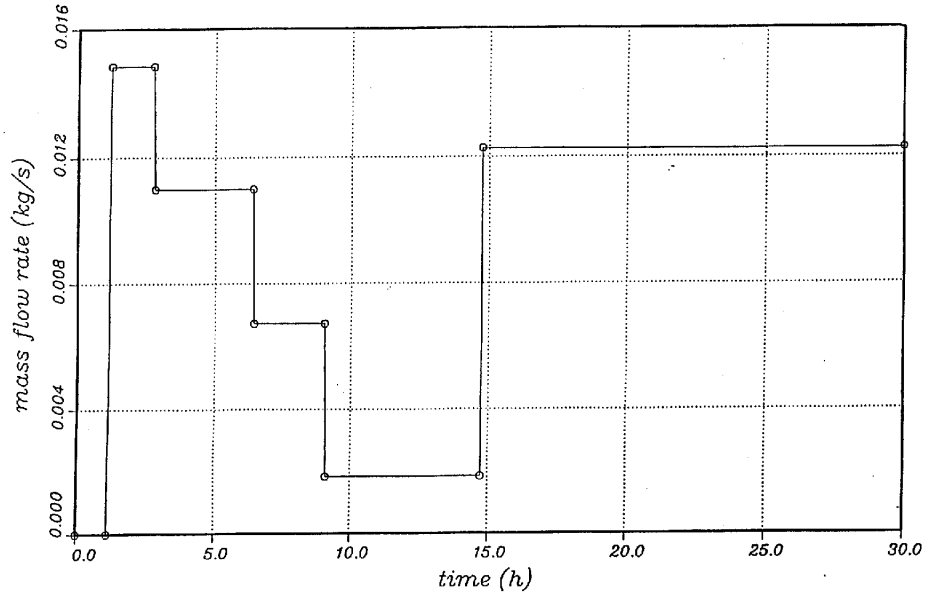

Figure 4-3. Total Air Leak Rate from the VANAM-M3 Test

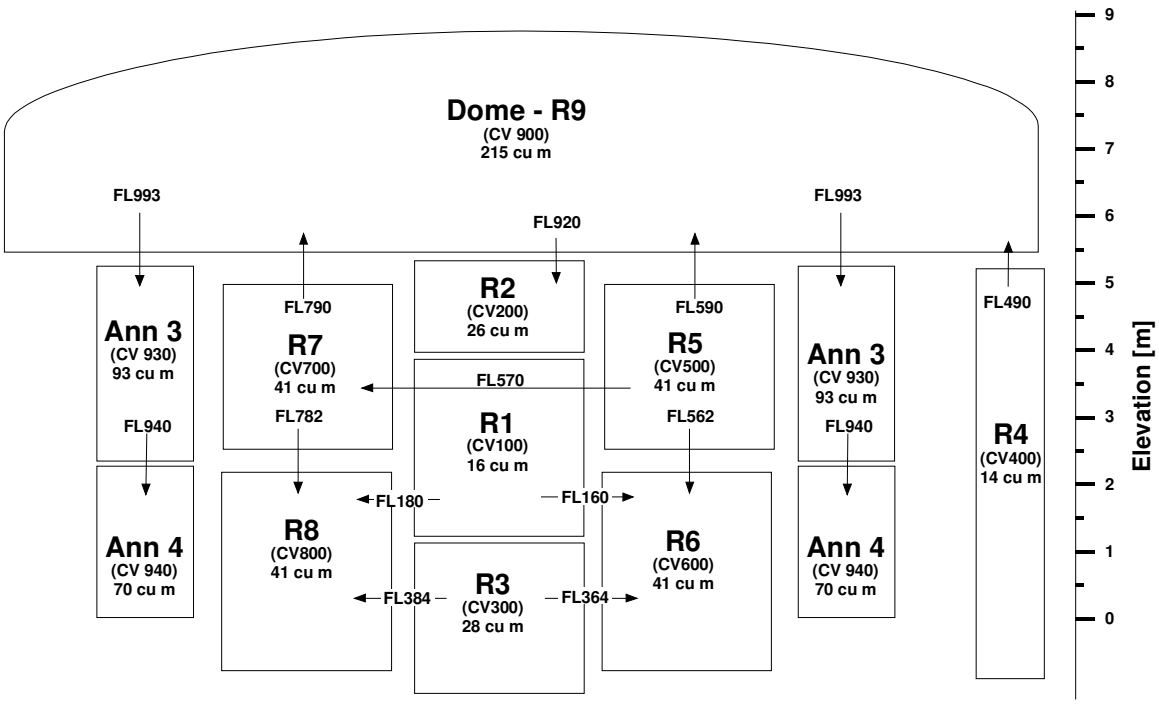

Figure 4-4. Original MELCOR Nodalization Used in ISP-37 Exercise

4.3 MELCOR Parameter Specification

The MELCOR options used in the analysis of this test, in addition to the default settings, included activating the RN package and the hygroscopic aerosol option. Steam and aerosol sources were modeled as specified in the test conditions. Control functions were constructed to represent the steam and air injections into the facility as well as the overall air leakage rate. The input deck is provided in an appendix to this report.

4.4 Sensitivity Studies

One sensitivity study was performed for this assessment. This consisted of a modification to the original nodalization of the experiment facility where the lower rooms R6 and R8 were split into lower and upper halves in order to capture greater detail in the known thermal stratification characteristics of the experiment. This is described in greater detail in the following sections.

4.5 Calculational Results

The dominant parameters of interest in this analysis are the room temperatures (with respect to the thermal signature characterizing the natural and forced circulation flows in the facility and the thermal stratification that occurred between the upper and lower rooms of the facility), the building pressure (as influenced by the steam and air mass and enthalpy sources to the building and the participating heat transfer with structures), and the aerosol depletion characteristics that were observed during the pertinent phases of the experiment. All of these aspects are discussed in the following sections.

4.5.1 MELCOR Results

4.5.1.1 MELCOR-Predicted Temperatures with Standard Nodalization

During the first part of the test, the steam that was injected into room R5 was observed to rise directly into the dome region, causing atmosphere from the adjacent room R7 to move laterally into R5; and likewise, the dome atmosphere was drawn downward into room R7. This flow pattern was predicted in the original MELCOR analysis to involve the lower rooms R8, R3, and R6 as well, in contrast to the more stratified and quiescent conditions observed for the lower floors in the test during that time. The predicted temperatures from the original calculation are shown in Figure 4-5.

The original MELCOR analysis predicted the temperatures in the upper rooms of the facility very well but overpredicted the mixing between upper floors and lower floors, resulting in an overprediction of the temperatures in the lower rooms of the facility. The stratification of hot atmosphere that was observed in the experiment between the lower rooms (R8, R3,

and R6) and the upper rooms (R7, R1, and R5) was not captured in the calculation. This was presumed to be an effect of the averaging of atmosphere conditions in R6 and R8.

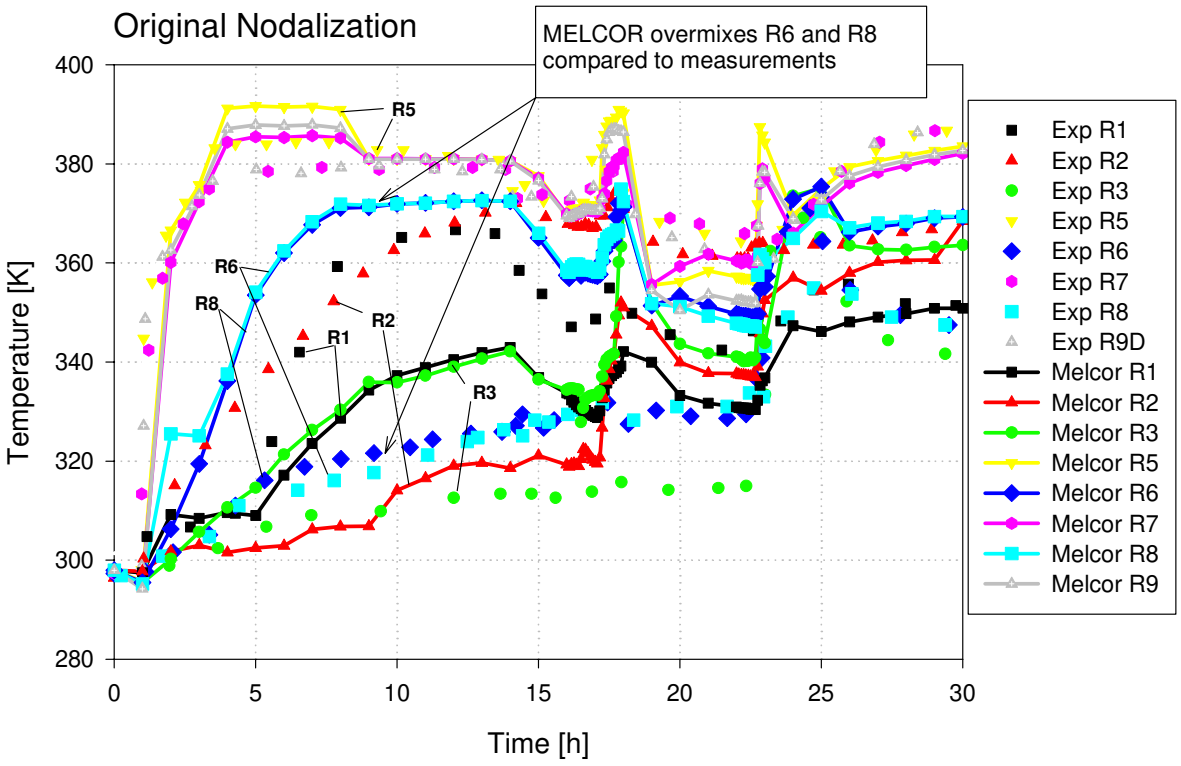

Figure 4-5. Room Temperatures Predicted by MELCOR for Original ISP-37 Nodalization

4.5.1.2 MELCOR-Predicted Temperatures with Revised Nodalization

A modified nodalization was developed to see if the stratified zone could be resolved by splitting rooms R6 and R8 into upper and lower regions, as shown in Figure 4-6. In the modified nodalization, the upper half of rooms R6 and R8 was made to communicate by flow paths with R5, R1, and R7 in addition to the lower halves of R6 and R8. Similarly, the lower halves of R6 and R8 were made to communicate with R3 in addition to the upper halves of R6 and R8.

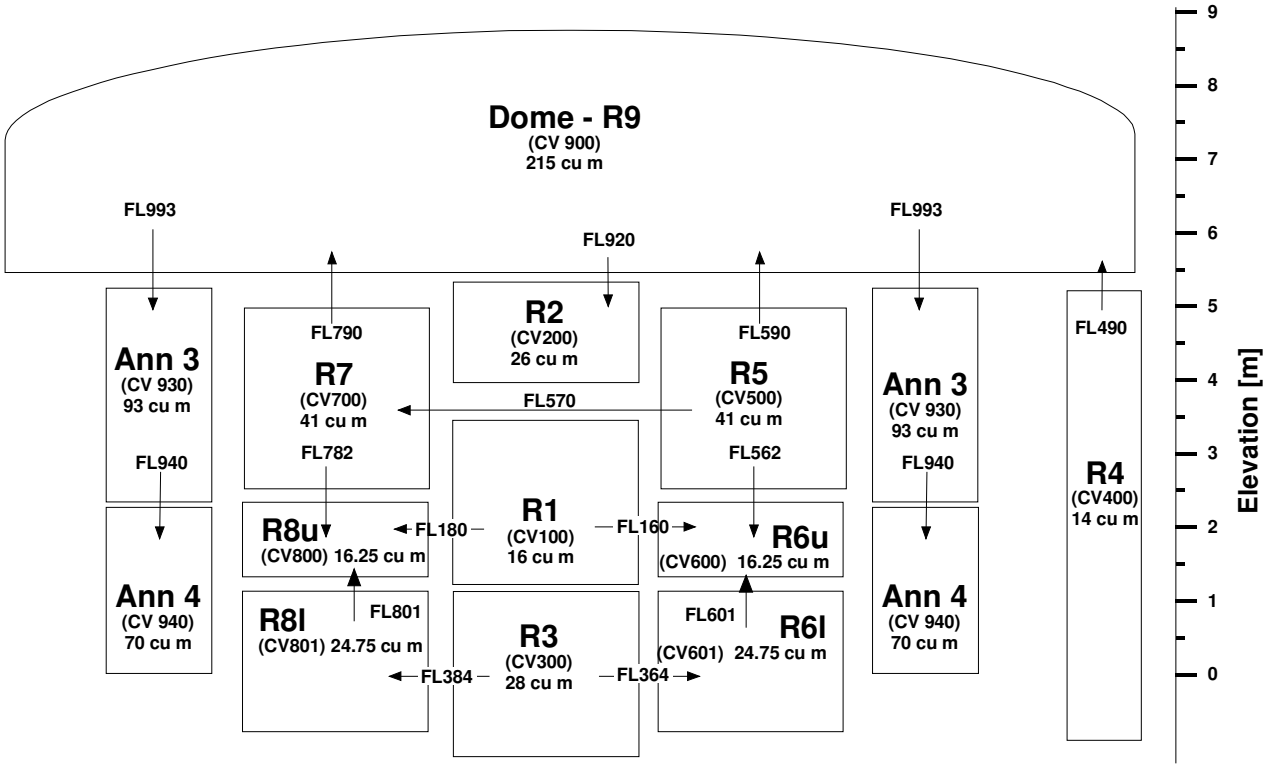

Figure 4-6. Modified Nodalization Where R6 and R8 are Divided into Upper and Lower Regions

The predicted room temperatures resulting from the revised nodalization are shown in Figure 4-7 and Figure 4-8. As can be seen from the temperatures predicted for rooms R7 and R5 versus those for R8 (lower) and R6 (lower), the stratification between the upper and lower rooms was captured fairly well using the revised nodalization. The temperatures of the lower regions of rooms R6 and R8 compare much better with the experimental measurements. In addition, significant improvements in the predicted temperatures for rooms R1 and R2 are also obtained with the revised nodalization.

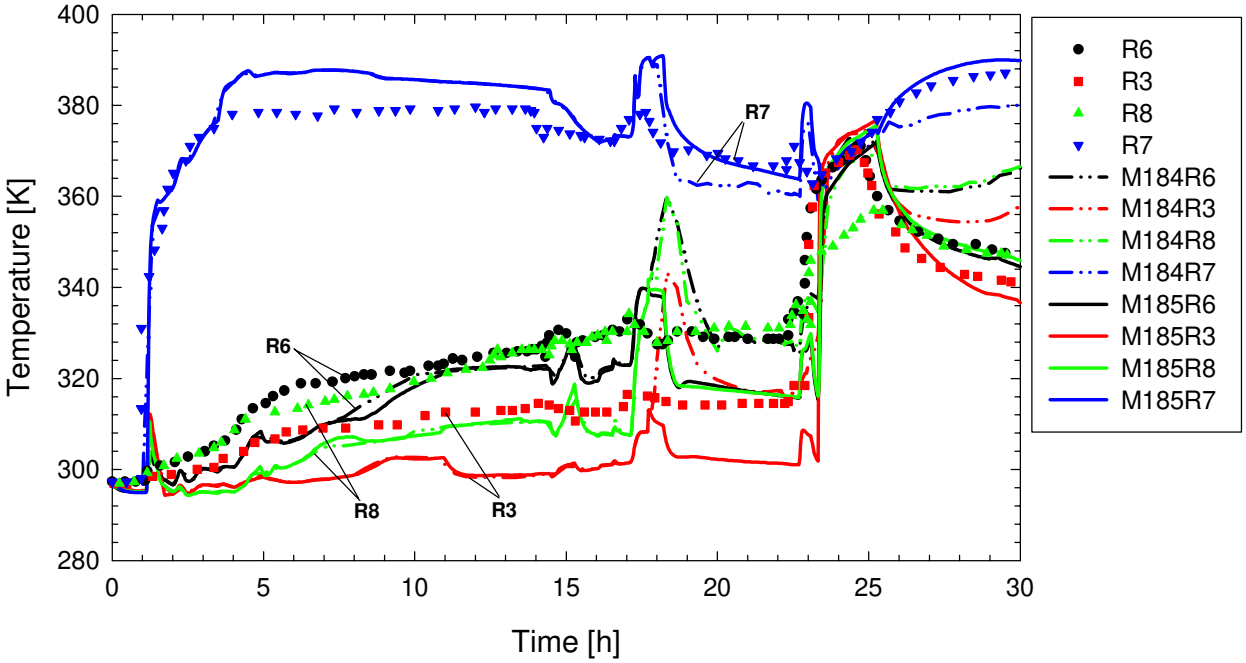

Figure 4-7. Temperatures Predicted for Rooms R6, R3, R8, and R7

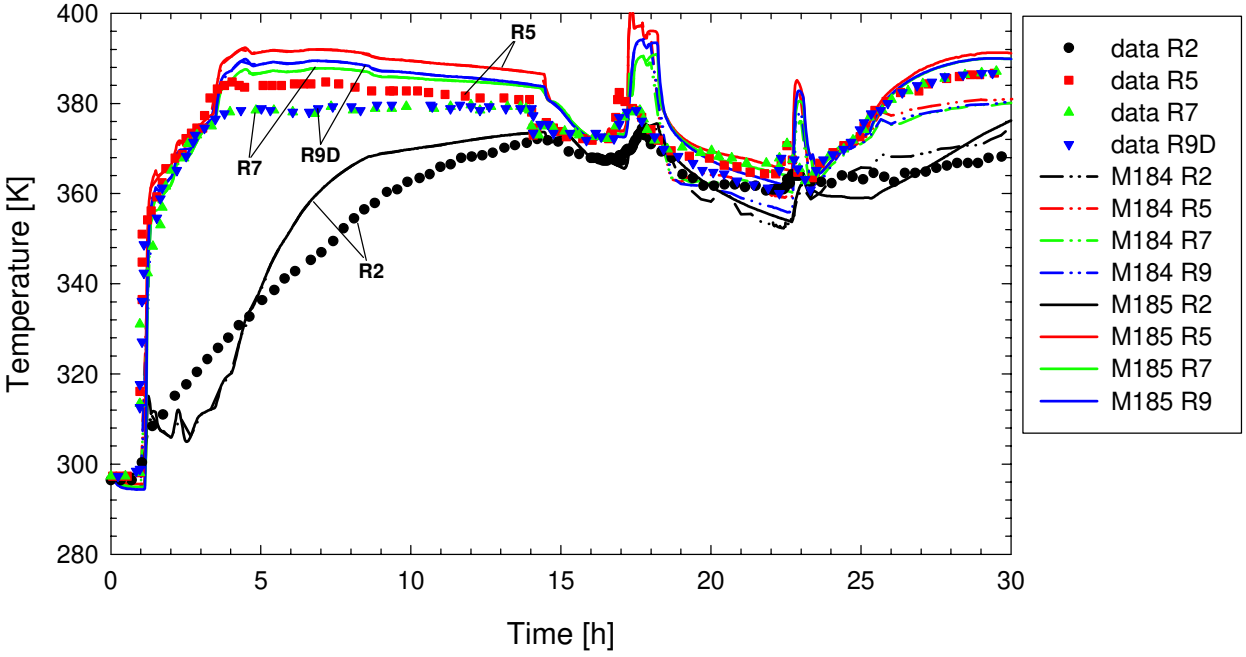

Figure 4-8. Temperatures Predicted for Rooms R2, R5, R7, and R9

4.5.1.3 MELCOR-Predicted Pressure

Figure 4-9 shows the predicted facility pressure for both nodalizations. The predicted pressures compare reasonably well with the measured values in both analyses, especially with respect to the peak pressure attained in the experiment and for the pressure predicted in the second half of the experiment. In both cases, there is some slight overprediction of the pressure in the first half of the test. This is believed to be due in part to differences between the modeled air leakage rate and the actual leakage from the facility. Although characterized as being well known in the test report, the leakage was acknowledged as being from the multitude of cracks in the external seams of the structure. Additionally, the well-known air leakage rate was only approximately characterized, as indicated by the crude plot of the leak rate shown in Figure 4-3. A possible sensitivity study which might provide improved pressure predication would be to assume that the air leakage rate was, in fact, constant over the entire experiment at a value of 0.012 kg/s. (See Figure 4-3.) The pressure differences may also be due in part to an underprediction of heat transfer to the structures, an area not examined by any sensitivity analyses in this study.

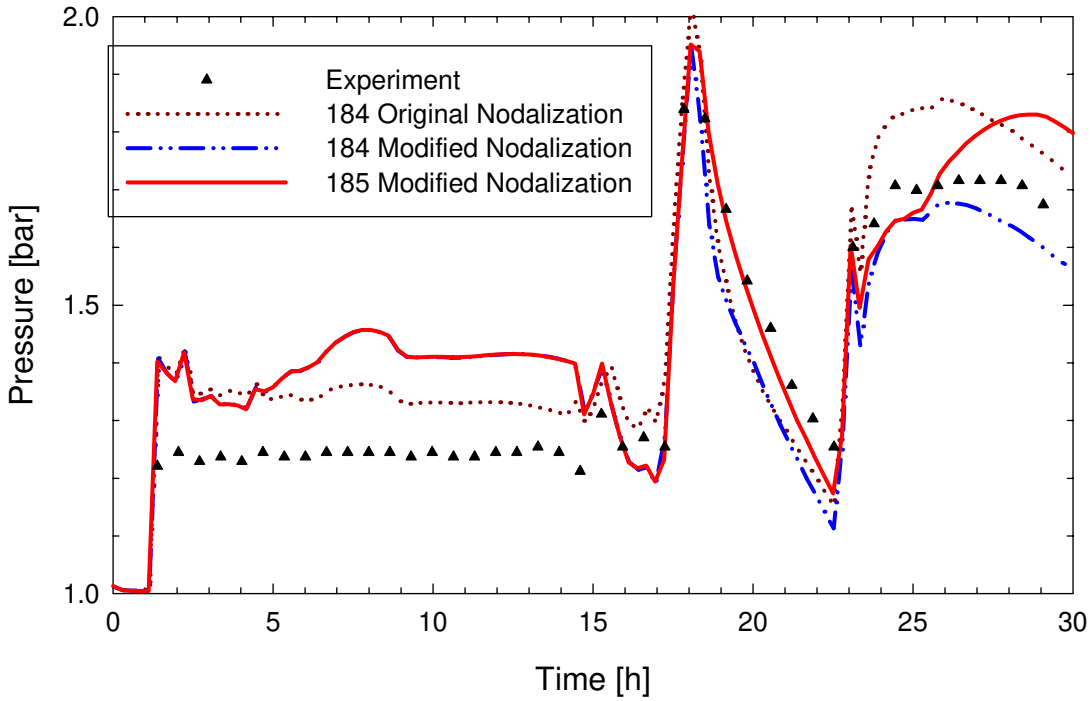

Figure 4-9. Predicted Pressure in the VANAM-M3 Test

4.5.1.4 MELCOR-Predicted Aerosol Depletion

The depletion behavior for the NaOH aerosol cloud in the dome region (R9) predicted by MELCOR is shown in Figure 4-10. Predictions for both facility nodalizations are shown in the following figure, in addition to the measured data. The comparisons in both cases are judged to be excellent. It should be pointed out that an important characteristic of the aerosol depletion behavior is the rate of decrease following the two peak aerosol concentrations. Because the aerosol material (NaOH) is hygroscopic, the particles have a very strong affinity for water vapor in the atmosphere such that the initially dry particles

rapidly grow in size by absorbing water from the atmosphere. This rapid growth in particle size results in an increased gravitational settling rate and a corresponding rapid depletion in the airborne concentration. Without the hygroscopic or solubility effect, a supersaturated environment (relative humidity >1) is required in order to cause water condensation on the aerosol particles and would result in a significantly lower calculated depletion rate than that predicted with the hygroscopic effect.

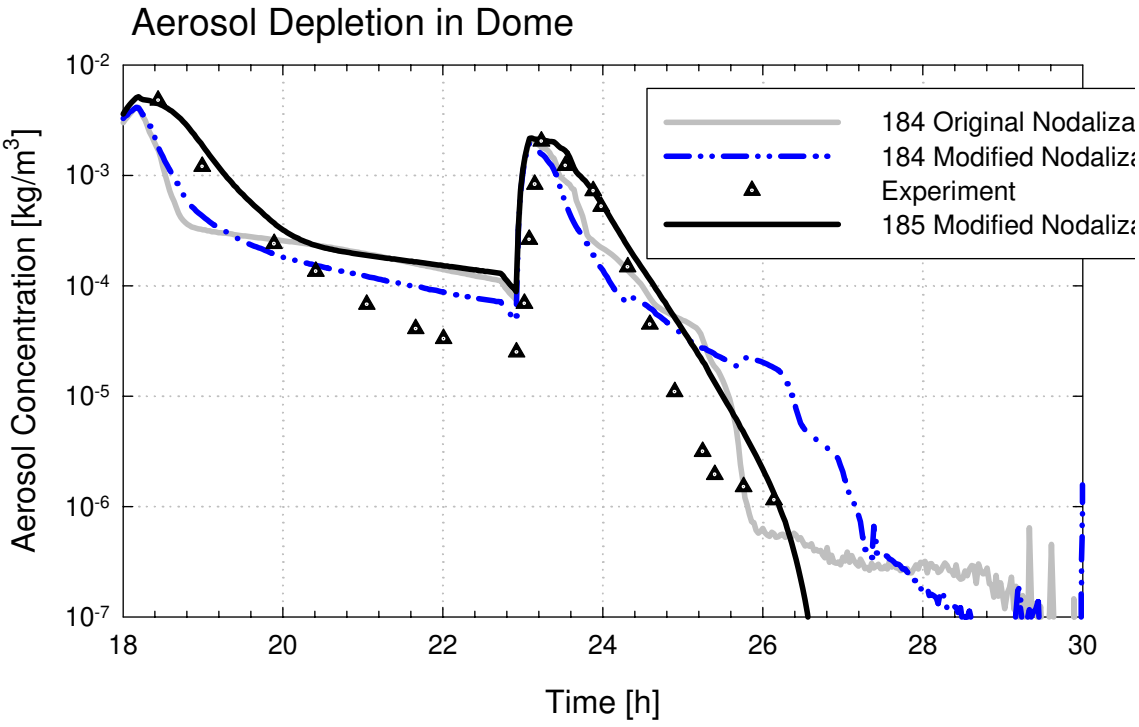

Figure 4-10. Aerosol Depletion Behavior in Dome, as Predicted by MELCOR

4.5.2 CONTAIN Results

4.5.2.1 CONTAIN-Predicted Temperatures

The following section shows, for comparison purposes, selected results of CONTAIN calculations that were performed by two organizations participating in the ISP-37 exercise [2]. The CONTAIN analyses used essentially the same nodalization as was used in the original MELCOR analysis described earlier. As mentioned earlier, this was the nodalization suggested by the organizers of the ISP exercise. The results obtained by CONTAIN using this nodalization are remarkably similar to the results obtained in the MELCOR analysis, which used a similar nodalization. Figure 4-11 shows the CONTAIN-predicted temperatures for the various rooms in the facility compared with the experimental data. Like the original MELCOR results, the CONTAIN predictions for the temperatures in the upper rooms (R5 and R7) and the dome (R9) compare well with the experimental data. However, the temperatures in the lower rooms (R6 and R8), also like the original MELCOR

calculations, are overpredicted by CONTAIN, presumably due to the mixing caused by the circulation pattern involving these rooms. Similar to the comparable MELCOR analysis, the temperatures in rooms R1 and R3 are significantly underpredicted. Unlike the comparable MELCOR analysis, the CONTAIN predictions beyond 25 hours compare somewhat less favorably with the experiment, failing to capture the facility-wide mixing that occurs in most of the rooms at just before 25 hours.

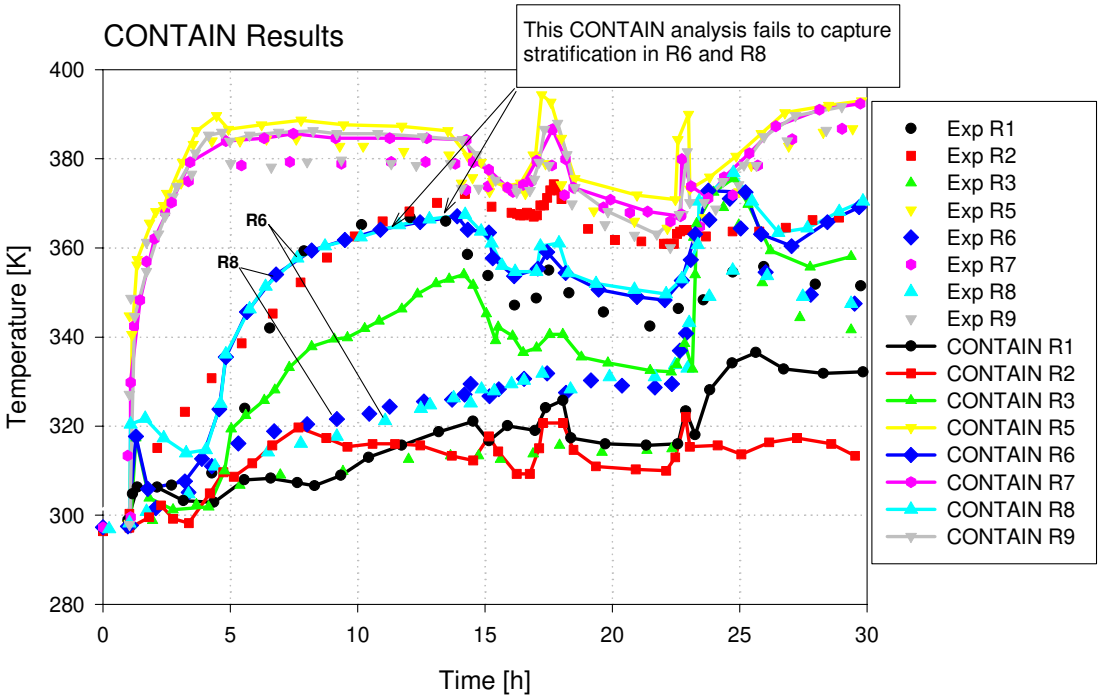

Figure 4-11. Temperatures Predicted by CONTAIN as Applied by VUJE (Slovakia)

4.5.2.2 CONTAIN-Predicted Pressure

CONTAIN-predicted pressures, calculated by several CONTAIN users for the ISP-37 exercise, are summarized in Figure 4-12. Overall, the CONTAIN analyses correctly predicted the observed pressure trends and magnitude. However, the scatter in the calculated results provides an indication of the degree of variability in predicted behavior that can be expected simply due to differences in user application of a given code. Certainly the MELCOR-predicted results fall within the scatter predicted by the various CONTAIN users participating in the exercise. The principal reasons for the variability were due to differences in the air leakage rate assumed by each user, and to differences in calculated heat transfer to the building structures.

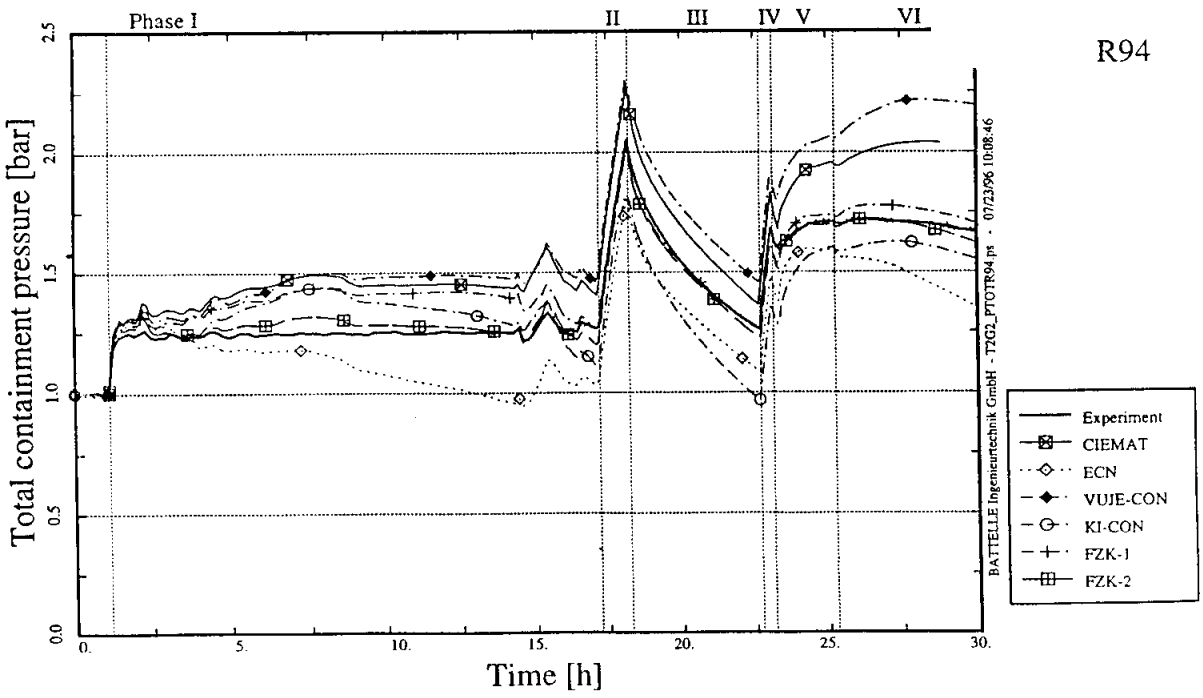

Figure 4-12. VANAM-M3 Building Pressure Predicted by Different CONTAIN Calculations

4.5.2.3 CONTAIN-Predicted Aerosol Depletion

The CONTAIN-predicted aerosol depletion behavior is illustrated in Figure 4-13. Here again, a notable user effect is observed in the differing depletion behaviors predicted by the same code. Both analyses correctly predict the peak aerosol concentration attained while the aerosol source was present; however, important differences are seen in the aerosol depletion phases after the source was terminated. The VUJE CONTAIN submittal did not use the hygroscopic aerosol model option available in CONTAIN, whereas the ECN CONTAIN submittal did use the hygroscopic option. As a result, the ECN results show the characteristic rapid depletion signature in the aerosol concentration associated with the hygroscopic solubility effect, whereas VUJE overpredicts the suspended aerosol concentration during the depletion phases by about an order of magnitude.

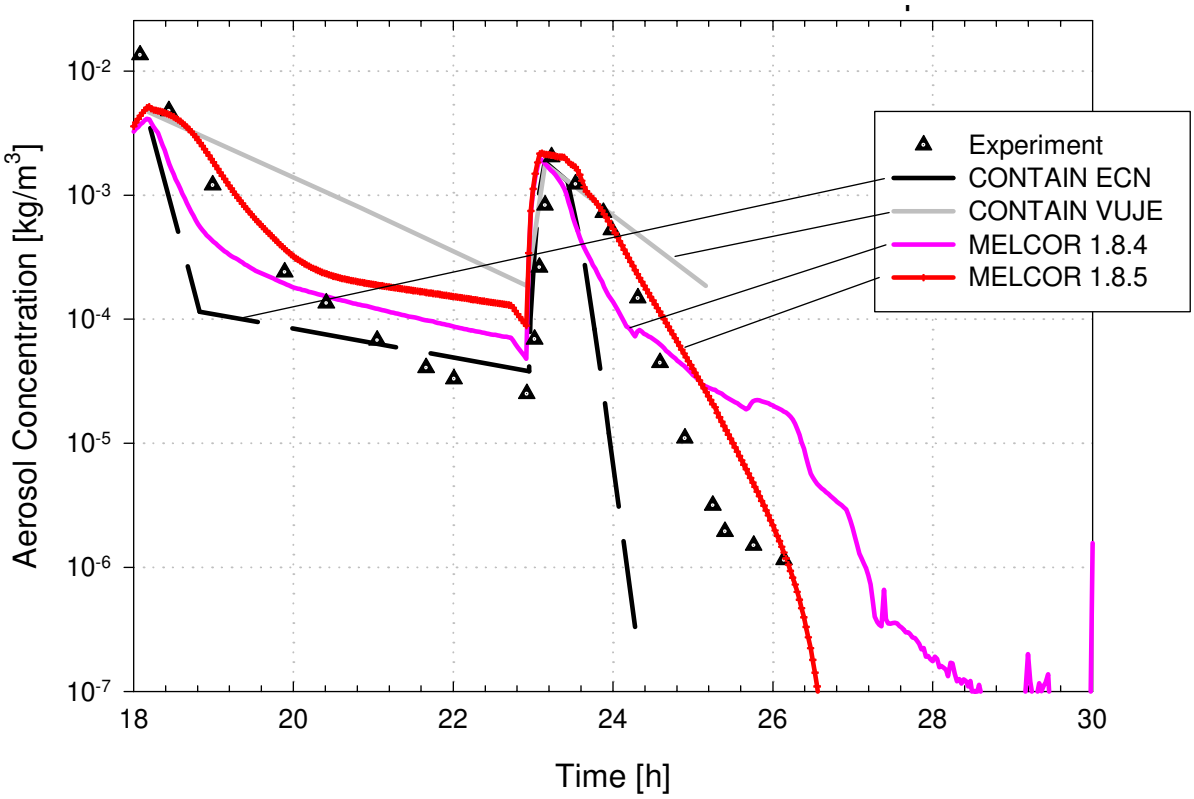

Figure 4-13. Aerosol Depletion Predicted by CONTAIN Users With Comparison to MELCOR

4.5.3 Significance of Comparisons

4.5.3.1 Significance of Predicted Temperatures

The temperatures predicted by the codes for the room environments are a strong indicator of the codes' ability to correctly capture the forced and natural circulation patterns that occur at different times in the test. The initial circulation induced in the upper rooms during the heatup stage during the experiment served to equalize the temperatures in the upper rooms. In the initial nodalization, this resulted in too-high temperatures predicted for the lower adjoining rooms, R8 and R6. Some of the mixing could also have resulted from a numerical diffusion effect. Splitting rooms R6 and R8 into upper and lower sections improved the comparison significantly. The overall correctness of the temperature distribution is an indicator of the degree to which the circulation was correctly predicted. Additionally, the predicted temperatures indicate the degree to which heat transfer to the structures is correctly predicted.

4.5.3.2 Significance of Predicted Pressure

The predicted pressure behavior tests the code's ability to calculate the response of the complex multi-room facility to sources and sinks of steam and air. Sources include mass

and thermal energy sources from the steam and mass source from the injected air. Sinks include leaks in the facility and heat transfer from the atmosphere to the structures, including steam condensation effects. The correctness of the pressure prediction is a measure of the code's integration of these simultaneously occurring processes in a realistic, complicated facility.

4.5.3.3 Significance of Predicted Aerosol Depletion

The predicted aerosol depletion behavior is a measure of the robustness of the aerosol mechanics modeling in the code. The aerosol mechanics models involve predicting particle growth rate by agglomeration with other particles and by absorption of water vapor from the moist atmosphere, the particle transport through the facility by the induced flows, and the depletion of the aerosol from the atmosphere principally by gravitational settling. This integral behavior is important with respect to predicting the amounts of transportable fission products present in a reactor containment building at any point in time following a severe accident. Specifically, the depletion behavior is an important mitigating factor in the transport pathway to the environment.

4.6 Conclusions

The ISP-37 experiment provided a quite excellent multi-effect exercise for the various containment phenomena codes, including many of the most important containment phenomena. These included realistic and complex geometry with realistic mass and energy sources and aerosol transport effects. On the whole, both MELCOR and CONTAIN predicted the important behaviors of the experiment quite well.

4.7 References

1. Kanzleiter, T., VANAM Multi-Compartment Aerosol Depletion Test M3 with Soluble Aerosol Material, Technical Report BleV-R67.0098-304, July 1993.

2. Firnhaber, M, et al., International Standard Problem ISP37: VANAM-M3—A Multi Compartment Aerosol Depletion Test with Hygroscopic Material, OCDE/GD(97)16, December 1996.

5. Analysis of the Cora 13 (ISP 31) Experiment

5.1 Background

The CORA Facility was used to conduct ISP-31 [1]. The ISP-31 test bundle consisted of 16 heater rods, 7 unheated rods representing typical pressurized water reactor (PWR) fuel elements, and 2 absorber rods (Figure 5-1). The heater rods were 1.96 m long and made of tungsten, while the cladding was made of Zircaloy-4. The test bundle was cooled with an argon/steam mixture that entered at the bottom of the bundle.

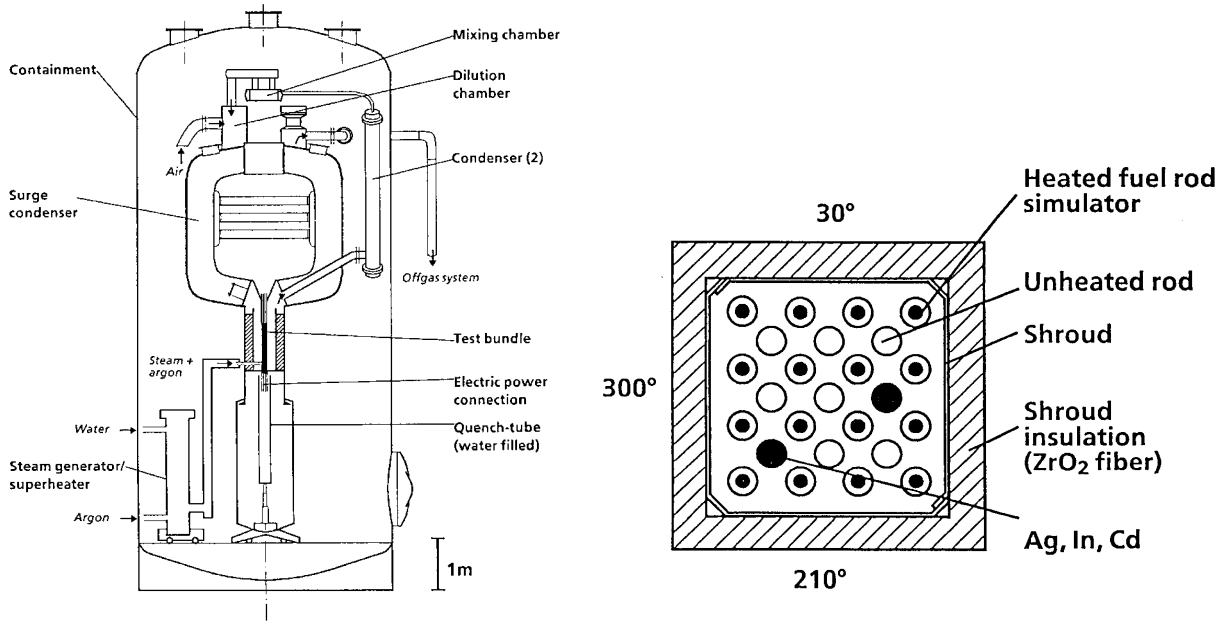

CORA Facility Cross section of test bundle

Figure 5-1. CORA Test Facility and Cross Section of Test Bundle

The experiment consisted of 3 phases: a preheat phase, a transient heat-up phase, and a cool-down phase. The preheat phase lasted from 0 to 3000 s. During this time, the rods were heated at a low electric power input of 0.65 kW in preparation for the protracted heating phase during which the actual test is performed. During the transient heat-up phase, which lasted from 3000 to 4870 seconds, the heater rod power was increased linearly in time from 6 to 27 kW. Of course, the electrical heating produced a heating of the fuel rod temperatures. By 4000 seconds, fuel cladding temperatures were beginning to exceed 1273 K whereupon measurable hydrogen production was detected. After this point, oxidation energy became increasingly important as it accounted for nearly 50% of the total

heat input during the experiment. Shortly after 4200 seconds, cladding temperatures in the upper regions of the bundle were observed to increase very rapidly, exceeding the melting point of both the thermocouples in use as well as the zircaloy cladding. The final phase was initiated at 4870 seconds when the bundle was quenched by means of a water-filled quench cylinder that rose directly into the test bundle. Finally, the rods were cooled for 180 seconds.

Key phenomena in the CORA-13 tests were oxidation/hydrogen generation, relocation of core materials, forced convection, conduction, radiation, and fluid-structure heat transfer.

5.2 Nodalization

The present MELCOR analysis is based on an earlier study performed with MELCOR 1.8.1 [2]. The MELCOR model for the fuel rod section split the test bundle into four radial rings. Referring to Figure 5-1, the first ring included a central unheated rod. The second ring had four heated rods, while the third ring had two absorber rods and six unheated rods. The last ring had twelve heated rods. The MELCOR CVH nodalization is shown in Figure 5-2. The fuel bundle is split into three control volumes: CV210, CV220, and CV23 using six 4- and 6-axial COR cells, respectively.

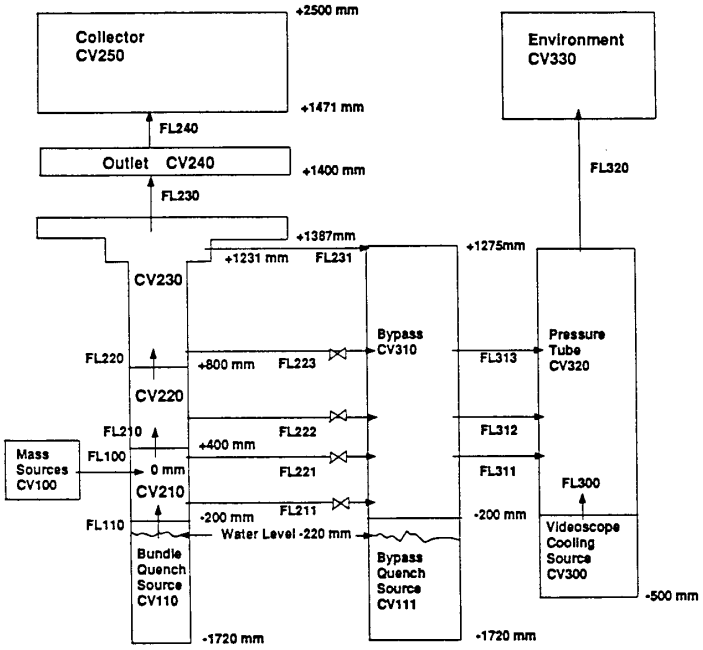

Figure 5-2. MELCOR CVH Nodalization of the CORA-13 Experiment Facility

5.3 MELCOR Input Specifications

For the most part, default parameter options were used in the present MELCOR model of CORA-13, with the following exceptions that were required primarily because of the specific nature of the CORA Facility:

```
* SC1132 ROD FAILURE TEMPERATURE:

SC11322   1132   2800.0   1


* SC1151 CONGLOMERATE DEBRIS SURFACE AREA COEFFS:

SC11511   1151   1.0   3   5   * FAMIN(CAN) = 1.0
SC11512   1151   0.0   3   6   * FBMAX(CAN) = 0.0


*SC1501 CANISTER MASS/SURFACE AREA SPLITS:

SC15011   1501   0.0   1
SC15012   1501   0.0   2
SC15013   1501   0.0   3
SC15014   1501   1.0   4
SC15015   1501   0.0   5


* SC1502 MINIMUM COMPONENT MASSES:

SC15021   1502   1.0E-9   1     * Min Total Mass of Component
SC15022   1502   1.0E-3   2     * Min Mass Subject to Timestep
```

The final version of the MELGEN/MELCOR file is “ncora185final.inp. The corresponding plot file for Hispltm is “plot1.inp.”

5.4 Results of Analysis

The CORA 13 experiment was simulated using MELCOR 1.8.5. The simulation was run on a DEC Alpha computer and required 0.4 hours to run to 5051 seconds, the normal simulation end time.

Figure 5-3 through Figure 5-5 compare the calculated and measured first-ring axial fuel temperature at various levels. The figures show that the code was able to calculate the fuel temperature mostly to within 100 K, especially during the first 4200 seconds of the transient. For comparison, MELCOR 1.8.4 fuel temperatures at two different axial levels are shown in Figure 5-6 and Figure 5-7. They show that the MELCOR 1.8.4 and 1.8.5 temperature histories were about the same.

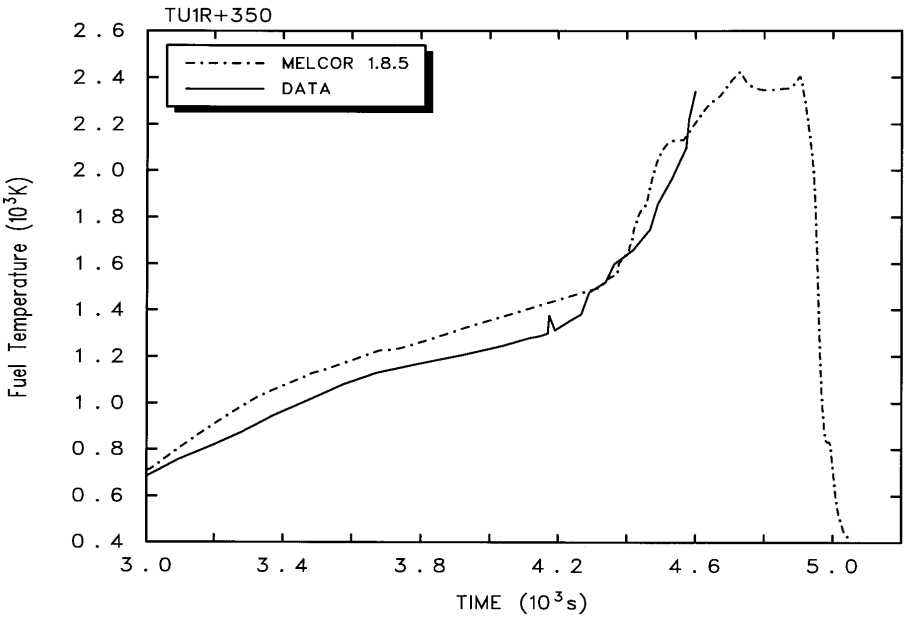

Figure 5-3. Measured and Calculated Fuel Temperature at 350 mm

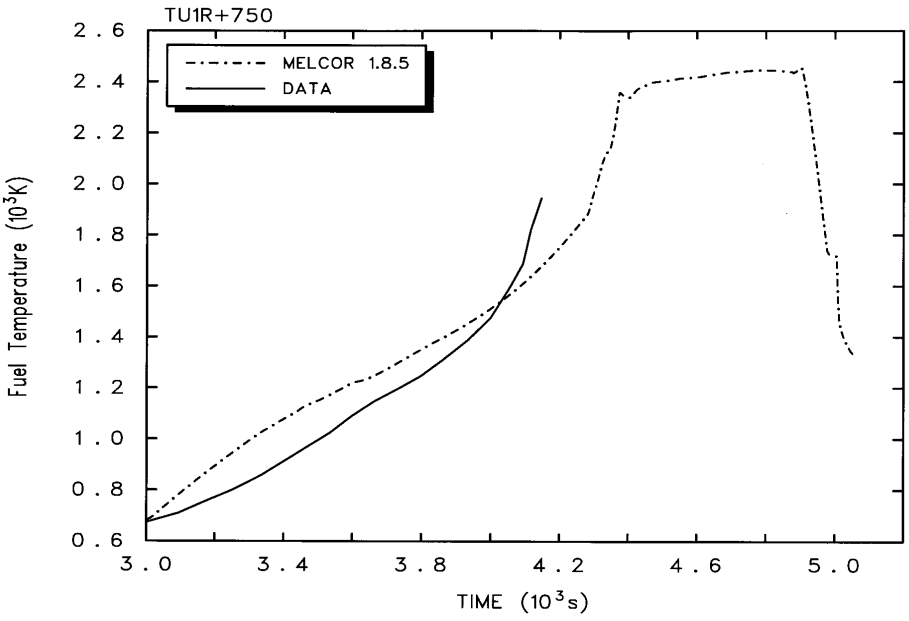

Figure 5-4. Measured and Calculated Fuel Temperature at 750 mm

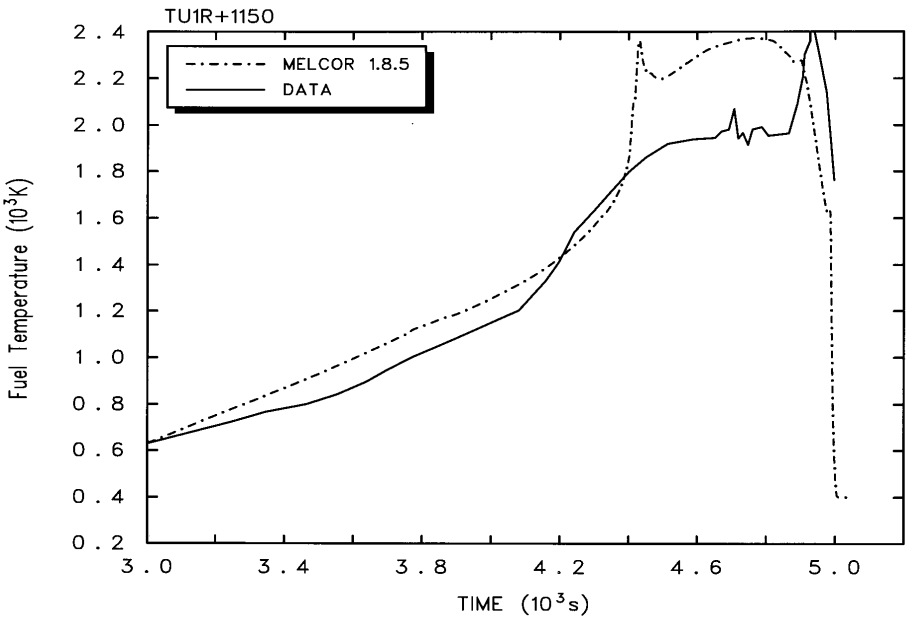

Figure 5-5. Measured and Calculated Fuel Temperature at 1150 mm

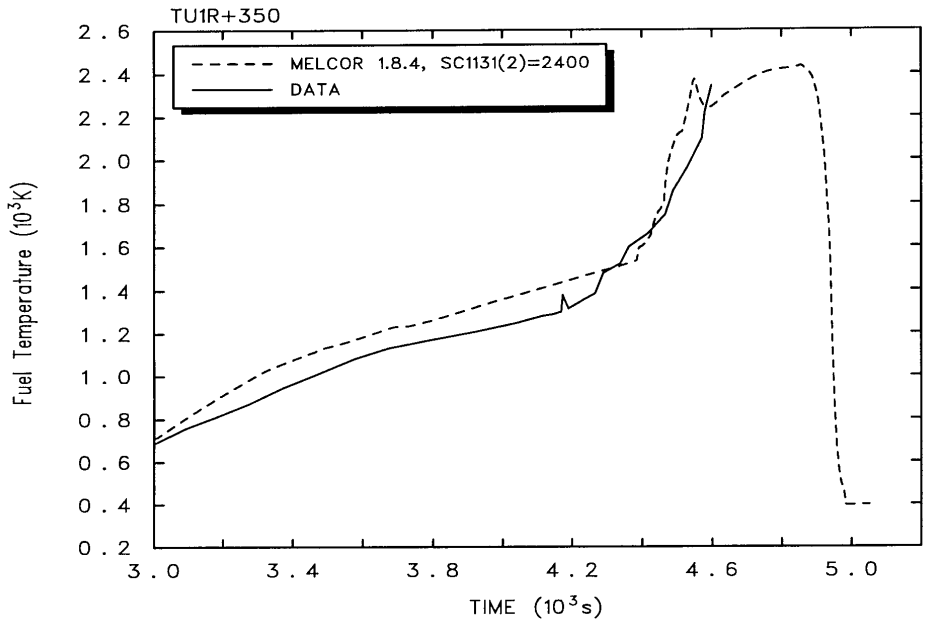

Figure 5-6. Measured and Calculated Fuel and Temperature at 350 mm, MELCOR 1.8.4

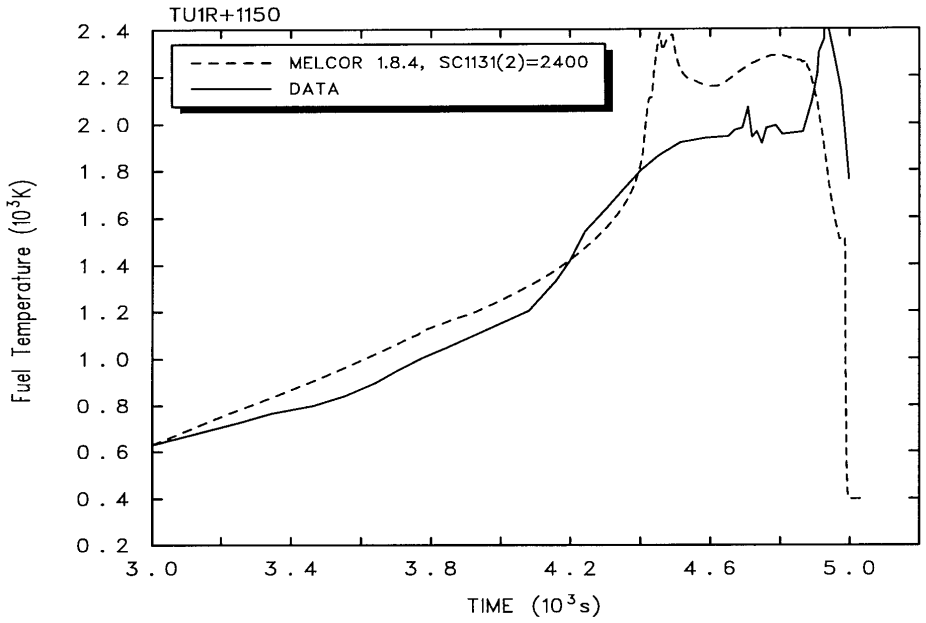

Figure 5-7. Measured and Calculated Fuel Temperature at 1150 mm, MELCOR 1.8.4

From 0 to 3000 seconds, the experiment was being cooled by forced convection and the fuel temperature was predicted within 15 K or less. Radiation heat transfer was not important at this point as the fuel temperature was ~700 K. As a rule of thumb, radiation becomes important when the temperature exceeds about 1000 K. Furthermore, the amount of oxidation energy released from 0 to 3000 seconds was negligible. The comparisons between MELCOR and the experiment during this time period are excellent, indicating that MELCOR's treatment of conduction and convection processes for this test are also reasonably good.

From 3000 to 4870 seconds, oxidation accounted for nearly 50% of the total heat input during the experiment. About 90% of the oxidation energy was released from 4300 to 4800 seconds, and that timeframe is also where the largest difference between the calculated and measured temperatures occurred. These differences were on the order of 200 to 400 K and are believed due more to uncertainties in modeling of the heat losses from the test bundle than to deficiencies in the physics models themselves. In addition, the hydrogen production rate predicted by MELCOR differs somewhat from the measured value, especially with respect to the time signature (Figure 5-8). A large part of this discrepancy in the time signature is believed to be due to a delay in the response of the hydrogen measurement devices owing to the presence of long flow paths and volumes between the test bundle and the measurement sensor. These errors have been discussed in CORA and QUENCH workshops held annually at the KfK facility but have never been published. The magnitude of the hydrogen produced up until the time of the quench compares fairly well with the experiment, however, MELCOR 1.8.5 fails to capture the burst of hydrogen produced when the reflooding action produces steam during the quench

phase. The MELCOR 1.8.4 simulation produced 185 g, while the MELCOR 1.8.5 simulation generated 160 g. The experimental value, including the quench-phase hydrogen was 210 g. If we subtract the amount of hydrogen generated during the quench, roughly 170 g were generated during the experiment, well in line with the MELCOR 1.8.5 calculated results.

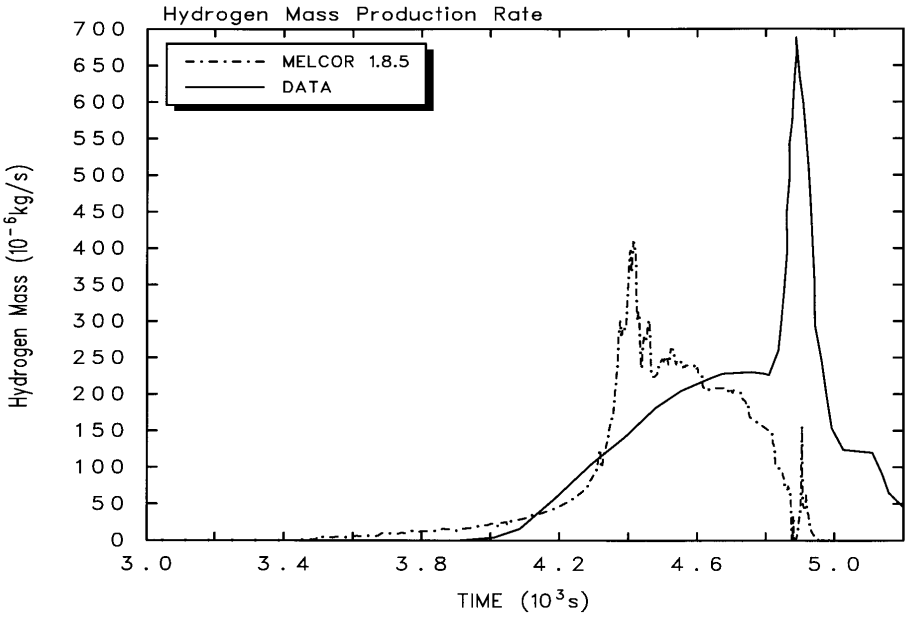

Figure 5-8. Measured and Calculated Hydrogen Generation Rate

The causes of MELCOR's failure to predict significant hydrogen during the quench phase is attributable to two factors. One of these is MELCOR's current lack of adequate reflooding thermal-hydraulic modeling. Work is currently underway to improve MELCOR in this area by including correlations for tracking a quench front which generally lies below the two-phase water level in an inverted annular flow boiling regime. When completed, this model will allow separate tracking of quenched and unquenched fuel rod regions and permit more accurate calculation of steam generation rates and corresponding oxidation rates. Another factor not included in MELCOR is any quench-induced fracturing of the otherwise protective oxide layer on the cladding surface. Some experiments in the QUENCH facility suggest that such fracturing can result in high transient oxidation rates owing to the exposure of fresh metallic zircaloy following cool-down fracturing of the oxide layer. If needed, such features will be added to MELCOR following improvement to the quenching thermal-hydraulics modeling.

In the intermediate period where radiation was important (3500 seconds and on) and the oxidation energy was relatively negligible (0–4300 seconds), we have an overlapping period (3500–4300 seconds) where radiation was important and not overshadowed by oxidation. We note from the temperature figures that the calculated and measured temperatures

were in good agreement, generally within 100 K in that regime. This shows the adequacy of the radiation model.

5.5 Summary

Overall, the MELCOR 1.8.5 component temperatures were about the same as those predicted using MELCOR 1.8.4. Calculated and experimental values for hydrogen generation are close if the quench period is not considered. In future versions of MELCOR, improved quench front modeling and oxidation treatments are expected to improve on the weaknesses revealed in this analysis. Additionally, future assessment of MELCOR in this area is likely to come from more recent (and better-characterized) experiments from the QUENCH program.

5.6 References

1. Hagen, S., et al., Results of SFD Experiment CORA-13 (OECD International Standard Problem 31) KfK 5054, February 1993.

2. Gross, R.J. S.L. Thompson and G.M. Martinez, MELCOR 1.8.1 Calculations of ISP-31: The CORA-13 Experiment, SAND92-2863, June 1993.

6. Analysis of the PHEBUS B9+ Experiment

6.1 Background

The PHEBUS facility located at the Cadarache Nuclear Testing Site in France provides an environment for simulating core conditions during severe accident scenarios. It consists of a driver reactor core to provide neutronic heating to the test bundle, a fluid supply system to inject steam and helium into the test bundle, and associated cooling systems for the bundle and driver core. The main experimental conditions measured are coolant flow, power level, and bundle temperatures.

The following is an analysis of the PHEBUS B9+ test performed in the French SFD program [1]. The B9+ test bundle consisted of a 5x5 square fuel rod assembly with the corner rods removed (21 rods). The fissile length was 80 cm, and the total rod length was about 1 m. The test section was insulated by a radial shroud composed of several layers of porous ZrO_2 insulator to limit radial heat losses.

The B9+ experiment was designed to provide data principally on fuel degradation. There is an initial phase in which steam is supplied to the test section to preoxidize the cladding, followed by helium coolant supply and several increasing power steps. This was followed by a gradual cool-down phase.

Essentially, because this experiment provides information on core material relocation, temperature histories, and hydrogen production. The experiment is very sensitive to the amount of radial heat loss, the main MELCOR models tested are the heat conduction/convection and fuel relocation models. Hydrogen production only occurs during the initial steam phase before any relocation so it is relatively insensitive to simulation parameters.

6.2 Nodalization

The current analysis builds on work performed earlier by Martinez using MELCOR 1.8.1 [2, 3]. The B9+ experiment was modeled in MELCOR with five control volumes representing the inlet, lower plenum, test rod bundle, upper plenum, and environment. The rod bundle was modeled using three COR module rings and twelve axial levels. Level 1 is in the lower plenum, and Levels 2–12 are in the test bundle, with Level 2 being unfueled. A support plate in Level 2 supports the rods. Grid spacers were represented as fixed nonsupporting structure (NS) components. Input gas flow rates were read from an external data file (EDF). The core was specified as a boiling water reactor (BWR), although it is a PWR layout, to allow the zircaloy inner shroud to be represented as a canister component. The rest of the radial insulating shroud was represented as a heat structure with porous ZrO_2, dense ZrO_2, and outer steel layers.

6.3 MELCOR Input Specifications

In the input, the ring-to-ring radiation view factors were increased to give a better match to the experimental temperatures. The fuel failure temperature, defaulted to 2500 K in MELCOR 1.8.5 to reflect irradiated fuel effects, was changed to 2800 K in order to better represent the behavior of fresh (unirradiated) fuel. The COR input was changed to the new 1.8.5 specification insofar as was reasonable.

6.4 Results of Analysis

Principal results from the B9+ experiment examined in this comparison were temperature histories and hydrogen generation. MELCOR 1.8.5 results were found to be essentially identical to the previous MELCOR 1.8.4 results in spite of considerable modifications to the version 1.8.5 melt progression models. This is largely because the test bundle heatup and oxidation periods involved very little melting or material relocation until the very end of the test. Cladding oxidation occurring below the Zr melting temperature generated the most hydrogen produced in the test. Because of this, the version 1.8.5 models performed very much the same as the version 1.8.4 models. Several representative temperature histories are shown in Figure 6-1 through Figure 6-3, and the hydrogen production is shown in Figure 6-4.

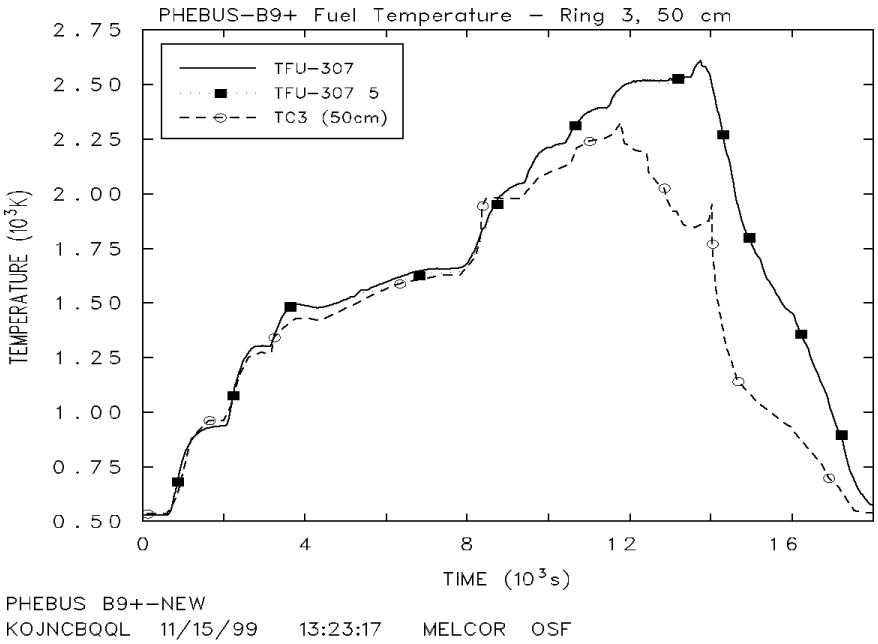

Figure 6-1. MELCOR 1.8.4 and 1.8.5 Fuel Temperature and Thermocouple Data

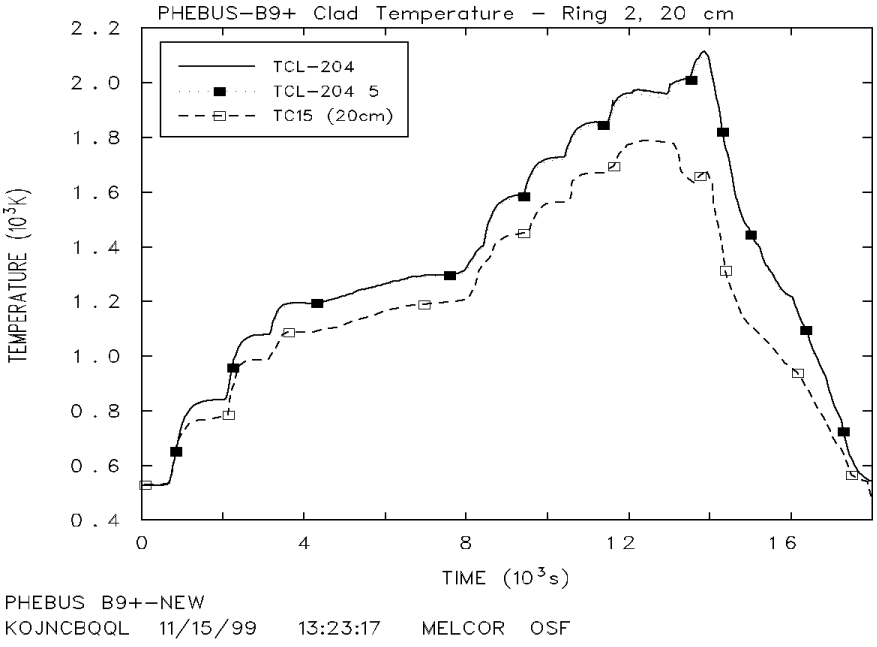

Figure 6-2. MELCOR 1.8.4 and 1.8.5 Clad Temperature and Thermocouple Data

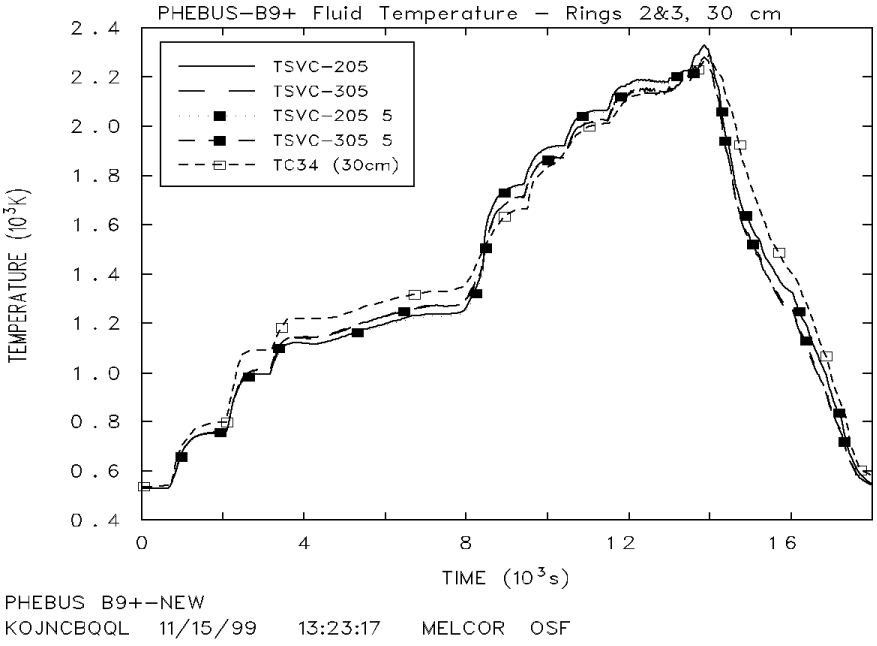

Figure 6-3. MELCOR 1.8.4 and 1.8.5 Fluid Temperature and Thermocouple Data

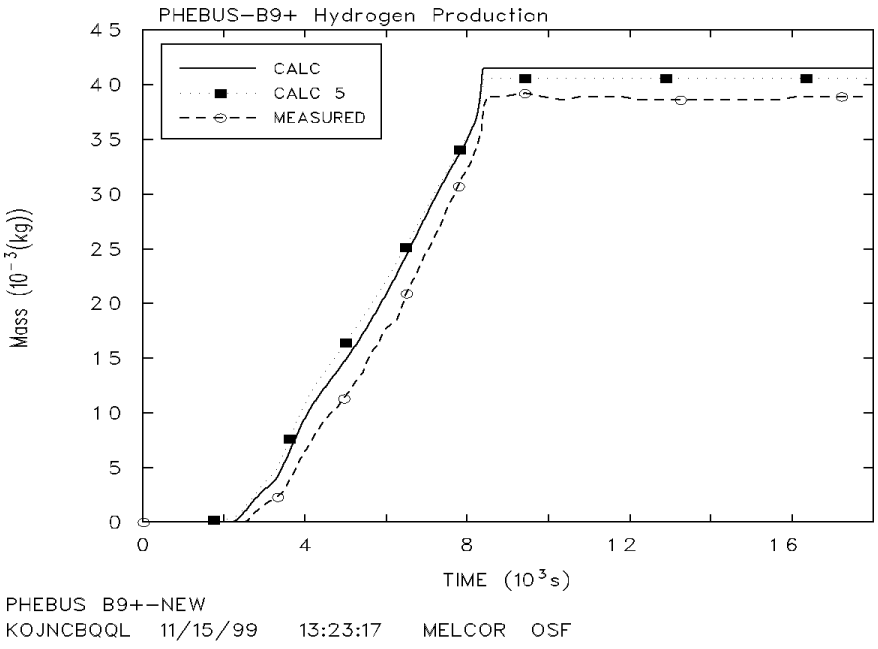

Figure 6-4. MELCOR 1.8.4 and 1.8.5 Calculated Hydrogen Production and Data

6.5 Discussion

The MELCOR 1.8.5 temperature and hydrogen results are in reasonable agreement with the experimental data and virtually identical to the 1.8.4 results. The comparisons to the B9+ test provide a limited verification of the convection and radiation heat transfer processes modeled in MELCOR as well as the prediction of oxidation and hydrogen prior to extensive melting and relocation of materials in the test bundle. In the future, greater emphasis will be placed on more recently conducted PHEBUS experiments, such as the FPT-1 experiment that made use of irradiated fuel and characterized fission product release, as described in the following section.

6.6 References

1. Gonnier, Ch., et al., PHEBUS SFD Programme—Main Results, ANS Topical Meeting, Portland, Oregon, July 21–25, 1991.

2. Martinez, G.M., “MELCOR Calculation of ISP-28 SFD PHEBUS Test: B9+,” Report to Farouk Eltawila and Bernard Androguer, Sandia Letter Report, December 1990.

3. Androguer, B. and P. Villalibre, “Review of B9+ Benchmark Results,” The PHEBUS Fission Product Project, Elsevier Applied Sciences, IBSN 1-85166-765-2, 1992.

7. Analysis of the PHEBUS FPT-1 Experiment

7.1 Background

The FPT-1 experiment was an in-pile, irradiated fuel experiment conducted in the PHEBUS Fission Product Facility by the Nuclear Safety and Protection Institute (IPSN) at Cadarache, France, on July 26, 1996 [1, 2]. This test was the second in a series of six in-pile source term experiments [3]. The FPT-1 system consisted of an in-pile fuel bundle assembly and upper plenum region, an external circuit including a steam generator U-tube and connecting lines, and a containment section. The objective of the fuel bundle assembly was to assess fuel degradation and fission product release from a degraded fuel assembly. In the circuit, the objective was to determine fission product transport and deposition in steam generator tubes.

The key models that were exercised in the MELCOR analysis of this test include those for cladding oxidation, thermal modeling, and core material relocation, and for the release, transport, and deposition of fission products in an LWR-type reactor coolant system. For purposes of model verification, the following measured parameters were available from the test database:

- Global-cladding oxidation was assessed from thermocouple responses and from measurements of hydrogen generation rates.

- Thermal modeling was assessed from thermocouple responses and temperature profiles.

- Material relocation was assessed from thermocouple responses (both time responses and axial profiles) caused by downward relocation of fuel material. In addition, radiography and transmission tomography provided information about the distribution of materials in the end state.

- Emission tomography of the fuel bundle and steam generator as well as measurements of activity along the external line to the containment provided data for fission product release, transfer, and deposition comparison.

7.2 Nodalization

A MELCOR input deck was developed to model the geometry and test conditions of the FPT-1 experiment. The deck was generated initially by KEMA (Netherlands) to model FPT-0 and was modified by Sandia to describe the details of the FPT-1 test. The current version incorporates data from the FPT-1data book and the FPT-1 quick-look report and includes further modifications to render it compatible with MELCOR 1.8.5. Figure 7-1 and Figure 7-2 show the MELCOR input model, including nodalization for the test section and the overall circuit control volume representations.

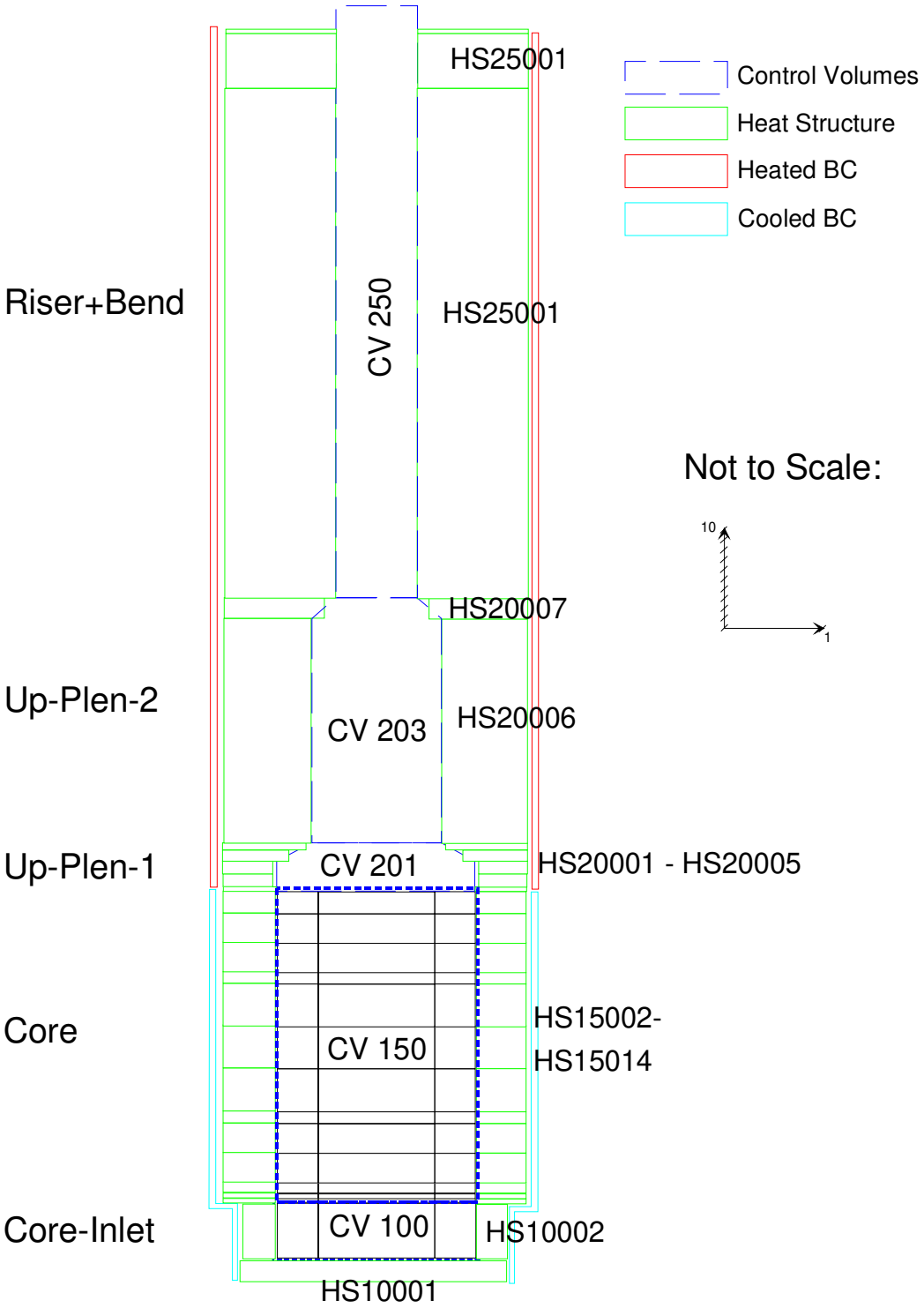

Figure 7-1. MELCOR FPT-1 Test Section Nodalization

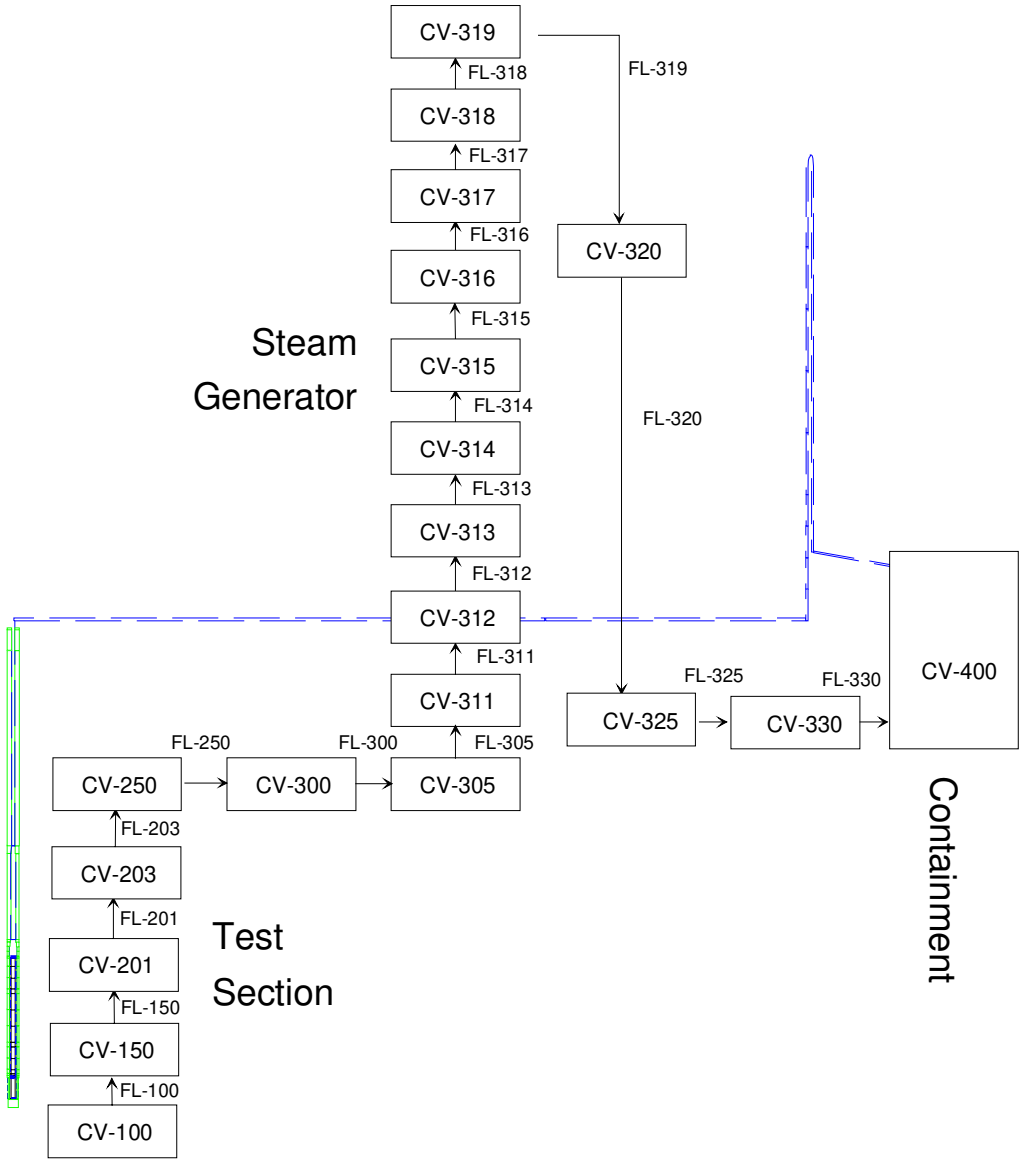

Figure 7-2. MELCOR FPT-1 Circuit Control Volume Nodalization

7.3 MELCOR Input Specifications

Input for the fuel bundle included two radial rings with eight fuel rods and a single control rod in ring 1 and twelve rods with a zircaloy stiffener in ring 2. Two grid spacers and a core support plate (CSP) were also modeled. The key differences between the MELCOR 1.8.4 and the MELCOR 1.8.5 input models have to do with how the other structures (OS) components were modeled. The grid spacers, CSP, control rod, and stiffener were all required to be modeled as OS in MELCOR version 1.8.4. The differentiation of OS into NS and supporting structure (SS) in MELCOR version 1.8.5 provided greater flexibility in modeling these structures. In the MELCOR 1.8.5 representation, the CRGTs, stiffeners

and grid spacers were modeled as NS and the CSP was modeled as an edge-supported SS-type structure.

Materials that were specific to the experiment, such as fiber insulation to reduce radial heat losses, required the addition of appropriate new material types and their associated thermophysical properties in the Materials Properties (MP) package input.

The default value of the fuel failure temperature in MELCOR 1.8.4 was 2800 K. That value was considered to be inappropriate for high burn-up fuel, and was changed to 2500 K in the previous 1.8.4 analyses of FPT-1. A value of 2500 K is now the default value for the 1.8.5 version, and it was retained in the 1.8.5 calculation of FPT-1.

The input decks for the 1.8.4 and 1.8.5 calculations are both named phebus1.cor and phebus1.gen. These cases were run in separate directories on the DEC Alpha system. Most of the actual input was introduced through the following set of R*I*F files: test-sec1.gen, rn1.gen, matprop1.gen, dch1.gen, core1.gen, contain1.gen, and circuit1.gen. These files and the corresponding output files have been retained for future reference.

7.4 Results of Analysis

In general, the MELCOR 1.8.5 simulation of the FPT-1 experiment produced results similar to those obtained using version 1.8.4. Peak fuel temperatures, although marginally higher in 1.8.5, are consistent with earlier code results. For example, Figure 7-3 and Figure 7-4 give the temperature history of the MELCOR nodes closest to thermocouple, TC-3, located in the lower half of the bundle in ring 2 about 400 mm above the bottom of the active core. This thermocouple was located in a channel drilled axially up through the fuel pellets within one of the fresh unirradiated fuel rods.

Figure 7-3 shows version1.8.5 results, while Figure 7-4 provides 1.8.4 results, both compared to the thermocouple data. Between MELCOR versions 1.8.4 and 1.8.5, there were no significant differences in the calculated temperatures until the latter reached the fuel failure temperature of 2500 K, at which time that node was converted to debris. Fuel failure was not predicted to occur in ring 2 in the MELCOR 1.8.4 calculation; but examination of Figure 7-4 shows that it came very close. Note that Figure 7-4 actually shows fuel temperatures of slightly over 2500 K at the time that power was reduced at 17,000 seconds, but the fuel failure criterion is applied to the clad temperature that lags slightly behind the fuel temperature.

Hydrogen production provides a measure of the level of steam/metal reactions within the bundle and is a strong indicator of whether the code is adequately modeling the overall temperature characteristics of the experiment. Figure 7-5 and Figure 7-6 show the total accumulated hydrogen as compared to the measured data for MELCOR 1.8.5 and 1.8.4, respectively. Again, version 1.8.5 results are slightly higher, mostly reflecting higher peak fuel temperatures compared to version 1.8.4 results. Both codes achieve results consistent with the measured data well within the estimated uncertainty in the data.

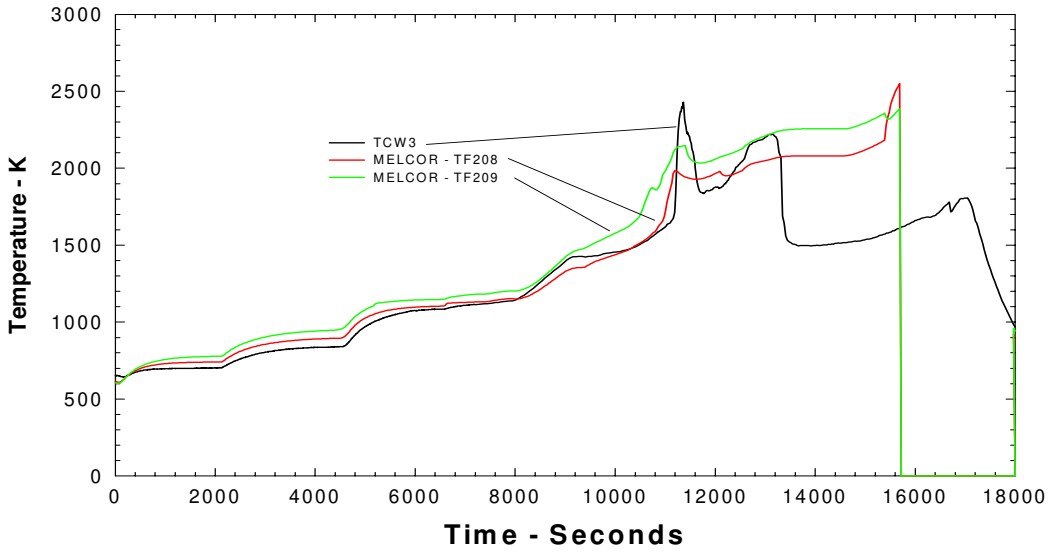

Figure 7-3. Comparison of Measured and Calculated Temperatures for MELCOR 1.8.5

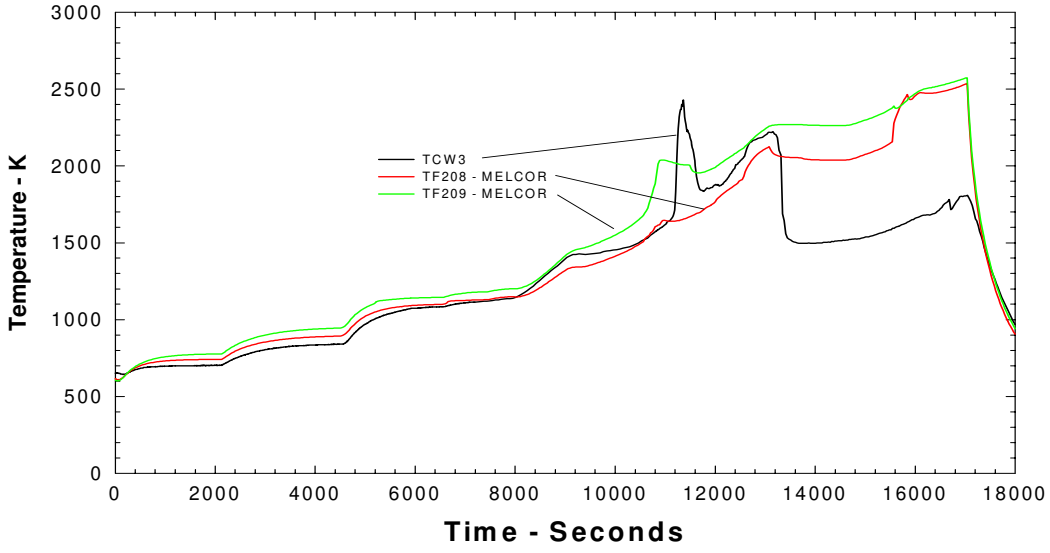

Figure 7-4. Comparison of Measured and Calculated Temperatures for MELCOR 1.8.4

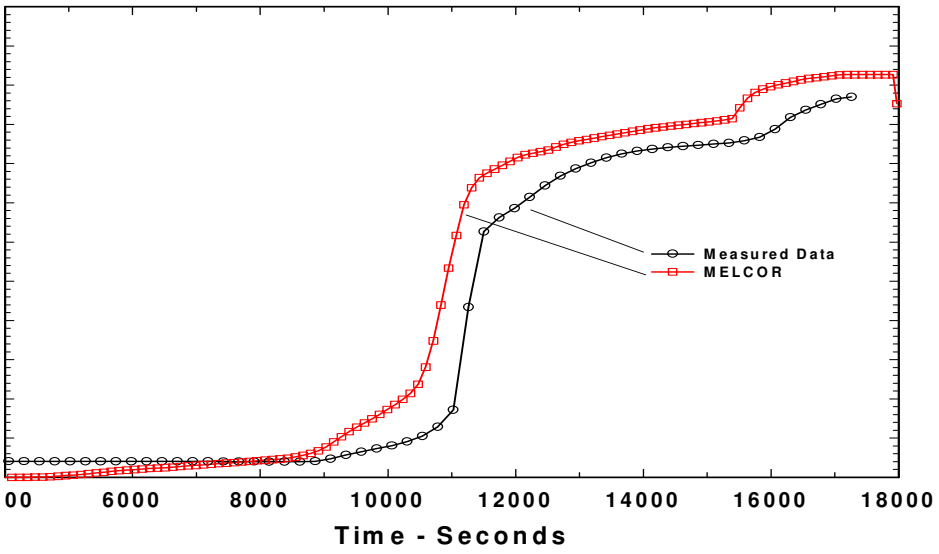

Figure 7-5. Comparison of Measured and Calculated Hydrogen Production for MELCOR 1.8.5 *(Note: Data values not publicly available)*

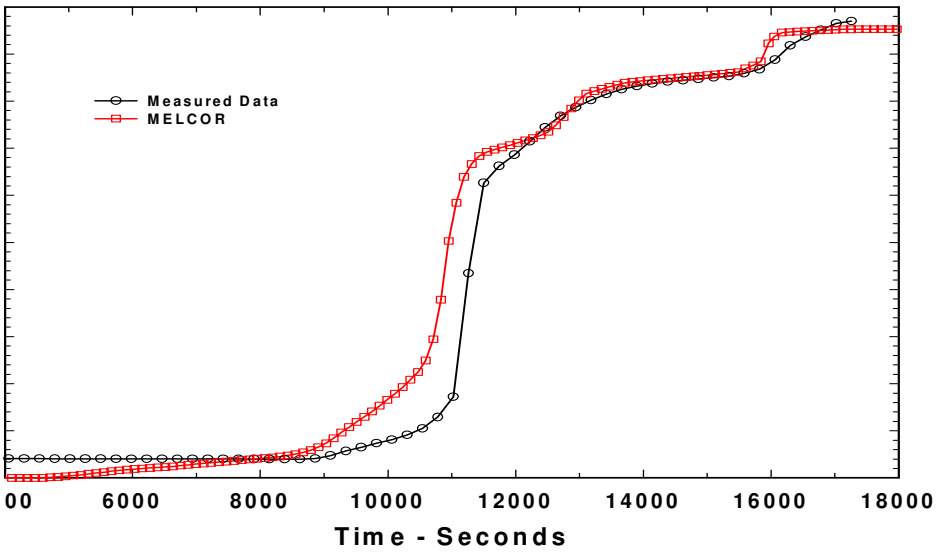

Figure 7-6. Comparison of Measured and Calculated Hydrogen Production for MELCOR 1.8.4. *(Note: Data values not publicly available)*

End-of-test estimates of the total fission product releases were also well characterized by version 1.8.5. For xenon, iodine and tellurium, the calculated releases were about 90% of

initial inventories for fission products, compared to numbers in the range of 83% to 88% from post-test measurements. These numbers are somewhat better than those obtained from 1.8.4, which ranged up to 95%. The fission product releases are presented in Figure 7-7 and Figure 7-8.

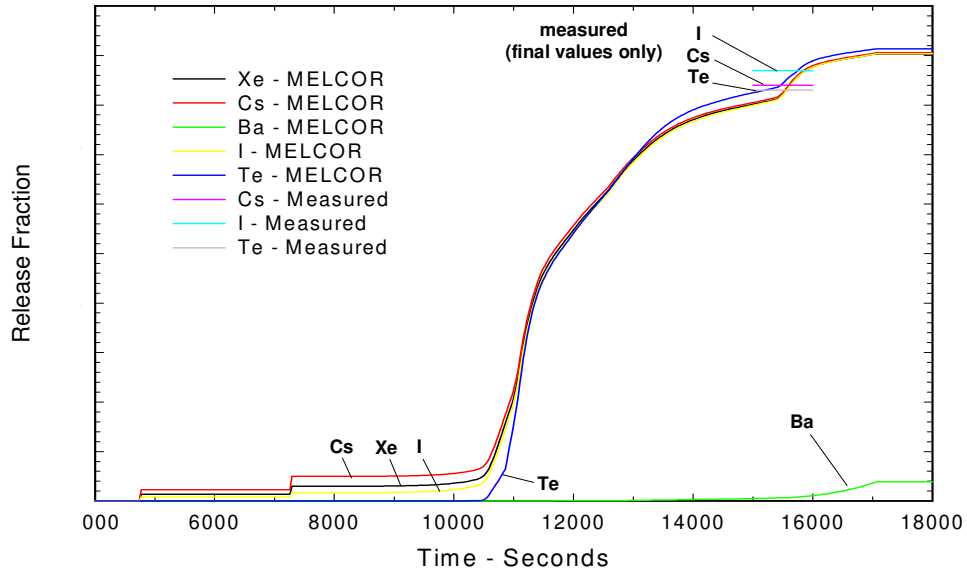

Figure 7-7. Comparison of Calculated and Measured Fission Product Releases for MELCOR 1.8.5. *(Note: Data values not publicly available)*

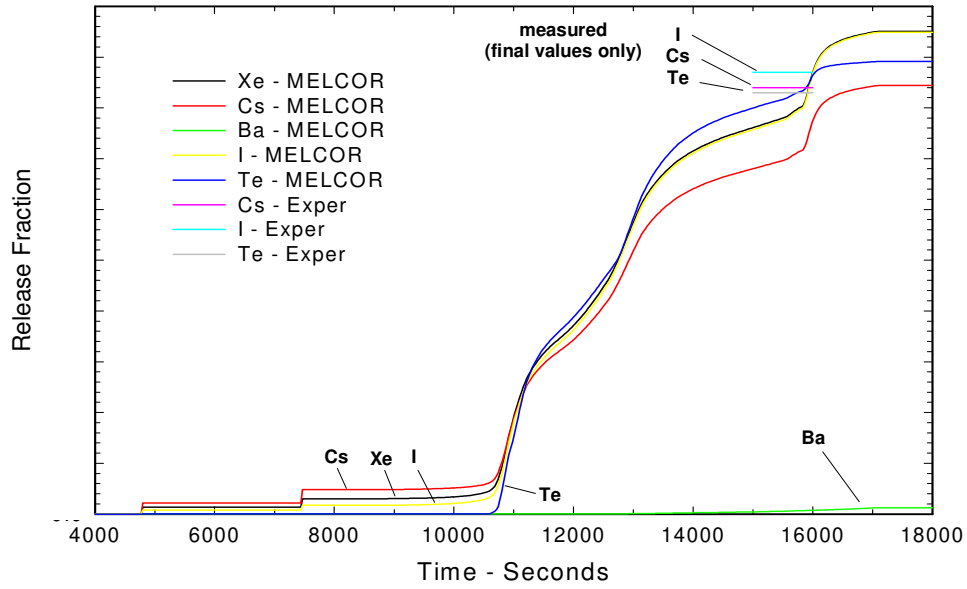

Figure 7-8. Comparison of Calculated and Measured Fission Product Releases for MELCOR 1.8.4. *(Note: Data values not publicly available)*

Fission product deposition in the steam generator tube was well characterized in terms of the relative deposition profile within the tube (see Figure 7-9 and Figure 7-10). That is, it was predicted to have high fission product deposition at the tube entrance gradually decreasing along the tube. The predicted total deposition in the U-tube was about four times higher than that measured in the post-test examination. This was a result of much less deposition in the upper plenum and the lines leading to the steam generator tube than appears to have occurred in the test. So the fission products that should have deposited in these locations were instead transported to the steam generator tube and deposited there. These results were essentially the same for both versions of the code.

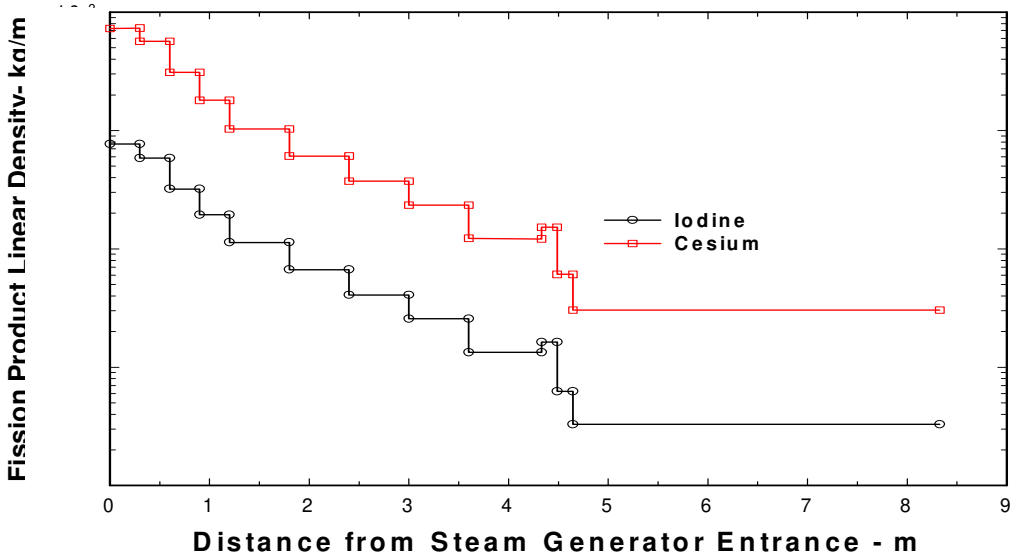

Figure 7-9. Distribution of Fission Products in the SG Tube for MELCOR 1.8.5. *(Note: Data values not publicly available)*

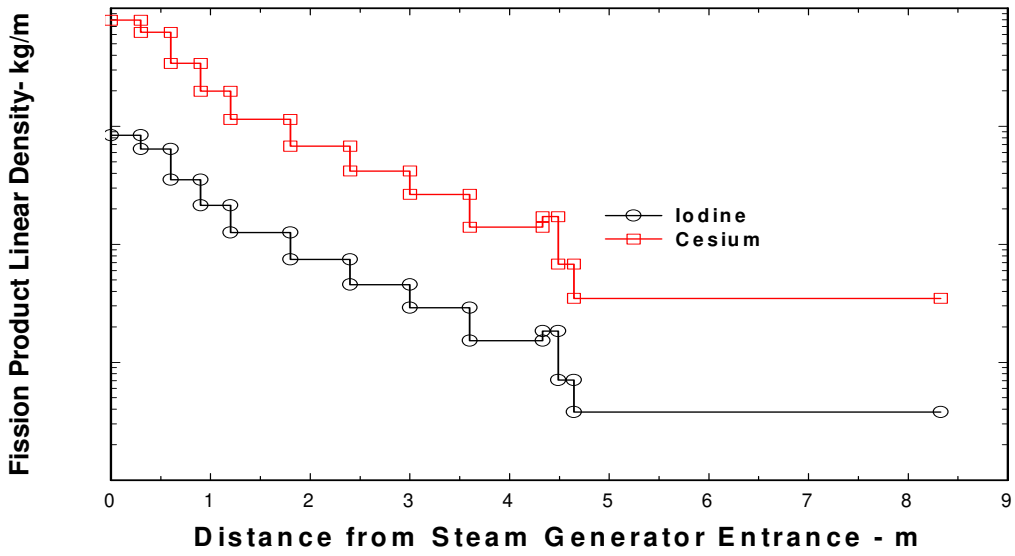

Figure 7-10. Distribution of Fission Products in the SG Tube for MELCOR 1.8.4. *(Note: Data values not publicly available)*

7.5 Discussion

The overall assessment of MELCOR 1.8.5 compared to version 1.8.4 relative to the simulation of the FPT-1 experiment is generally good. Because the CSP did not fail during the experiment, the threshold effects often associated with this event did not occur, and the effects of the OS modification did not appear to have a significant effect on the results. The 1.8.5 version of the code predicted slightly higher temperatures, which led to reduction of both rings 1 and 2 to particulate in the upper half of the bundle. This did not occur in 1.8.4 where only the inner ring was reduced.

As was the case for the MELCOR 1.8.4 analysis of this experiment, the code still predicts bundle and shroud temperatures higher than those measured in the test. However, it must be noted that the temperature generally diverges from the measured data late in time when the bundle is very hot and the thermocouples have begun to degrade. Total fission product releases as calculated by MELCOR 1.8.5 compare well with post-test estimates and the hydrogen production continues to be well characterized by the new version.

Further modifications to the MELCOR input models for this test, particularly for the heat structures associated with the upper plenum and lines that lead to the steam generator tube, would likely improve the calculated disposition of fission products within the circuit. A good deal of uncertainty still remains as to the actual effective bundle energy deposition during the test. This may be responsible for the differences in heatup rate.

7.6 References

1. Berthet, B., et al., FPT-1 Quick Look Report, PHEBUS Document PF IP/96/310, Note Technique Leres n 55/96, (Restricted Distribution) September 1996.

2. Schwarz, M., et al., "The PHEBUS PF International Research Program on Severe Accident: Status and Main Findings," 26th Water Reactor Safety Information Meeting, Bethesda, Maryland, October 26–28, 1998.

3. Schwarz, M., B. Clement and A.V. Jones, "Applicability of PHEBUS FP Results to Severe Accident Safety Evaluations and Management Measures," FISA 99 EU Research In Reactor Safety, EUR 19532 EN, IBSN 92-828-9588-2.

8. Simulation of LB LOCA at the Surry Nuclear Power Station (With No Emergency Core Cooling System [ECCS] Recovery)

8.1 Background

The Surry Nuclear Power Plant (Unit 1) is a Westinghouse three-loop PWR with a sub-atmospheric containment. A MELCOR model has been developed that is intended to be representative of the Surry plant. The MELCOR model has been used for many purposes, among them being support being the NRC's efforts to evaluate radiological consequences of design basis accidents using the revised source term [1,2]. The revised source term analysis for Surry was supported by MELCOR simulation of a Large-Break (LB) Loss-of-Coolant Accident (LOCA), specifically a double-ended guillotine rupture of the cold leg piping. That analysis is reproduced here in a scenario that represents complete failure of the LPSI system. In this analysis, core melting occurs with eventual vessel failure and release of core materials to the containment. Containment sprays and fan coolers are operative, mitigating the consequences of the ex-vessel accident phase.

8.2 Nodalization

The Surry plant model was based on that originally used in the analyses documented in NUREG/CR-6107 for the S2D sequence [3]. This model was subsequently modified by Sandia [1] to assess the impact of applying the NUREG-1465 rebaselining source term to the calculation of population dose for recovered LOCAs. The resulting Surry plant model for the LB LOCA is the model used in the analysis presented herein. MELCOR node diagrams for the primary system and containment are shown in Figure 8-1 and Figure 8-2, respectively. The core configuration for the Surry model is shown in Figure 8-3.

At this point, some discussion concerning nodalization of the reactor core and coolant system is appropriate. The nodalization used in this analysis follows an approach used extensively in prior MELCOR analyses, where, for reasons associated with previous (more limited) code capabilities and for computer economy, a relatively simple nodalization has been taken. Specifically, a single CVH volume has been assigned to the entire core region and relatively coarse nodalization is taken for the reactor vessel. Likewise, the coolant hot leg and RCS are described by 1-D volumes and flow paths. This nodalization precludes the prediction of recirculation flows either in the core/upper plenum regions or the sometimes-observed hot leg/steam generator counter current recirculation flow phenomena.

Generally speaking, these phenomena are more important for high pressure sequences where the core heatup and degradation takes place with the primary system at operating pressure. In this respect, the present LOCA analysis is not expected to exhibit recirculation effects. However, it is our recommendation that for MELCOR code versions beyond version 1.8.5, high-pressure analyses be performed using a greater number of CVH nodes to describe the reactor vessel and coolant system.

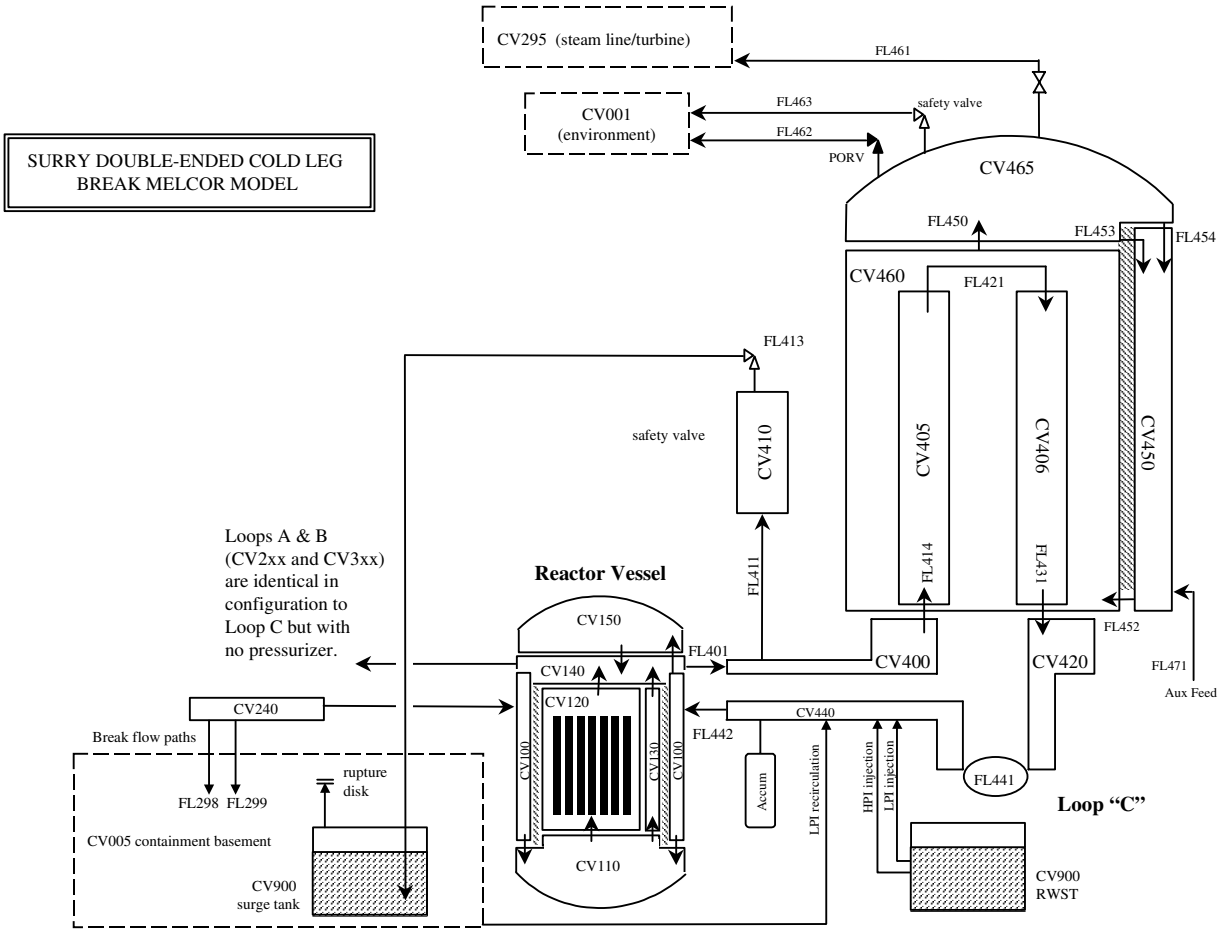

Figure 8-1. MELCOR Node Diagram for Surry Primary System

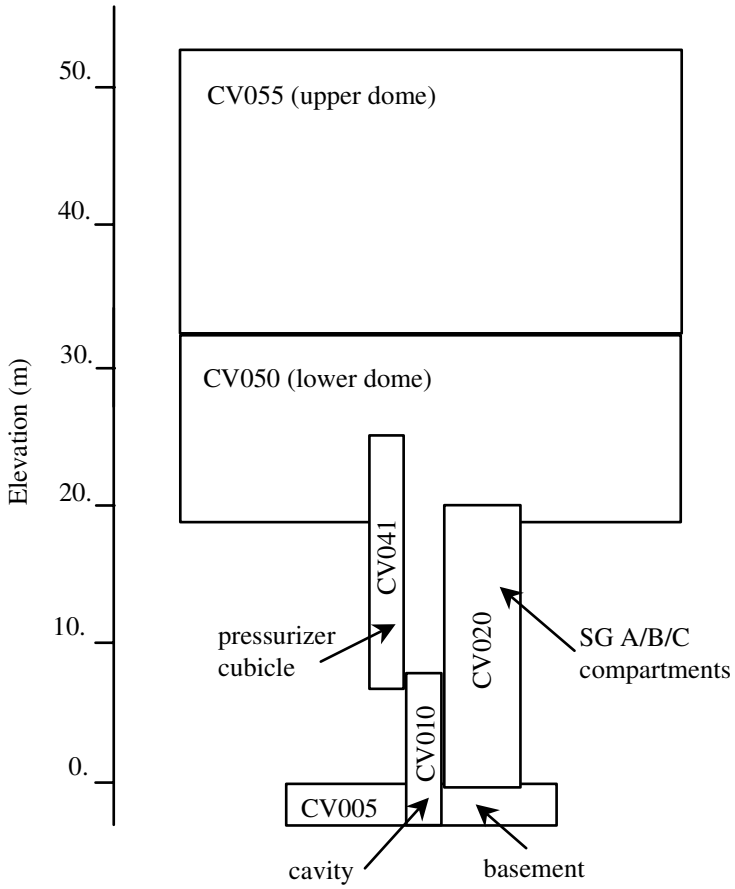

- Cold leg break discharges in CV005
- Surge tank located on floor of CV005
- Containment sprays discharge near top of CV050

Figure 8-2. MELCOR Node Diagram for Surry Containment

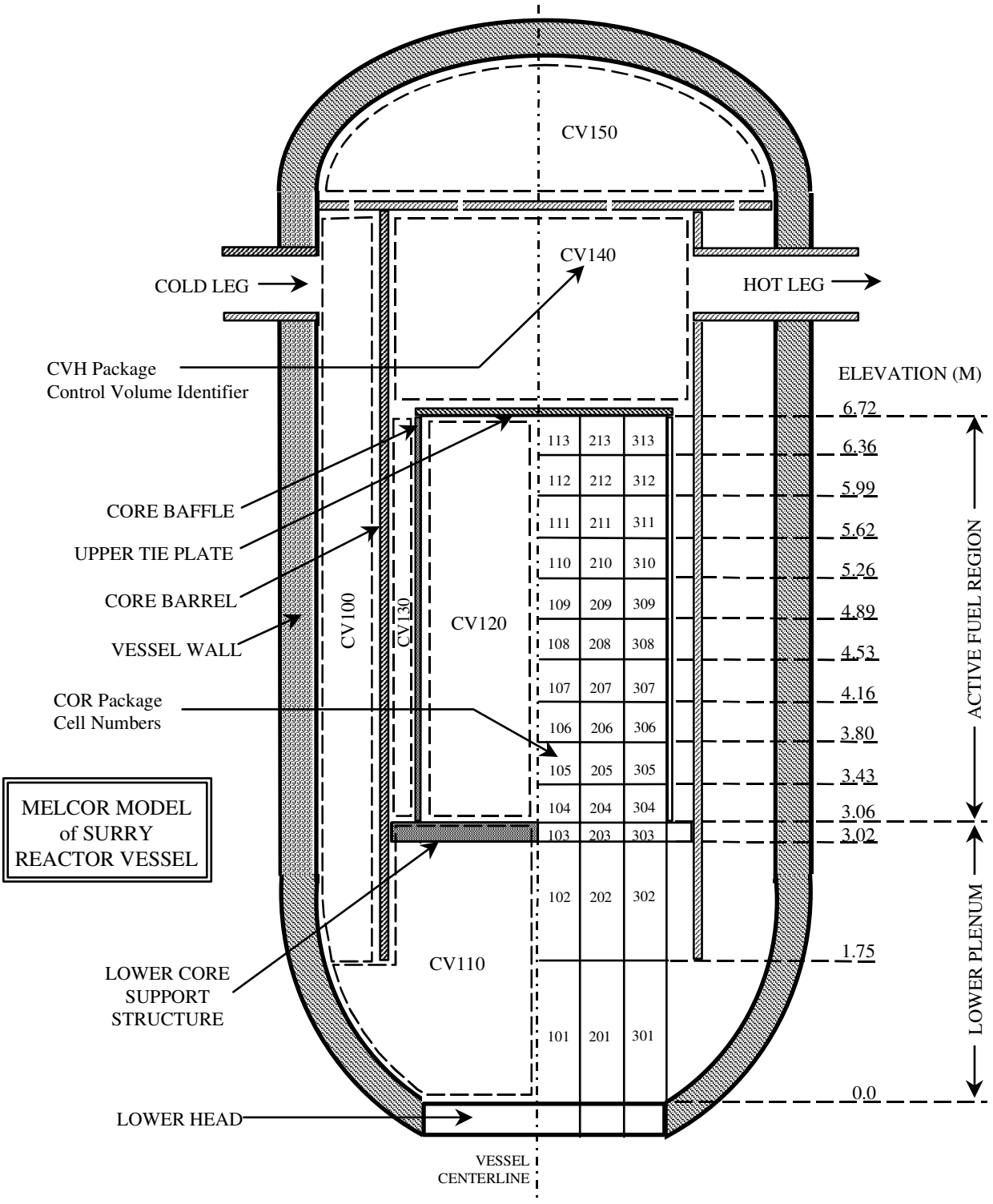

Figure 8-3. MELCOR Core Configuration for Surry Plant

8.3 MELCOR Input Specifications

The MELGEN input files for this calculation are “surry.gen” and “cor.gen”. The “surry.gen” file is the primary MELGEN file. The “cor.gen” file is automatically read in during MELGEN processing because it is identified by the “r*i*f” command in the “surry.gen” input file. The “cor.gen” file is a complete replacement for the COR package input that was developed during the rebaselining study. The modifications to the COR package input were made to allow future users to take advantage of the MELCOR SS and NS features now available in MELCOR 1.8.5.

The MELCOR input file for this calculation is “surry.cor.”

In general, the Surry model was developed using standard, default MELCOR modeling parameters. Key modeling input parameters are listed in Table 8-1. Other boundary conditions for the LB LOCA transient are listed in Table 8-2.

Table 8-1. Key Modeling Parameters for Surry LB LOCA

Parameter	Record	Description	Default Value	Surry Value
IUEMOD	COR00006	Eutectics model	0 (inactive)	0*
IHSDT	COR00006	Heat structure (HS) boundary condition option	0 (BC option required)	0*
IDTDZ	COR00006	DTdz inlet option switch	0 (dtdz from CVH/FL hydrodynmics calcs)	0*
MTUOZR	COR00007	Transport mech. Flag for UO_2 in molten zircaloy	1 (UO_2 transported as a fraction of the molten mass)	1*
MTZXZR	COR00007	Transport mech. Flag for ZrO_2 in molten zircaloy	1 (ZrO_2 transported as a fraction of the molten mass)	1*
MTSXSS	COR00007	Transport mech. Flag for steel oxide in molten steel.	2 (steel oxide transported as a fractional proportion to its existing fraction in the steel)	2*
HDBPN	COR00009	Lower head failure parameters: heat transfer coefficient from debris to penetration structures.	1000 W/m^2K	500 W/m^2K
HDBLH	COR00009	Lower head failure parameters: heat transfer coefficient from debris to lower head	1000 W/m^2K	500 W/m^2K
TPFAIL	COR00009	Failure temperature of penetrations or lower head.	1273.15 K	1273.15 K
ICONV	RN2001	Convection option switch	0 (flowpath convection of radionuclides calculated)	0*
ICOND	RNACOND	Aerosol condensation index	0 (condensation on all existing aerosols)	0*
ISPNUM	RN2SPRxx	Spray source number	None	1 (indicates spray source for injection mode and one source for recirculation mode)
ICRLSE	RNFP000	Core release model indicator	-2 (CORSOR-M model with surface to volume ratio option)	-2

Parameter	Record	Description	Default Value	Surry Value
IHYGRO	RN1002	Hygroscopic model	0 (not active)	1 (active)
ICA02	RNCA100	Chemisorption model	1 (on)	1

*Not included in input, default value is assumed by MELGEN.

Table 8-2. Surry LB LOCA Boundary Conditions

Boundary Condition	Surry LB LOCA
Accumulators	Operate as designed (injection at 4.2403 MPa RCS pressure).
High-pressure injection (HPI)	Assumed to fail.
LPSI	Assumed to fail.
RCS Pressure Boundary Status	Double-ended guillotine rupture of Loop A cold leg at time = 0.0 sec. Total break area is 0.8838 m^2.
Primary Pressure Control	power-operated relief valve (PORVs) and SRVs irrelevant because of rapid depressurization following rupture of cold leg.
Steam Generator PORVs	Assumed to open when secondary pressure reaches 16.2 MPa. (hysteresis cycle).
Steam Generator SRVs	Assumed to open when secondary pressure reaches 17.75 MPa. (hysteresis cycle).
Auxiliary Feedwater	Operates as designed following scram.
Reactor Power	Scram at t = 0.0 sec.
Containment Sprays	Operate single train in injection mode when ctmt pressure exceeds 172 kPa. Switch to recirculation mode at 20% RWST level. Two trains operate in recirculation mode.
Containment Fan Coolers	Operate as designed (low capacity fans on at time = 0.0 sec).
Containment Leakage	Assumed to be 0.1 vol % / day at containment design pressure from lower dome. Hole size is 2.42 mm equivalent.

8.4 Results of Analysis

The MELCOR 1.8.5 simulation of the Surry LB LOCA ran to completion and all results appeared to be reasonable. Calculated results are summarized in this section, and a discussion of these results is presented in the following section.

A double-ended guillotine rupture of the Loop A cold leg initiated the LOCA sequence analyzed. This resulted in coolant discharged out of the equivalent of two 0.44 m^2 (4.74 ft^2) holes. Table 8-3 summarizes the LOCA accident sequence MELCOR-calculated timing of events. Note that early event timing was essentially identical to that calculated by MELCOR 1.8.4. However, the MELCOR 1.8.5 accident proceeded more slowly than the 1.8.4 calculation after the initial fuel heatup and relocation. Reasons for this delay in accident progression are considered in the Discussion of Results.

Table 8-3. MELCOR-Calculated Timing of Events for Surry LB LOCA

1.8.4 (min)	1.8.5 (min)	Event
0	0	Double-ended rupture occurs in Loop A cold leg (Total break area = 0.88 m^2, 9.5 ft^2).
0.05	0.05	Containment spray signal of 0.17 MPa (25 psia) containment pressure.
0.22	0.22	Swollen reactor water level reaches bottom of active fuel (3.08 m, 10.1 ft above reactor bottom).
0.55	0.55	Containment sprays initiated in injection mode after 30 -second delay.
3.1	3.4	Gap release begins in core radial ring 1.
3.5	3.9	Gap release begins in core radial ring 2.

5.1	5.7	Gap release begins in core radial ring 3.
20.5	19.1	CSP fails in core radial ring 1.
20.0	38.0	Containment pressure drops below 0.10 MPa, 14.7 psia (containment leakage terminates).
23.6	38.8	CSP fails in core radial ring 3.
25.0	22.7	In-vessel hydrogen production terminated (approximately 105 kg in 1.8.5, 75 kg in 1.8.4).
25.1	38.5	Lower head penetration fails in core radial ring 3.
25.1	34.7	CSP fails in core radial ring 2.
25.1	43.4	Debris ejection to cavity begins–core-concrete interaction initiated in cavity.
96.8	96.8	Containment sprays (injection mode) terminated on low (20%) RWST level.
96.8	96.8	Containment sprays (recirculation mode) initiated.
244.	204.	Series of containment hydrogen deflagrations occur.
-	534.	Series of containment hydrogen deflagrations occur.
600.	600.	MELCOR calculation terminated.

The following figures show results for the Surry LB LOCA MELCOR 1.8.5 simulation. Results are compared to MELCOR 1.8.4 simulation results. General trends show reasonable comparison between MELCOR 1.8.4 and 1.8.5 calculated results. However, differences are apparently due to MELCOR code enhancements between the 1.8.4 and 1.8.5 code releases. The principal difference is a delay in the in-vessel accident progression after initial core heatup and relocation in 1.8.5 when compared with the 1.8.4 calculation. These differences are discussed in the following section.

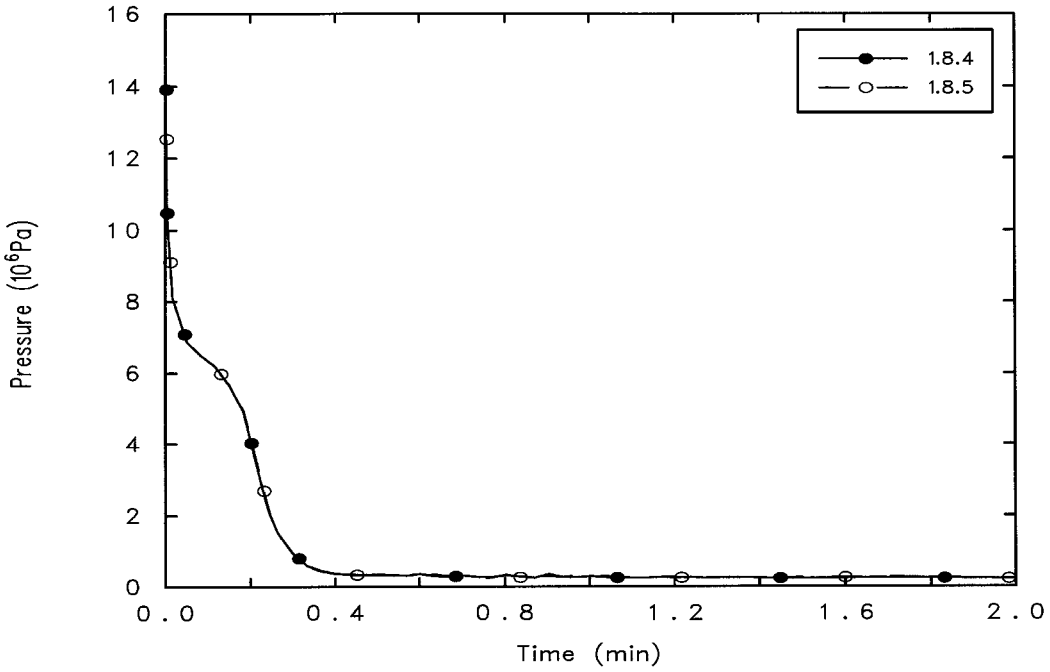

Figure 8-4. Surry LB LOCA: Primary System Pressure (short term)

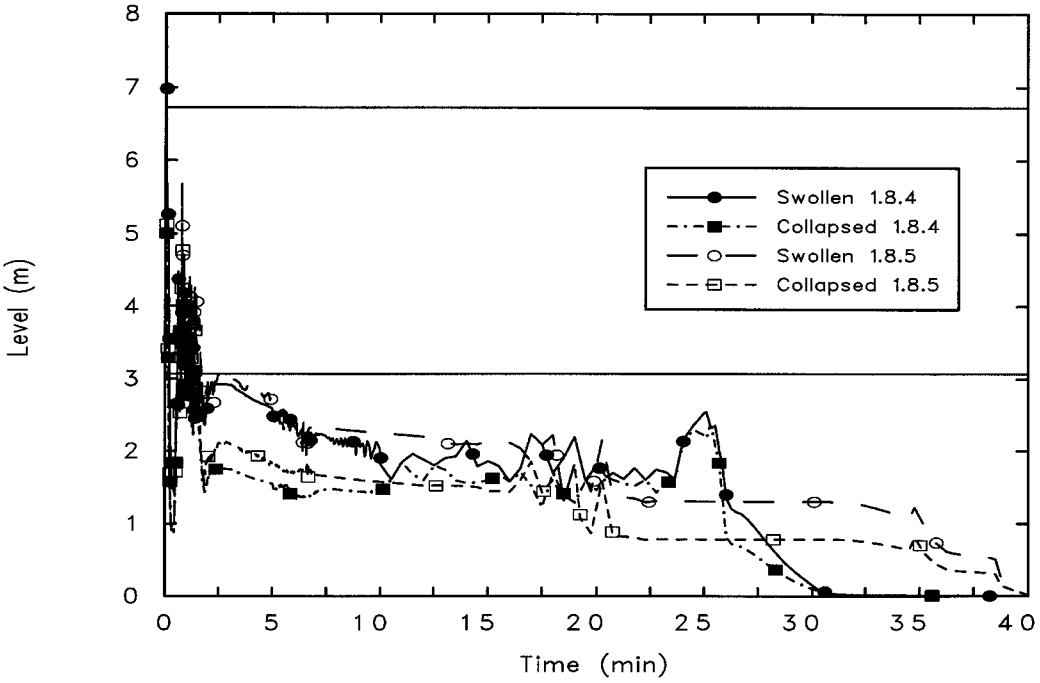

Figure 8-5. Surry LB LOCA: Reactor Water Level (short term)

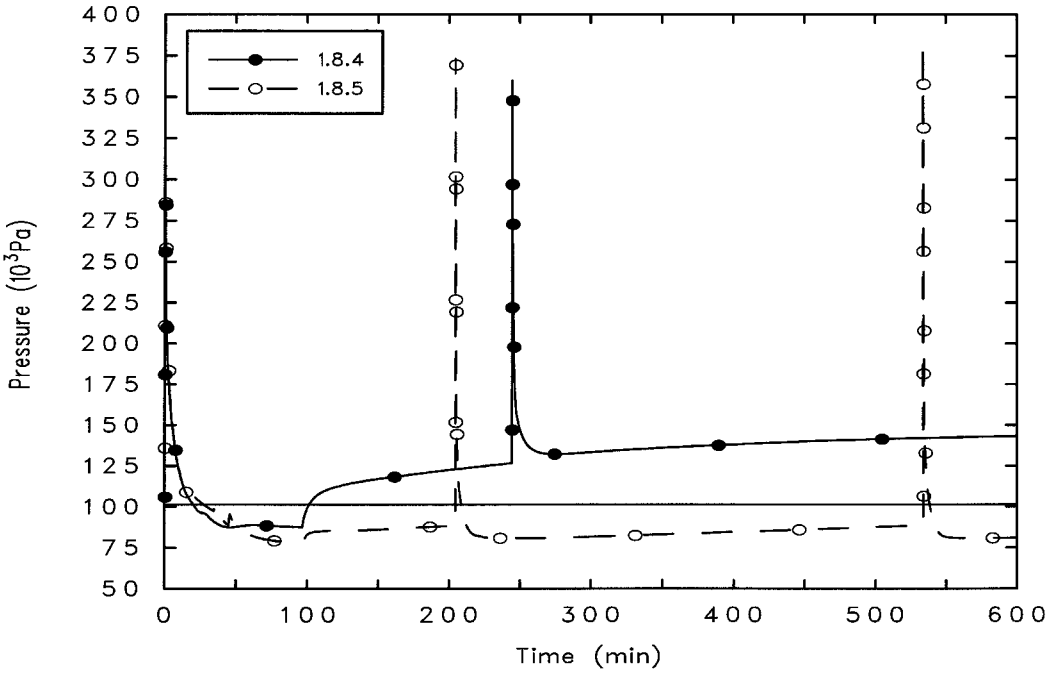

Figure 8-6. Surry LB LOCA: Containment Pressure

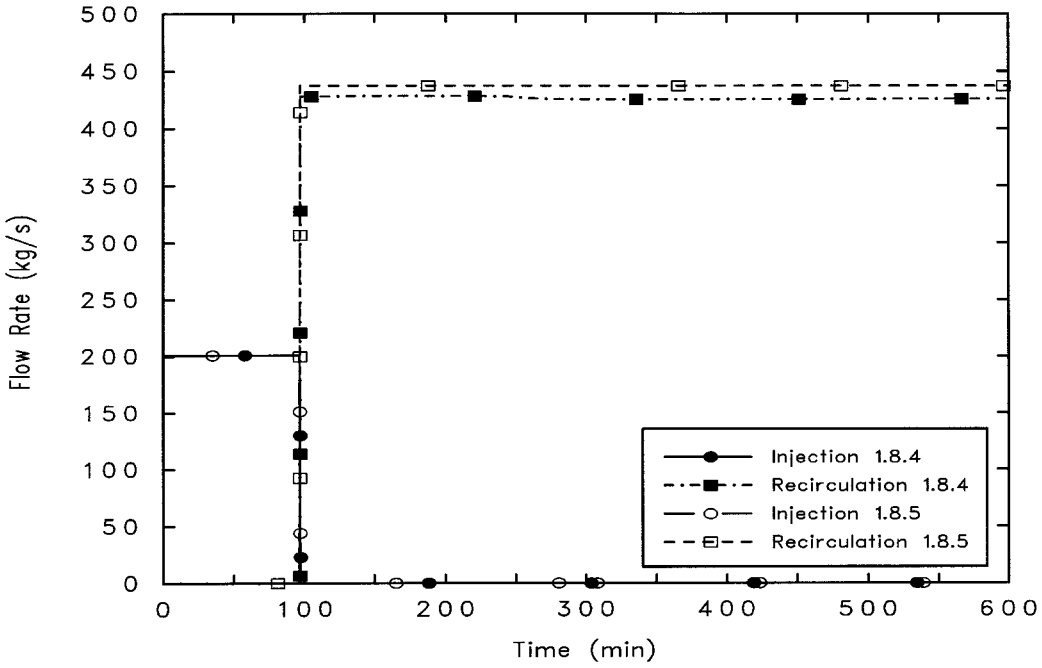

Figure 8-7. Surry LB LOCA: Containment Spray Flow

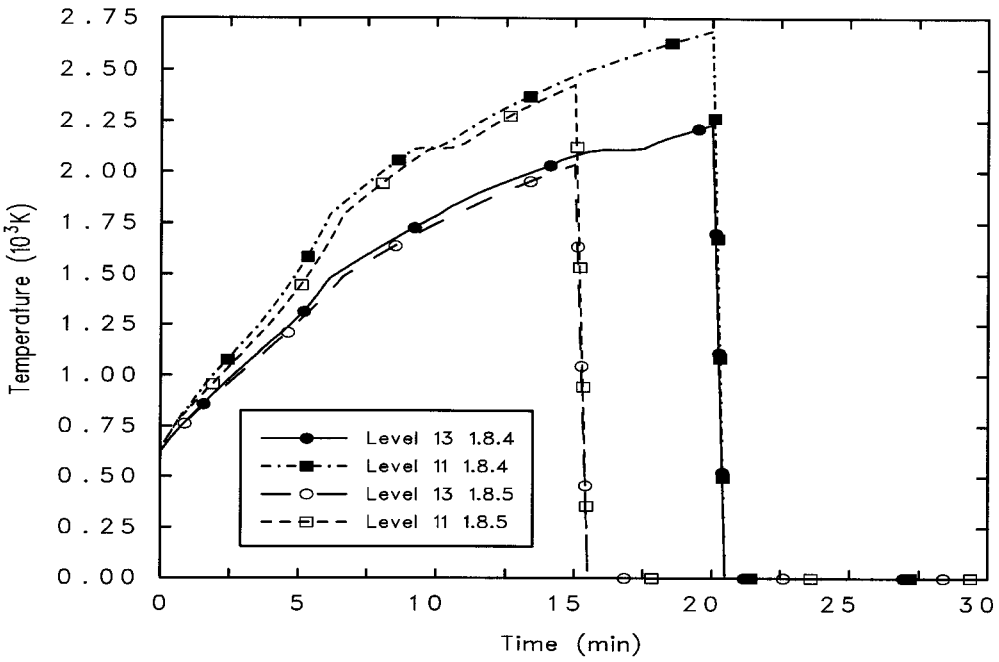

Figure 8-8. Surry LB LOCA: Ring 1 Fuel Temperature (top of core)

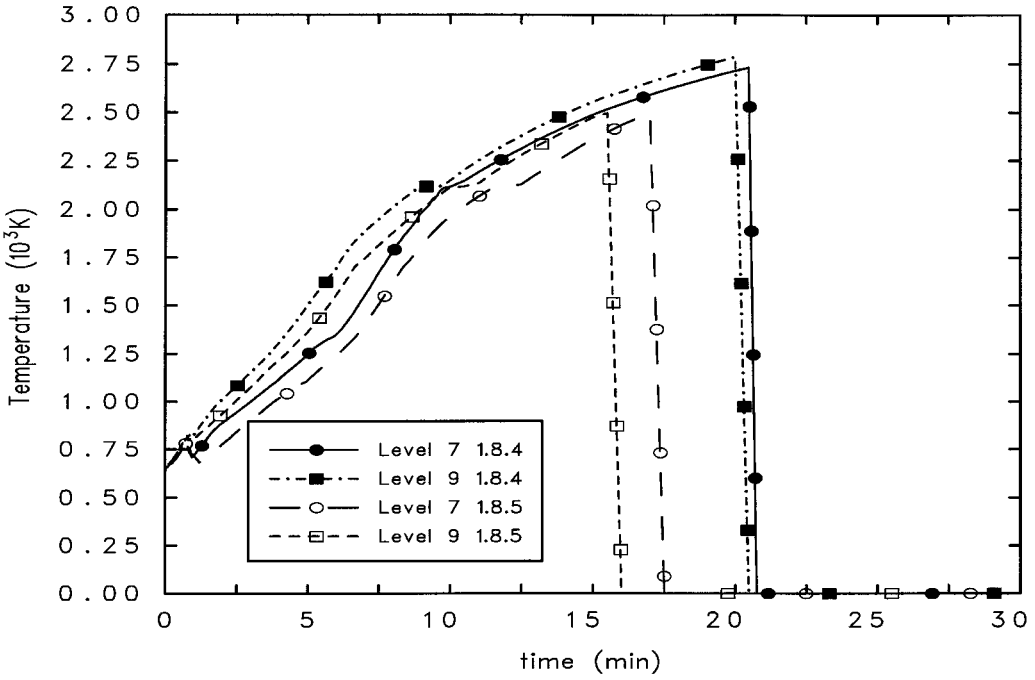

Figure 8-9. Surry LB LOCA: Ring 1 Fuel Temperature (mid-core)

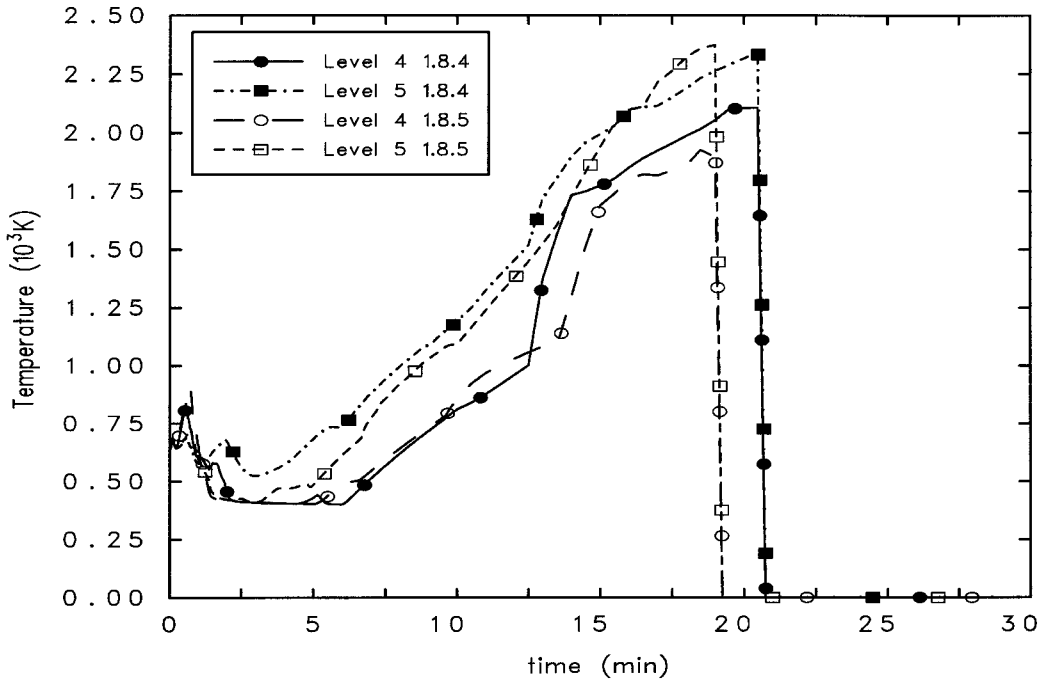

Figure 8-10. Surry LB LOCA: Ring 1 Fuel Temperature (bottom of core)

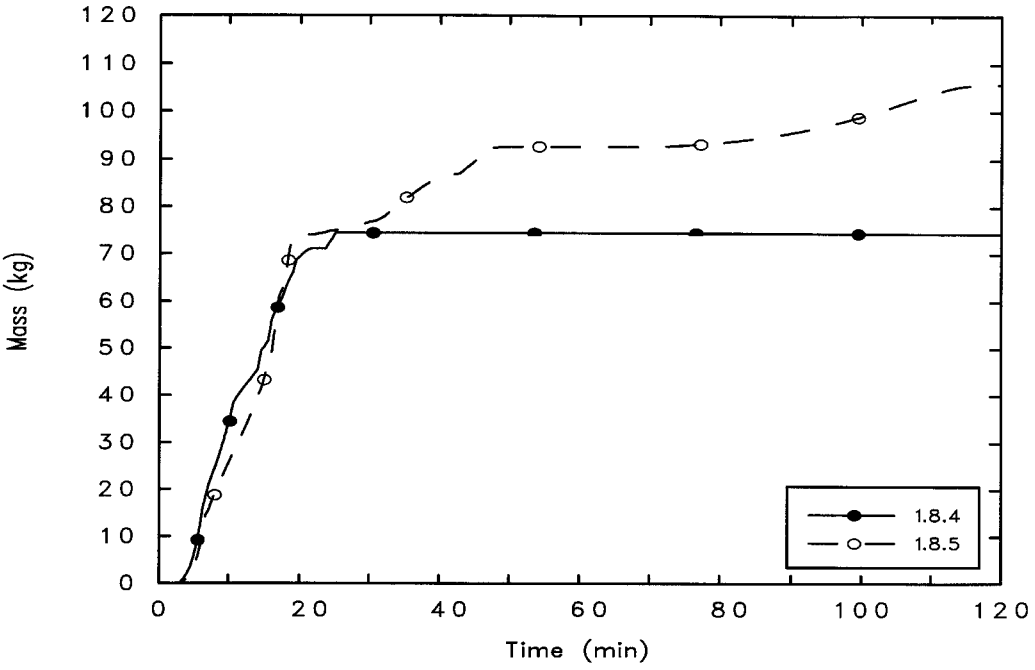

Figure 8-11. Surry LB LOCA: In-Vessel Hydrogen Production

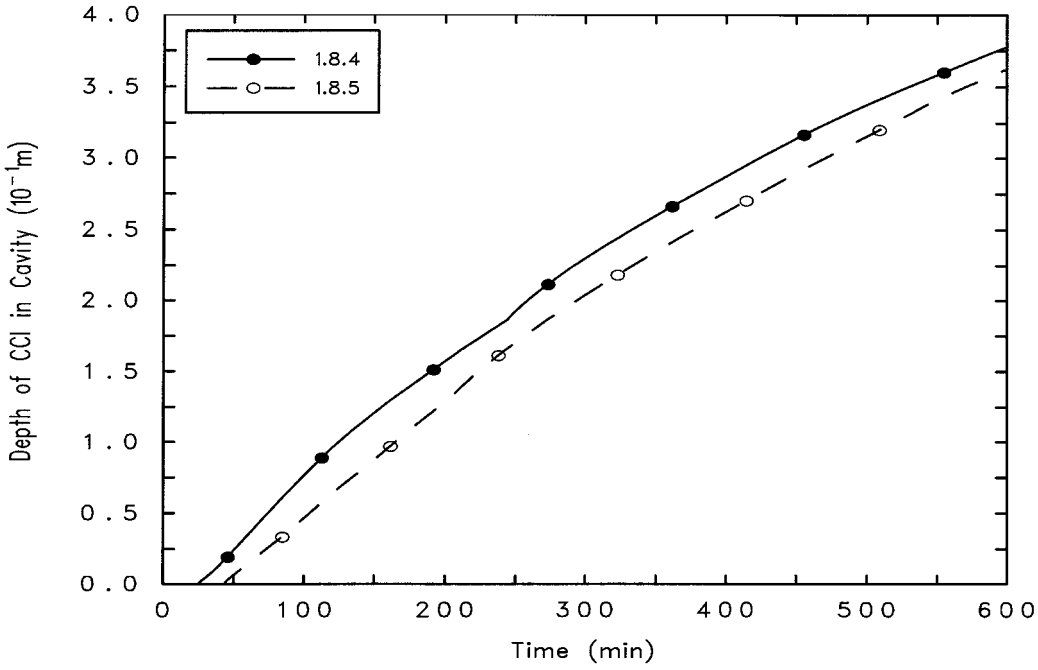

Figure 8-12. Surry LB LOCA: Depth of Core-Concrete Interaction in Cavity

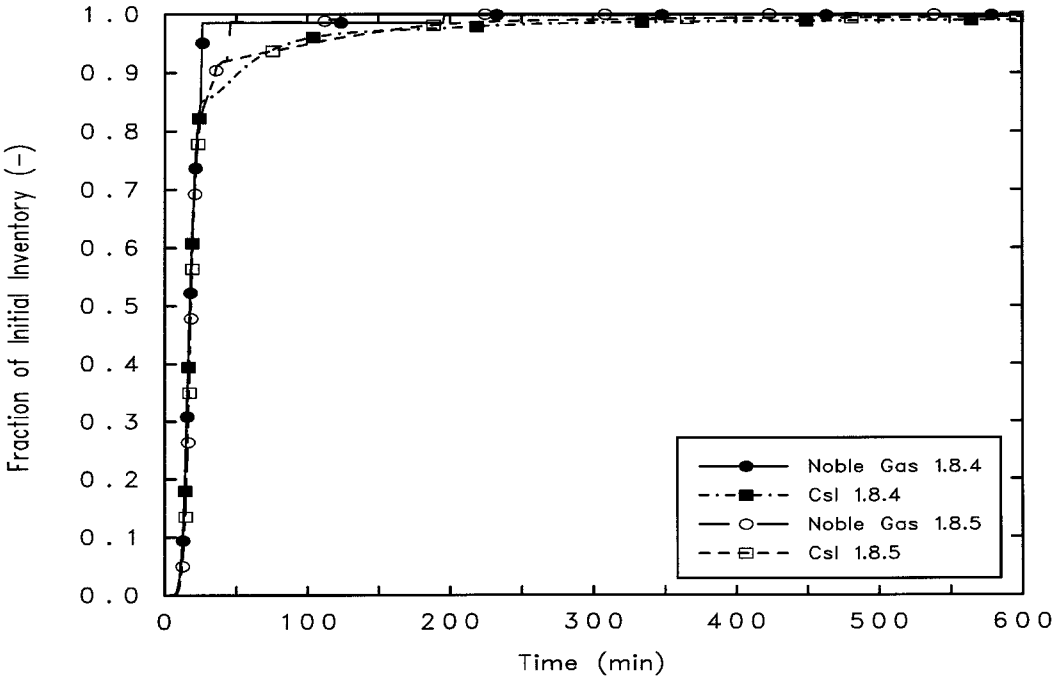

Figure 8-13. Surry LB LOCA: Noble Gas and CsI Release from Fuel

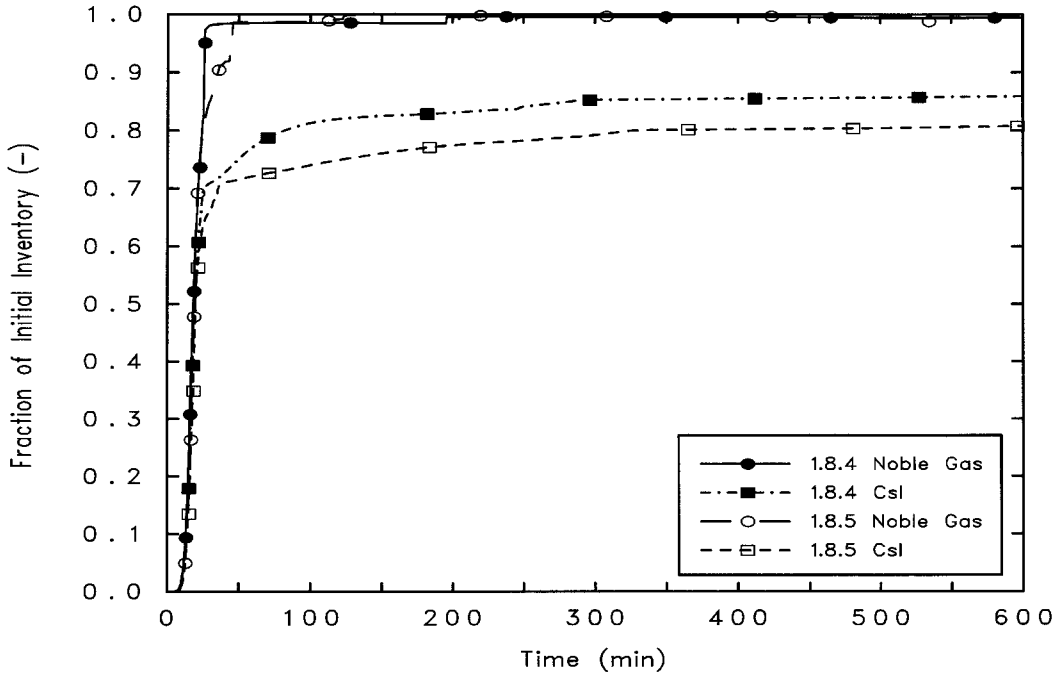

Figure 8-14. Surry LB LOCA: Noble Gas and CsI Release to Containment

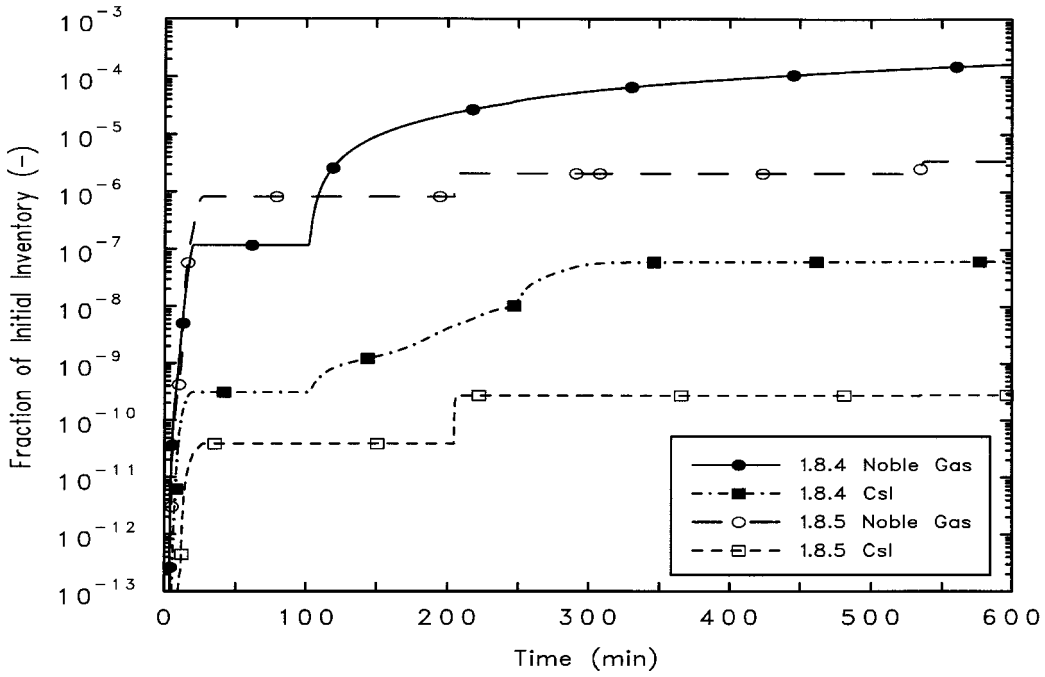

Figure 8-15. Surry LB LOCA: Noble Gas and CsI Environmental Release

8.5 Discussion

Discussion of the MELCOR 1.8.5 results is presented below. In general, qualitative results compared well with 1.8.4 results. Therefore, mention of comparison to 1.8.4 calculated results is only made when significant differences are seen.

Immediately following the rupture of the cold leg piping, the primary system rapidly depressurize, as shown in Figure 8-4. Discharge of the coolant through the break quickly uncover the fuel (Figure 8-5) and increased containment pressure (Figure 8-6) above the 25 psia (170 kPa) containment spray initiation setpoint. (Discussion of the differences in the containment pressure response at the time of switching from spray injection mode to spray recirculation mode is given later in this section.) Addition of core coolant from the accumulators recovered the bottom portion of the core (to approximately 4.8 m) at around 20 seconds. However, the coolant addition was insufficient to make up the entire level since one of the three accumulators dumped directly out the break, and the break was large enough that rapid coolant depletion was seen immediately following the accumulator dump.

After a 30-second delay, one train of containment sprays operated in injection mode (Figure 8-7), drawing coolant from the RWST. By this time, the primary system had already depressurized to within a few kPa of the containment. Operation of containment sprays and fan coolers quickly began to reduce containment pressure, after having reached a peak of approximately 305 kPa.

At approximately 4 minutes, fuel heatup was sufficient to induce gap release from the fuel. (See Figure 8-8 through Figure 8-10.) Fuel temperatures continued to increase until massive fuel relocation began. The MELCOR 1.8.5 estimated time of fuel relocation from the upper core region (approximately 15 minutes) led that calculated by 1.8.4 (approximately 20 minutes) by 5 minutes. This was due solely to modification of the default value for fuel collapse based on clad failure temperature (SC1132(1)–from 2800 K to 2500 K). In spite of the earlier inception of core relocation, the MELCOR 1.8.5 calculation predicted cooling of the core debris as it relocated downward. This slowed the progression of full-scale core relocation. Figure 8-10 shows that relocation in axial Levels 4 and 5 for the MELCOR 1.8.5 calculation only led the 1.8.4 prediction by 90 seconds.

The core plate reached its failure temperature almost immediately after relocation of hot debris to the plate. Relocation of the debris into the lower plenum followed at around 25 minutes. The MELCOR 1.8.5 calculation initially quenched the debris, resulting in an approximately 15-minute delay in progression of the accident until the debris reheated and began to boil the remainder of the coolant from the lower head. This behavior is fundamentally different from that calculated by MELCOR 1.8.4, and it is due to activation of the falling debris quench model (that enhanced heat transfer between core debris and liquid coolant) as the MELCOR 1.8.5 default. MELCOR 1.8.4, on the other hand, predicted that the remainder of the coolant is boiled away over a 5-minute period with no debris quench (Figure 8-5). Once all liquid coolant was gone, the vessel lower head failed and oxidation of the fuel cladding ceased, stopping in-vessel hydrogen production at 74 kg (Figure 8-11). However, MELCOR 1.8.5 continued to oxidize cladding due to a delay in lower head failure (39 minutes) and debris ejection to the cavity (43 minutes). Oxidation continued through 100 minutes, as the steam environment in the vessel oxidized any remaining clad and steel structures. Hydrogen production in the 1.8.5 calculation ceased at approximately 105 kg.

As shown in Figure 8-12, core-concrete interaction began immediately following relocation of the debris to the cavity and continued through the time the MELCOR calculation is terminated at 600 minutes. Essentially identical ablation rates were predicted by MELCOR 1.8.4 and 1.8.5.

As shown in Figure 8-6, MELCOR 1.8.4 predicted an increase in containment pressure above atmospheric shortly following switchover of containment sprays from injection to recirculation mode at 97 minutes. Not only did the pressure increase above atmospheric, allowing fission product leakage to the environment, but the pressure continued to increase as the fan coolers and sprays could not adequately cool the containment. A deficiency was discovered in the input prescription for the recirculation mode of the containment sprays in the MELCOR 1.8.4 analysis. The problem in the MELCOR 1.8.4 input description was found to be due to the sprays being described as a fog source (i.e., prescribed hydrodynamic source of water drops to the atmosphere). The spray models contained in the Containment Sprays (SPR) package were not used and as a result, heat transfer between the water drops and the atmosphere were not treated properly in the MELCOR 1.8.4 analysis. This deficiency was corrected for the 1.8.5 calculation by making use of

SPR package spray models to describe the spray actuation. As a result, more effective spray cooling was achieved in the MELCOR 1.8.5 analysis, and the pressure was maintained well below atmospheric. The containment peak pressure occurs during a short series of hydrogen deflagrations in each calculation. The peak containment pressure predicted by MELCOR 1.8.4 was 360 kPa at approximately 244 minutes, which is below the expected containment failure pressure. MELCOR 1.8.5 predicted a peak containment pressure of 376 kPa. This pressure was reached twice, once during a series of hydrogen deflagrations at 204 minutes, and once during a series of deflagrations at 534 minutes. Again, this peak pressure was well below the containment failure pressure. (Design pressure is approximately 517 kPa.)

Finally, Figure 8-13 through Figure 8-15 show radioactive releases for the MELCOR noble gas and CsI groups. Figure 8-13 shows release from fuel. Figure 8-14 shows release to containment, and Figure 8-15 shows the environmental release. Nearly 90% of the volatile fission products were released from fuel during the initial fuel heatup, and 99% were released in the long term. The only mechanism for these fission products to escape to the environment was through containment leakage; the rest were retained in the containment and primary system. Table 8-4 shows the fractional distribution of fission products at the time the MELCOR calculation was terminated. Note that the MELCOR 1.8.5 calculation predicted a significantly lower environmental release (factor of 100) because the containment pressure was maintained below atmospheric after the switchover of containment sprays to recirculation mode. The only environmental releases after switchover were small bursts that occurred during the two series of hydrogen deflagrations.

Table 8-4. Radionuclide Fractional Distribution at End of Problem

RN Class	Core (In-vessel)	Core Debris	Primary System	Containment	Environment
1 (Xe)	7.01E-05	0.00E+00	1.22E-03	9.99E-01	3.45E-06
2 (Cs)	7.64E-05	2.13E-09	1.97E-01	8.03E-01	1.79E-10
3 (Ba)	5.33E-04	8.15E-01	3.35E-02	1.51E-01	1.35E-11
4 (I)	6.62E-01	0.00E+00	6.02E-03	3.32E-01	2.85E-07
5 (Te)	5.58E-04	5.96E-01	2.66E-02	3.77E-01	3.61E-10
6 (Ru)	6.41E-04	9.93E-01	1.29E-03	5.53E-03	1.59E-13
7 (Mo)	5.98E-04	9.19E-01	1.54E-02	6.50E-02	2.13E-12
8 (Ce)	6.45E-04	9.99E-01	2.86E-05	5.50E-04	2.58E-13
9 (La)	6.45E-04	9.99E-01	8.99E-05	4.93E-04	4.53E-14
10 (U)	7.77E-04	9.99E-01	8.93E-05	4.76E-04	3.30E-14
11 (Cd)	3.00E-04	4.98E-01	9.72E-02	4.04E-01	2.90E-11
12 (Sn)	3.01E-04	4.96E-01	9.94E-02	4.04E-01	2.60E-11
16 (CsI)	3.01E-11	4.94E-03	1.84E-01	8.11E-01	2.81E-10

8.6 References

1. Pilch, M.M., et al., “Evaluation of Radiological Consequences of Design Basis Accidents At Operating Reactors Using The Revised Source Term,” Letter Report for Office of Nuclear Regulatory Research, U.S. Nuclear Regulatory Commission, Sandia National Laboratories, September 1998.

2. Soffer, L., et al., *Accident Source Terms for Light-Water Nuclear Power Plants*, NUREG-1465, U.S. Nuclear Regulatory Commission, February 1995.

3. Kmetyk, L. and L. Smith, *Summary of MELCOR 1.8.2 Calculations for Three LOCA Sequences (AG, S2D, and S3D) at the Surry Plant*,”NUREG/CR-6107, SAND93-2042, Sandia National Laboratories, March 1994.

9. Simulation of a LB LOCA at the Zion Nuclear Power Station (With ECCS Activation)

9.1 Background

The Zion Nuclear Power Plants (units 1 and 2) are Westinghouse 4-loop pressurized PWRs each with a large-dry reinforced concrete/steel containment. A MELCOR model has been developed based on the Zion plants with the intent that it be representative of U.S. commercial four-loop PWRs with large-dry containments. The MELCOR model has been used for many purposes, among them, support to the NRC's efforts to evaluate radiological consequences of design basis accidents using the revised source term [1,2]. The revised source term analysis for Zion was supported by MELCOR simulation of a LB LOCA, specifically a double-ended guillotine rupture of the pump suction piping. This analysis is presented in the following section. In this scenario, the LOCA event is followed by an initial failure of the LPSI system because of equipment failure. However, unlike the previous LOCA analysis of the Surry reactor, shortly after reactor water levels fall below the bottom of active fuel, the LPSI capability is assumed to be restored (approximately 27 minutes after the initial LOCA event). In this analysis, limited core damage is predicted during the time when the core is uncovered; however, this damage progression is arrested by core reflooding.

9.2 Nodalization

The Zion plant model was based on a model obtained from Brookhaven National Laboratory. This model was subsequently modified by Sandia [1] to assess the impact of applying the NUREG-1465 rebaselining source term to the calculation of population dose for recovered LOCAs. The resulting Zion plant model for the LB LOCA in the pump suction piping is the model used in the analysis presented herein. MELCOR node diagrams for the four-loop primary system and large-dry containment are shown in Figure 9-1 and Figure 9-2, respectively. As with the previously discussed Surry LOCA, this plant description makes use of a simplified core/vessel/RCS nodalization. More detailed CVH nodalizations are generally recommended for MELCOR versions beyond 1.8.5, especially for high-pressure sequences; however, the simplified version is retained in this analysis in order to facilitate comparisons to MELCOR 1.8.4.

9.3 MELCOR Input Specifications

The MELGEN input files for this calculation are "zionlbx.gen" and "cor.gen." The "zionlbx.gen" file is the primary MELGEN file. The "cor.gen" file is automatically read in during MELGEN processing because it is identified by the "r*i*f" command in the "zionlbx.gen" input file. The "cor.gen" file is a complete replacement for the COR package input that was developed during the source term (NUREG 1465) rebaselining study. The

modifications to the COR package input were performed to allow future users to take advantage of the MELCOR SS and NS features now available in MELCOR 1.8.5.

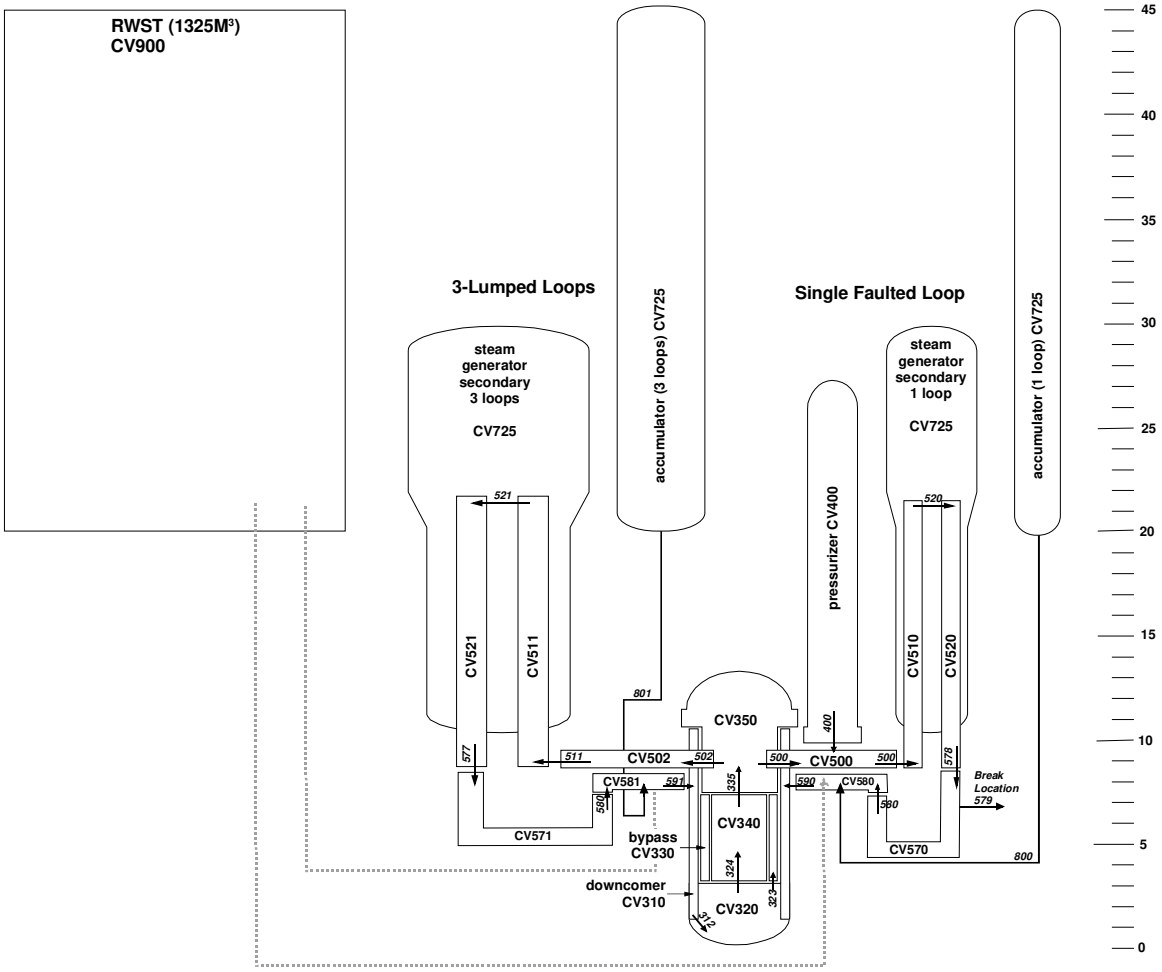

Figure 9-1. MELCOR Node Diagram for Zion Primary System (elevation in meters)

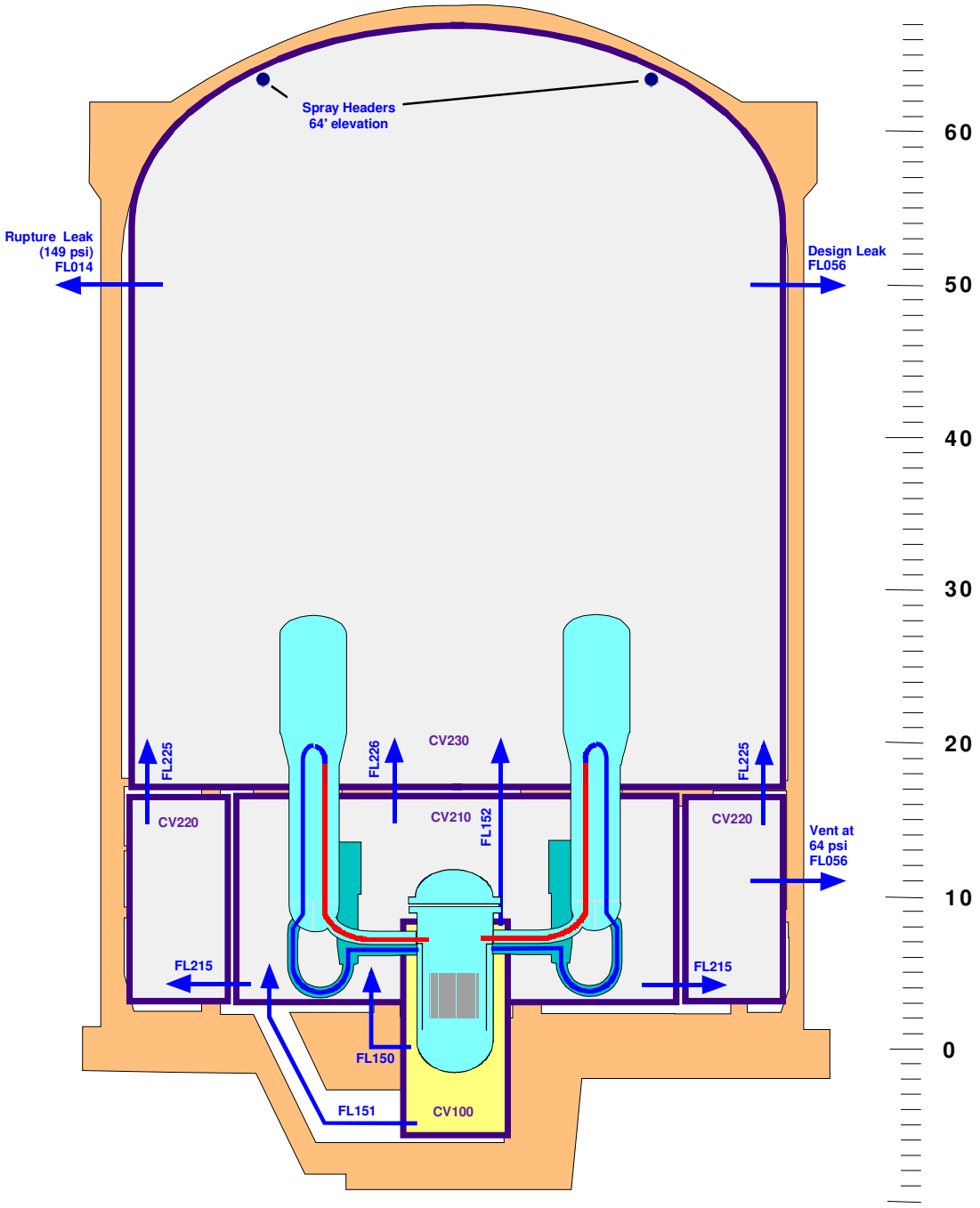

Figure 9-2. MELCOR Node Diagram for Zion Containment (elevation in meters)

The MELCOR input file for this calculation is “zionlbx.cor.” In general, the Zion model was developed using standard, default MELCOR modeling parameters. Key modeling input parameters are listed in Table 9-1. Other boundary conditions for the LB LOCA transient are listed in Table 9-2.

Table 9-1. Key Modeling Parameters for Zion LB LOCA

Parameter	Record	Description	Default Value	Zion Value
IUEMOD	COR00006	Eutectics model.	0 (Inactive)	0
IHSDT	COR00006	HS boundary condition option.	0 (BC option required)	0
IDTDZ	COR00006	DTdz inlet option switch.	0 (dtdz from CVH/FL hydrodynmics calculations)	0
MTUOZR	COR00007	Transport mech. Flag for UO_2 in molten zircaloy.	1 (UO_2 transported as a fraction of molten mass)	1
MTZXZR	COR00007	Transport mech. Flag for ZrO_2 in molten zircaloy.	1 (ZrO_2 transported as a fraction of the molten mass)	2 (ZrO_2 transported as a fractional proportion to existing fraction in matl)
MTSXSS	COR00007	Transport mech. Flag for steel oxide in molten steel.	2 (steel oxide transported as fractional proportion to its existing fraction in the steel)	2
HDBPN	COR00009	Lower head failure parameters: heat transfer coefficient from debris to penetration structures.	1000 W/m^2K	500 W/m^2K
HDBLH	COR00009	Lower head failure parameters: heat transfer coefficient from debris to lower head.	1000 W/m^2K	500 W/m^2K
TPFAIL	COR00009	Failure temperature of penetrations or lower head.	1273.15 K	1273.15 K
ICONV	RN2001	Convection option switch.	0 (flowpath convection of radionuclides calculated)	0
ICOND	RNACOND	Aerosol condensation index.	0 (Condensation on all existing aerosols)	0*
ICRLSE	RNFP000	Core release model indicator.	-2 (CORSOR-M model with surface to volume ratio option)	-2
IHYGRO	RN1002	Hygroscopic model.	0 (not active)	1
ICA02	RNCA100	Chemisorption model.	1 (active)	1

**Not included in input, default value is assumed by MELGEN.*

Table 9-2. Zion LB LOCA Boundary Conditions

Boundary Condition	Zion LB LOCA
Accumulators	Operate as designed (injection at 4.275 MPa RCS pressure).
HPI	Assumed to fail.
LPSI	Assumed to fail initially, but recovered by operator at 27 minutes.
RCS Pressure Boundary Status	Double-ended guillotine rupture of Loop A pump suction piping at time = 0.0 sec Total break area is 0.9738 m^2.
Primary Pressure Control	PORVs and SRVs irrelevant because of rapid depressurization following rupture of cold leg.
Steam Generator SRVs	Assumed to open when secondary pressure reaches 7.41 MPa. (hysteresis cycle).
Reactor Power	Scram at t = 0.0 sec.
Containment Sprays	Operate in injection mode when ctmt pressure exceeds 260 kPa. Switch to recirculation mode when RWST volume reaches 50 m^3.
Containment Fan Coolers	Operate as designed at time = 0.0 sec.
Containment Leakage	Assumed to be 0.1 vol % / day at containment design pressure from lower dome. Hole size is 2.3 mm equivalent.

9.4 Results of Analysis

The MELCOR 1.8.5 simulation of the Zion LB LOCA ran to completion and all results appeared to be reasonable. Calculated results are summarized in this section, and a discussion of these results is presented in the following section.

A double-ended guillotine rupture of the pressurizer loop at the reactor coolant pump (RCP) inlet initiated the LOCA sequence analyzed. This resulted in coolant discharge out of the equivalent of two 0.49 m^2 (5.24 ft^2) holes. Table 9-3 summarizes the LB LOCA accident sequence MELCOR-calculated timing of events. Note that event timing was essentially identical to that calculated by MELCOR 1.8.4. The only notable difference was the relocation of the top portion (1.5 m) of the core as the Zr clad temperature reached 2500 K. No core relocation occurred in the MELCOR 1.8.4 simulation. The reason for this difference is described in the discussion of results.

Table 9-3. MELCOR-Calculated Timing of Events for Zion LB LOCA

1.8.4 (min)	1.8.5 (min)	Event
0	0	Double-ended rupture occurs in pressurizer loop pump suction (Break area = 0.97 m^2, 10.5 ft^2).
0.08	0.08	Containment fan coolers initiated on signal of 152 KPa (22 psia) containment pressure.
0.10	0.10	Containment spray (injection) signal of 262 KPa (38 psia) containment pressure.
0.12	0.12	Swollen reactor water level reaches minimum (below active fuel).
0.13	0.13	Accumulator injection begins.
13.1	13.2	Gap release begins in core radial ring 1.
13.2	13.3	Gap release begins in core radial ring 2.
14.5	14.6	Gap release begins in core radial ring 3.
16.6	16.6	Gap release begins in core radial ring 4.
-	23.0	Upper-most portion (top 1.5 m) of core begins to relocate downward as Zr clad temperature reaches 2500 K.
27.0	27.1	Series of containment hydrogen deflagrations occur (duration 27 seconds).
27.0	27.0	LPSI recovered–injection begins from RWST.
32.2	30.7	In-vessel hydrogen production terminated (at 267kg, 588 bm).
38.8	31.1	Core (fuel) temperature in lower axial levels reaches steady state of approximately 400 K (250 F) due to ECCS flow.
51.1	48.2	LPSI injection terminated on low (<50 m^3) RWST level.
51.1	48.2	Containment sprays (injection mode) terminated on low (<50 m^3) RWST level.
51.1	48.2	LPSI recirculation initiated.
51.1	48.2	Containment sprays (recirculation mode) initiated.
360	360	MELCOR calculation terminated.

The figures below show results for the Zion LB LOCA MELCOR 1.8.5 simulation. Results are compared to MELCOR 1.8.4 simulation results. General trends show reasonable comparison between MELCOR 1.8.4 and MELCOR 1.8.5 calculated results. The observed differences result from MELCOR code enhancements between the 1.8.4 and 1.8.5 code releases. These differences are discussed in the following section.

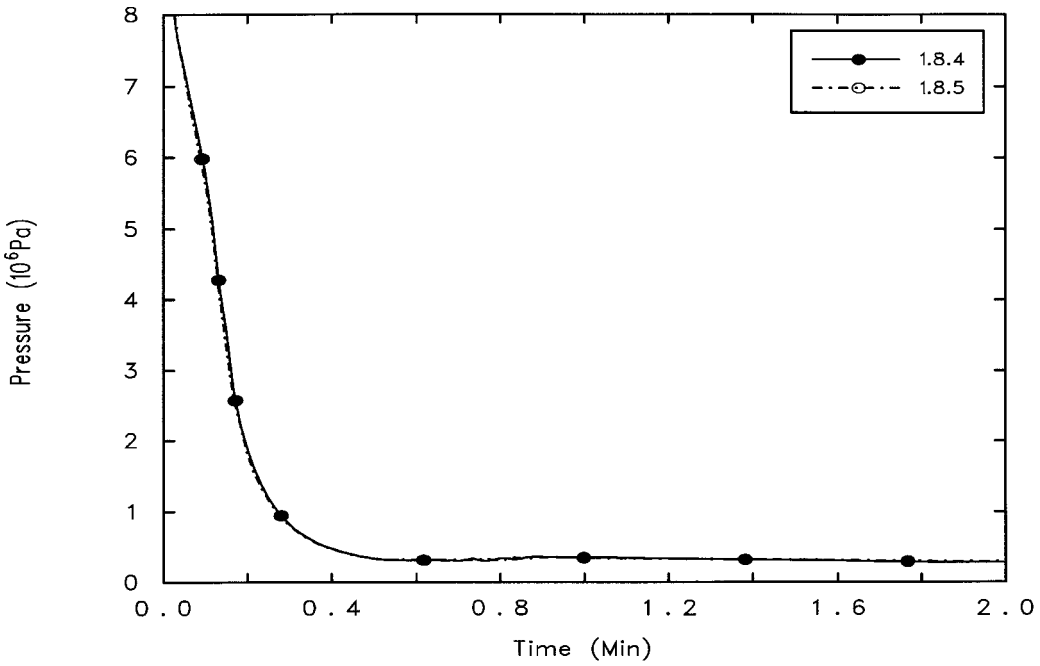

Figure 9-3. Zion LB LOCA: Primary System Pressure (short term)

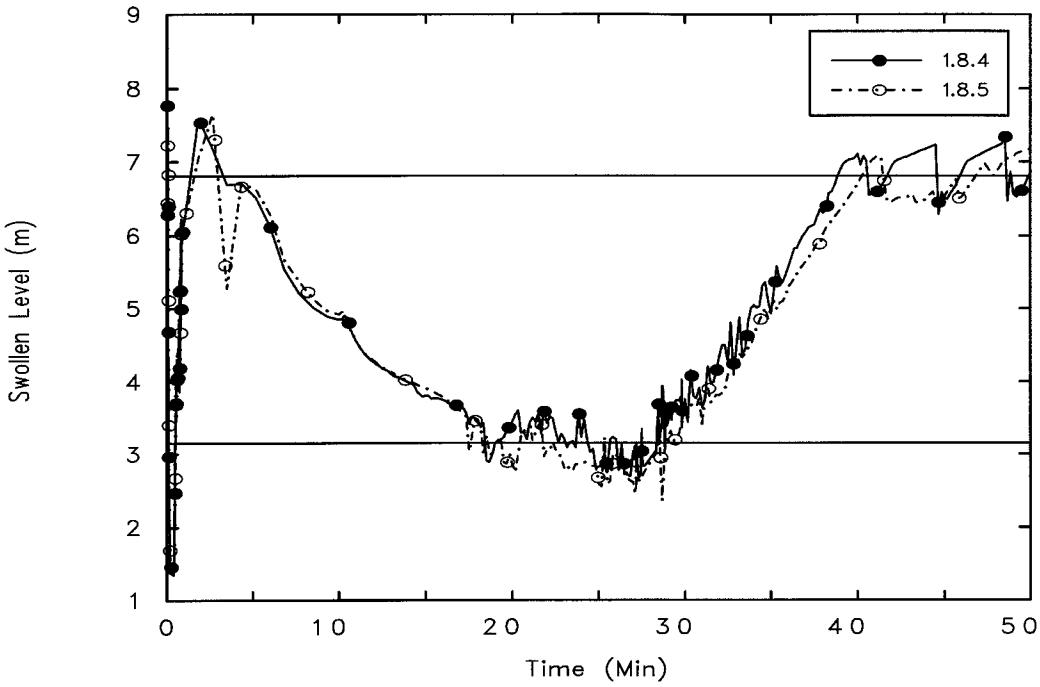

Figure 9-4. Zion LB LOCA: Reactor Water Level (short term)
Note: The horizontal lines on the figure above bound the active fuel region of the core.

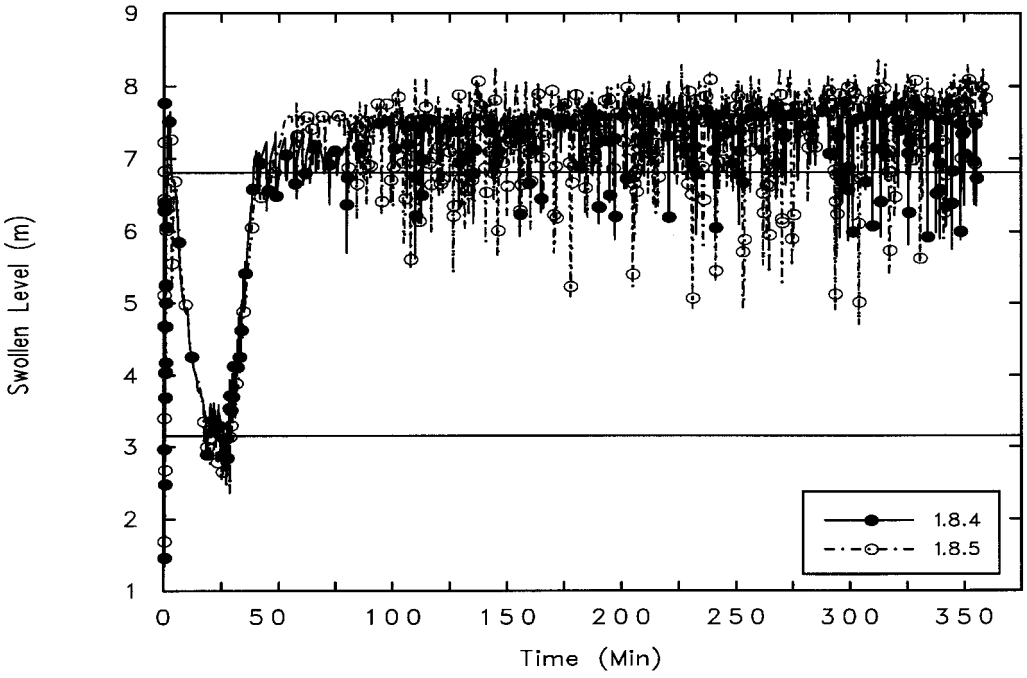

Figure 9-5. Zion LB LOCA: Reactor Water Level (long term)
Note: The horizontal lines on the figure above bound the active fuel region of the core.

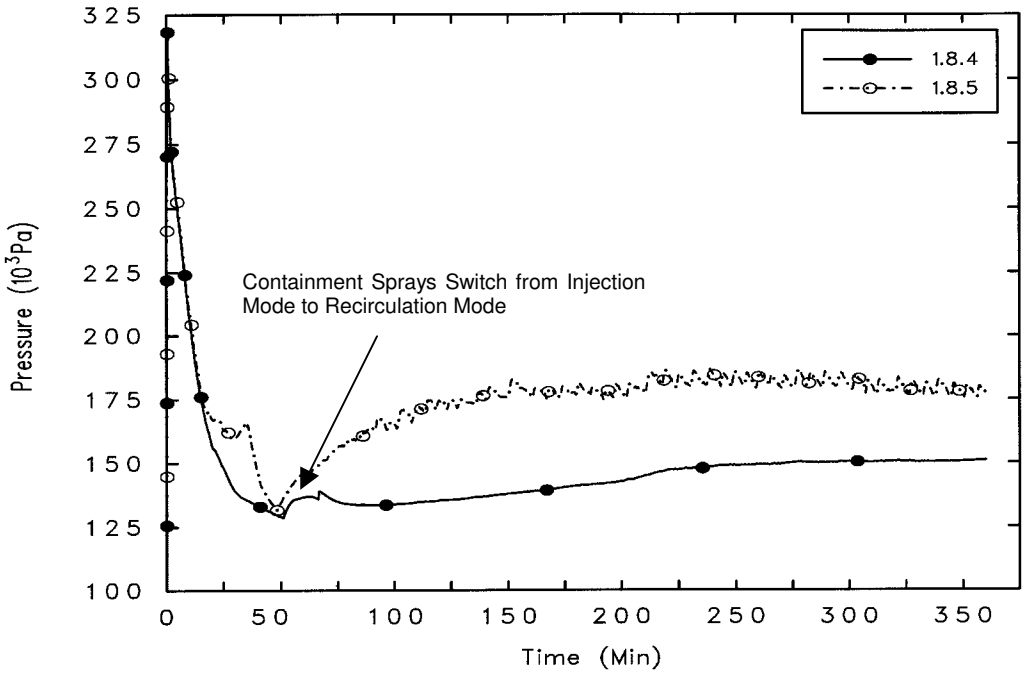

Figure 9-6. Zion LB LOCA: Containment Pressure

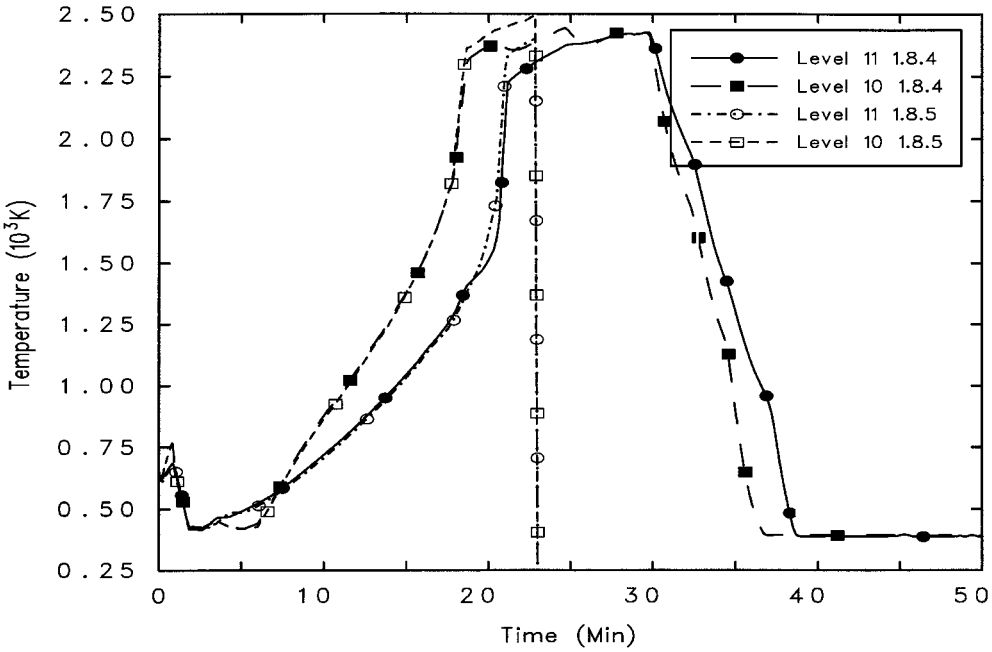

Figure 9-7. Zion LB LOCA: Ring 1 TAF Fuel Temperatures (short term)
Note: Vertical drop in 1.8.5 temperatures at approximately 23 minutes represent fuel relocation.

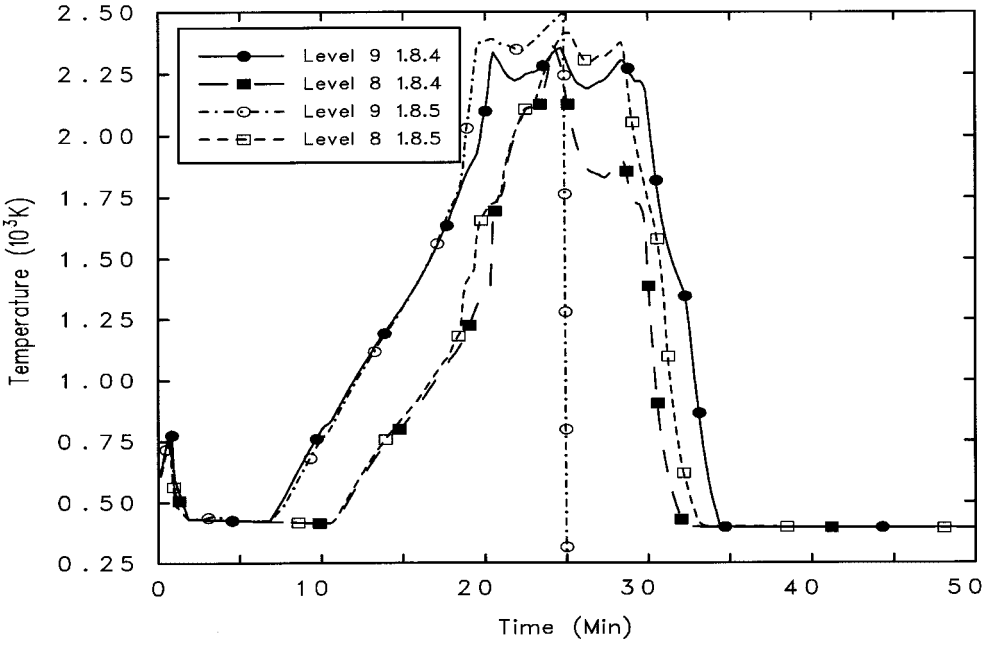

Figure 9-8. Zion LB LOCA: Ring 1 Upper Level Fuel Temperatures (short term)
Note: Vertical drop in 1.8.5 Level 9 temperature at approximately 23 minutes represent fuel relocation.

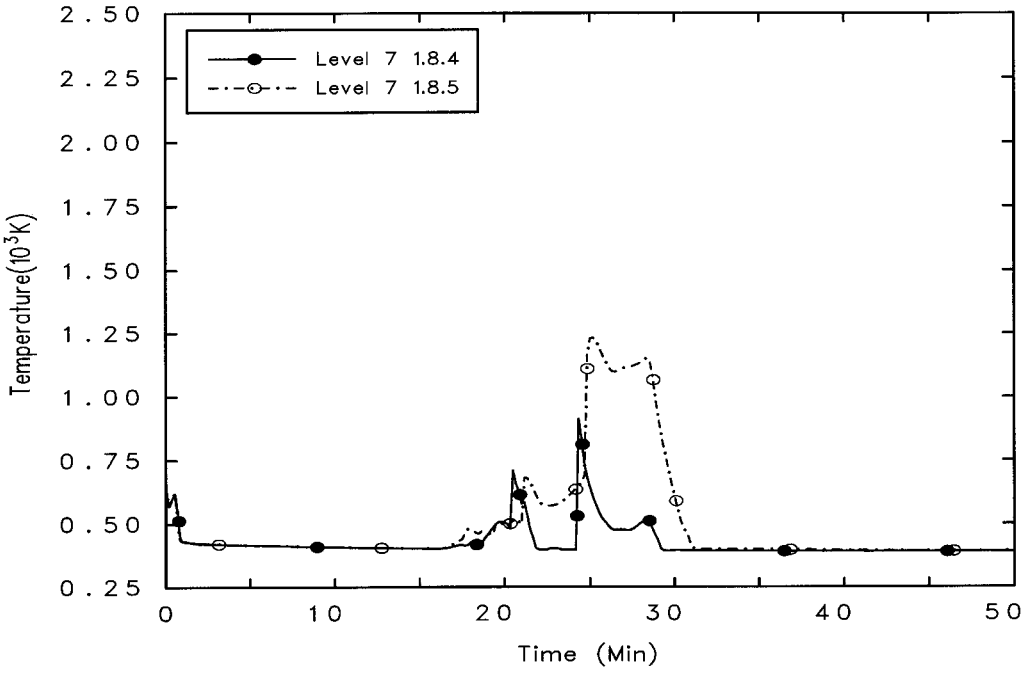

Figure 9-9. Zion LB LOCA: Ring 1 Mid-Level Fuel Temperatures (short term)
Note: Larger temperature increase in 1.8.5 prior to 25 minutes is result of debris relocation from above.

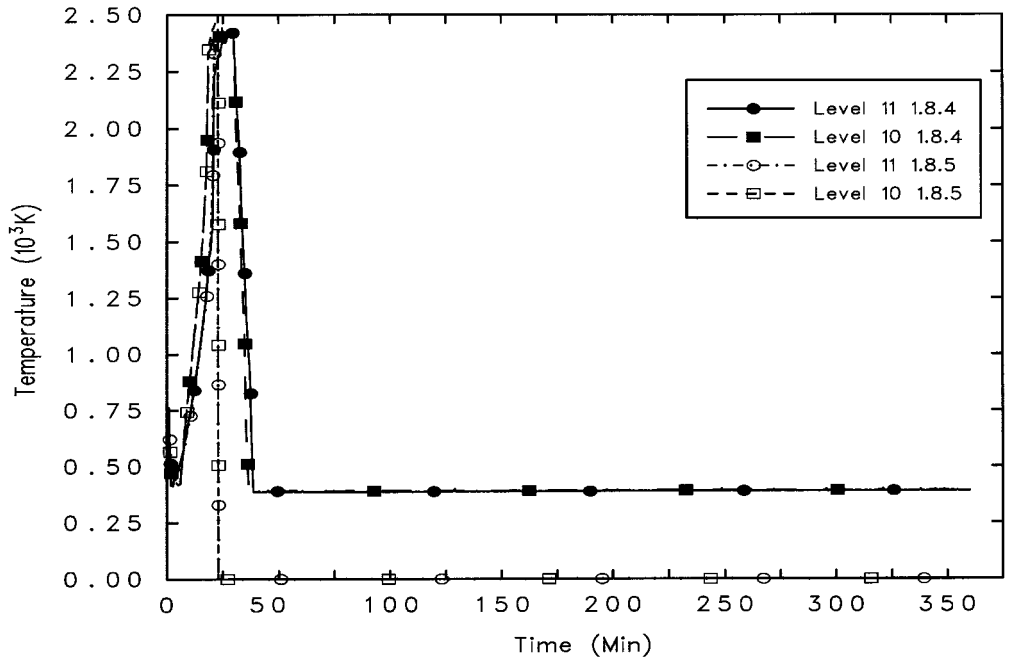

Figure 9-10. Zion LB LOCA: Ring 1 TAF Fuel Temperatures (long term)

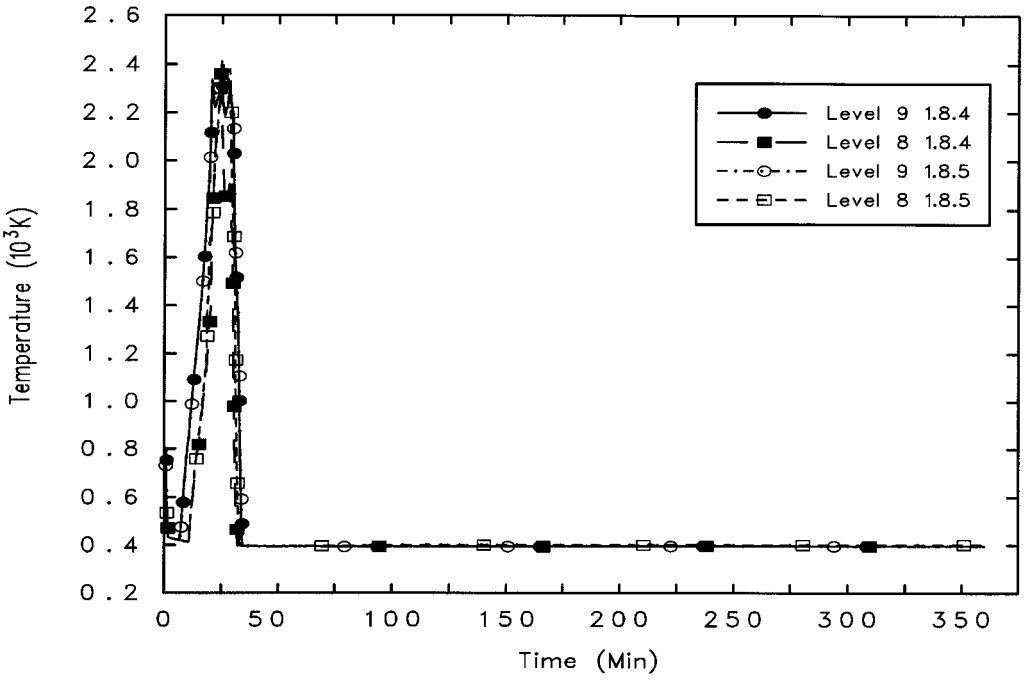

Figure 9-11. Zion LB LOCA: Ring 1 Upper Level Fuel Temperatures (long term)

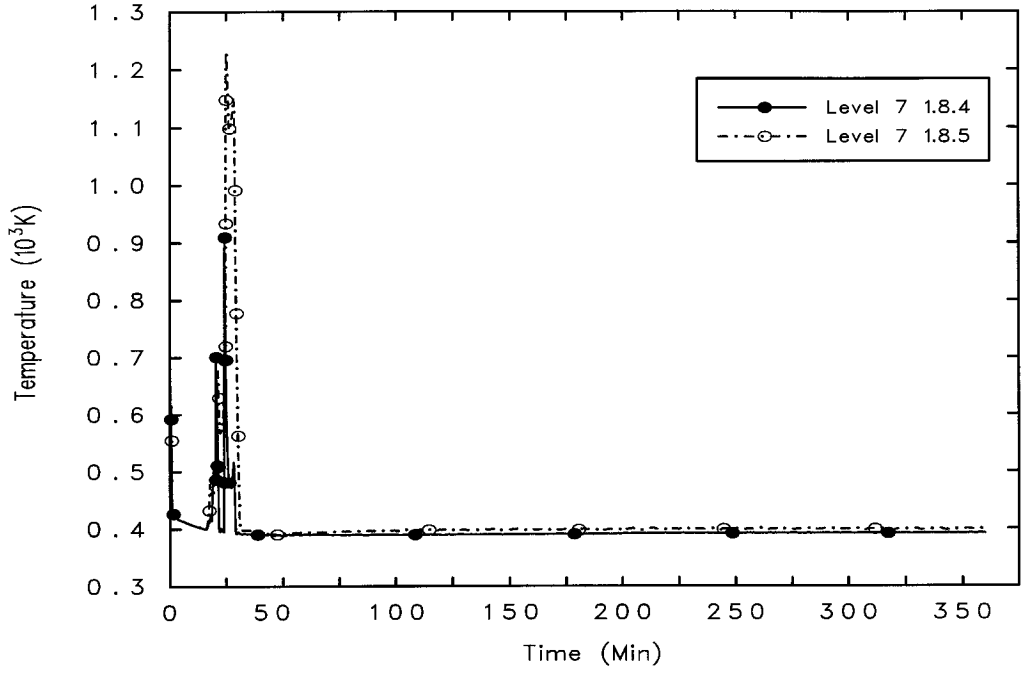

Figure 9-12. Zion LB LOCA: Ring 1 Mid-Level Fuel Temperatures (long term)

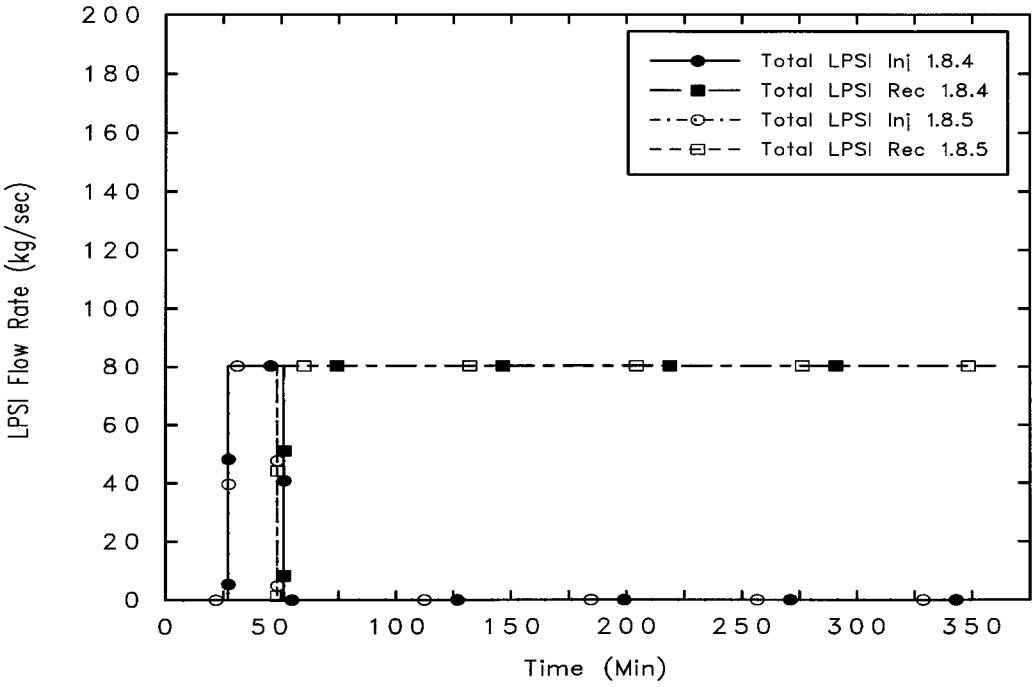

Figure 9-13. Zion LB LOCA: LPSI Flow

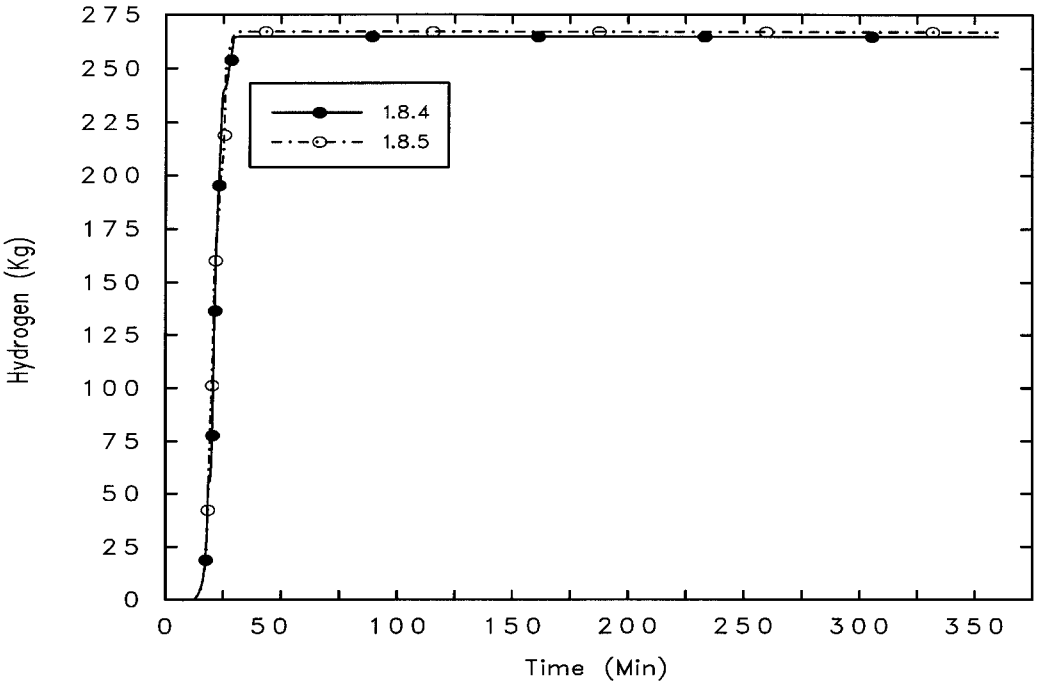

Figure 9-14. Zion LB LOCA: In-Vessel Hydrogen Production

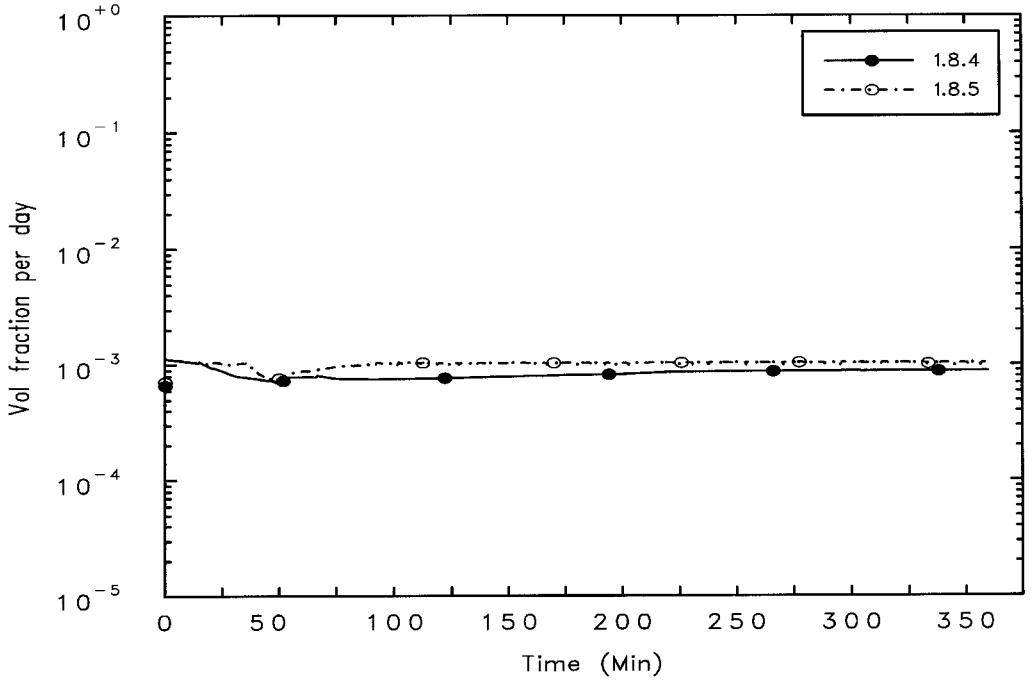

Figure 9-15. Zion LB LOCA: Containment Leak Rate

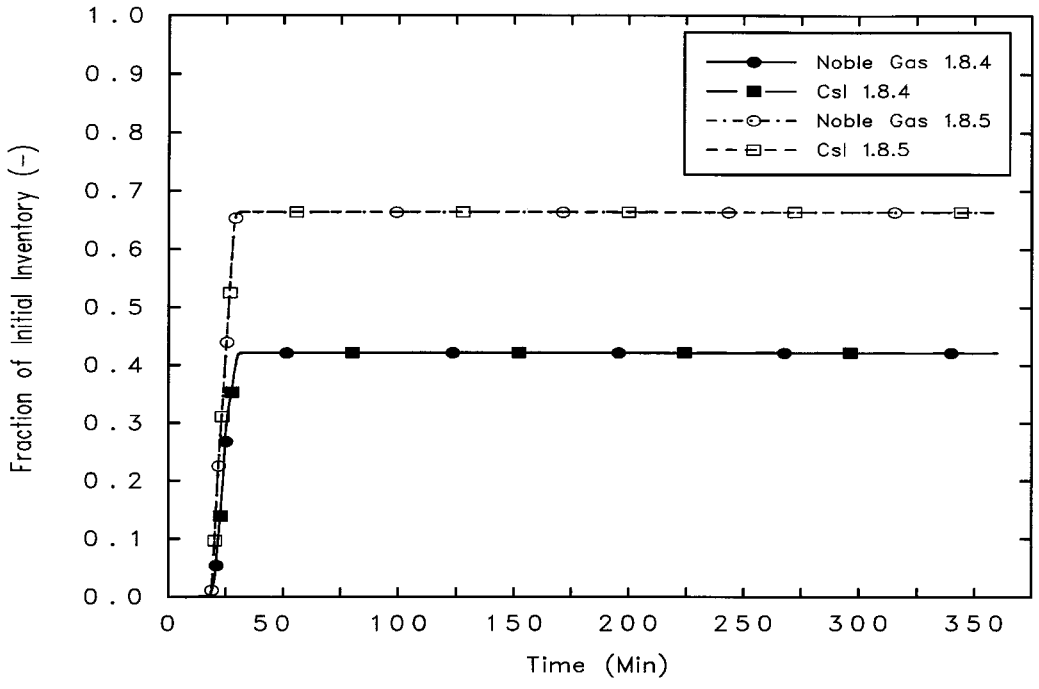

Figure 9-16. Zion LB LOCA: Noble Gas and CsI Release from Fuel

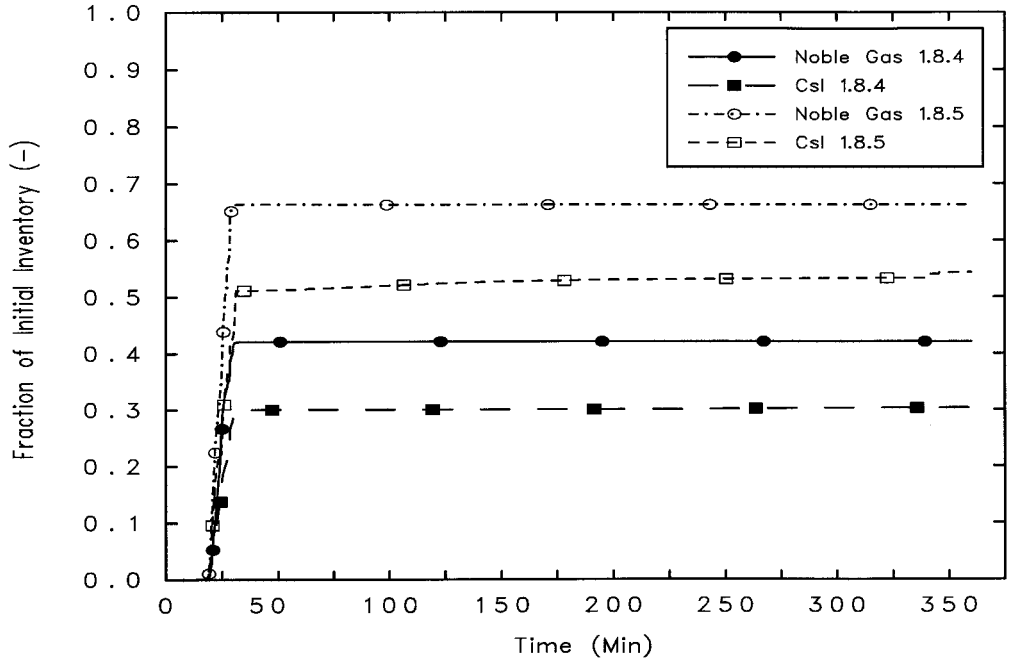

Figure 9-17. Zion LB LOCA: Noble Gas and CsI Release to Containment

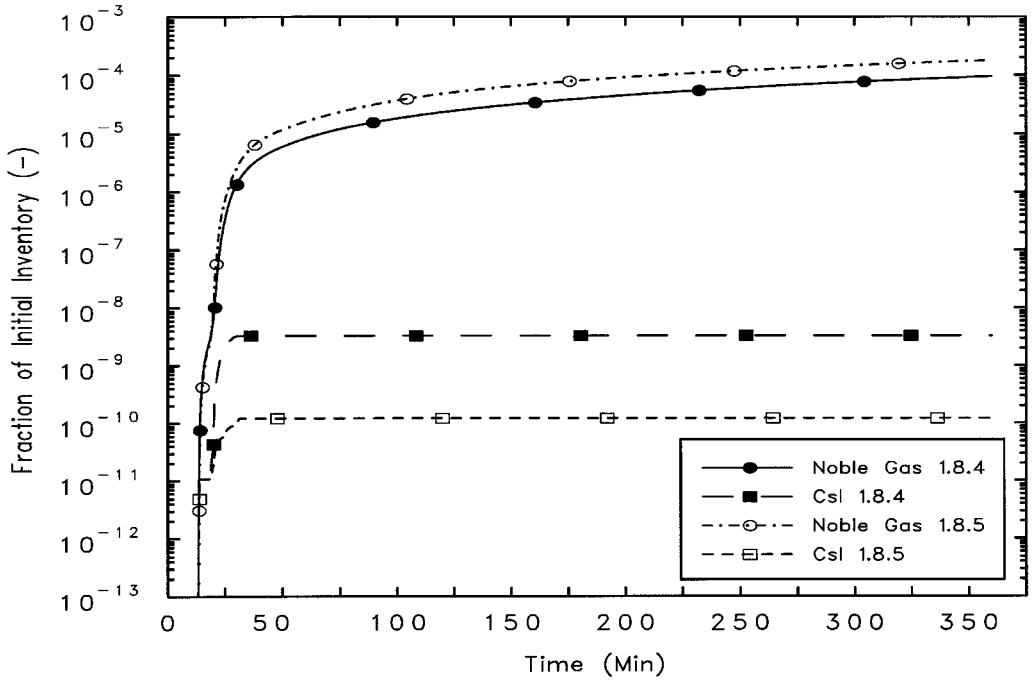

Figure 9-18. Zion LB LOCA: Noble Gas and CsI Environmental Release

9.5 Discussion

MELCOR 1.8.5 results are presented below. In general, results compared well with 1.8.4 results. Therefore, mention of comparison to 1.8.4 calculation results is only made when significant differences are seen.

Immediately following the rupture of the cold leg piping, the primary system rapidly depressurizes, as shown in Figure 9-3. Discharge of the coolant through the break quickly uncovers the fuel (Figure 9-4 and Figure 9-5) and increases containment pressure (Figure 9-6) above the 22 psia (152 kPa) fan cooler and 38 psia (262 kPa) containment spray initiation setpoints. Operation of containment sprays and fan coolers quickly begin to reduce containment pressure after having reached a peak of approximately 320 kPa. Following the rapid RCS depressurization, addition of core coolant from the accumulators restores water level to the top of active fuel (TAF) by 51 seconds. However, failure to initiate active ECCS allows the coolant to gradually boil away, and the coolant level drops below TAF at approximately 4 minutes and below the lower CSP at approximately 18.5 minutes. The drop in coolant level is accompanied by a sharp increase in fuel temperatures, as shown in Figure 9-7 through Figure 9-12. At approximately 13 minutes, fuel heatup is sufficient to induce gap release from the fuel. The temperature of the zirconium cladding in the uppermost 1.5 meters of the core reach 2500 K and the fuel relocates, as can be seen in Figure 9-7 and Figure 9-8 (axial fuel Levels 9 through 11). This fuel relocation was not predicted by MELCOR 1.8.4 for two reasons. First, as can be seen in Figure 9-7 and Figure 9-8, MELCOR 1.8.5 predicts slightly higher fuel temperatures (by a few degrees K) than MELCOR 1.8.4 in the 20- to 25-minute time period, which just happens to exceed the new default fuel failure criterion based on a clad temperature of 2500 K–SC1132(1). In MELCOR versions before 1.8.5, this failure temperature was 2800 K. However, based on experimental data that suggest a lower failure temperature for irradiated fuel, this default has been changed to 2500 K in version 1.8.5. A sensitivity calculation confirmed that this change in default was indeed the cause of this difference in the MELCOR 1.8.4 and 1.8.5 calculations. Figure 9-9 shows a slightly higher fuel temperature in Level 7 as hot fuel debris from upper levels relocates downward during the 25- to 30-minute time period.

As the default treatment, MELCOR 1.8.5 activates the falling debris quench model in the COR package. This model allows heat transfer to be properly calculated for core debris that is falling into/through a water pool. Given the core debris that is relocated when the clad in Levels 8 through 11 reaches 2500 K, the 1.8.5 calculation creates a significant amount of steam when the core debris is cooled as it relocates in the water-filled lower plenum. In contrast, in MELCOR 1.8.5, the falling debris heat transfer option was not active by default and in this calculation (1.8.4), quench-induced steam generation was not predicted. This difference in treatment results in differences in the containment pressurization behavior as shown in Figure 9-6.

The explanation for the difference in pressurization behavior is as follows: In the MELCOR 1.8.5 analysis, the steam generation produced from debris quenching in the lower plenum resulted in more energy being transported from the core materials to containment. The

energy transported by steam to the containment eventually resulted in greater enthalpy content of the atmosphere and higher condensate temperatures in the sumps. When the containment sprays were switched from injection model to recirculaton mode, the spray, although still removing heat from the containment atmosphere, was considerably less effective than in the MELCOR 1.8.4 calculation.

Recovery of LPSI at 27 minutes (Figure 9-13) results in the rapid decrease of fuel/debris temperatures. By approximately 31 minutes, the coolant has reduced fuel temperatures to approximately 400 K, where they remain for the remainder of the accident. Cooling of the fuel causes cladding oxidation to cease at 31 minutes, after generating 267 kg of hydrogen from the oxidation reaction (Figure 9-13).

Note that containment pressure gradually increases at 48 minutes when containment sprays are switched to recirculation mode. (See Figure 9-6.) Greater energy transfer from the fuel to the coolant/containment (as discussed above) renders the sprays less effective in the 1.8.5 calculation after switching to recirculation mode. However, the peak pressure during this time period is only 1.75 bar, and pressure is decreasing by 250 minutes as the containment fan coolers and sprays begin to remove more heat than is being generated in the primary system.

The containment leak rate during the transient (Figure 9-15), which was assumed to be equal to the design leak rate of 0.1 volume percent per day. As a result of this leakage, there is a small environmental source term due to core damage that occurred prior to ECCS recovery and reflooding of the core. Figure 9-16 through Figure 9-18 show radioactive releases for the MELCOR noble gas and CsI groups. Figure 9-16 shows release from fuel. Figure 9-17 shows release to containment, and Figure 9-18 shows the environmental release. Approximately 65% of the volatile fission products are released from fuel during the fuel heatup. This is higher than the 1.8.4 calculations, partially due to slightly higher fuel temperatures, but mostly due to the fragmentation and relocation of the core from Levels 8 and up that did not occur in the 1.8.4 calculation (see discussion above). It should be noted that the 1.8.5 calculation was modified to use the CORSOR-M fission product release model (with the surface-to-volume correction) instead of the original CORSOR correlation. This change in release model is not a change in MELCOR default, but rather a modification to user input. Data suggest that these two release models should predict similar behavior in the temperature range in question, so this is not postulated as a reason for the difference in fission product behavior between the 1.8.4 and 1.8.5 calculations. Table 9-4 shows the fractional distribution of fission products at the time the MELCOR calculation was terminated.

Table 9-4. Radionuclide Fractional Distribution at End of Problem

RN Class	Core (In-vessel)	Primary System	Containment	Environment
1 (Xe)	3.37E-01	5.34E-05	6.63E-01	1.80E-04
2 (Cs)	3.55E-01	1.17E-01	5.28E-01	1.18E-10
3 (Ba)	9.98E-01	4.72E-04	2.03E-03	4.08E-13
4 (I)	1.00E+00	6.15E-10	8.49E-06	2.11E-09

RN Class	Core (In-vessel)	Primary System	Containment	Environment
5 (Te)	3.74E-01	9.30E-02	5.33E-01	1.07E-10
6 (Ru)	1.00E+00	5.26E-08	2.67E-07	4.59E-17
7 (Mo)	9.80E-01	3.51E-03	1.69E-02	2.84E-12
8 (Ce)	1.00E+00	6.67E-09	3.54E-08	6.22E-18
9 (La)	1.00E+00	3.42E-06	1.70E-05	2.98E-15
10 (U)	1.00E+00	3.32E-06	1.64E-05	2.77E-15
11 (Cd)	9.80E-01	4.03E-03	1.65E-02	3.28E-12
12 (Sn)	9.80E-01	3.38E-03	1.72E-02	2.99E-12
16 (CsI)	5.26E-08	1.76E-01	8.24E-01	1.72E-10

Note: Classes 2 and 4 combine to form CsI (Class 16) when released from fuel

9.6 References

1. Pilch, M.M., et al., “Evaluation of Radiological Consequences of Design Basis Accidents At Operating Reactors Using The Revised Source Term,” Letter Report for Office of Nuclear Regulatory Research, U.S. Nuclear Regulatory Commission, Sandia National Laboratories, September 1998.

2. Soffer, L., et al., *Accident Source Terms for Light-Water Nuclear Power Plants*, NUREG-1465, U.S. Nuclear Regulatory Commission, February 1995.

10. Simulation of a Station Blackout at the Zion Nuclear Power Station

10.1 Background

The Zion Nuclear Power Plants (Units 1 and 2) are Westinghouse four-loop PWRs, each with a large-dry reinforced concrete steel containment. A MELCOR model has been developed based on the Zion plants, with the intent that it be representative of U.S. commercial four-loop PWRs with large-dry containments. The MELCOR model has been used for many purposes including support to the NRC's efforts to evaluate radiological consequences of design basis accidents using the revised source term [1,2]. The revised source term analysis for Zion was supported by MELCOR simulation of a LB LOCA, specifically a double-ended guillotine rupture of the pump suction piping. The model used for the revised source term study was modified to simulate a station blackout (TMLB) accident sequence. A summary of that simulation is presented herein.

10.2 Nodalization

The Zion plant model was based on a model obtained from Brookhaven National Laboratory. This model was subsequently modified by Sandia [1] to assess the impact of applying the NUREG-1465 rebaselining source term to the calculation of population dose for recovered LOCAs. This model was then modified to remove logic that controls operation of Engineered Safety Features and the flow paths representing the LOCA break. The resulting Zion plant model for the TMLB is the model used in the analysis presented herein. MELCOR node diagrams for the four-loop primary system and large-dry containment are shown in Figure 10-1 and Figure 10-2, respectively.

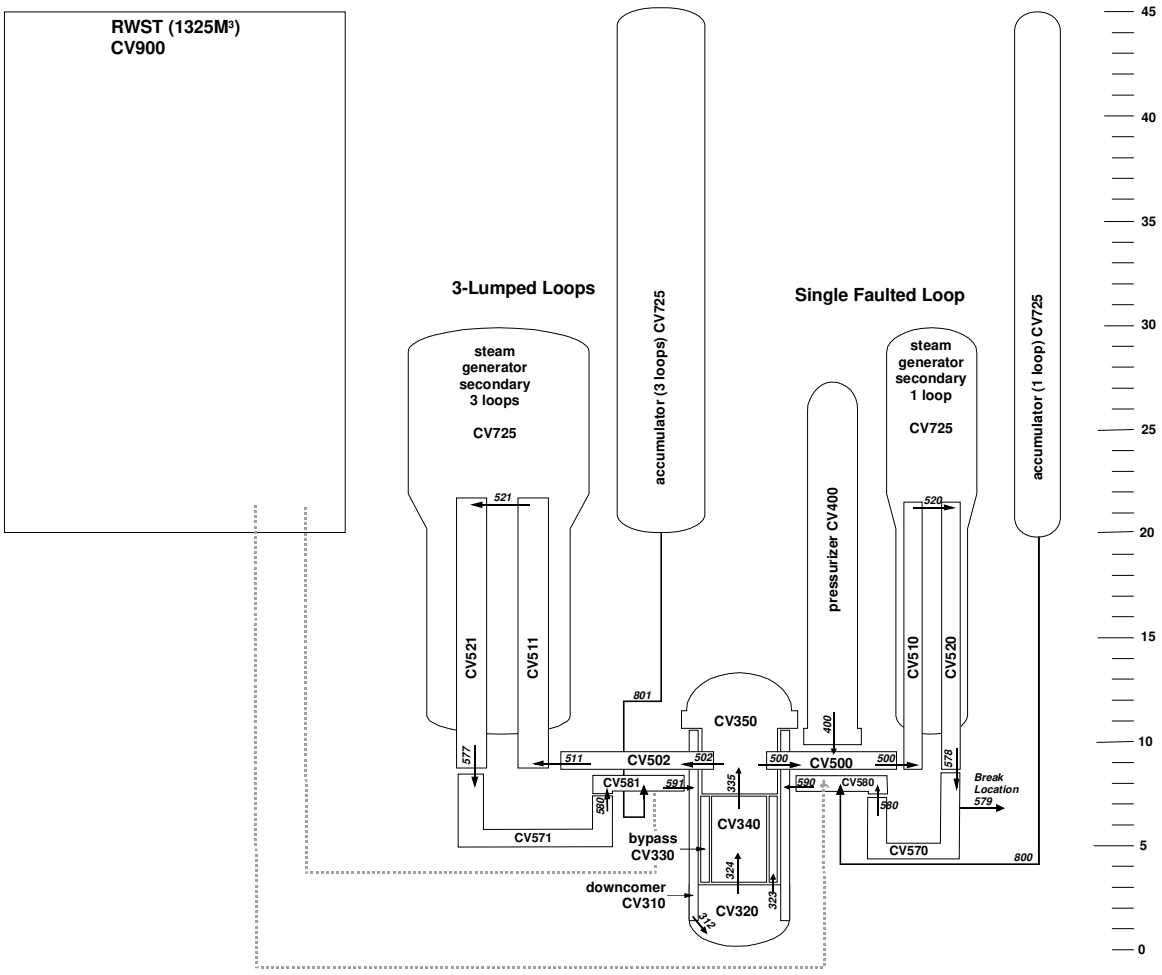

Figure 10-1. MELCOR Node Diagram for Zion Primary System (elevation in meters)

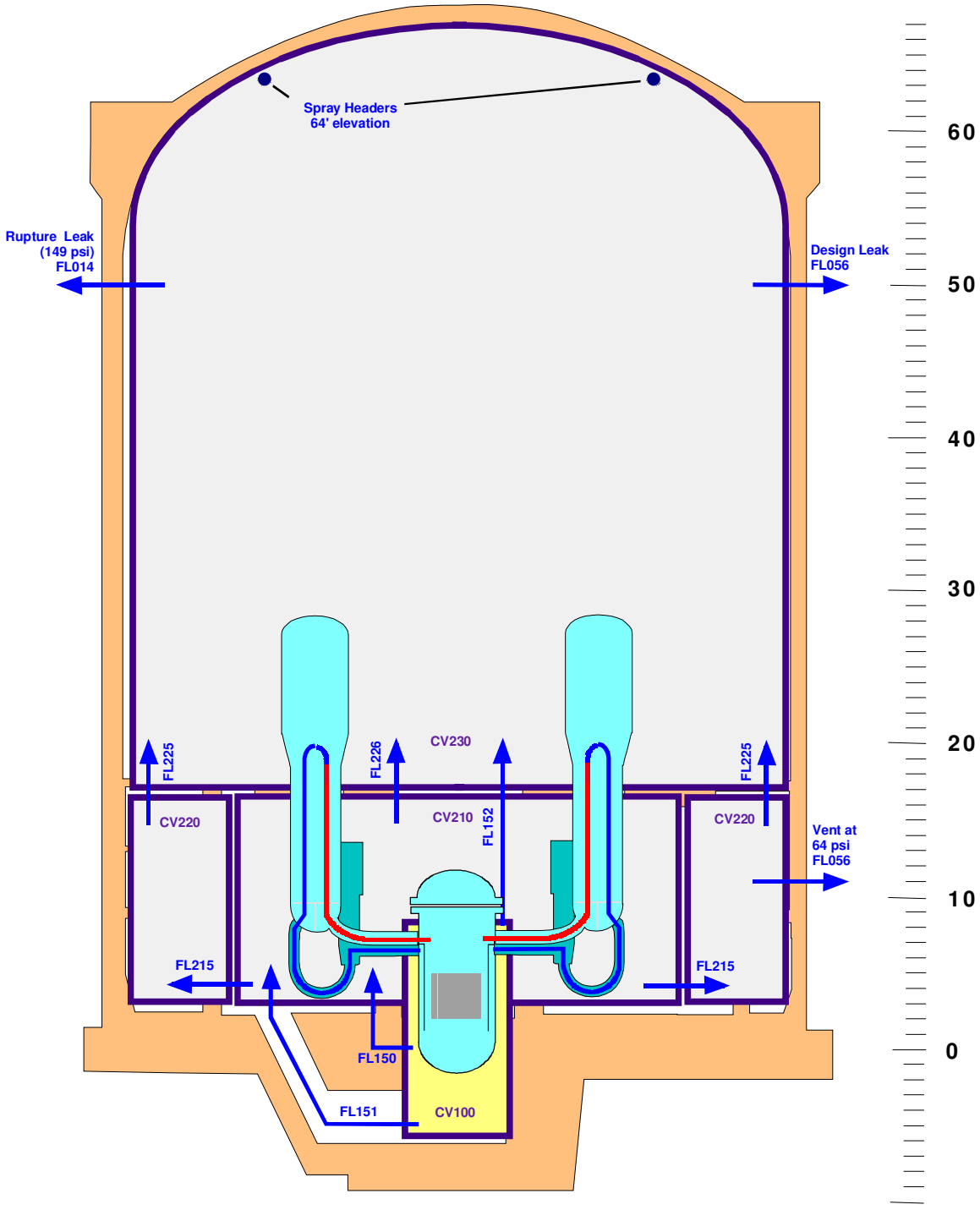

Figure 10-2. MELCOR Node Diagram for Zion Containment (elevation in meters)

As with the previously discussed Surry analyses, this plant description makes use of a simplified core/vessel/RCS nodalization. More detailed CVH nodalizations are generally recommended for MELCOR versions beyond 1.8.5, especially for high pressure sequences (and this sequence indeed is a high-pressure sequence); however, the simplified version is

retained in this analysis in order to facilitate comparisons to MELCOR 1.8.4. Currently, revised plant input models are being prepared that include significantly expanded CVH nodalizations in the core and RCS in order to capture important effects of natural circulation. Natural circulation loops in the core/upper plenum and upper plenum/steam generator regions have the potential to delay core degradation and to shift RCS failure locations from the lower vessel head to the hot leg or surge line. Future versions of this test problem will make use of improved plant models to capture these important effects.

10.3 MELCOR Input Specifications

The MELGEN input files for this calculation are “ziontmlb.gen” and “cor.gen.” The “ziontmlb.gen” file is the primary MELGEN file. The “cor.gen” file is automatically read in during MELGEN processing because it is identified by the “r*i*f” command in the “ziontmlb.gen” input file. The “cor.gen” file is a complete replacement for the COR package input that was developed during the rebaselining study. The modifications to the COR package input were performed to allow future users to take advantage of the MELCOR SS and NS features now available in MELCOR 1.8.5.

The MELCOR input file for this calculation is “ziontmlb.cor.”

In general, the Zion model was developed using standard default MELCOR modeling parameters. Key modeling input parameters are listed in Table 10-1. Other boundary conditions for the TMLB transient are listed in Table 10-2.

Table 10-1. Key Modeling Parameters for Zion TMLB

Parameter	Record	Description	Default Value	Zion Value
IUEMOD	COR00006	Eutectics model.	0 (Inactive)	0
IHSDT	COR00006	HS boundary condition option.	0 (BC option required)	0
IDTDZ	COR00006	DTdz inlet option switch.	0 (dtdz from CVH/FL hydrodynmics calculations)	0
MTUOZR	COR00007	Transport mech. Flag for UO_2 in molten zircaloy.	1 (UO_2 transported as a fraction of molten mass)	1
MTZXZR	COR00007	Transport mech. Flag for ZrO_2 in molten zircaloy.	1 (ZrO_2 transported as a fraction of the molten mass)	2 (ZrO_2 transported as a fractional proportion to existing fraction in material)
MTSXSS	COR00007	Transport mech. flag for steel oxide in molten steel.	2 (steel oxide transported as fractional proportion to its existing fraction in the steel)	2
HDBPN	COR00009	Lower head failure parameters: heat transfer coefficient from debris to penetration structures.	1000 W/m^2K	500 W/m^2K
HDBLH	COR00009	Lower head failure parameters: heat transfer coefficient from debris to lower head.	1000 W/m^2K	500 W/m^2K
TPFAIL	COR00009	Failure temperature of	1273.15 K	1273.15 K

Parameter	Record	Description	Default Value	Zion Value
		penetrations or lower head.		
ICONV	RN2001	Convection option switch.	0 (flowpath convection of radionuclides calculated)	0
ICOND	RNACOND	Aerosol condensation index.	0 (Condensation on all existing aerosols)	0*
ICRLSE	RNFP000	Core release model indicator.	-2 (CORSOR-M model with surface to volume ratio option)	-2
IHYGRO	RN1002	Hygroscopic model.	0 (not active)	1
ICA02	RNCA100	Chemisorption model.	1 (active)	1

**Not included in input, default value is assumed by MELGEN.*

Table 10-2. Zion TMLB Boundary Conditions

Boundary Condition	Zion TMLB
Accumulators	Operate as designed (injection at 4.275 MPa RCS pressure).
HPI	Assumed to fail.
LPSI	Assumed to fail.
RCS Pressure Boundary Status	Intact until vessel failure. (See Table 10-3.)
Primary Pressure Control	SRV assumed to open at RCS pressure of 17.2 MPa.
Steam Generator SRVs	Assumed to open when secondary pressure reaches 7.41 MPa. (hysteresis cycle).
Reactor Power	SCRAM at t = 0.0 sec.
Containment Sprays	Assumed to fail.
Containment Fan Coolers	Assumed to fail.
Containment Leakage	Assumed to be 0.1 vol % / day at containment design pressure from lower dome. Hole size is 2.3 mm equivalent.

Table 10-3. MELCOR-Calculated Timing of Events for Zion TMLB

1.8.4 (min)	1.8.5 (min)	Event
0	0	Loss of all onsite and offsite power.
56	56	SRV opened first time.
95	95	Water level dropped below top of active fuel.
134	134	Gap release begins in core radial ring 1.
134	134	Gap release begins in core radial ring 2.
134	134	First fission products leak from containment.
134	136	Gap release begins in core radial ring 3.
142	141	Gap release begins in core radial ring 4.
216	394	Lower head fails (1.8.4 penetration failure, 1.8.5 creep rupture).
215	469	CSP fails.
216	469	Debris ejection to cavity begins–core-concrete interaction initiated in cavity Accumulators discharge.
304	475	In-vessel hydrogen production terminated (1.8.4 at 590 kg, 1.8.5 at 547 kg).
-	502	Debris quench ends–remainder of core material released to cavity.
600.		MELCOR calculation terminated.

10.4 Results of Analysis

The MELCOR 1.8.5 simulation of the Zion TMLB ran to completion and all results appeared to be reasonable. Calculated results are summarized in this section, and a discussion of these results is presented in the following section. Note that event timing is identical between 1.8.4 and 1.8.5 until fuel damage occurs. Core melt progression proceeds differently between the two calculations. Reasons are considered in the discussion of results.

The following figures show results for the Zion TMLB MELCOR 1.8.5 simulation. Results are compared to MELCOR 1.8.4 simulation results. General trends show reasonable comparison between MELCOR 1.8.4 and MELCOR 1.8.5 calculated results. Timing differences are apparent due to MELCOR code enhancements made to the 1.8.5 code release. These differences are discussed in the following section.

10.5 Discussion

Discussion of MELCOR 1.8.5 results is presented below. In general, results compared well (qualitatively) with MELCOR 1.8.4 results. A difference in the accident event timing is seen following the onset of core damage due to changes in MELCOR default treatment of COR parameters between code versions 1.8.4 and 1.8.5. The differences are pointed out in the discussion below.

Following loss of power and the resulting total loss of all core cooling, the primary system coolant heats as the reactor pressure (Figure 10-3) increases to the ~17MPa (2500 psia) SRV setpoint at 56 minutes. The primary system pressure was then maintained at that level as the SRVs cycled. SRV flow is shown in Figure 10-4.

As the SRVs relieved pressure and discharged coolant to the containment, the water level in the reactor vessel dropped until the core was exposed. The reactor vessel water level is shown in Figure 10-5.

Following uncovery, the core heated rapidly (Figure 10-6 and Figure 10-7) until fuel relocation began from the uppermost region of the core. During core heatup, the zirconium cladding was oxidized, producing hydrogen (shown in Figure 10-8). MELCOR 1.8.4 predicted massive core collapse at around 220 minutes. MELCOR 1.8.5 predicted relocation of portions of the fuel as heatup occurred. However, as particulate debris moved downward, it spilled into the water pool that remains in the core. This debris quenched, producing steam, which had a cooling effect on the remaining intact fuel. This continued until complete vessel dryout occurred just before 400 minutes. At that time, the fuel experienced a nearly adiabatic heatup (due to the comparative absence of cooling steam flow) and massive core collapse occurred at approximately 460 minutes.

The effluent from the primary system (i.e., the SRV water flow) and the lower head-expelled core debris, water, and gases all contributed to the pressurization of the

containment (Figure 10-9). Note that containment pressure response is nearly identical for both calculations, except that the rapid pressurization that occurs at vessel failure is delayed in the 1.8.5 calculation due to the debris quench. Core debris began to erode the concrete of the reactor cavity following vessel failure, contributing to containment pressurization. The slopes of the two containment pressure curves following vessel failure are very similar. Note that the calculation was stopped before the cavity water was completely gone (Figure 10-10).

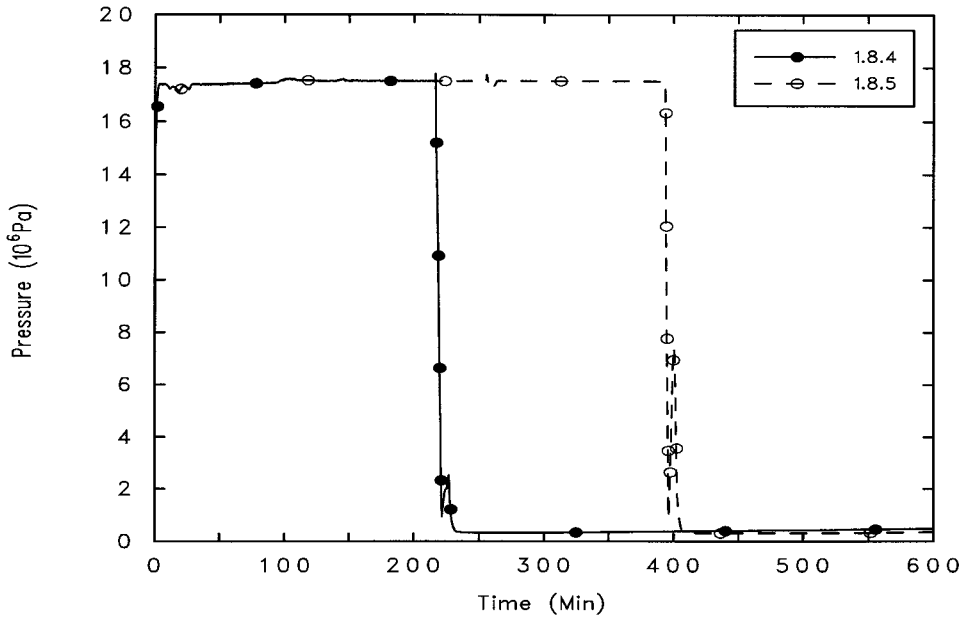

Figure 10-3. Zion TMLB: Primary System Pressure

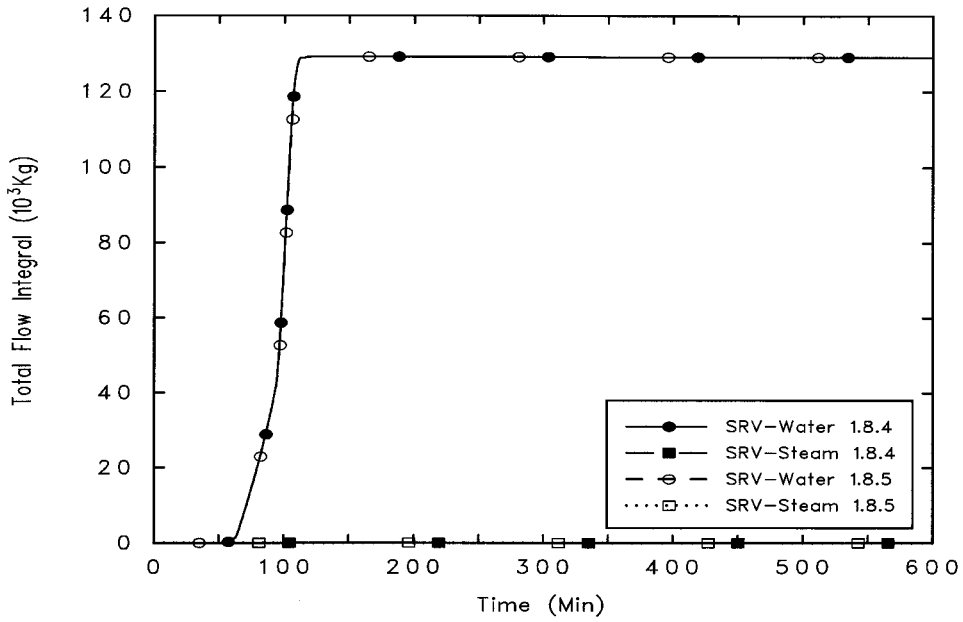

Figure 10-4. Zion TMLB: Integrated SRV Flow

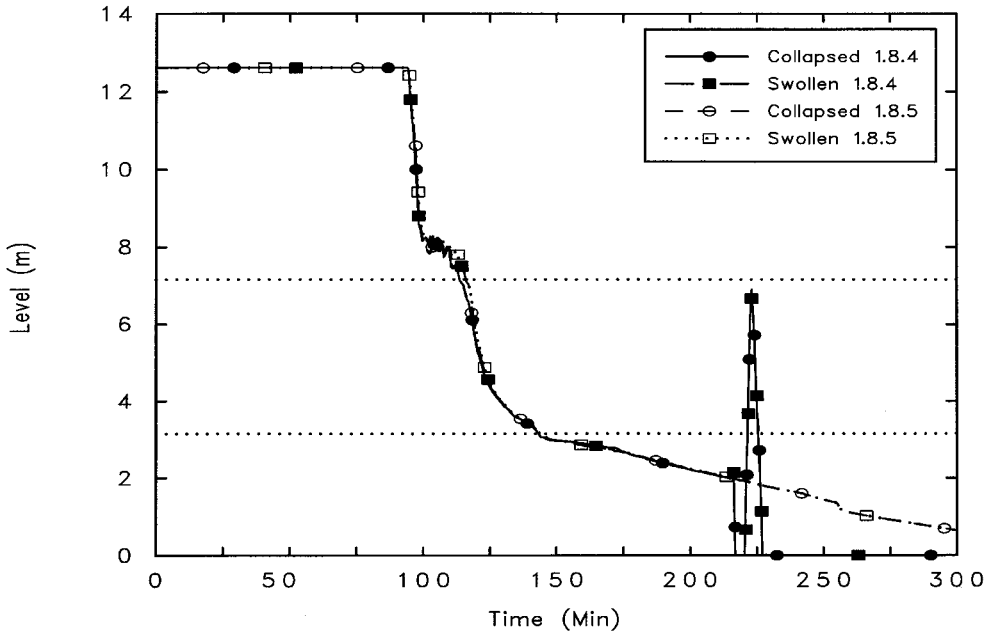

Figure 10-5. Zion TMLB: Reactor Vessel Water Level

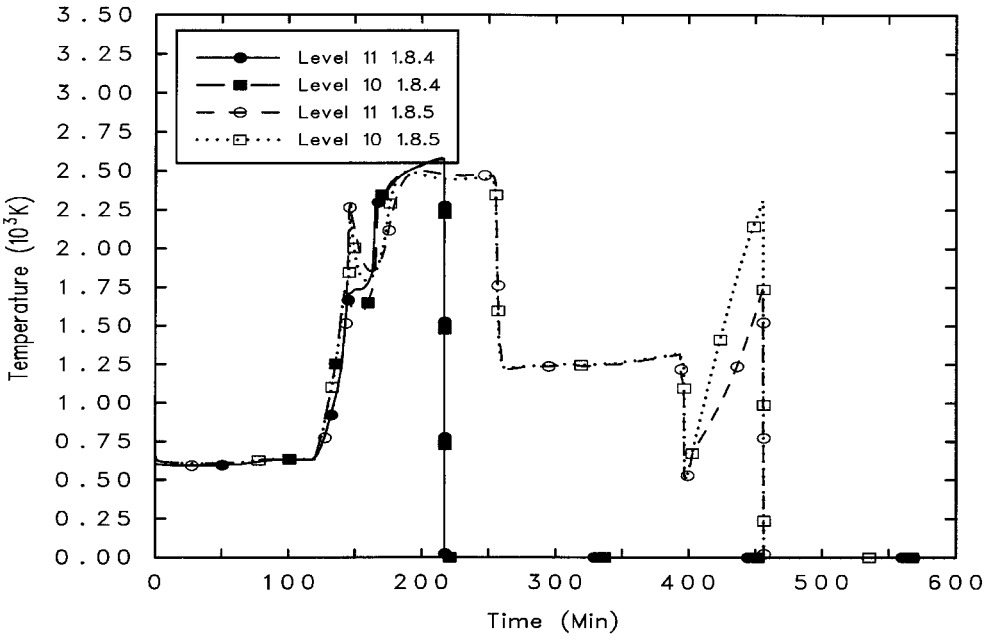

Figure 10-6. Zion TMLB: Inner Core Fuel Temperatures (top of core)

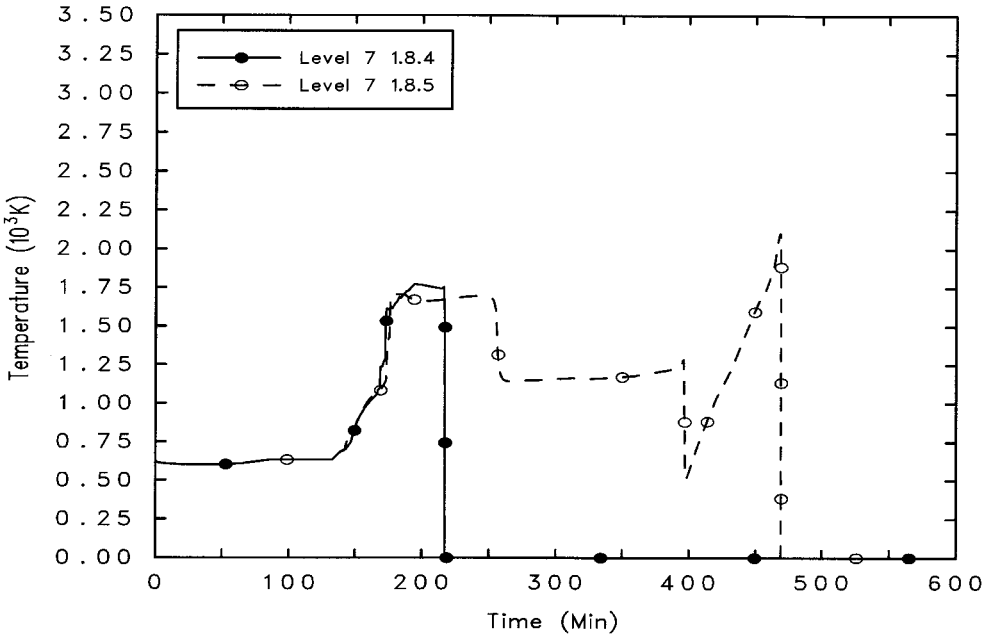

Figure 10-7. Zion TMLB: Inner Core Fuel Temperatures (mid-core)

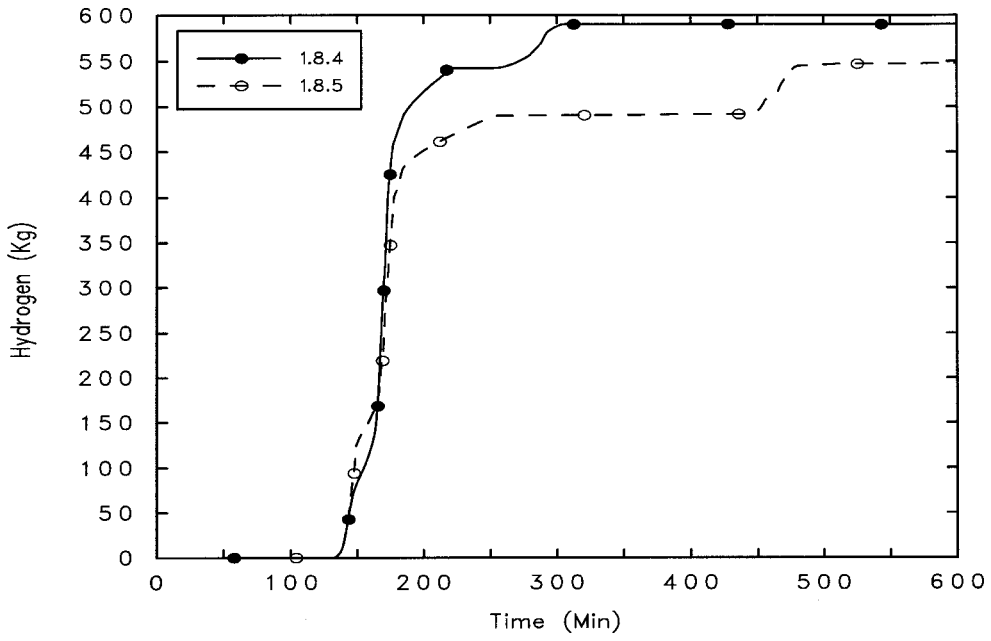

Figure 10-8. Zion TMLB: In-Vessel Hydrogen Production

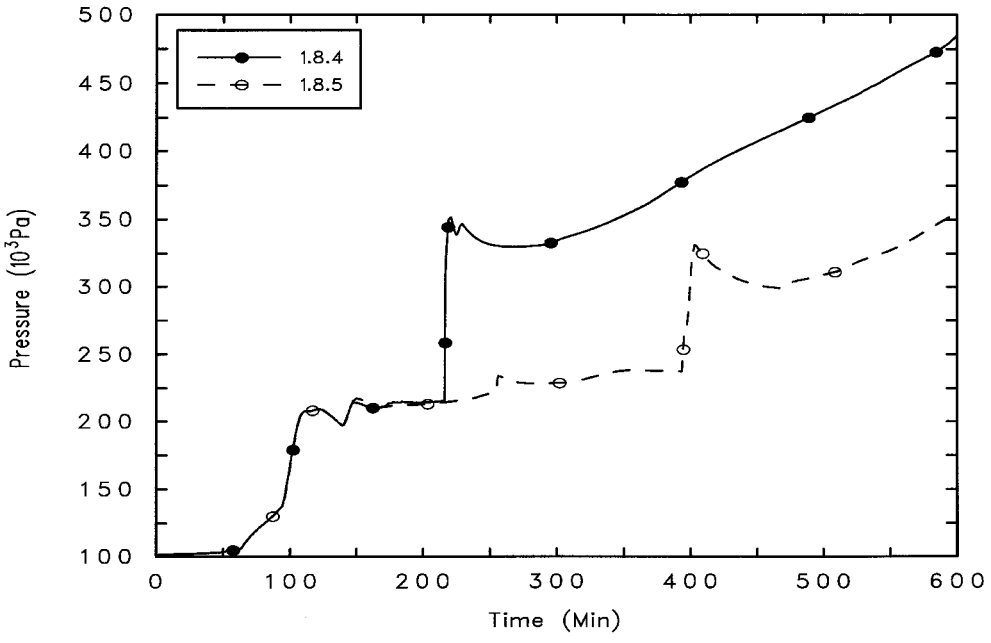

Figure 10-9. Zion TMLB: Containment Pressure

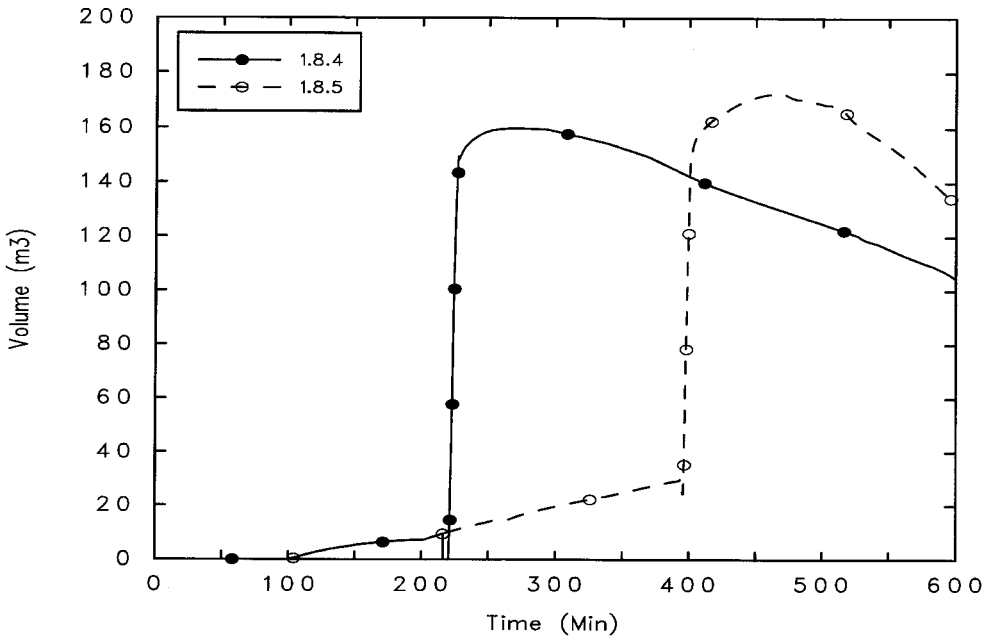

Figure 10-10. Zion TMLB: Reactor Cavity Water Volume

Figure 10-11 through Figure 10-13 show radioactive releases for the MELCOR noble gas and CsI groups. Figure 10-11 shows release from fuel. Figure 10-12 shows release to containment, and Figure 10-13 shows the environmental release. Approximately 80% of the volatile fission products are released from fuel during the fuel heatup, with nearly all of them being released in the long term. Figure 10-12 shows the delay in release of volatiles to the containment due to the slowing of accident progression resulting from the difference in core relocation behavior. More CsI was retained in the primary system due to the longer period prior to vessel failure. This resulted in slightly lower environmental releases (predicted by 1.8.5), as can be seen in Figure 10-13. Table 10-4 shows the fractional distribution of fission products at the time the MELCOR calculation was terminated.

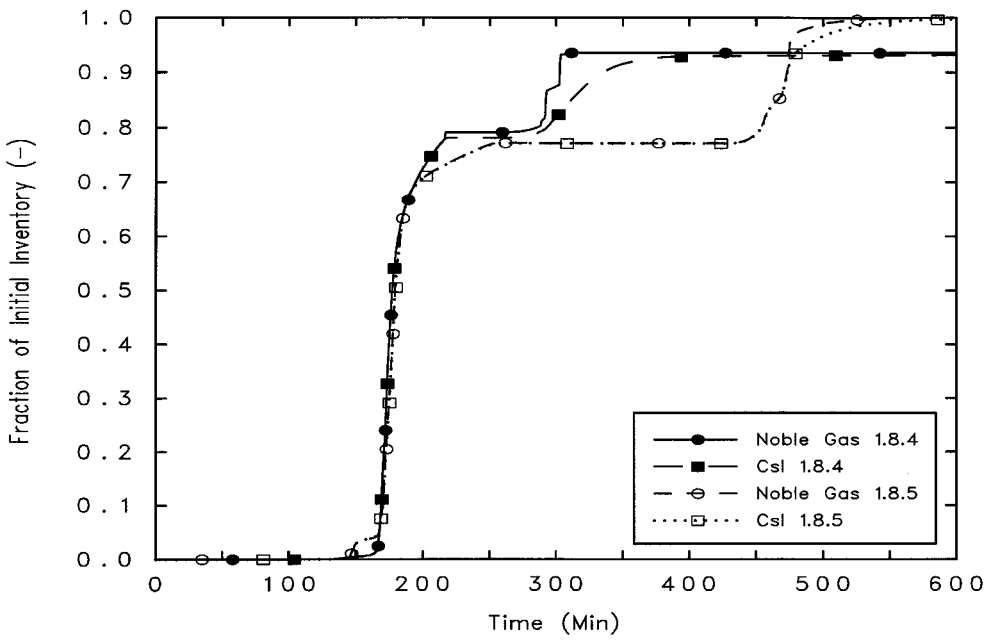

Figure 10-11. Zion TMLB: Radioactive Fission Product Release from Fuel

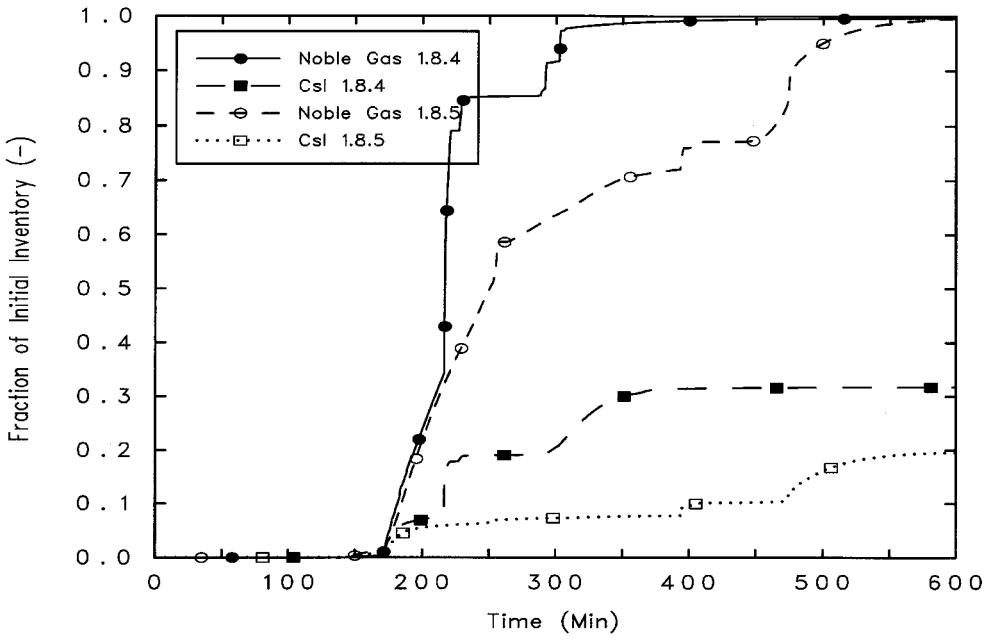

Figure 10-12. Zion TMLB: Radioactive Fission Product Release to Containment

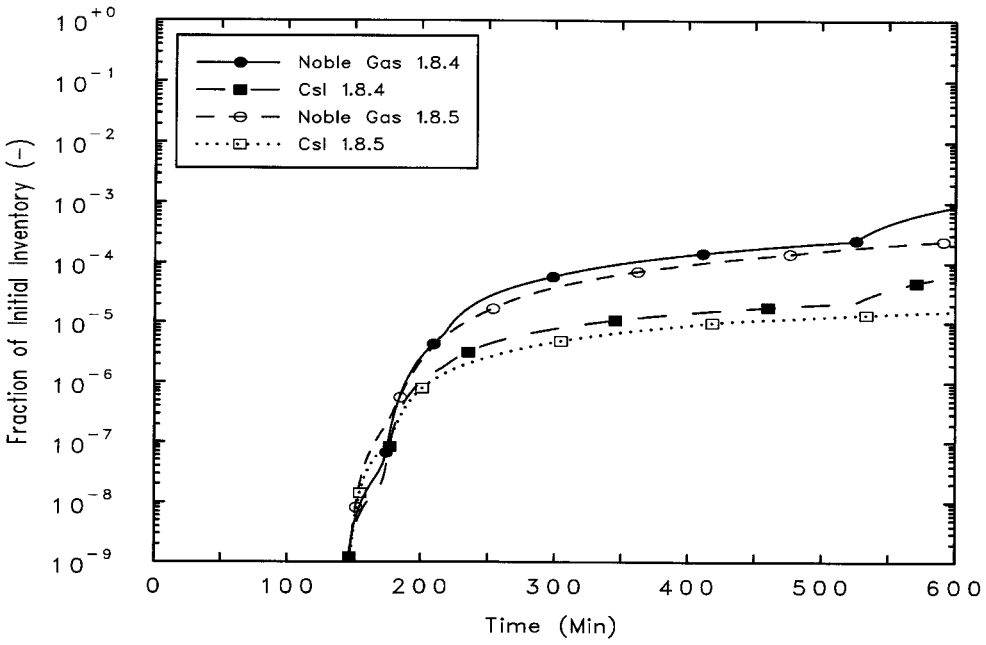

Figure 10-13. Zion TMLB: LPSI Flow Radioactive Fission Product Release to Environment

Table 10-4. Radionuclide Fractional Distribution at End of Problem

RN Class	Core (In-vessel)	Debris (In Cavity)	Primary System	Containment	Environment
1 (Xe)	5.04E-04	0.00E+00	5.51E-03	9.94E-01	2.35E-04
2 (Cs)	5.49E-04	5.92E-06	8.17E-01	1.83E-01	1.41E-05
3 (Ba)	2.52E-03	9.10E-01	8.22E-03	7.91E-02	3.60E-07
4 (I)	4.39E-02	0.00E+00	2.93E-02	9.27E-01	1.58E-04
5 (Te)	5.74E-04	2.36E-02	7.19E-01	2.57E-01	2.00E-05
6 (Ru)	2.52E-03	9.98E-01	9.83E-07	4.72E-07	1.47E-11
7 (Mo)	2.38E-03	8.68E-01	1.15E-01	1.49E-02	1.58E-06
8 (Ce)	2.52E-03	9.77E-01	1.07E-07	2.05E-02	1.16E-08
9 (La)	2.52E-03	9.97E-01	6.62E-05	8.41E-04	1.59E-09
10 (U)	3.08E-03	9.97E-01	6.77E-05	3.92E-05	8.95E-10
11 (Cd)	2.43E-03	7.00E-01	9.17E-02	2.06E-01	1.96E-06
12 (Sn)	2.43E-03	8.31E-01	9.48E-02	7.23E-02	1.59E-06
16 (CsI)	8.90E-11	2.72E-02	6.41E-01	3.32E-01	3.10E-05

Note: Classes 2 and 4 combine to form CsI (Class 16) when released from fuel.

10.6 References

1. Pilch, M.M., et al., “Evaluation of Radiological Consequences of Design Basis Accidents At Operating Reactors Using The Revised Source Term,” Letter Report for Office of Nuclear Regulatory Research, U.S. Nuclear Regulatory Commission, Sandia National Laboratories, September 1998.

2. Soffer, L., et al., *Accident Source Terms for Light-Water Nuclear Power Plants*, NUREG-1465, U.S. Nuclear Regulatory Commission, February 1995.

11. Simulation of a LB LOCA in the Grand Gulf Plant

11.1 Background

An important element in the assessment of MELCOR 1.8.5 involves the baselining of the code against the previous version (1.8.4). The matrix of calculations for implementing this procedure includes both analyses of experiments, which may look at a limited number of phenomena, and of plant calculations, which may run the entire range of phenomena associated with reactor accidents. This assessment evaluates the new version with respect to its application for the analysis of a Grand Gulf LB LOCA accident sequence. Thus, for this application, the key models that are exercised in these calculations include all those associated with core heatup, meltdown, relocation, clad oxidation, containment pressurization, and fission product release and transport.

In particular, the new models that most strongly affect the results are early transition to the BH package, and the improved OS treatment in the COR package. The first model provides for the transition from COR to BH in the lower plenum models as soon as sufficient core material has been relocated. This was changed from the 1.8.4 version, which required both sufficient core material and a dry lower plenum region. The new models now allow two main types of OS, NS, which is nonsupporting structure, and SS, which is supporting structure. This modeling provides for greater flexibility in modeling the various types of structures in the core and lower plenum regions, such as support plates and CRGTs.

11.1.1 Plant Description

The Grand Gulf reactor plant is a General Electric BWR with a BWR-6 nuclear steam supply system and a Mark-III containment system. The steam supply system features a nuclear core with 800 fuel assemblies and a rated power level of 3833 MWt (design level of 4025 MWt.) The Mark-III containment system combines the suppression pool concept with a large noninerted containment volume. The containment itself consists of a steel-lined, reinforced concrete structure.

Engineered safety features include the ECCS, the containment spray cooling system, and the automatic depressurization system (ADS). The ECCS consists of a high-pressure core spray system (HPCS), a low-pressure core spray system (LPCS), and a low-pressure coolant injection (LPCI) system. The containment spray system provides containment cooling through two independent loops using the residual heat-removal system pumps and heat exchangers. The ADS system uses a subset of the safety relief valves to depressurize the vessel when the core coolant level has been reduced to one-third of the core height. All of these engineered safety features are represented in the general MELCOR model; however, not all of these may be exercised in any given accident sequence. In particular,

the ADS system is assumed to operate while the ECCS system remains unavailable in the current calculations.

The containment system also includes a number of hydrogen igniters at key locations in the drywell and wetwell compartments. These devises are designed to ensure that hydrogen burns are initiated at lower H_2 concentrations, thus preventing the accumulation of hydrogen at such concentrations as might threaten massive deflagrations or detonations.

11.1.2 Accident Description

The sequence considered in this analysis involves a break in a large recirculation system pipe. It is further assumed that ECC and containment spray systems are unavailable. The reactor plant is automatically scrammed under this condition with the main steam isolation valves closing in order to isolate the primary system. The input was adapted for the LB LOCA from the station blackout model by adding a flow path from the downcomer to the drywell to simulate a break in a main recirculation system pipe. In the current analysis, the ECCS was assumed not to be available but hydrogen igniters were assumed to be operable.

11.2 MELCOR Model Decription

The basic MELCOR model for the Grand Gulf reactor plant was developed by ORNL and has been used widely as the best available description of the BWR-6 Mark-III reactor plant. The LB LOCA control volume and flow path nodalization is depicted in Figure 11-1. The reactor vessel is modeled using six thermal-hydraulic control volumes, one each for the lower plenum, core channel and bypass, upper plenum/separators, dome/dryers, and downcomer volumes. The volumes associated with the two external water recirculation loops are modeled as a single volume. The MSIV are assumed to have closed upon initiation of the break so that the piping and equipment (turbines, condensers, pumps, etc.) associated with the primary power conversion system are not required for this sequence. The containment was simulated using three control volumes. The first is for the drywell, which includes the reactor cavity. The second one is for the wetwell, which includes the annular compartments above the suppression pool, the suppression pool, and the containment dome region. The third volume is included for the weir compartment, which includes the part of the suppression pool located on the inside of the drywell between the drywell and weir walls. . The containment (Figure 11-1) consists of the three volumes labeled Drywell CV201, Wetwell CV301 and Wier Compartment CV202. For the purpose of tracking fission product disposition, one additional volume is included to model the environment.

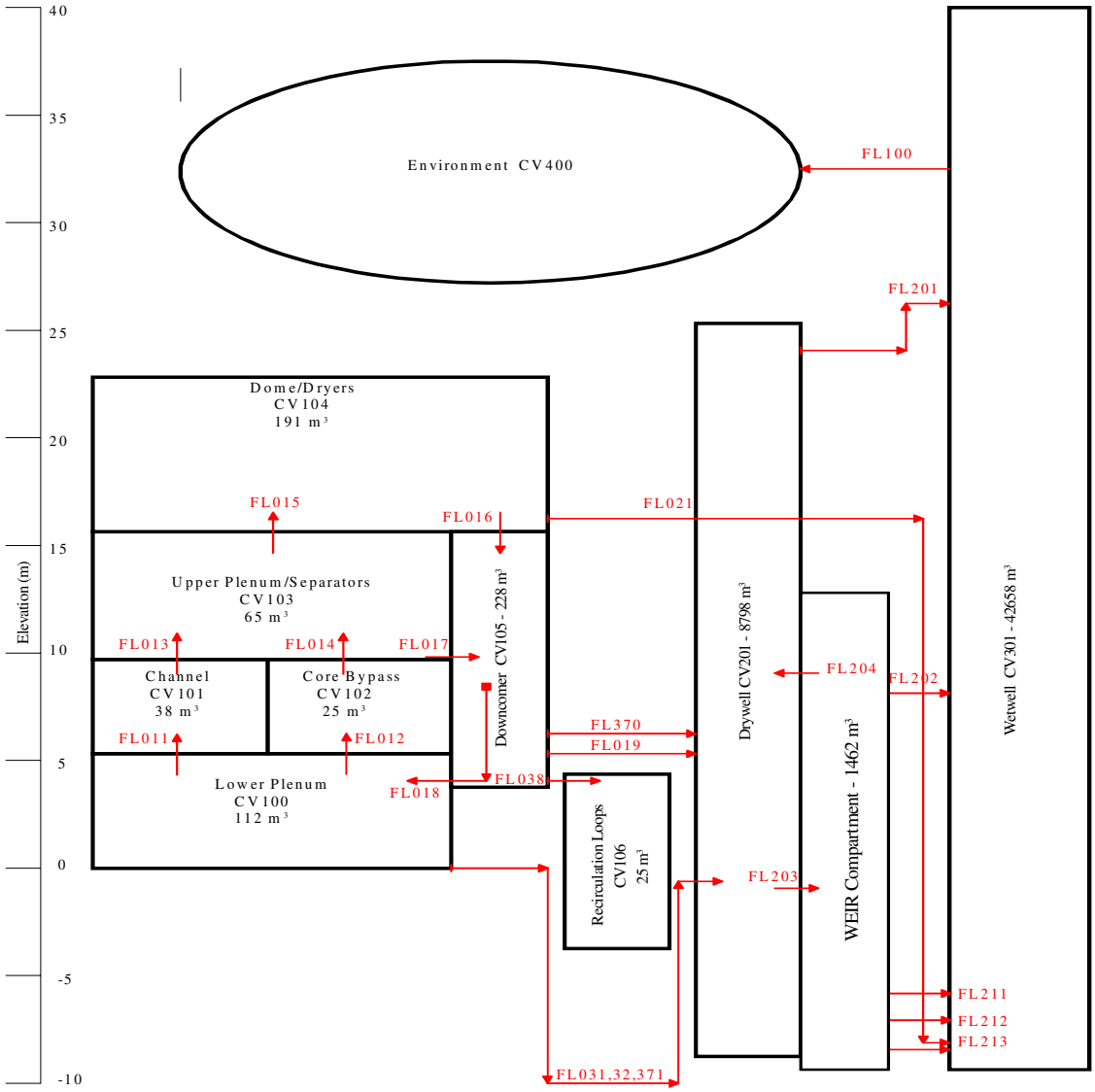

Figure 11-1. Control Volume and Flow Path Nodalization

Beyond the obvious flow paths connecting the various control volumes used to model the reactor vessel, there were a number of flow paths modeled between the primary system and the containment, between the two containment volumes, and between the containment and the environment. Reactor vessel pressure control and the automatic de-pressurization system were modeled by flow path FL021. This path consists of a set of safety relief valves that have high and low set points to simulate the behavior of these valves. A subset of these valves is programmed to simulate the ADS by opening and remaining open upon a core water level reduction to one-third of normal water level. The ADS can be overridden by operator action, but the current sequence assumes that no such override occurs.

Leakage flow paths between the reactor vessel and the containment were modeled with FL370 and FL371. Flow path FL370 was used to simulate a pump seal leak between the

downcomer and the drywell compartment. A leakage path through the control rod drive penetrations was included in the model using FL371. This path connected the lower plenum volume to the drywell compartment.

Two vessel breach paths were included in the flow network. Path FL031 connected the lower plenum volume to the drywell compartment and was set to open when the COR lower head model predicted BH failure (via the COR-ABRCH parameter). A second vessel breach path, FL032, was set to open when the BH package indicated lower vessel head failure through the BH-FFLAG flag. These paths covered the two possible timings for lower head failure before or after transition from the COR to the BH package treatment of the molten core/vessel head interaction.

Several flow paths were included to allow for flow between the drywell and the wetwell compartments. The suppression pool vent paths that connect the drywell atmosphere with the wetwell suppression pool were altered from the station blackout sequence by introducing an intervening control volume between the two volumes. As mentioned above, the new control volume consists of the volume of the region that lies between the weir wall and the drywell wall. The three flow paths that simulate the suppression pool vents, one for each level of vents in the drywell wall (flow paths FL211, FL212, and Fl213), now connect the weir control volume with the wetwell compartment. The weir volume is connected to the drywell with two flow paths, one of which represents the cross-sectional area at the top of the weir wall and the other a higher elevation to ensure that the weir does not become water-locked. These two paths are designated as FL203 and FL204, respectively. In addition, a drywell-to-wetwell leakage path (FL202) and a vacuum breaker path (FL201) were included between the wetwell and the drywell.

The large primary system break was modeled using an area of 0.2356 m^2 and located at an elevation of 4.376 m. This flow path is identified as FL019.

Finally, a flow path connecting the wetwell atmosphere to the environment was included using a valve model that opens based on a wetwell pressure set point. The flow area for the containment failure flow path was set to an initial value of zero and opened to a cross-sectional area of 0.1 m^2 when the wetwell pressure exceeds 70 psia (487 kPa).

The sequence was run assuming that ECCS was unavailable.

The core nodalization diagram for this plant is shown in Figure 11-2. The core region is divided into 4 radial rings and 13 axial levels. Levels 1 through 5 are located in the lower plenum. Level 5 represents the CSP. Level 6 consists of the lower, unfueled sections of the fuel canisters including such components as the nose pieces and tie plates. Levels 7 through 12 represent the active fuel region. Level 13 contains the upper tie plates, rod end plugs, and top guide. The region associated with the COR package model consists of three CVH control volumes, the channel, bypass, and lower plenum. The zircaloy rod cladding and canister walls as well as control rod poisons, cruciform stainless steel control blades, and other structural materials are included in the core region material inventory.

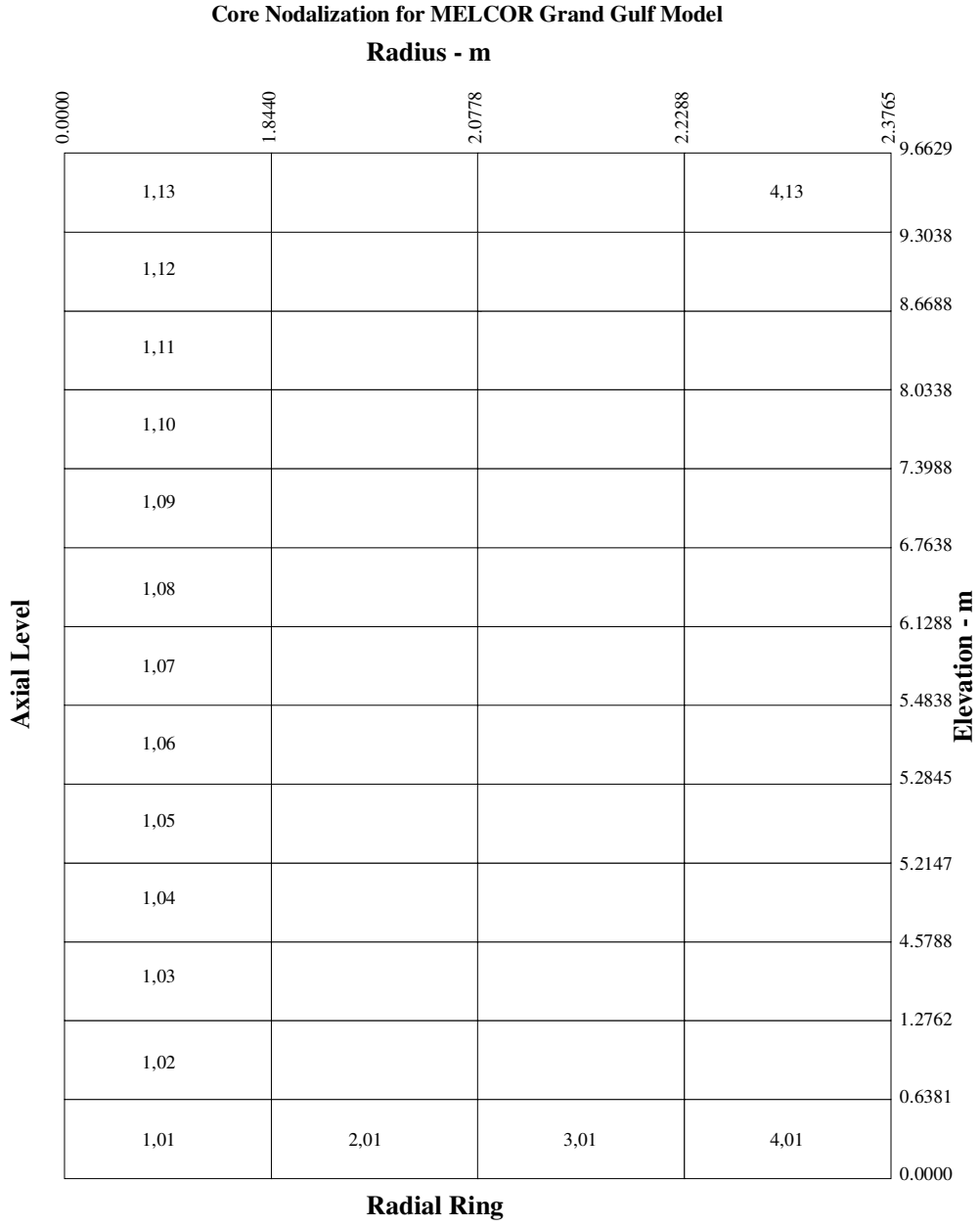

Figure 11-2. Core Nodalization

A number of heat structures (~40) were defined in the model to simulate the various components of the reactor vessel, primary system piping, containment walls, and sundry equipment. Appendix A contains listings of the 58M3 MELCOR input decks for both the 1.8.5 and the 1.8.4 calculations. The sections of the listings for the heat structure input provide a description and location of the heat structures for this model.

11.3 MELCOR Input Specifications

The decay heat curve used to determine whole core power was supplied by ORNL (without reference) and was applied to an operating power level of 3833 MW thermal. The fraction of full power at zero run time on this decay heat curve was 6%.

The present cases were run utilizing the CORSOR-M fission product release model corrected for the area/volume ratio.

The chemisorption and hygroscopic models were employed in both the version 1.8.4 and the version 1.8.5 calculations.

The primary differences between the input models for 1.8.4 and 1.8.5 relate to the treatment of OS. The standard OS was used in the 1.8.4 calculation while the new support models were employed in the 1.8.5 case. For example, this involved assigning the CSP in axial Level 5 to be SS, specified as a PLATEB structure with the failure criterion defined by control functions (in this case, the CFs defined a failure temperature for each ring). In addition, the control rod guide tubes in the lower plenum were defined as SS and specified as COLUMN support structures. Thus, the intact rods in the core region will not collapse into the lower plenum when the CSP fails. Upon CSP failure, only the particulate debris can relocate into the lower plenum in the 1.8.5 calculation, and this has a significant effect on the sequence timing and progression.

The input decks for the 1.8.4 and 1.8.5 calculations currently reside on the DEC Alpha where they were run. The 1.8.5 input decks are called “ggqxloca.gen” and “ggqxloca.cor,” while the 1.8.4 decks are named “gg_7.gen” and “gg_7.cor.” A listing of these input decks is provided in Appendix A.

11.4 Results of Analysis

11.4.1 Sequence of Events

A summary of the key events for the Grand Gulf LB LOCA sequence comparing the 1.8.4 and the 1.8.5 results is given in Table 11-1.

Table 11-1. Sequence of Events for the Grand Gulf LB LOCA Simulation

Event	Time (Seconds)	
	MELCOR 1.8.5	MELCOR 1.8.4
Accident Initiation	0	0
ADS Activation	133	134
Gap Release–Ring 1	744	738
Gap Release–Ring 2	802	797
Gap Release–Ring 3	1034	1025

Event	Time (Seconds)	
	MELCOR 1.8.5	MELCOR 1.8.4
Gap Release–Ring 4	1909	1925
Hydrogen Burns	2769,3038,4057, 4919,8266	4110
CSP Fails–Ring 1	2600	4020
CSP Fails–Ring 2	2942	4554
CSP Fails–Ring 3	2858	4701
CSP Fails–Ring 4	9968	4768
Lower Plenum Dryout	9300	4987
BH Turned on	2652	4987
Core Shroud Fails	12571	13765
CRGTs Fails–Ring 1	12572	-
CRGTs Fails–Ring 2	12572	-
CRGTs Fail–Ring 3	12572	-
CRGTs Fail–Ring 4	12572	-
Lower Vessel Head Fails	21587	31059
Calculation Terminated	40,000	40,000

11.4.2 Core Relocation

Examination of Table 11-1 shows that until CSP failure began, the version 1.8.4 and version 1.8.5 calculations produced fairly comparable results with the gap releases, for example, occurring at comparable times. Significant differences between the times for CSP failure in the inner three rings is evident. This is the direct result of differences between the core support parameters. Figure 11-3 shows axial disposition of fuel (particulate and intact) for the 1.8.5 calculation at 3000 seconds, just after the CSP failed in rings 1 to 3. Figure 11-4 shows the same information for the 1.8.4 calculation. Note that the UO_2 has moved further down toward the bottom of the core in 1.8.5 and none of the rings have failed in 1.8.4. Consequently, the total UO_2 in the core in both cases is about the same. Figure 11-5 and Figure 11-6 show the situation at 4,000 seconds. It is immediately obvious that despite the failure of the CSP in all three of the rings most of the fuel remains in the core for 1.8.5. At 5000 seconds the ring 4 CSP has not yet failed in the 1.8.5 calculation. However, by 5000 seconds the CSP has failed in all four rings in 1.8.4, and the entire core fuel inventory has relocated into the lower plenum. Core debris remains in the core region significantly longer in the 1.8.5 calculation, where ring 1 retains debris until 5800 seconds and rings 2, 3, and 4 are not emptied until 11,600, 12,600, and 12,600 seconds, respectively. For 1.8.5, the CRGTs in the lower plenum continued to support the core despite the loss of the CSP. As stated above, in 1.8.5 some fuel still remained in the core region out to 12,600 seconds. In 1.8.5, the presence of so much fuel just above the plate drove the temperature very high in the lower half of the core and contributed to the earlier CSP failure times for rings 1 through 3.

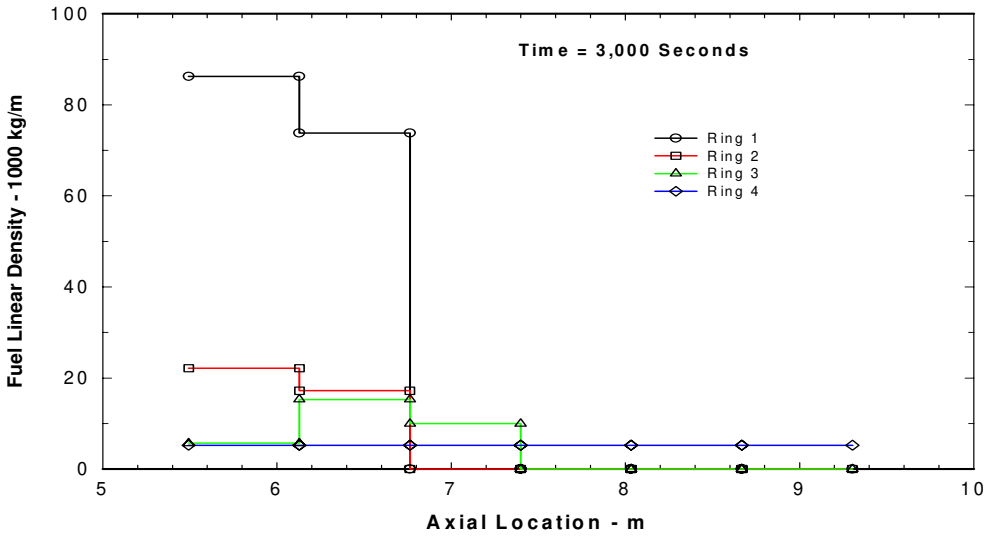

Figure 11-3. Core Material Disposition at 3000 Seconds–Version 1.8.5 Calculation

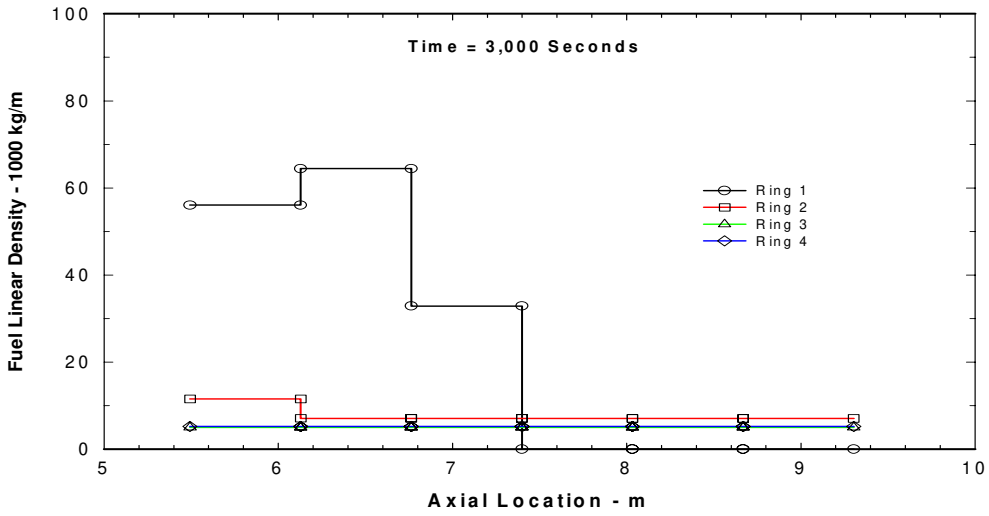

Figure 11-4. Core Material Disposition at 3000 Seconds–Version 1.8.4 Calculation

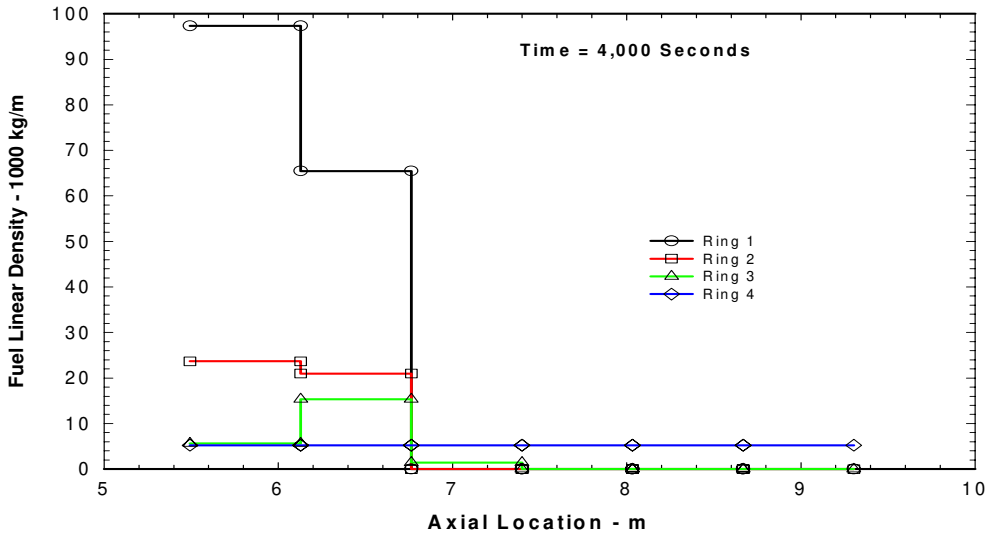

Figure 11-5. Core Material Disposition at 4000 Seconds–Version 1.8.5 Calculation

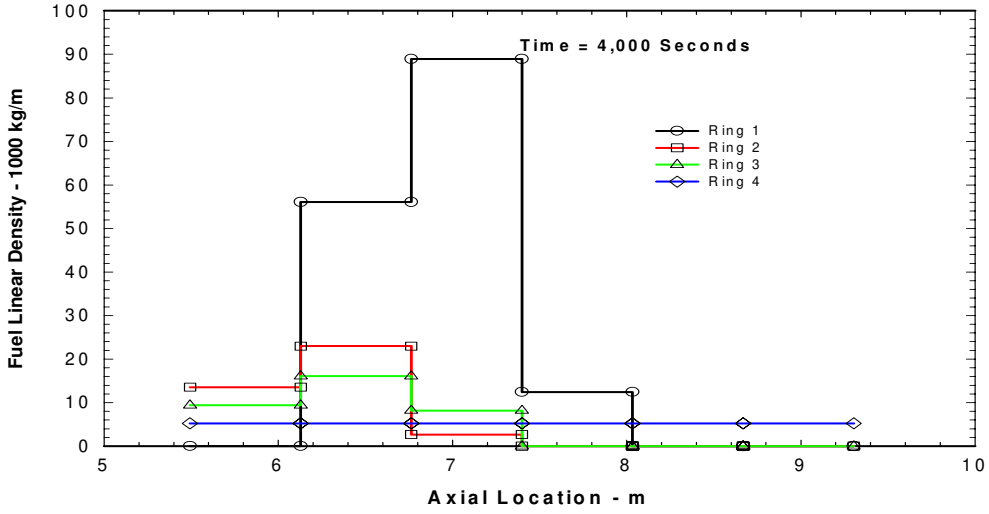

Figure 11-6. Core Material Disposition at 4000 Seconds–Version 1.8.4 Calculation

11.4.3 Primary System Thermal Response

Temperatures in the active core region of ring 1 (Levels 7 through 12) are presented in Figure 11-7 and Figure 11-8 for 1.8.5 and 1.8.4 calculations, respectively. The temperatures reported here are the maximum of the fuel and debris temperatures. It is clear from these figures that the peak fuel temperature resulting from the extended holdup time in the core region for 1.8.5 was significantly higher than in the 1.8.4 calculation (3000 K compared to 2650 K).

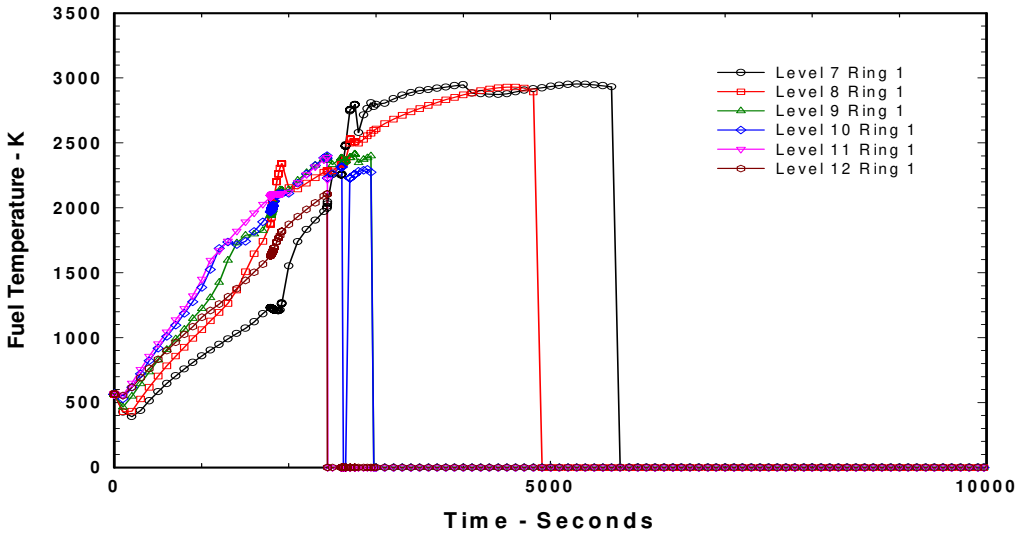

Figure 11-7. Core Fuel Temperatures–Version 1.8.5 Calculation

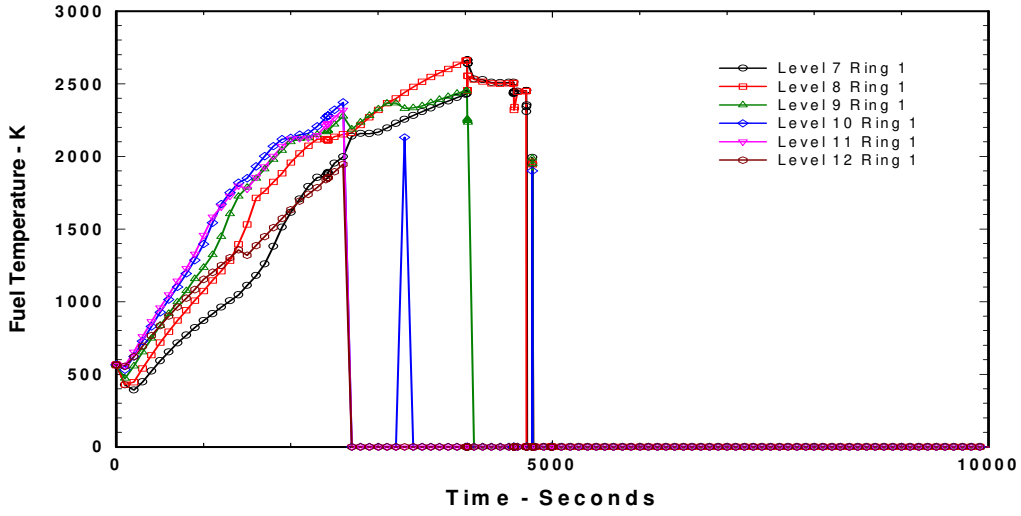

Figure 11-8. Core Fuel Temperatures–Version 1.8.4 Calculation

The effects of “early transition” to the BH package can be seen in the lower plenum dryout times and the time of transition to BH. The 1.8.5 case switched to BH at 2652 seconds, while 1.8.4 did not transition until 4987 seconds, when the lower plenum dried out. The result was that for 1.8.5, the transition was made to BH with much smaller quantities of core debris being relocated. The effects on the water mass in the lower plenum are seen in Figure 11-9 and Figure 11-10. The transfer of significantly less fuel from the CSP failure in 1.8.5 resulted in less water boil-off in the lower plenum and the retention of a significant quantity of water that did not boil off until 9,300 seconds.

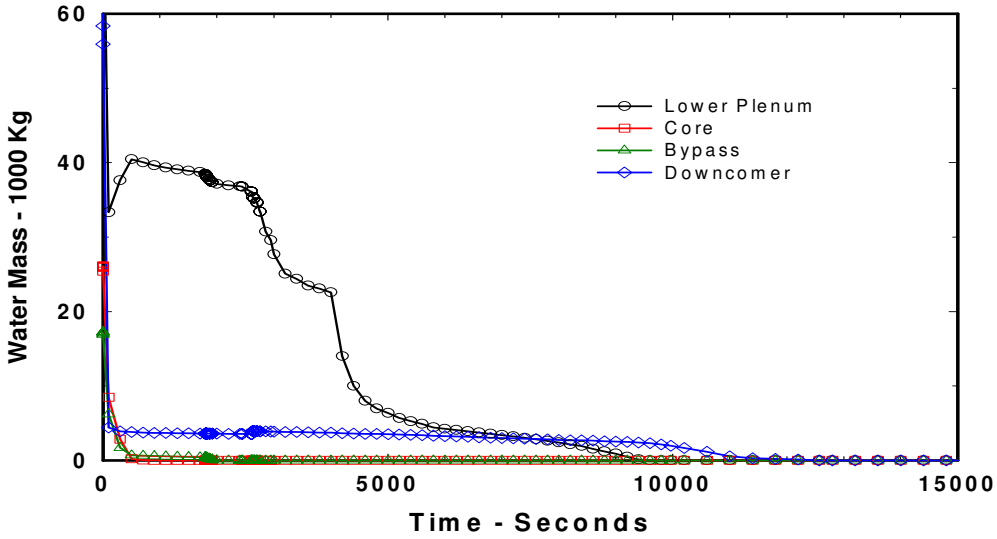

Figure 11-9. Core Coolant Inventory–Version 1.8.5 Calculation

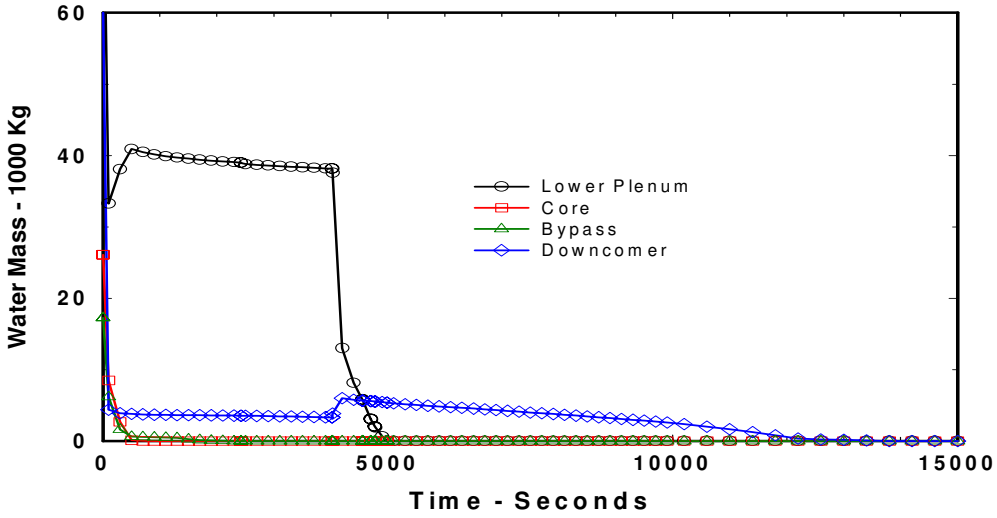

Figure 11-10. Core Coolant Inventory–Version 1.8.4 Calculation

11.4.4 Hydrogen Generation

The reduced coolant boil-off rate in the lower plenum provided a longer period of steam source for oxidation of cladding and other zircaloy in the core. This effect produced more than twice as much hydrogen in the 1.8.5 calculation. This is seen by comparing Figure 11-11 and Figure 11-12, which show the total in-core H_2 production for 1.8.5 and 1.8.4 cases, respectively. Much of the additional hydrogen in the 1.8.5 calculation was generated in the BH package, which predicts a more vigorous oxidation rate in the lower plenum than do the CVH models.

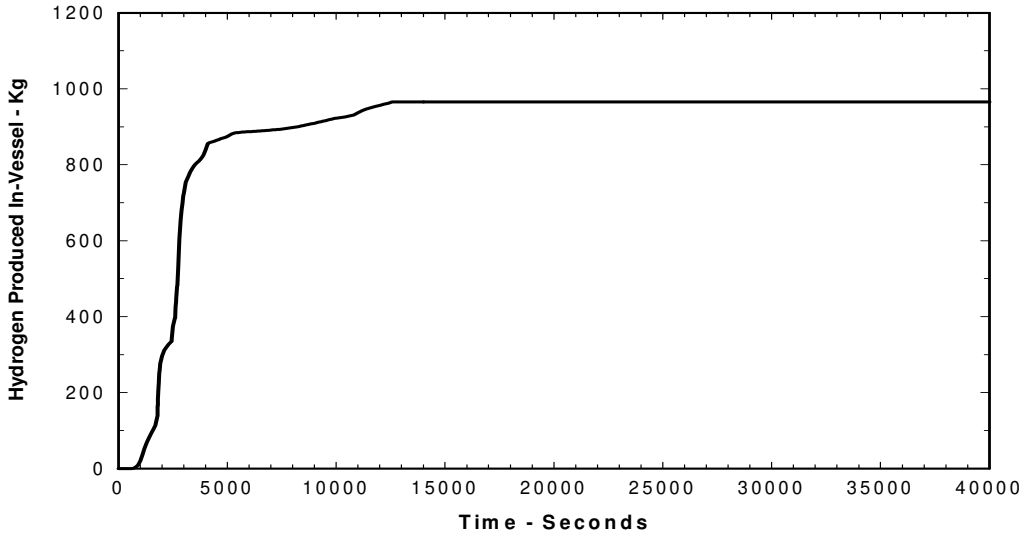

Figure 11-11. In-core Hydrogen Produced–Version 1.8.5 Calculation

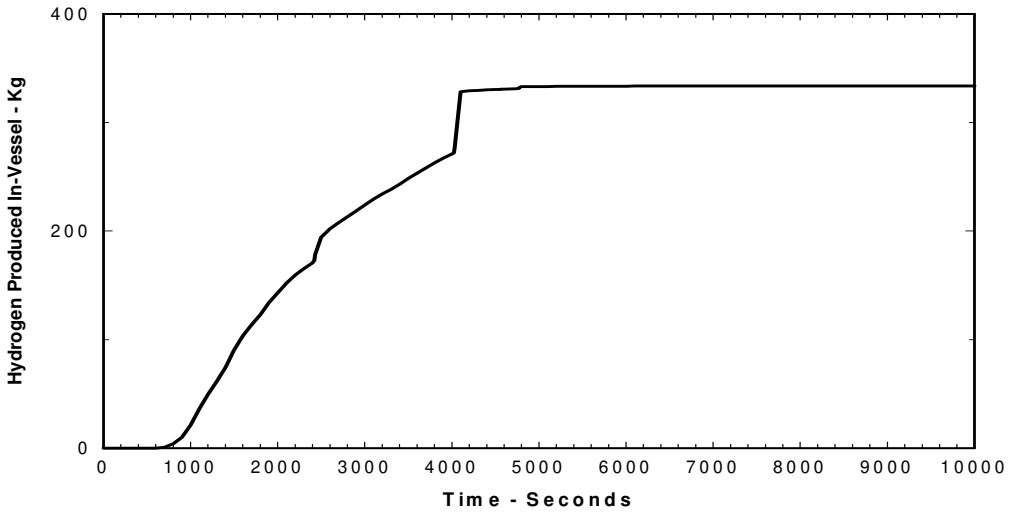

Figure 11-12. In-core Hydrogen Produced–Version 1.8.4 Calculation

11.4.5 Containment Response

Significantly larger hydrogen produced, in turn, a number of H_2 deflagrations in both the drywell and the wetwell in the 1.8.5 case; whereas, only a single burn occurred in the 1.8.4 calculation. Figure 11-13 and Figure 11-14 show the wetwell H_2 masses for the two calculations and reveal the effects of the H_2 deflagrations.

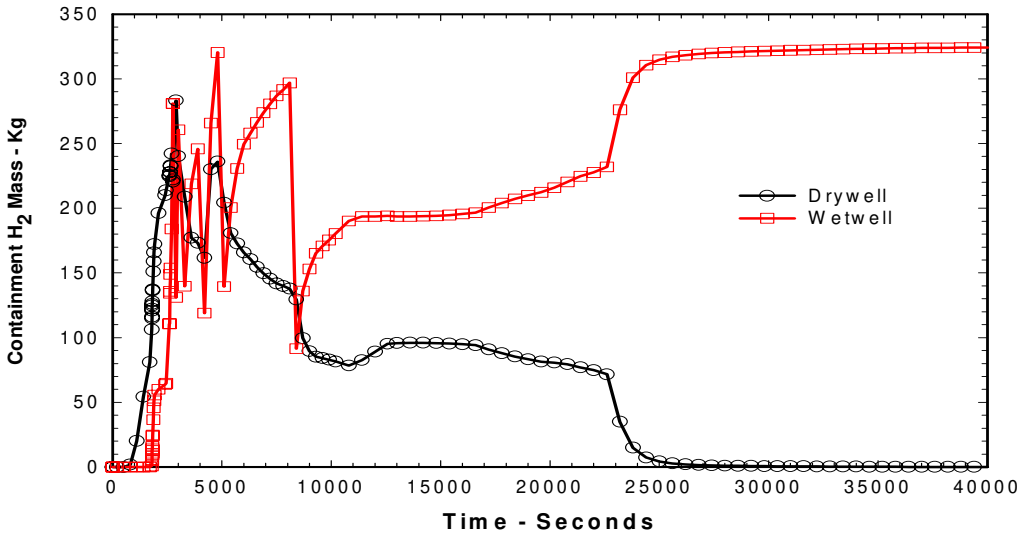

Figure 11-13. Hydrogen in Containment–Version 1.8.5 Calculation

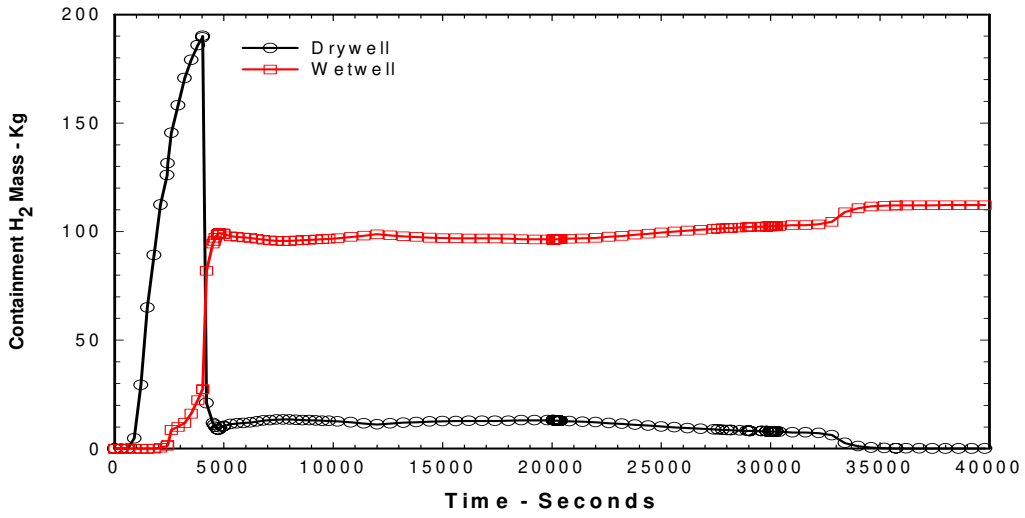

Figure 11-14. Hydrogen in Containment–Version 1.8.4 Calculation

Except for the transient effects of the hydrogen burns, the containment pressure as calculated for the two code versions was not significantly different, with the long term pressure in both cases being about 1.5 atmospheres with peak burn pressures exceeding 2.6 (1.8.4) and 3.6 (1.8.5) atmospheres. See Figure 11-15 and Figure 11-16 for the containment pressure histories. The increasing pressures after vessel head failure in both cases is due to the boil-off of the water remaining in the reactor drywell and the production of noncondensable gases from the core-concrete interaction. The peak containment pressure did not exceed the failure criterion (4.8 atm.), so that the containment remained intact in both calculations.

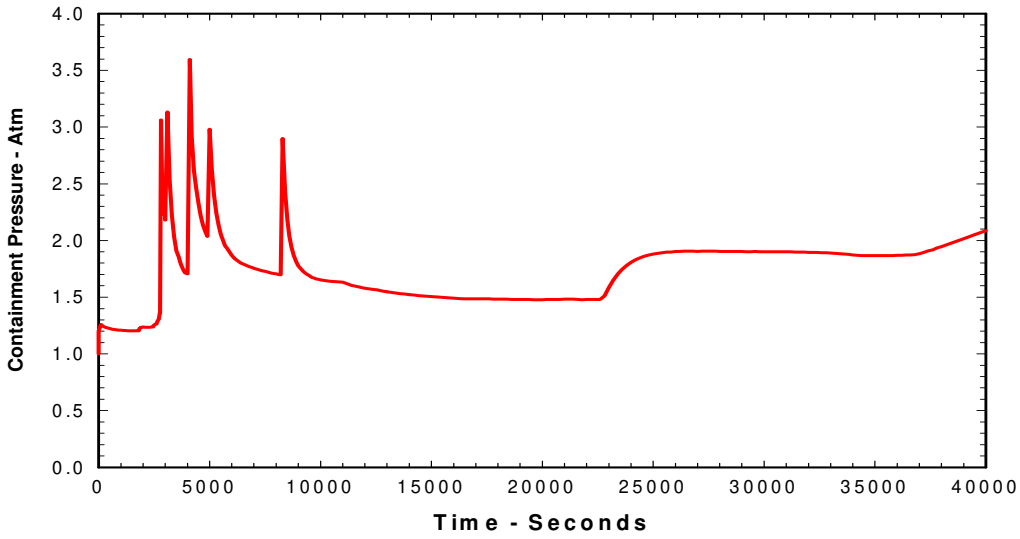

Figure 11-15. Containment Pressure–Version 1.8.5 Calculation

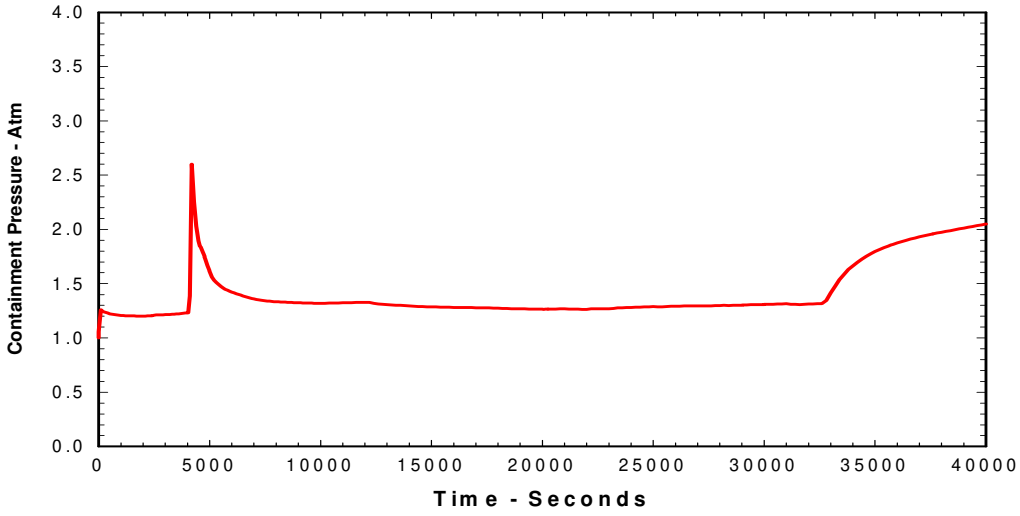

Figure 11-16. Containment Pressure–Version 1.8.4 Calculation

11.4.6 Fission Product Releases and Disposition

Extended holdup of core materials in the core region for 1.8.5 resulted in somewhat higher temperatures and longer time-at-temperature. This yielded higher predicted release rates of fission products from the fuel. Figure 11-17 and Figure 11-18 give the fractional releases of the more volatile fission products. Although the long-term releases were essentially the same (for I, Cs, Te, and Xe), nearly 100%, these fission products were released from the fuel more rapidly for the 1.8.5 calculation.

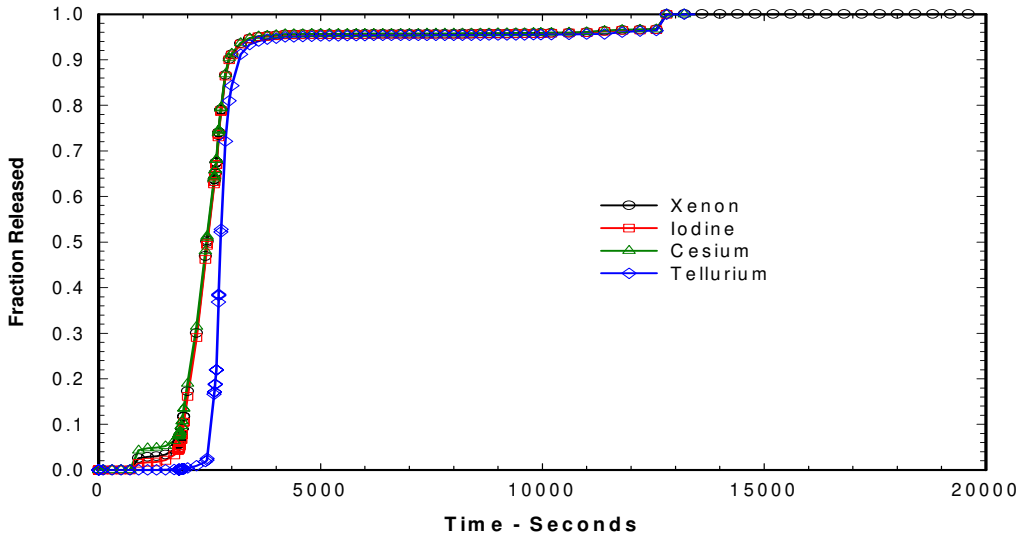

Figure 11-17 Fuel Fission Product Releases–Version 1.8.5 Calculation

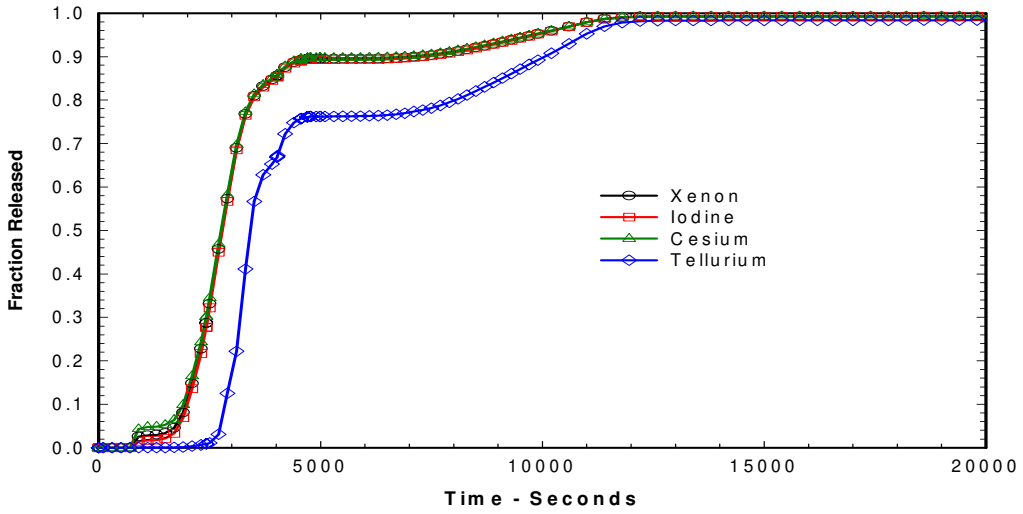

Figure 11-18. Fuel Fission Product Releases–Version 1.8.4 Calculation

Finally, in order to relate the disposition in the containment system of the fission products released from the fuel, Figure 11-19 and Figure 11-20 show the fraction of the original inventories located in the containment wetwell. These numbers include aerosol and vapor fission products in the atmosphere, pool, and deposited on heat structures in the wetwell. Higher wetwell fission product concentrations are observed in the 1.8.5 calculation. This is due likely to the higher temperatures and extended holdup of fuel in the core region, and to

the more prolonged flow of steam through the core region that carried fission products out into the containment more effectively. It should be noted, however, that most of the fission products present in the wetwell were retained in the suppression pool.

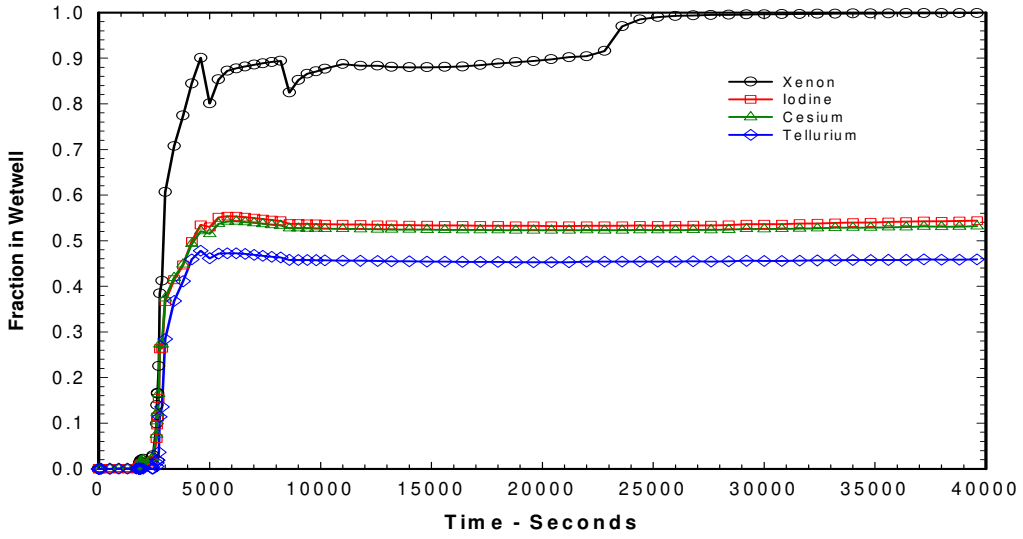

Figure 11-19. Fission Products in Containment–Version 1.8.5 Calculation

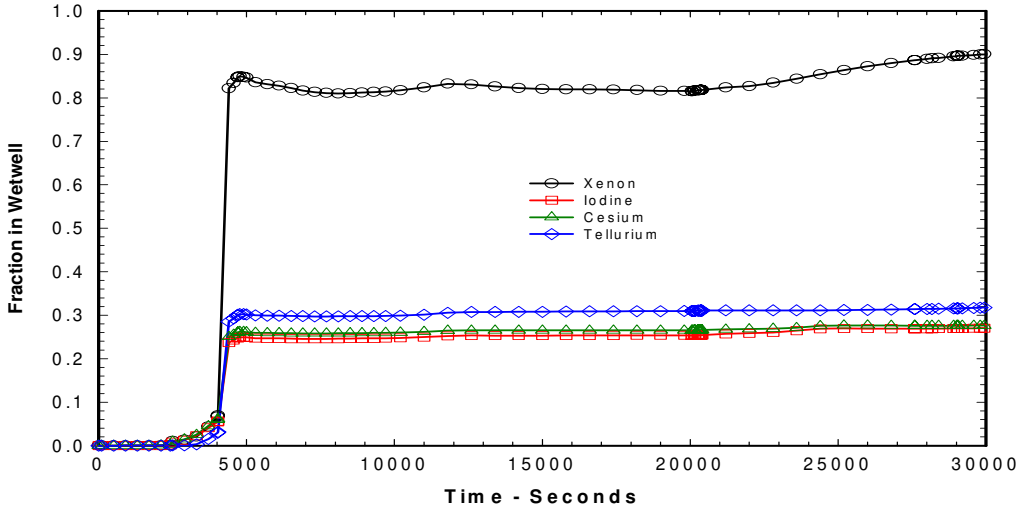

Figure 11-20. Fission Products in Containment–Version 1.8.4 Calculation

11.5 Sensitivity calculations

Subsequent to the official 1.8.5 MELCOR release, considerable experience with the new version has been acquired and the inevitable code bugs have been identified and eliminated. In addition, as part of a task for developing a consistent set of MELCOR reactor plant decks, the Grand Gulf plant model has been updated and improved. This section, therefore, has been added to update the original analysis to take advantage of the post-release version of MELCOR and the improved plant model.

11.5.1 Plant Deck Improvements and Bug Fixes

The original input model for the Grand Gulf station blackout sequence featured a very simple model of the reactor core region as described in Section 11.1.1. It included only three control volumes for the core region, one for the channel, one for the BWR flow bypass region, and one for the lower plenum. The COR models included 4 radial rings and 13 axial levels, 6 of which were fueled zones. Thus, a total of 52 COR cells occupied just 3 thermo-hydraulic control volumes. It was impossible with this model to determine the effects of local channel plugging due to relocation and refreezing of molten core materials in the lower extremities of the core region. One problem with this model was the large quantity of hydrogen produced due to the inability to prevent steam flow through plugged channels. Thus, there was a failure to cut off steam sources to metallic components. These components continued to produce hydrogen under conditions in which they would normally be steam-starved.

This problem was addressed by subdividing the core and bypass CVH control volumes into 20 separate volumes. An additional ring was added for a total of 5 rings. Other than the addition of an extra ring, the axial COR nodalization was retained, but the CVH nodalization was changed to include a set of control volumes that included 13 axial levels for each of the 5 rings. This was done for both the channel and bypass regions. Thus, there were now 4 control volumes for each ring in the fueled core region and steam flow could be detoured around plugged regions, limiting metal/water reactions in those locations. The net effect on core region CVH nodalization was an increase from 3 control volumes to 41 control volumes, and an increase from 4x13=52 to 5x13=65 COR cells.

Flow path connections were provided between adjacent control volumes in the expanded CVH nodalization scheme. For example, where there were originally 2 flow paths between the lower plenum and the core region (one to the channel and one to the bypass), there were now 10 flow paths–5 to the channel control volumes and 5 to the bypass. A similar set of flow paths connected one axial level to the next higher level in each ring. Thus, there were a total of 50 vertical flow paths into, within, and out of the core region. In addition, there were 16 new horizontal flow paths that connected bypass control volumes on the same axial level in one ring to bypass control volumes in adjacent rings. These were open continuously, of course. A second set of 20 flow paths from channel control volumes in each axial level to the adjacent bypass control volume in the same ring was added, then opened only when the canister wall at a given location had failed. Plugging in flow channels

was activated in the new model by using the FLnnnBk input in the flow path definition cards to allow the CVH/FL flow modeling to adjust flow between control volumes using input conditions from other packages.

Currently, the information used can come only from the COR package, and flow constriction through a given path can be calculated as a function of the open volume fraction in a given set of specified COR cells.

A second major change to the Grand Gulf input deck consisted of incorporating a more realistic configuration for the suppression pool. The older model used just two control volumes to model the drywell/wetwell/weir configuration characteristic of the Mark-III containment system. The seal between the wetwell and the drywell provided by the pool of water that resides between the weir wall and the drywell wall was modeled by assuming that water to be a pool within the drywell. Although this arrangement could adequately simulate the function of the suppression pool vents, it resulted in the presence of a pool in the drywell compartment. Upon vessel head failure, the ejected debris was quenched by this “pool”, thus preventing the expected debris/concrete interactions.

The problem was solved by adding a third control volume to the containment system, consisting of the weir volume. A large flow path was added to connect the weir to the drywell, and the old set of vent paths that connected the drywell to the wetwell were redefined to connect the weir to the wetwell. Thus, the drywell in the new model is actually dry, the water in the weir being confined to the weir volume. This does not mean, however, that water cannot enter the drywell from the wetwell through the weir. Despite the action of vacuum breakers, hydrogen burns in the wetwell may, for example, pressurize the wetwell fast enough to force significant quantities of water into the weir and over the weir wall into the drywell compartment.

The bugs that were fixed in the post-release version of 1.8.5 were mostly functional rather than significant with regard to code accuracy. The most troublesome bug that came to light in the application of the 1.8.5 version to the finely noded Grand Gulf sequences had to do with the disposition of decay heat from aerosols and fission-product vapor-phase components. When control volumes have been voided of solid components, such as rods, structures, and debris, the existing models simply put the decay heat into the cell atmosphere. The decay heat from this source can be significant; this, together with the limited heat capacity of steam, can result in the cell gas temperature being elevated to extremely high levels (in excess of 10,000 K). This situation is usually trapped as an unrealistically high temperature, automatically terminating the run, or it can feed into a properties function that will overrun a table, producing an error, which terminated the run.

This problem seems to have manifested itself here due to the juxtaposition of two modeling practices incorporated into the new Grand Gulf model: The fine CVH nodalization of the core region, in which an entire control volume within the core could become completely voided; and the flow path blockage model, which can result in essentially zero convective flow rates through a control volume due to plugging. With no solid material to absorb the decay heat and no convective cooling or convective flow to sweep fission-products out of

the control volume, the result can be unrealistic gas-phase temperatures. In reality, the decay heat is primarily in the form of gamma and beta radiation that are not be absorbed by the atmosphere in any case, because of low absorption cross sections of gas phase components. This energy would be absorbed on whatever surfaces it encounters along the beam path. The solution is to provide a mechanism by which the code searches for the appropriate surfaces in adjacent control volume if the source control volume is voided of material or lacks surfaces for absorption.

11.5.2 Sensitivity Case Descriptions

As part of the sensitivity studies performed with the improved plant model and the updated code version, two additional calculations have been performed and are reported here. Of particular concern was the apparent increase in hydrogen production between the 1.8.4 version and the original 1.8.5 calculation, as discussed in Section 11.4.4. (See Figure 11-11 and Figure 11-12.) In order to explore the causes of the additional hydrogen source and its apparent association with the BH model, and, in particular, the early transition to BH, the improved Grand Gulf deck was run both with BH activated and without BH activated. In the first case, the BH model input was left intact except for those BH input that were affected by the new plant models, such as the addition of a fifth radial ring. For the case without BH, the BH input was simply removed and the COR package was allowed to handle the heat-up of debris and its thermal interaction with water in the lower plenum. With one exception, all other MELCOR input parameters were identical between the two cases. The exception was a parameter that specifies the time shift on the decay heat curve, which was changed from 1700 seconds to 0 seconds. What follows is a brief discussion of the most significant aspects of the results from these two cases.

11.5.3 Results of Sensitivity Calculations

The sequence of events that occurred during the calculations for the sensitivity cases are summarized in Table 11-2 and Table 11-3. The data are divided into two separate tables because the failure modes were significantly different and for the most part could not be compared one-to-one. For example, the case with BH activated (Table 11-2) shows that the CSP failures occurred as the result of overheating the plate (PLATE-B failure mode). On the other hand, for the NO-BH case (BH inactive, Table 11-3), both the PLATE-B failure mode and the CRGT column failure mode contributed to CSP failure.

By way of explanation, the PLATE-B model consists of a horizontal, flat, edge-supported plate, which has a failure mode based either on a fixed plate temperature or a logical control function that provides a signal when a user-specified condition has been met. When this failure mechanism has been activated, only particulate debris above the plate location can relocate downward. Intact structure and rods cannot relocate. The COLUMN support model assumes that the support of overlying structures remains in place due to the presence of CRGT columns. These columns, while remaining in place, support overlying structure until a specified temperature or logical control function signals a loss of ability to

support overlying material. When such a signal is indicated, all structure or debris including intact rods lose support and are relocated downward.

Table 11-2 and Table 11-3 show that PLATE-B CSP failure in radial rings 1 through 4 occurred at comparable times between about 1800 and 2100 seconds. Thus, particulate debris in these three rings that was present on or above the CSP began moving into the lower plenum during this period for both cases. These, however, are significantly different from the failure times for the version QL and QX calculations, as seen in Table 11-1 for the inner three rings, the earlier failure times being accounted for by starting at the top of the decay heat curve. This trend to faster heat-up and more rapid accident progression due to the shift on the decay heat curve is observed in nearly all the events in the summary tables, including gap releases and CSP failure times. The vessel head failure times are comparable to the earlier calculations. Note that the new rings 1 and 2 together constitute the old ring 1, which was divided into two equal-area rings.

A key difference between the two sensitivity cases occurs in the NO-BH case. Debris that has entered the lower plenum via the PLATE-B mechanism begins heating up the CRGT columns, resulting in the columns failing starting with ring 3 at about 3000 seconds. The failure criterion was defaulted at 1273 K. Failure of the CRGTs in the COLUMN failure mode results in the remaining intact rods and structure being dumped into the lower plenum fairly early in the NO-BH case. This does not occur in the case with BH activated because BH subsumes the CRGTs and the debris, thus bypassing the COLUMN failure logic in the COR package. Instead, BH has an internal logic that sends a signal to COR when it decides that the CRGTs have failed or that the core boundary heat structure (core shroud) has overheated. In this case that signal was sent at about 12,500 seconds based on the attainment of a core shroud failure temperature of 850 K. At this user-specified temperature, the core boundary is assumed to fail and the entire core slumps into the lower plenum. Note that the failure of the shroud occurred soon after dryout of the downcomer. This resulted in gross failure of the CSP and the addition of all remaining fuel and core materials into the lower plenum. Thus, the timing of material relocation from the core into the lower plenum is somewhat different in each of the two cases.

Table 11-2 shows that the vessel head failed due to creep rupture at 18,954 seconds. BH has two mechanisms for vessel head failure: gross failure of the head by creep rupture, and failure of the welds at the vessel penetrations (CRGT and instrumentation penetrations). The criterion for vessel head failure is hard-coded in the BH model and is based on a Larson-Miller creep-rupture model. The weld failure model is also a creep rupture model based on user input failure temperatures of 1672 K for failure at 6 minutes and 1560 K for failure at 60 minutes. In the present case, the former mechanism failed the vessel head. Inspection of Table 11-3 shows that in the NO-BH calculation, the vessel head did not fail in the creep rupture mode but rather through the vessel penetration failure mode. The COR model has a Larson-Miller parameter creep-failure mode and also a simple temperature-driven penetration failure model. The failure criterion for this model was set at 1700 K in the NO-BH case, and this is the mechanism that caused vessel breach. Table 11-3 shows that the vessel was breached due to failure of CRGT tube

penetrations in ring 1 starting at about 19.084 seconds. Thus, vessel head failure occurred at approximately comparable times in the two sensitivity case.

Table 11-2. Sequence of Events for Grand Gulf Sensitivity Case with BH

Event	Time(Seconds)
Accident Initiation	0.0
ADS Actuation	33
Gap Release in Ring 1	432
Gap Release in Ring 2	433
Gap Release in Ring 3	467
Gap Release in Ring 4	612
First H_2 Burn in Weir Compartment	1229
Gap Release in Ring 5	1359
PLATE-B Failure of Ring 2 CSP	1883
PLATE-B Failure of Ring 1 CSP	1939
Initiation of BH Package	1960
PLATE-B Failure of Ring 3 CSP	1983
First H_2 Burn in Wetwell	2098
First H_2 Burn in Drywell	2102
PLATE-B Failure of Ring 4 CSP	2113
Second H_2 Burn in Wetwell	2670
Second H_2 Burn in Weir Compartment	2894
Third H_2 Burn in Weir Compartment	3371
Fourth H_2 Burn in Weir Compartment	5001
PLATE-B Failure of Ring 5 CSP	8996
Baffle Plate Fails	12,503
BH Failure of CSP in All Rings	12,503
Creep Rupture of Vessel Head	18,954
Third H_2 Burn in Wetwell	38,788
Fifth H_2 Burn in Weir Compartment	38,868
Sixth H_2 Burn in Weir Compartment	39,165
Seventh H_2 Burn in Weir Compartment	39,602
End of Calculation	40,000

Table 11-3. Sequence of Events for Grand Gulf Sensitivity Case without BH

Event	Time (Seconds)
Accident Initiation	0.0
ADS Actuation	33
Gap Release in Ring 1	429
Gap Release in Ring 2	429
Gap Release in Ring 3	466

Event	Time (Seconds)
Gap Release in Ring 4	611
First H_2 Burn in Weir Compartment	1240
Gap Release in Ring 5	1356
PLATE-B Failure of CSP in Ring 1	1820
PLATE-B Failure of CSP in Ring 3	1851
PLATE-B Failure of CSP in Ring 2	1872
COLUMN Failure of CSP in Ring 4	1908
First H2 Burn in Wetwell	1978
First H2 Burn in Drywell	1982
COLUMN Failure of CSP in Ring 3	2975
COLUMN Failure of CSP in Ring 2	3168
PLATE-B Failure of CSP in Ring 1	3905
COLUMN Failure of CSP in Ring 4	4240
COLUMN Failure of CSP in Ring 5	5073
Lower Head Penetration Failure in Ring 1	19,084
PLATE-B Failure of CSP in Ring 5	19,333
Second H2 Burn in Weir Compartment	19,333
Third H_2 Burn in Weir Compartment	19,562
Fourth H_2 Burn in Weir Compartment	19,912
Fifth H_2 Burn in Weir Compartment	20,373
Sixth H_2 Burn in Weir Compartment	20,577
Second H2 Burn in Drywell	20,589
Lower Head Penetration Failure in Ring 3	24,118
End of Calculation	40,000

To illustrate the progression of material relocation and thermal response predicted by MELCOR for the sensitivity calculations, a new technique was developed. The method uses the EDF capability to write output files in an XYZ format that can be used by many plotting packages to plot two-dimensional contour graphs at selected times during the calculated accident progression. The sequence of events associated with core heatup, melt/rubblization, and downward relocation was similar for both of the sensitivity calculations. Therefore, the results shown here are for only the NO-BH case. This case was selected because the contours can be shown for both the core and lower plenum regions. In the other case, when BH takes over the lower plenum calculations, COR output parameters for the lower plenum are lost and the corresponding BH output is not available.

The disposition of core material for the NO-BH case is shown here in Figure 11-21 to Figure 11-25. These figures show the solid volume fraction in the core and lower plenum. More accurately, it is the fraction of the total volume that is occupied by non-CVH components (core materials). Figure 11-21 represents the distribution of core materials at the beginning of the calculation prior to any relocation. Note that the bottom of the lower plenum is at an axial location of 0.0 m. The bottom of the core corresponds to the located

of the CSP, which is seen here as the horizontal 0.4 contour (5.25 m). The top of the core is at about 9.66 m (the top of active core is 9.16 m). The original solid volume fraction is about 0.33 in the core region except in the outer ring, which includes the core shroud and therefore has a volume fraction of about 0.45, similar to the volume of the CSP.

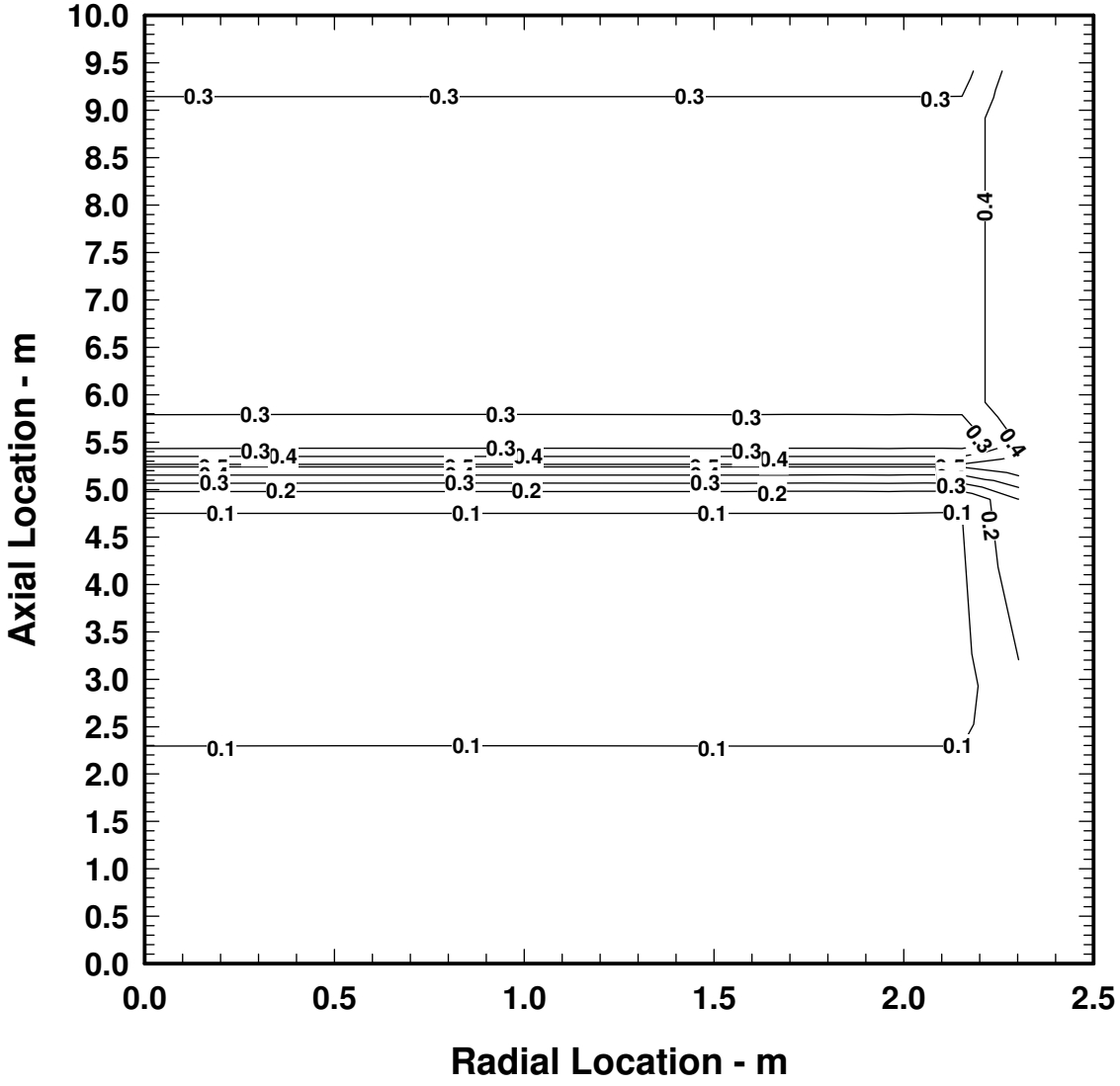

Figure 11-21. Core Material Volume Fraction at 500 Seconds

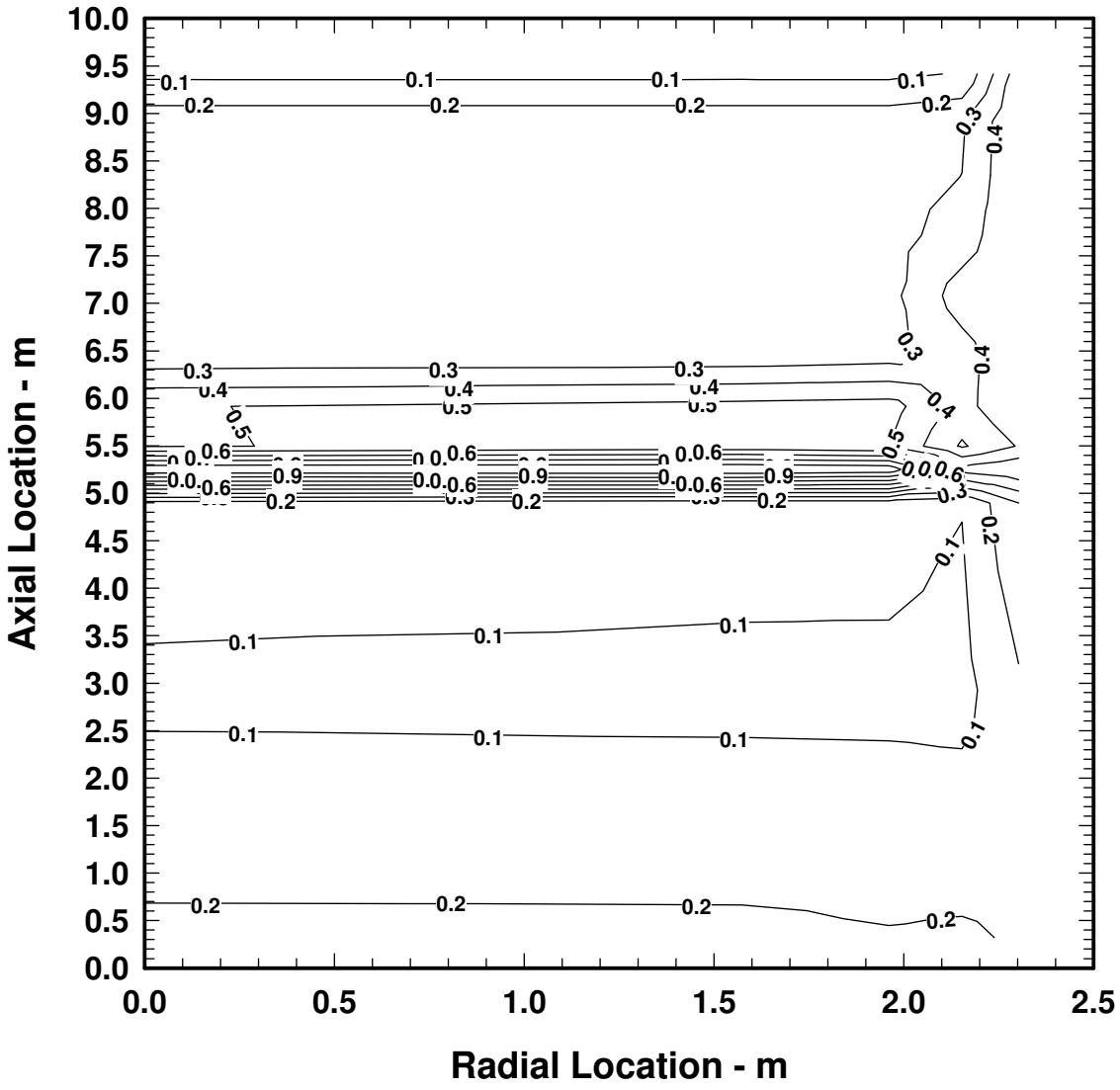

Figure 11-22. Core Material Volume Fraction at 1500 Seconds

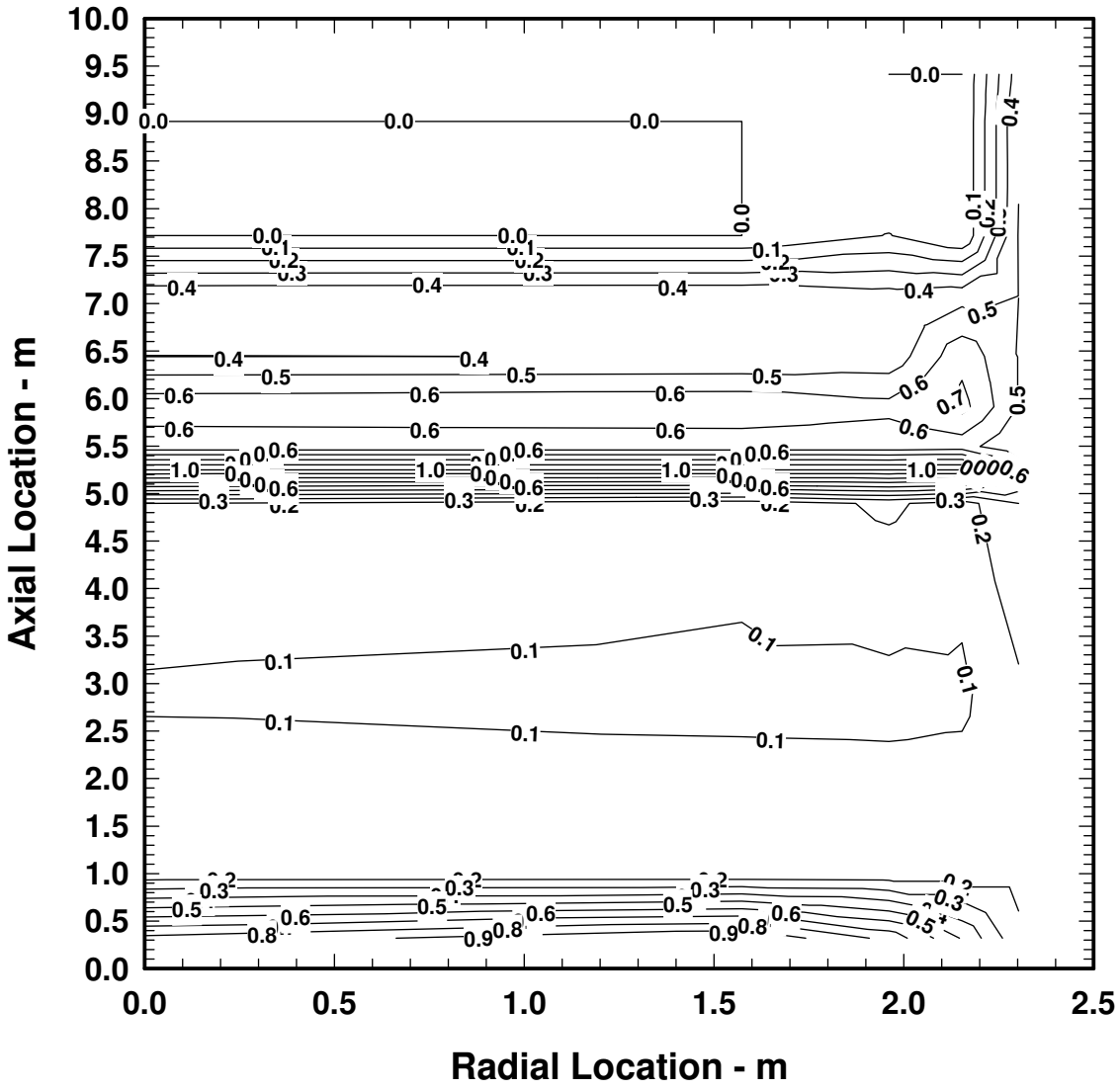

Figure 11-23. Core Material Volume Fraction at 2000 Seconds

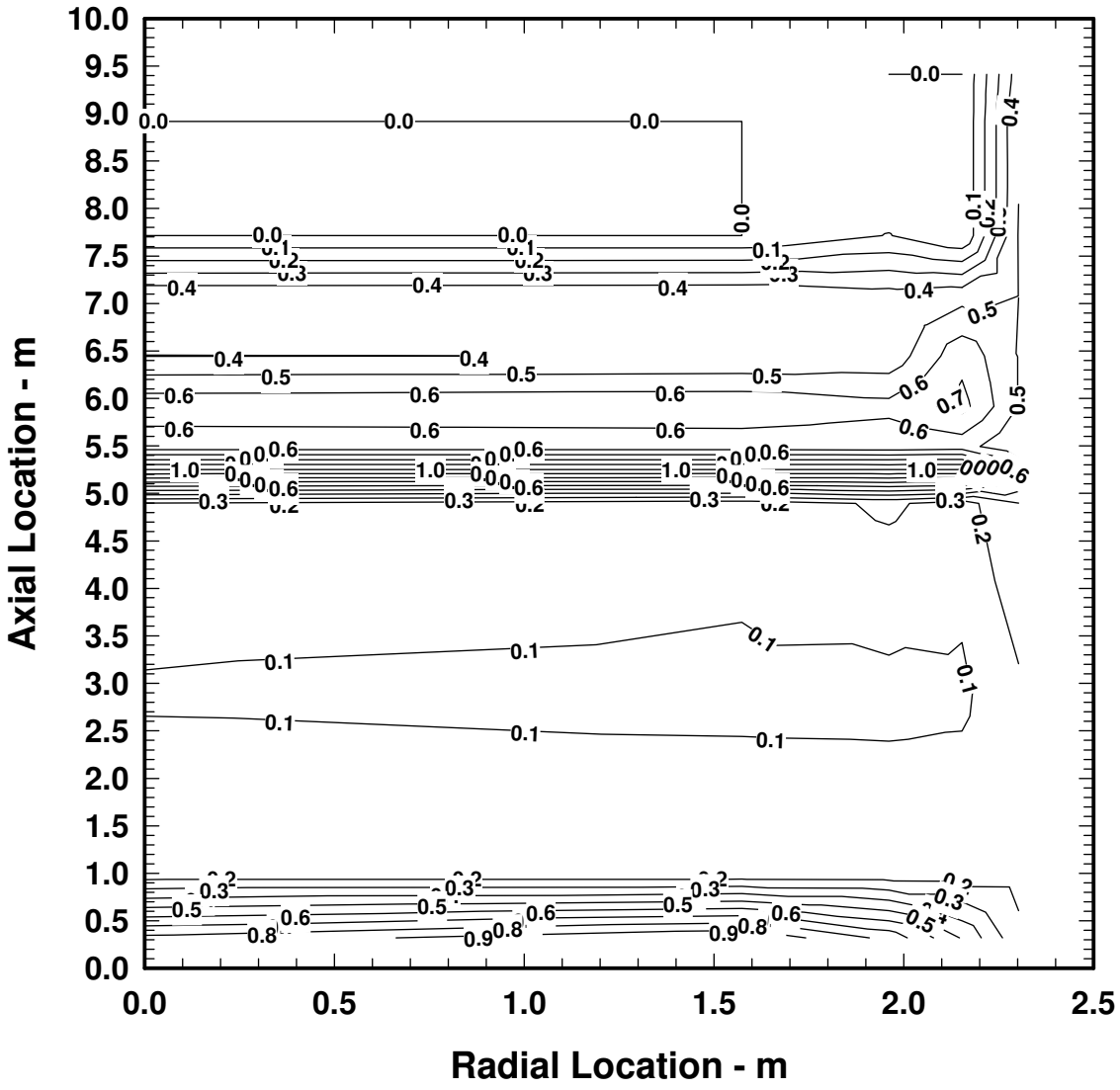

Figure 11-24. Core Material Volume Fraction at 2500 Seconds

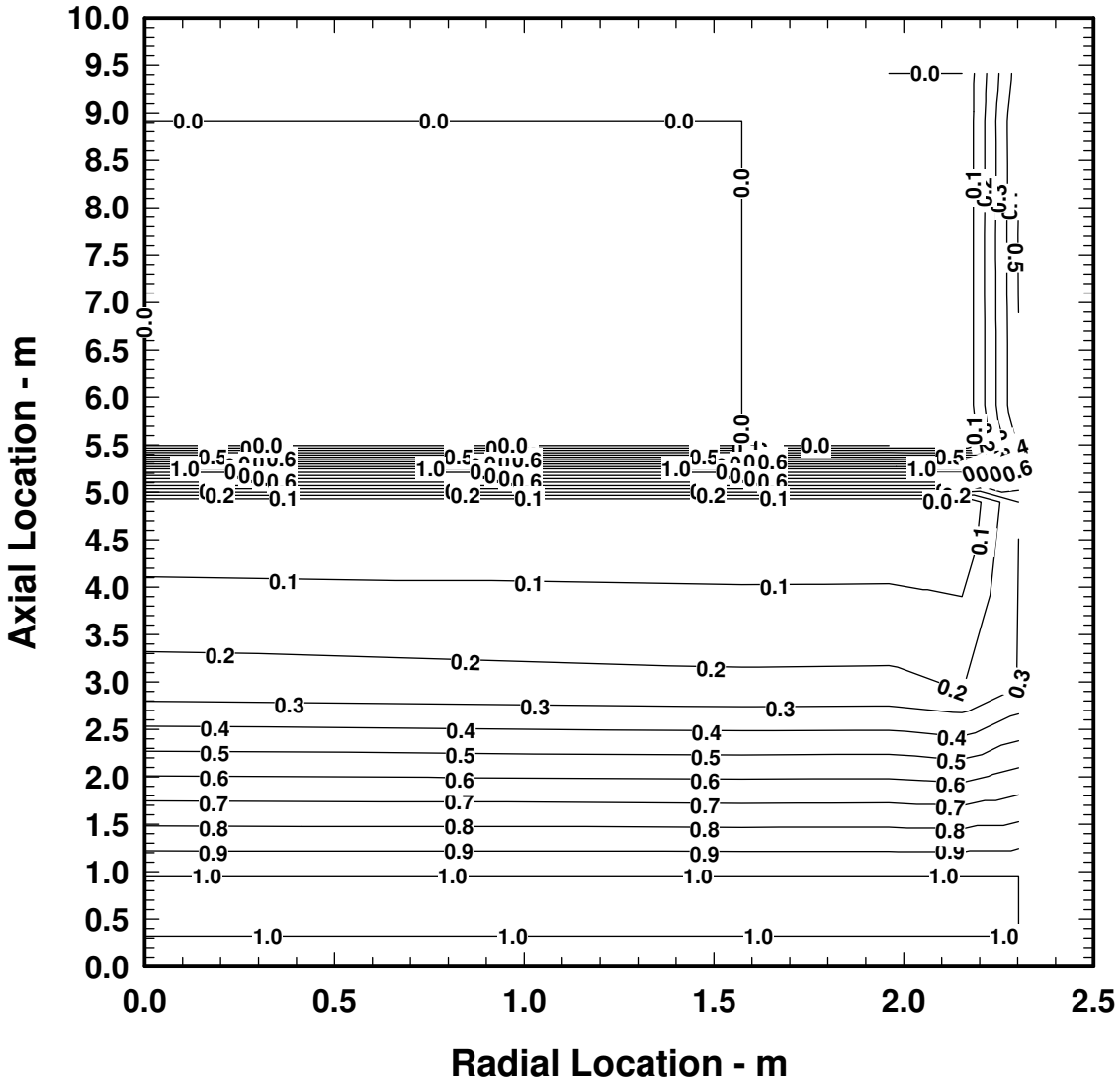

Figure 11-25. Core Material Volume Fraction at 5000 Seconds

The distribution of core material at 1500 seconds is given in Figure 11-22. This time slice is prior to CSP failure and shows incipient slumping of material from the upper half of the core into the lower half and the accumulation of resolidified metallic components in the vicinity of the CSP. Also, it is clear that some metallic components have flowed through CPS and come to rest on the lower vessel head

At 2000 seconds, just after the first CSP failure, Figure 11-23 shows that the upper third of the core region is essentially void. There is still some intact material retained above the CSP, but the particulate core material has accumulated on the lower vessel head.

At 2500 seconds (Figure 11-24), the CSP the material remaining above the CSP seems to be in about the same configuration; whereas the material on the vessel head appears to have slumped into a denser mass.

The entire core region is essentially void at 5,000 seconds, due to the COLUMN failure of all five rings beginning at 2973 seconds and finishing at 5073 seconds when ring 5 CSP failed. The COLUMN failure results in all the remaining intact components losing their support and slumping into the lower plenum. This condition is depicted in Figure 11-25.

The calculated thermal response of the core and lower plenum regions is given in Figure 11-26 to Figure 11-29. The data from which these plots were made were extracted from the COR package output through control functions that selected the maximum of all the component temperatures including fuel, structures, particulate, conglomerate, and gas phase. For example, where a region is voided, the corresponding temperature is the atmospheric temperature.

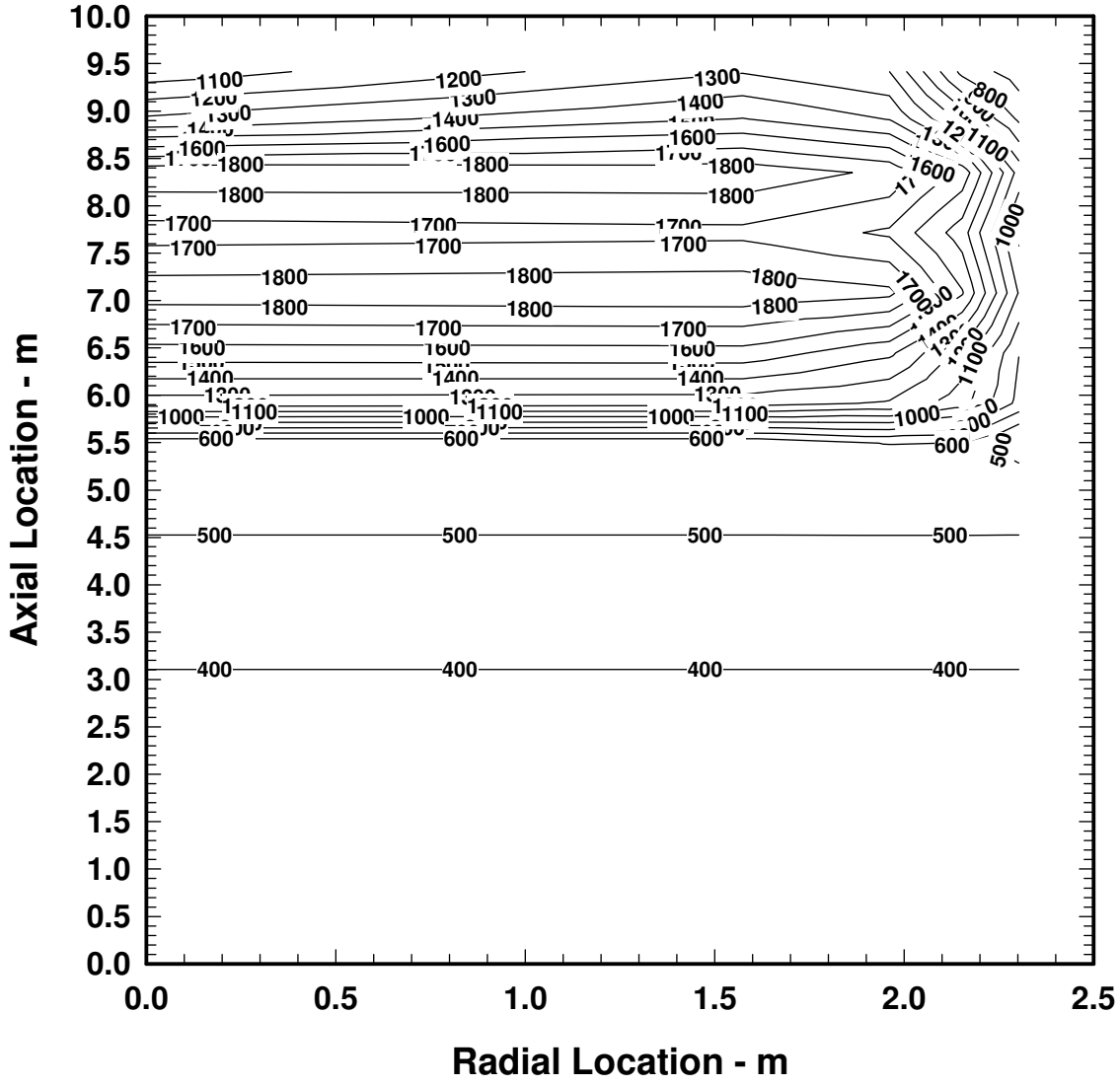

Figure 11-26. Core Temperature Profile at 1000 Seconds

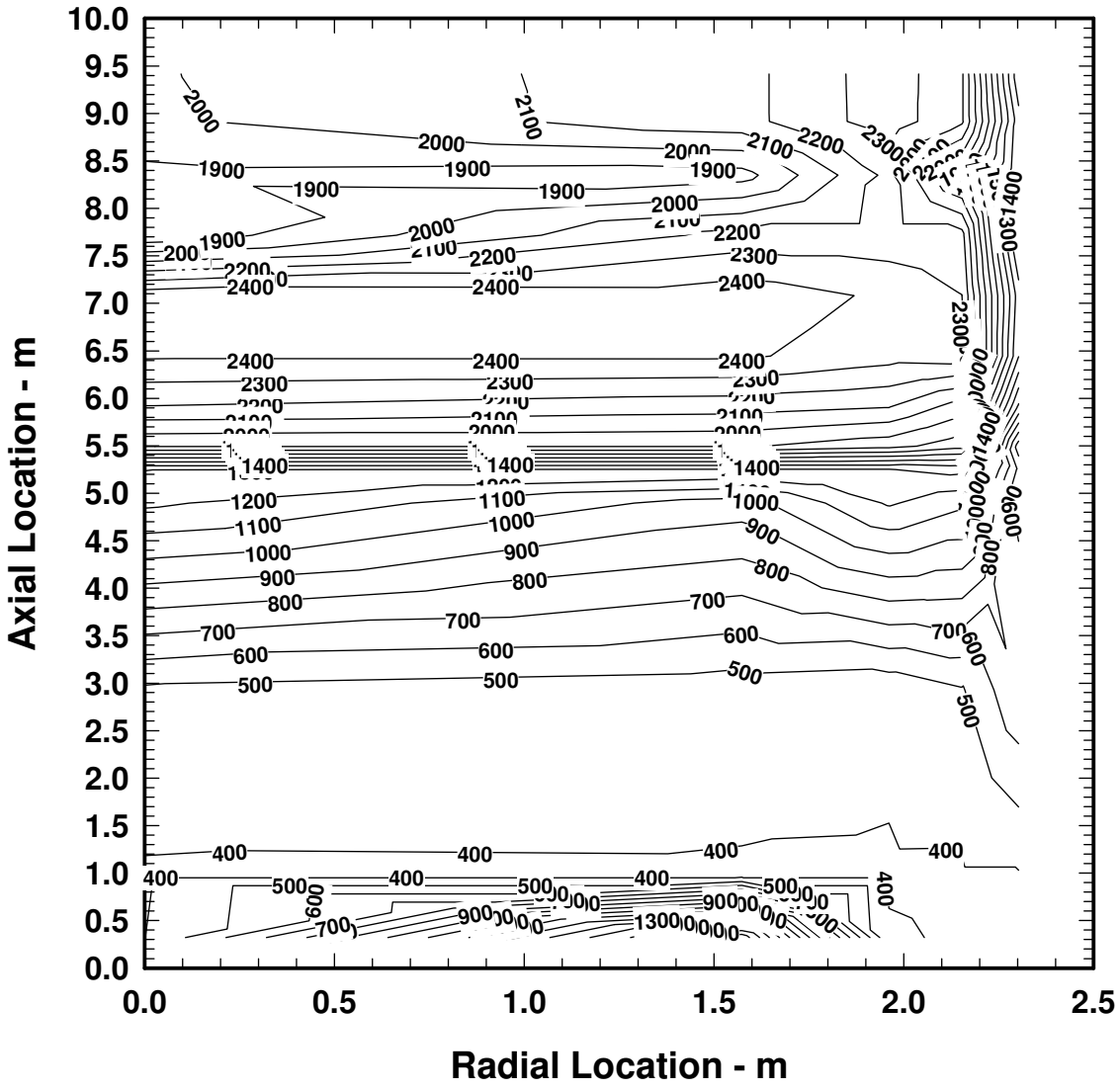

Figure 11-27. Core Temperature Profile at 1500 Seconds

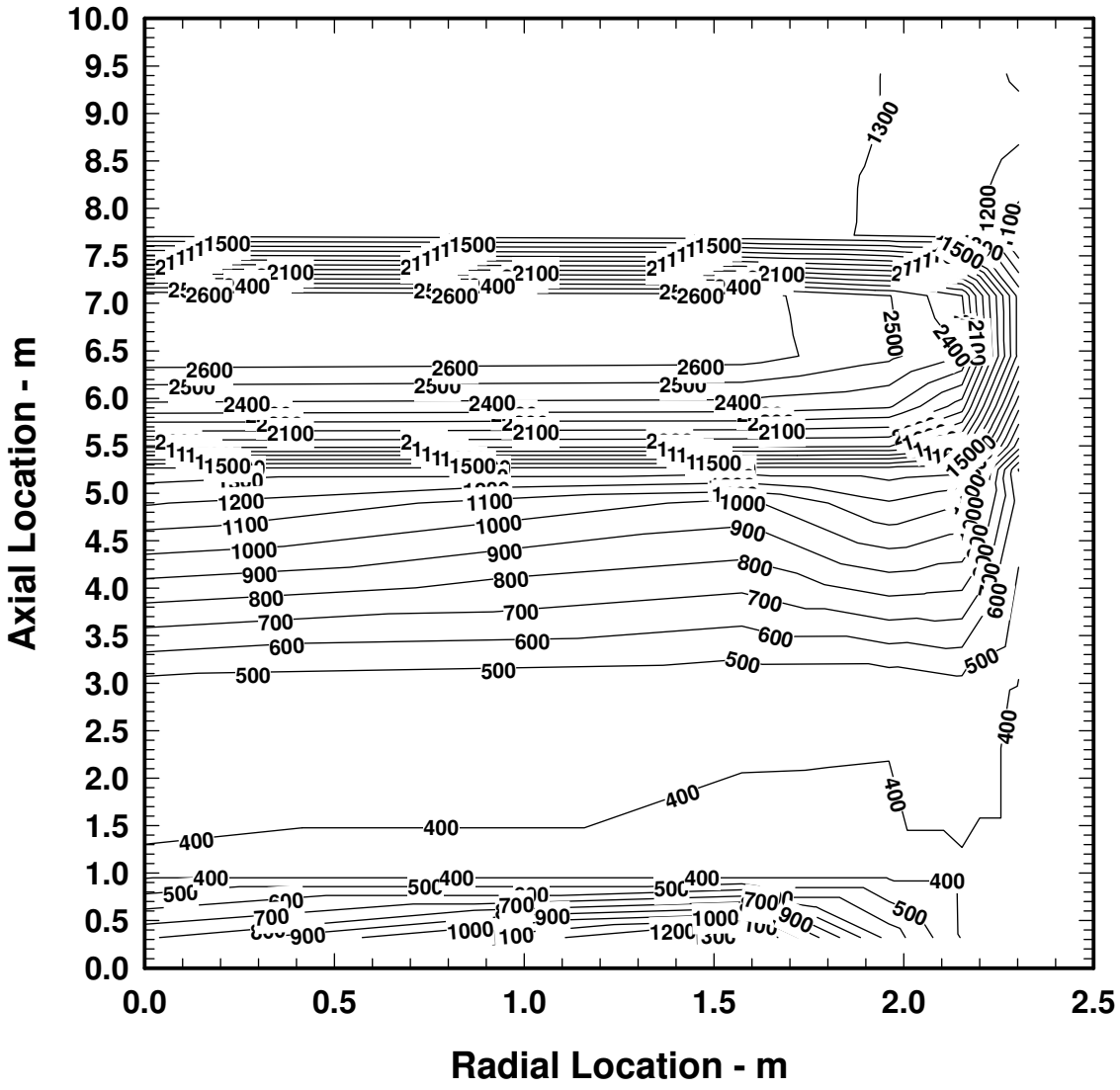

Figure 11-28. Core Temperature Profile at 2000 Seconds

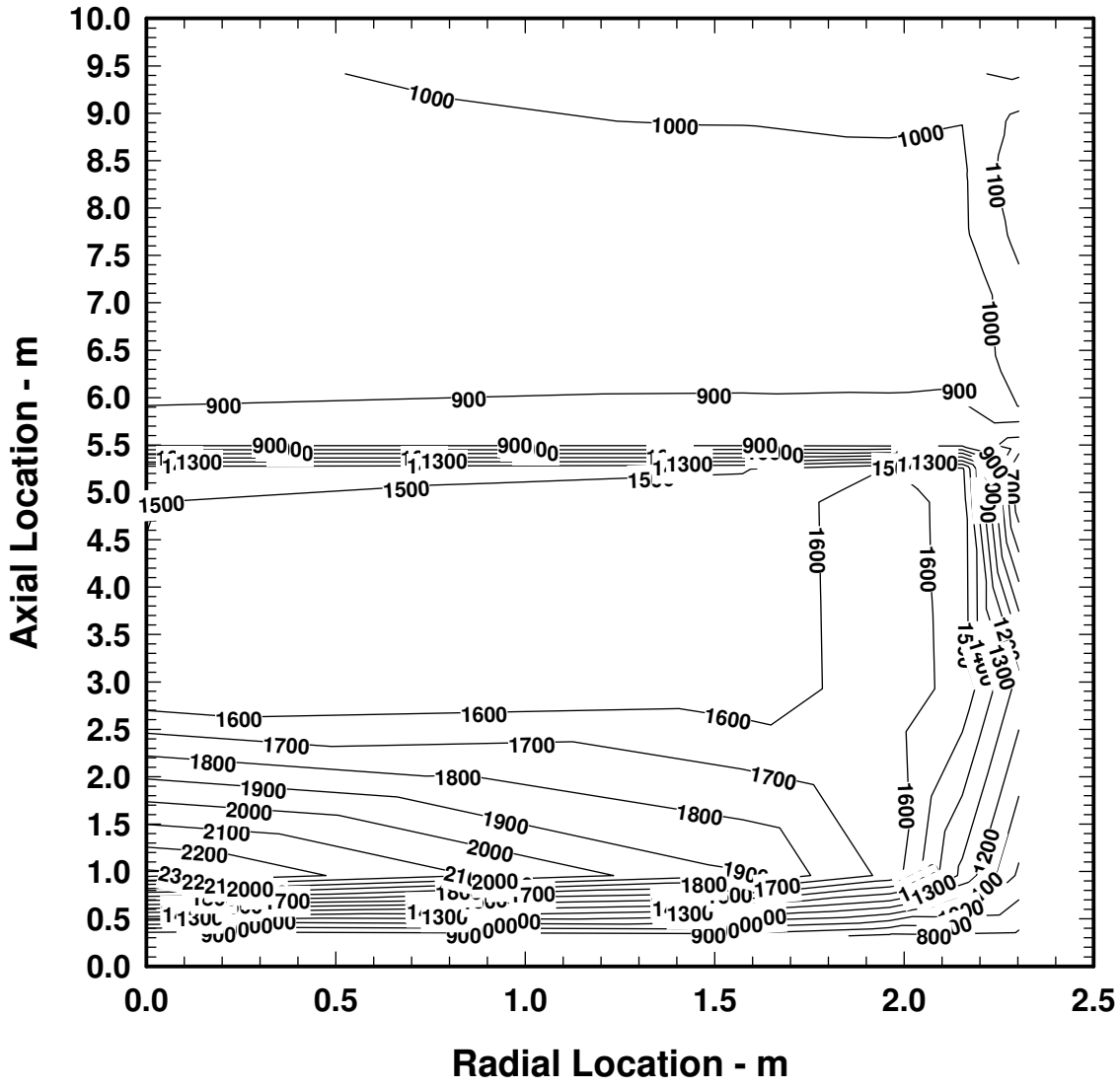

Figure 11-29. Core Temperature Profile at 5000 Seconds

Figure 11-26 shows the temperature contours at 500 seconds. The peak temperature, in excess of 1800 K, appears at about the 7-meter elevation in a core that still retains an intact fuel rod geometry.

The situation at 1500 seconds, as seen in Figure 11-27, includes peak temperatures above 2400 K but probably below the fuel failure temperature of 2500 K. A clear signature is seen, however, for the metallic components that have relocated to the vessel head (compare with Figure 11-22).

At 2000 seconds, the CSP has failed in rings 1 through 4, and the debris from those rings has relocated to the lower plenum. The temperature distribution (Figure 11-28) reflects this redistribution of core materials. The temperature peak in the core region has shifted somewhat outward radially due to the loss of core material in the inner rings and downward axially due to slumping of core material. The temperature distribution in the lower plenum is characterized by high temperatures on the vessel head decreasing from the bottom to top of the debris bed, while increasing from bottom to top of the gas space above the debris bed.

By 5000 seconds (Figure 11-29), all the core debris is in the lower plenum, but the water has not been completely boiled off and continues to cool the debris. The temperature profile in the debris bed has been inverted from the 2000-second time slice, with the coolest temperature now located next to the vessel head and increasing upward in the bed. Heatup of this debris bed ultimately leads to the boil-off of all the coolant in the lower plenum by about 7500 seconds, and to vessel head penetration failure and transfer of core debris to the reactor cavity at about 19,000 seconds.

The final graph in this section (Figure 11-30) shows a comparison of the total hydrogen produced for the 4 calculations considered in this report. Differences in hydrogen production between MELCOR 1.8.4 and the originally released version of 1.8.5, the QX version, has been viewed as problematic. As discussed in Section 11.4.4, early transition to the BH package leads to increased hydrogen production by the COR package as seen by comparing Figure 11-11 and Figure 11-12. The situation is even worse when the total hydrogen produced is shown by adding that generated by the BH package and that produced by the CAV package (core/concrete interactions). Figure 11-30 shows the total hydrogen. It is immediately obvious that the 1.8.5 QX version actually produced 1570 Kg of H_2 versus only 330 Kg in the 1.8.4 QL version of the code. As noted in 11.4.4, an extended period of coolant boil-off in the lower plenum produced about three times as much hydrogen by the COR package, but the BH itself has a metal/water reaction model that produced an additional 600 Kg.

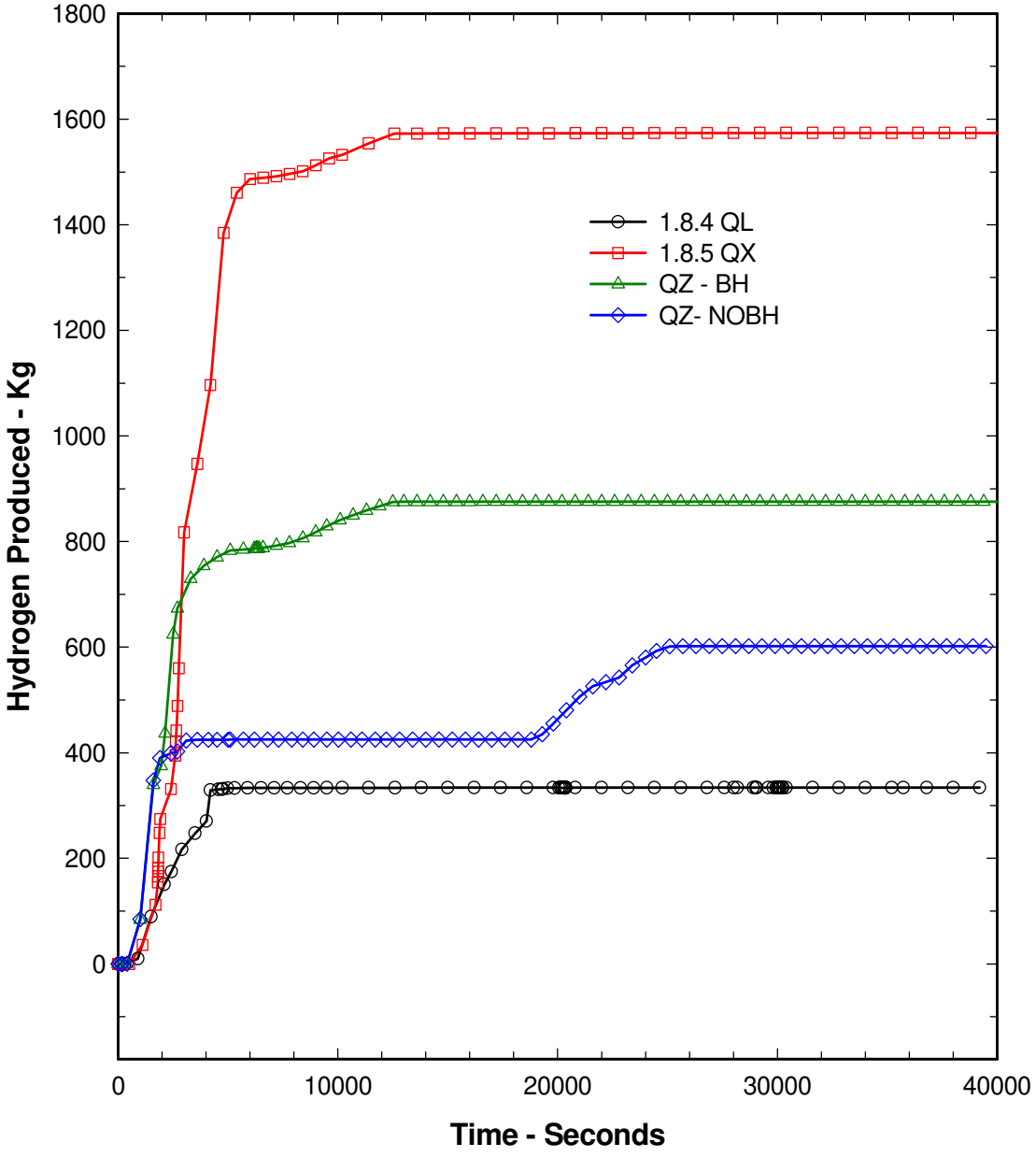

Figure 11-30 Comparison of Total H_2 Production

It was proposed that the COR package production of hydrogen was being significantly overestimated by the code because of the single control volume representation of the core and its associated inability to plug and restrict steam flow through blocked channels. The primary purpose of the two sensitivity calculations reported in this section was, first, to more finely nodalize the control volumes in the core region and to add the flow blockage model to restrict flow in blocked regions; and second, to determine hydrogen production when the COR package was allowed to perform the heatup of debris in the lower plenum

compared with the hydrogen production generated by the BH package treatment of the process.

The results of the first effect, fine nodalization and local channel blockage are seen in Figure 11-30, where it is noted that the total hydrogen was reduced from 1570 Kg in the QX case to only 870 Kg in the QZ version run with BH active. This difference can be directly attributed to denying or limiting steam access to metallic components in core zones that have been blocked or in which the flow has been significantly restricted.

The second effect, that due to differences in the COR and BH metal/water reaction models for particulate debris, is seen by comparing the last two curves in Figure 11-30. The QZ code version, run without the BH package activated (the NOBH case), generates quantities of hydrogen much more consistent with that seen in the 1.8.4 QK version of MELCOR. For this case, hydrogen was only about 100 Kg higher than the QK version until about 19,000 seconds, when the vessel head failed and the core debris was deposited in the reactor cavity. The subsequent production of hydrogen was then due to core/concrete interactions produced by the CAV package.

It is apparent that the COR metal/water reaction model produces very small quantities of hydrogen compared to the BH models. On the surface, the models appear to be similar and it may require a detailed examination to determine the differences and decide which is the more accurate. Such an assessment is nontrivial because it not only involves the differences in the way COR and BH model the metal/water reaction, but also the disposition of the debris/molten pool that forms in the lower plenum. For example, when BH takes possession of the lower plenum and its debris components, it reconfigures the bed into 3 axial levels and 3 radial zones in the lower axial level and 5 radial levels in each of the other 2 layers. What goes into these layers depends of what is in the lower plenum at the time that BH takes over. In general, the lowest level is assumed to be metallic components that candled into the lower plenum early in the sequence. There is a hierarchy in the model for depositing the remaining debris in the other two layers. Where the molten debris resides determines to some extent how available it is for oxidation. A reflood model is used in both packages, and those models determine the availability of steam at various locations in the bed.

Both packages use a parabolic diffusion limited oxidation rate model for calculating the oxidation rate. However, BH allows for the periodic sloughing and removal of the oxide layer from the metallic surface and, although it is not clear from the model description, it may commence the calculation with a zero initial oxide layer thickness. The COR package, on the other hand, calculates an oxide layer thickness from the start based on the assumption that the entire zirconium oxide inventory in the debris forms a layer on the metallic particle surfaces. This oxide layer apparently is not allowed to slough off. These differences alone, aside from the question of steam/water/metal proximity, would seem to indicate that the COR package should generate less hydrogen than the BH package.

11.6 Discussion

The comparisons presented here for the Grand Gulf LB LOCA sequence analyses using MELCOR versions 1.8.4 and 1.8.5 did not produce surprises beyond those expected, given the significant modeling changes that have been incorporated in the new version. The changes in the OS modeling were anticipated to result in the extended retention of core material in the core region, especially for BWR-type reactors in which the CRGTs are expected to continue to support the fuel assemblies even after failure of the CSP. This feature could not be properly modeled in earlier code versions. The holdup of fuel in the core was also expected to produce higher temperatures and more in-vessel fission product releases. These effects were clearly observed.

Early transition into the BH package was expected to produce earlier boil-off of coolant inventory from the lower plenum. In combination with the extended fuel holdup in the core, however, this effect was not seen. In fact, the boil-off of coolant inventory was extended far beyond that seen in version 1.8.4 due to limited core debris transfer into the lower plenum. In retrospect this is not a surprise.

Enhanced hydrogen production, more numerous hydrogen deflagrations, more rapid fission product releases, and enhanced transport of fission products into the containment building are all predictable results, given the effects that were produced by the OS and BH modeling changes. However, the increase in hydrogen production was perceived to be excessive and beyond what might be expected. Sensitivity calculations were performed and the case was made that care must be taken in nodalizing the core and lower plenum regions in order to take advantage of blockage models. When this was done, hydrogen production was reduced to more defensible quantities. An issue still remains unresolved, however, regarding the oxidation of metallic debris in the BH and COR packages. A possible future task may involve a merging of the COR and BH models to eliminate the discontinuities that currently exist between these two models. The resolution of this problem will be forthcoming.

It can be concluded that the version 1.8.5 calculation of the Grand Gulf station blackout sequence did not reveal any anomalous behavior this new version, and, in fact, produced results that were consistent with those that were anticipated, given the nature and extent of the associated modeling improvements.

12. Simulation of a Station Blackout in the Grand Gulf Plant

12.1 Background

An important element in the assessment of MELCOR 1.8.5 involves the baselining of the code against the previous version (1.8.4). The matrix of calculations for implementing this procedure includes both analyses of experiments, which may look at a limited number of phenomena, and plant calculations, which may run the entire range of phenomena associated with reactor accidents. This assessment evaluates the new version with respect to its application for the analysis of a Grand Gulf station blackout accident sequence. Thus, for this application, the key models that are exercised in these calculations include all those associated with core heatup, meltdown, relocation, clad oxidation, containment pressurization, and fission product release and transport.

In particular, the new models that most strongly affect the results are “Early Transition to the BH package”, and the improved OS treatment in the COR package. The first model provides for the transition from COR to BH in the lower plenum models as soon as sufficient core material has been relocated. This was changed from the 1.8.4 version, which required both sufficient core material and a dry lower plenum region. The new models now allow two main types of other structures: NS, which is nonsupporting structure, and SS, which is supporting structure. This modeling provides for greater flexibility in modeling the various types of structures in the core and lower plenum regions, such as support plates and CRGTs.

12.1.1 Plant Description

The Grand Gulf reactor plant is a General Electric BWR with a BWR-6 nuclear steam supply system and a Mark-III containment system. The steam supply system features a nuclear core with 800 fuel assemblies and a rated power level of 3833 MWt (designed level of 4025 MWt.) The Mark-III containment system combines the suppression pool concept with a large noninerted containment volume. The containment itself consists of a steel-lined, reinforced concrete structure.

Engineered safety features include the ECCS, the containment spray cooling system, and the ADS. The ECCS consists of a HPCS, a LPCS, and a LPCI system. The containment spray system provides containment cooling through two independent loops using the residual heat removal system pumps and heat exchangers. The ADS system uses a subset of the safety relief valves to depressurize the vessel when the core coolant level has been reduced to one-third of the core height. All of these engineered safety features are represented in the general MELCOR model; however, all of these may not be exercised in any given accident sequence. In particular, the ADS system is assumed to operate while the ECCS system remains unavailable in the current calculations.

The containment system also includes a number of hydrogen igniters at key locations in the drywell and wetwell compartments. These devices are designed to ensure that hydrogen burns are initiated at lower H_2 concentrations, thus preventing the accumulation of hydrogen at such levels as might threaten massive deflagrations or detonations. Although current regulations do not require battery backup for igniters and would not normally function without AC power, it has been assumed in these calculations that igniters are operable. The effect is that hydrogen deflagrations begin at 7% H_2 mole fraction. Without igniters, the LeChatelier burn criteria are taken as the default burn limit and would initiate burns at 10% H_2.

12.1.2 Accident Description

The station blackout sequence dominates the total risk for the Grand Gulf power plant. This sequence involves the loss of offsite power and the failure to start the diesel generators. As a consequence, power is not available to run the coolant pumps and other systems. The reactor plant is automatically scrammed under this condition, with the main steam isolation valves closing in order to isolate the primary system. Without offsite or diesel power the ECC system and the containment spray system also cannot be operated. Thus, this sequence is an unrecovered station blackout.

12.2 MELCOR Model Description

The basic MELCOR model for the GRAND GULF reactor plant was developed by ORNL and has been used widely as the best available description of the BWR-6 Mark-III reactor plant.

The control volume and flow path nodalization is depicted in Figure 12-1. The reactor vessel is modeled using six thermal-hydraulic control volumes, one each for the lower plenum, core channel, core bypass, upper plenum/separators, dome/dryers, and downcomer volumes. The volumes associated with the 2 external water recirculation loops are modeled as a single volume. The MSIV are assumed to have closed upon loss of offsite power so that the piping and equipment (turbines, condensors, pumps, etc.) associated with the primary power conversion system are not required for this sequence. The containment was simulated using two control volumes, one for the drywell, which includes the reactor cavity, and one for the wetwell, which includes the annular compartments above the suppression pool, the suppression pool, and the containment dome region. The containment, as seen in Figure 12-1, therefore, consists of the two volumes labeled Drywell CV201 and Wetwell CV301. For the purpose of tracking fission product disposition, one additional volume was included to model the environment. For this case the containment had not failed and there were no calculated releases to the environment during the 11 hours of simulation time in present calculations.

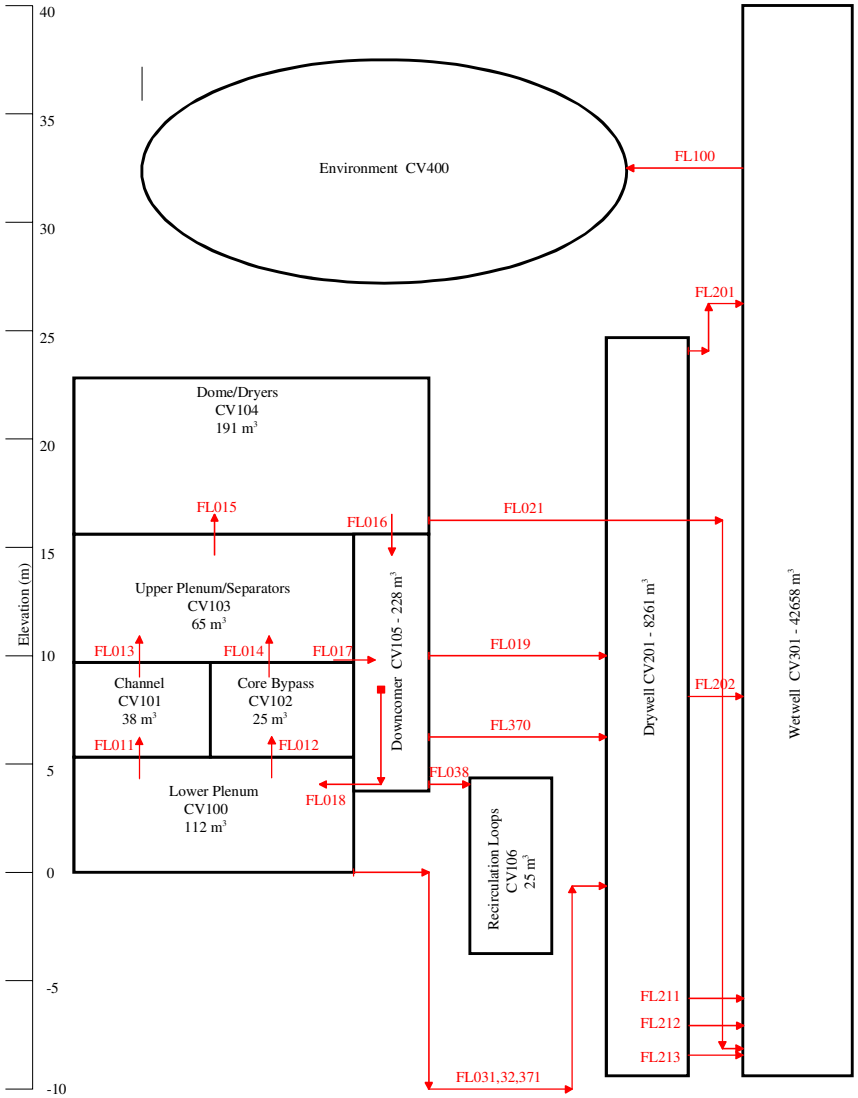

Figure 12-1. Control Volume and Flow path Nodalization

Beyond the obvious flow paths connecting the various control volumes used to model the reactor vessel, there were a number of flow paths modeled between the primary system and the containment, between the two containment volumes, and between the containment and the environment. Reactor vessel pressure control and the automatic de-pressurization system were modeled by flow path FL021. This path consists of a set of safety relief valves which have high and low set points to simulate the behavior of these valves. A subset of these valves is programmed to simulate the ADS by opening and remaining open upon a core water level reduction to one-third of normal water level. The ADS can be overridden by operator action, but the current sequence assumes that no such override occurred. This path terminates in the wetwell suppression pool.

Leakage flow paths between the reactor vessel and the containment were modeled with FL370 and FL371. Flow path FL370 was used to simulate a pump seal leak between the

downcomer and the drywell compartment. A leakage through the control rod drive penetrations was included in the model using FL371. This path connected the lower plenum volume to the drywell compartment.

Two vessel breach paths were included in the flow network. Path FL031 connected the lower plenum volume to the drywell compartment and was set to open when the COR lower head model predicted BH failure (via the COR-ABRCH parameter). A second vessel breach path was modeled (FL032), which was set to open when the BH package indicated lower vessel head failure through the BH-FFLAG flag. These paths covered the two possible timings for lower head failure, before or after transition from the COR to the BH package treatment of the molten core/vessel head interaction.

Several flow paths were included to allow for flow between the drywell and the wetwell compartments. The suppression pool vent paths that connect the drywell pool with the wetwell suppression pool were simulated using three paths, one for each level of suppression pool vents in the drywell wall outside the weir wall (flow paths FL211, FL212, and Fl213). In addition, a drywell-to-wetwell leakage path (FL202) and a vacuum breaker path (FL201) between the wetwell and the drywell were included.

Finally, a flow path connecting the wetwell atmosphere to the environment was included using a valve model that opens based on a wetwell pressure set point. The flow area for the containment failure flow path was set to an initial value of zero and opened to a cross-sectional area of 0.1 m^2 when the wetwell pressure exceeds 70 psia (487 kPa).

The core nodalization diagram for this plant is shown in Figure 12-2. The core region is divided into 4 radial rings and 13 axial levels. Levels 1 through 5 are located in the lower plenum. Level 5 represents the CSP. Level 6 consists of the lower, unfueled sections of the fuel canisters including such components as the nose pieces and tie plates. Levels 7 through 12 represent the active fuel region. Level 13 contains the upper tie plates, rod end plugs, and top guide. The region associated with the COR package model consists of three CVH control volumes, the channel, bypass, and lower plenum. The zircaloy rod cladding and canister walls, as well as control rod poisons, cruciform stainless steel control blades, and other structural materials are included in the core region material inventory.

A number of heat structures (~40) were defined in the model to simulate the various components of the reactor vessel, primary system piping, containment walls, and sundry equipment. Appendix A contains a listing of the 58M3 MELCOR input decks for both the 1.8.5 and the 1.8.4 calculations. The sections of the listings for the heat structure input provide a description and location of the heat structures for this model.

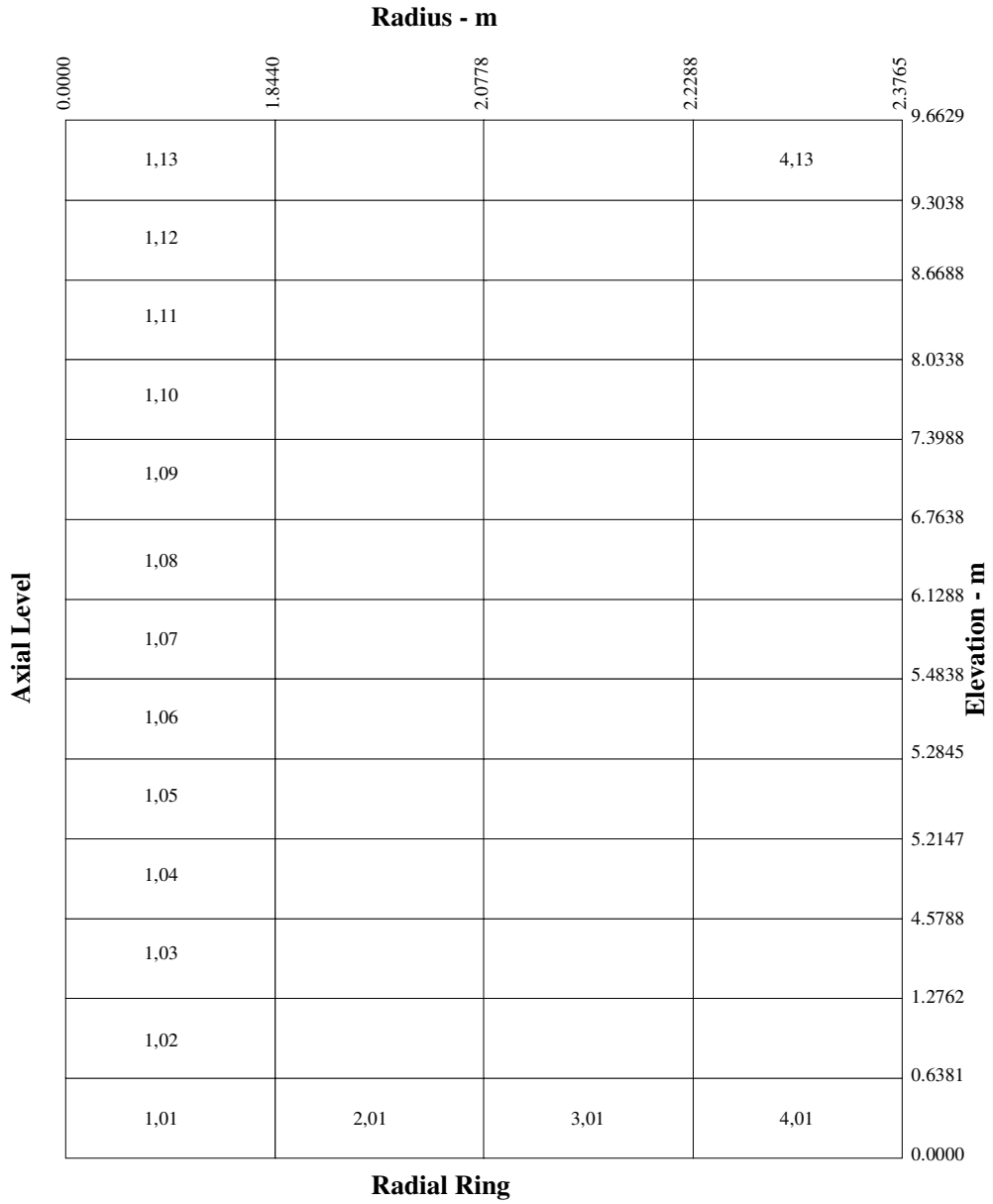

Figure 12-2. Core Nodalization

12.3 MELCOR Input Specifications

The decay heat curve used to determine whole core power was supplied by ORNL (without reference) and was applied to an operating power level of 3833 MW thermal. The fraction of full power at zero run time on this decay heat curve was 6%.

The present cases were run utilizing the CORSOR-M fission product release model corrected for the area/volume ratio. Due to problems with the chemisorption and

hygroscopic models in 1.8.4, they were not employed in that case, but were used in the 1.8.5 model.

The primary differences between the input models for version 1.8.4 and version 1.8.5 relate to the treatment of OS. The standard OS was used in the version 1.8.4 calculation while the new support models were employed in the 1.8.5 case. For example, this involved assigning the CSP in axial Level 5 to be SS, specified as a PLATEB structure with the failure criterion defined by control functions. (In this case, the CFs defined a failure temperature for each ring.) In addition, the control rod guide tubes in the lower plenum were defined as SS and specified as COLUMN support structures. Thus, the intact rods in the core region will not collapse into the lower plenum when the CSP fails. Upon CSP failure, only the particulate debris can relocate into the lower plenum in the 1.8.5 calculation. This has a significant effect on the sequence timing and progression.

The input decks for the 1.8.4 and 1.8.5 calculations currently reside on the DEC Alpha where they were run. The 1.8.5 input decks are called “ggqxtb.gen” and “ggqxtb.cor,” while the 1.8.4 decks are named “gg_5.gen” and “gg_5.cor.” A listing of these input decks is provided in Appendix A.

12.4 Results of Analysis

12.4.1 Sequence of Events

A summary of the key events for the station blackout sequence comparing the 1.8.4 and the 1.8.5 results is given in Table 12-1.

Table 12-1. Sequence of Events for the Grand Gulf Station Blackout Simulation

Event	Time (Seconds)	
	MELCOR 1.8.5	MELCOR 1.8.4
Accident Initiation	0	0
ADS Activation	1043	1177
Gap Release–Ring 1	2160	2269
Gap Release–Ring 2	2233	2340
Gap Release–Ring 3	2510	2616
Gap Release–Ring 4	3478	3611
Hydrogen Burns	3763,4703,4902, 5419,8142, 21418	5576
CSP Fails–Ring 1	4636	5718
CSP Fails–Ring 2	4658	13796
CSP Fails–Ring 3	4740	14453
CSP Fails–Ring 4	7411	14467
Lower Plenum Dryout	17,000	7930

Event	Time (Seconds)	
	MELCOR 1.8.5	MELCOR 1.8.4
BH Turned on	4709	7930
Core Shroud Fails	20,109	17586
CRGTs Fails–Ring 1	20,111	-
CRGTs Fails–Ring 2	20,111	-
CRGTs Fail–Ring 3	20,111	-
CRGTs Fail–Ring 4	20742	-
Containment Failure	21,419	No Failure
Lower Vessel Head Fails	33,184	34631
Calculation Terminated	40,000	40,000

12.4.2 Core Relocation

Examination of the data in Table 12-1 shows that until after failure of the ring 1 CSP, the 1.8.4 and 1.8.5 calculations produce fairly comparable results, with events occurring only slightly sooner for 1.8.5. The first indication of significant differences between versions is the disparity between the times for ring 2 CSP failure. This trend continued for rings 3 and 4. This is the direct result of differences between the core support parameters. Figure 12-3 shows axial disposition of fuel (particulate and intact) for the 1.8.5 calculation at 5000 seconds, after ring 3 failed in 1.8.5. Figure 12-4 shows the same information for the 1.8.4 calculation. Note that the UO_2 has moved further down toward the bottom of the core in 1.8.5 and none of the rings have failed in 1.8.4. Thus, the total UO_2 in the core in both cases is about the same. Figure 12-5 and Figure 12-6 show the situation at 10,000 seconds. Despite the failure of the CSP in all four rings, most of the fuel remains in the core for 1.8.5, while in 1.8.4, with only ring 1 CSP failed, most of the fuel has relocated into the lower plenum. For 1.8.5, then, the CRGTs in the lower plenum continued to support the core despite the loss of the CSP. The presence of so much fuel just above the plate drove the temperature very high in the lower half of the core and contributed to the earlier CSP failure time for rings 2 through 4 in 1.8.5.

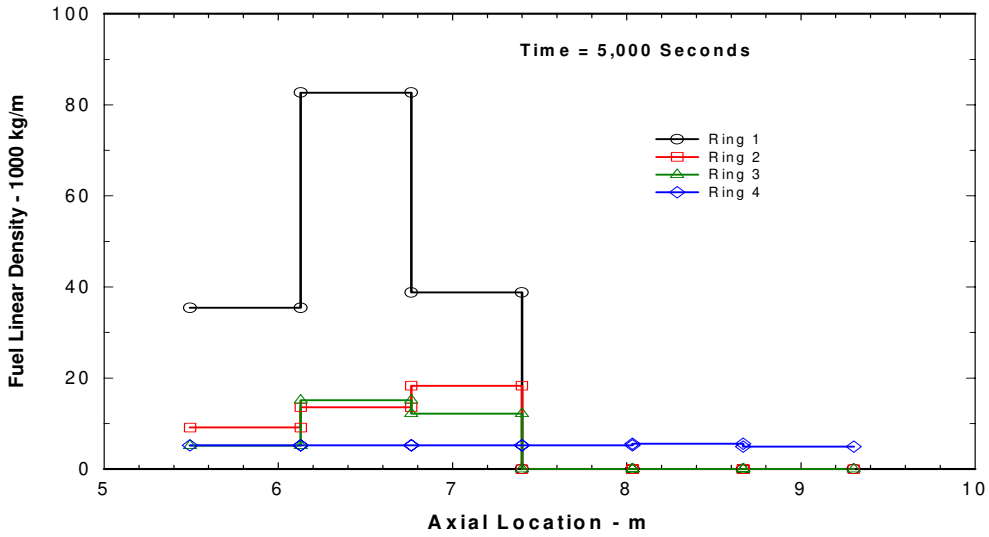

Figure 12-3. Core Material Disposition at 5000 Seconds– Version 1.8.5 Calculation

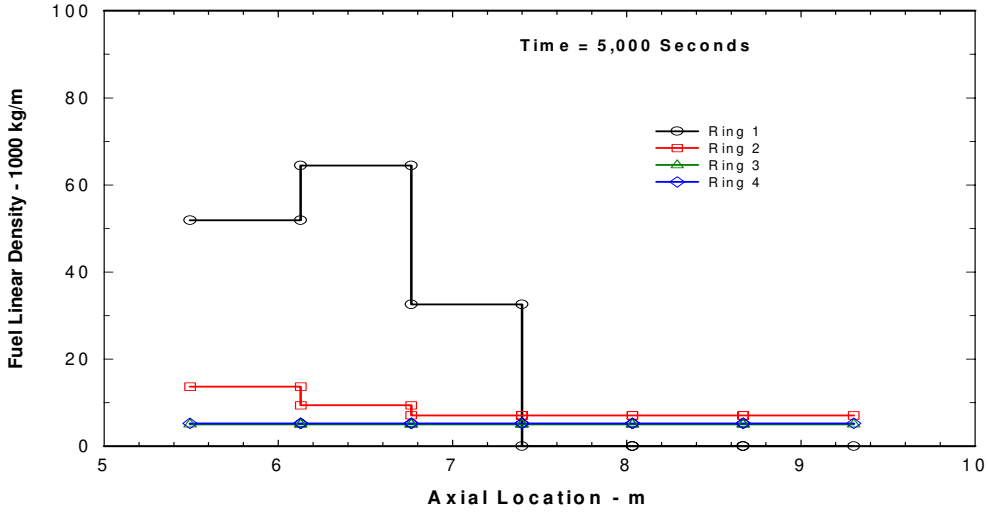

Figure 12-4. Core Material Disposition at 5000 Seconds–Version 1.8.4 Calculation

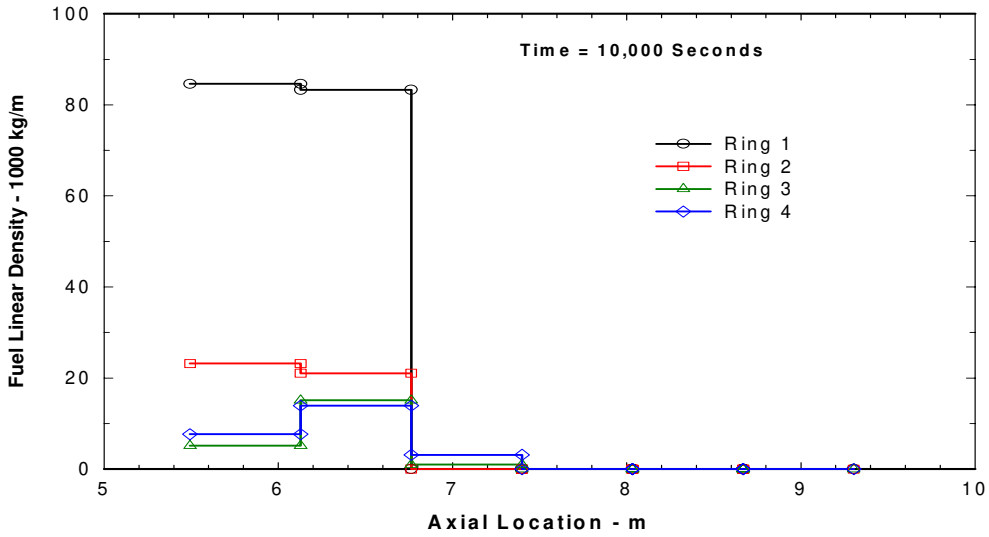

Figure 12-5. Core Material Disposition at 10,000 Seconds–Version 1.8.5 Calculation

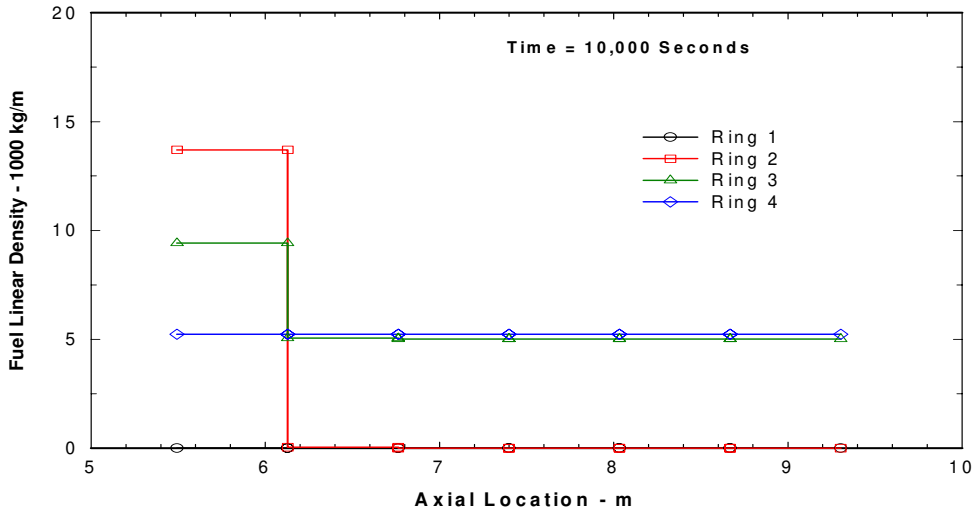

Figure 12-6. Core Material Disposition at 10,000 Seconds–Version 1.8.4 Calculation

12.4.3 Primary System Thermal Response

Temperatures in the active core region of ring 1(Levels 7 through 12) are presented in Figure 12-7 and Figure 12-8 for the version 1.8.5 and version 1.8.4 calculation, respectively. The temperatures reported here are the maximum of the fuel and debris temperatures. It is clear from these figures that the peak fuel temperature resulting from the extended holdup time in the core region for the 1.8.5 case was significantly higher than in the 1.8.4 calculation (3100 K compared to 2600 K).

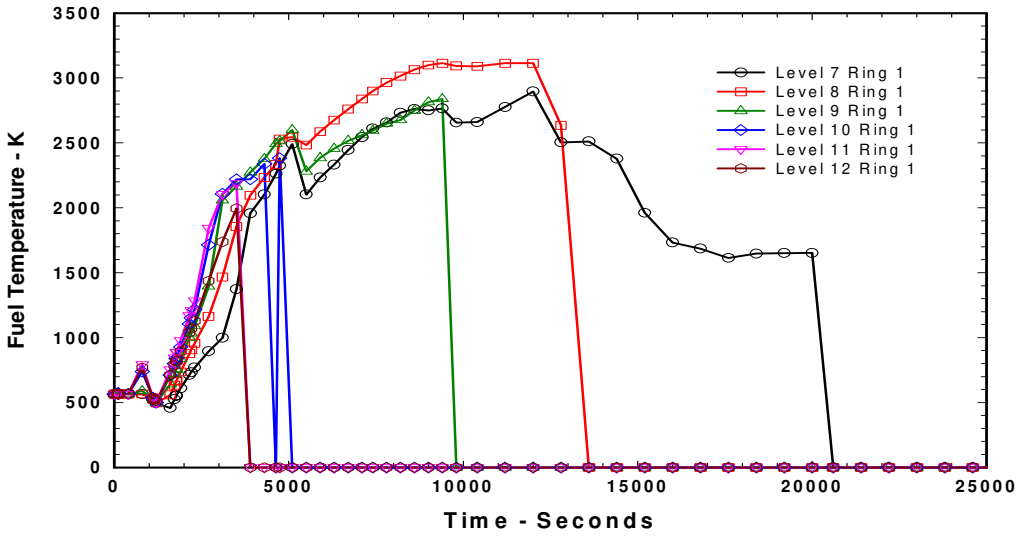

Figure 12-7. Core Fuel Temperatures–Version 1.8.5 Calculation

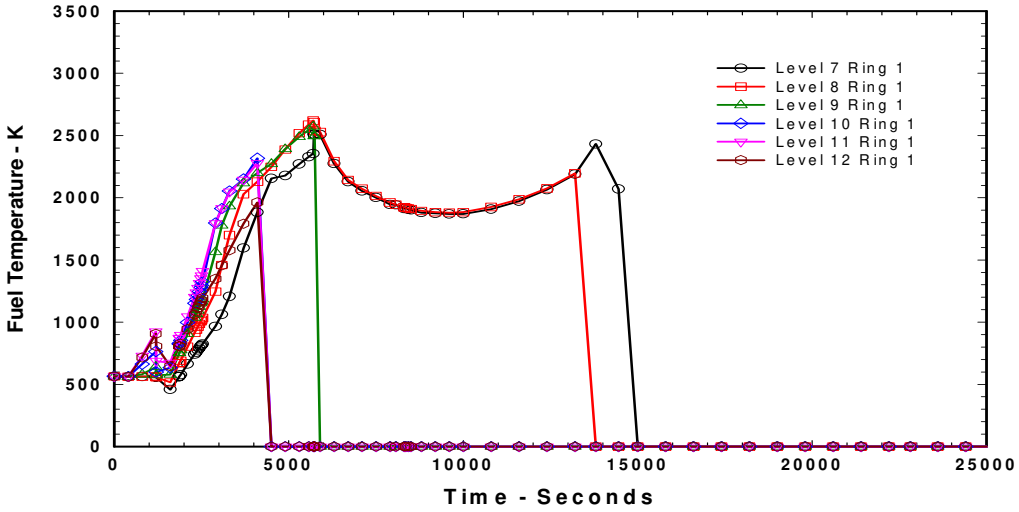

Figure 12-8. Core Fuel Temperatures–Version 1.8.4 Calculation

The effects of early transition to the BH package can be seen in the lower plenum dryout times and the time of transition to BH. The 1.8.5 case switched to BH at 4709 seconds, while 1.8.4 did not transition until 7930 seconds when the lower plenum dried out. The result was that the transition was made to BH with much smaller quantities of core debris having relocated. The effects on the water mass in the lower plenum are seen in Figure 12-9 and Figure 12-10. The transfer of significantly less fuel from the ring 1 failure in 1.8.5 resulted in less water being boiled off in the lower plenum and the retention of a significant quantity of water that did not boil off until 17,000 seconds.

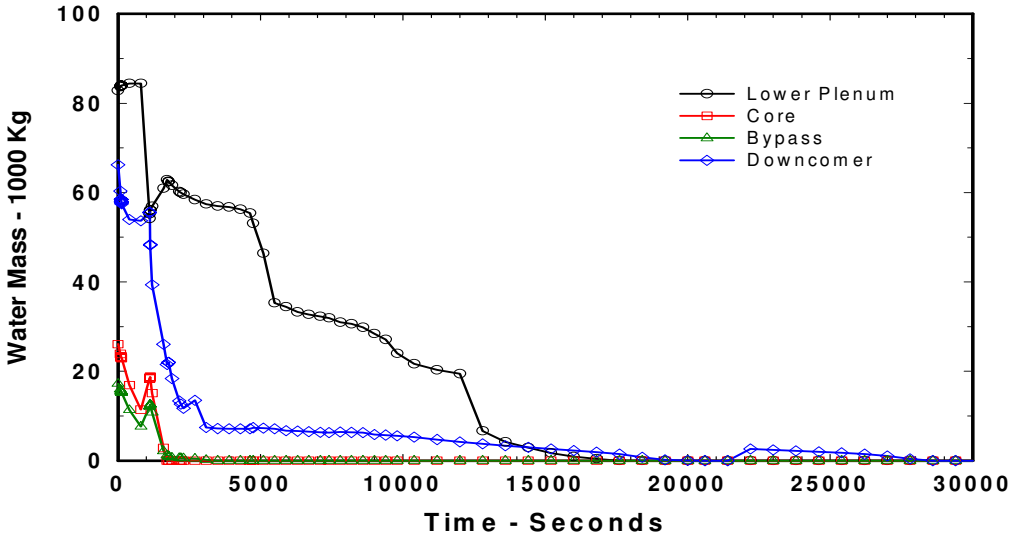

Figure 12-9. Core Coolant Inventory–Version 1.8.5 Calculation

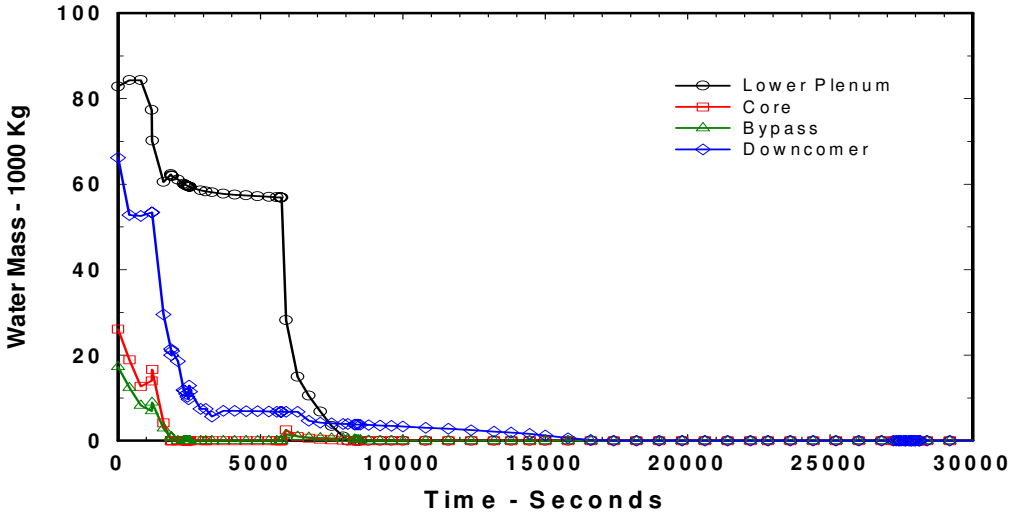

Figure 12-10. Core Coolant Inventory–Version 1.8.4 Calculation

12.4.4 Hydrogen Generation

The reduced coolant boil-off rate in the lower plenum provided a longer period of steam source for oxidation of cladding and other zircaloy in the core. This effect produced more than twice as much hydrogen in the 1.8.5 calculation. This is seen in comparing Figure 12-11 and Figure 12-12, which show the total in-core H_2 production for the 1.8.5 and 1.8.4 cases, respectively.

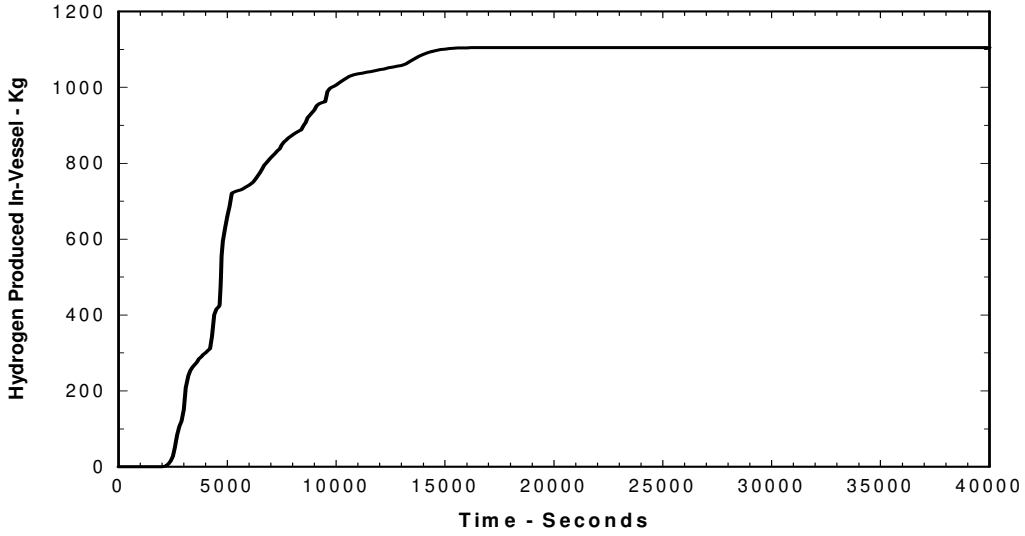

Figure 12-11. In-core Hydrogen Produced–Version 1.8.5 Calculation

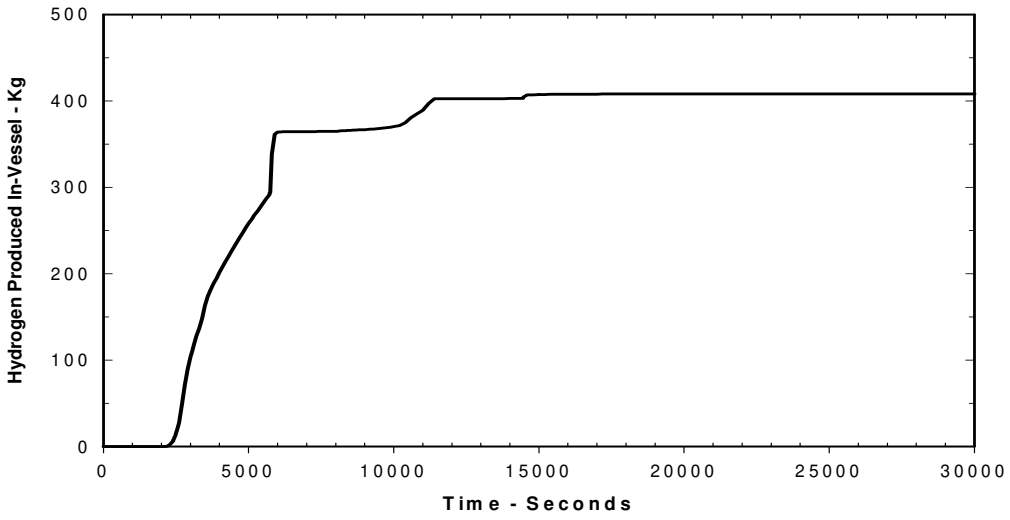

Figure 12-12. In-core Hydrogen Produced–Version 1.8.4 Calculation

12.4.5 Containment Response

Significantly larger hydrogen production, in turn, led to a number of H_2 deflagrations occurring in the wetwell in the 1.8.5 case, whereas only a single burn occurred in the 1.8.4 calculation. Figure 12-13 and Figure 12-14 show the wetwell H_2 masses for the two calculations and reveal the effects of the H_2 deflagrations. The large mass of hydrogen that accumulated in the wetwell after about 10,000 seconds represents over 15% hydrogen, but it did not burn immediately because the earlier burn events depleted the oxygen concentration below the 5% burn limit. The large deflagration at 21,500 seconds occurred when the O_2 concentration again exceeded 5%, mostly due to steam condensation and some transfer of O_2 from the drywell.

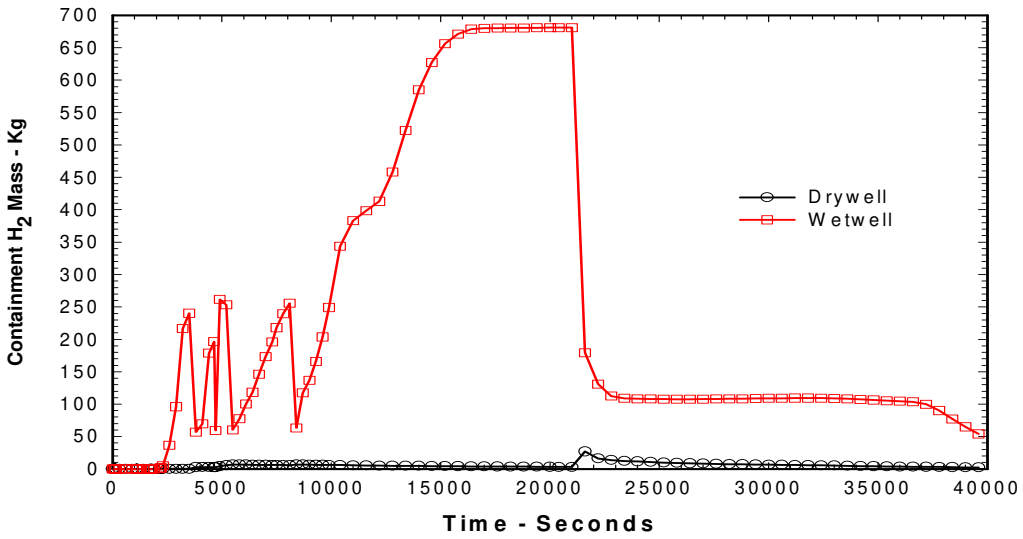

Figure 12-13. Hydrogen in Containment–Version 1.8.5 Calculation

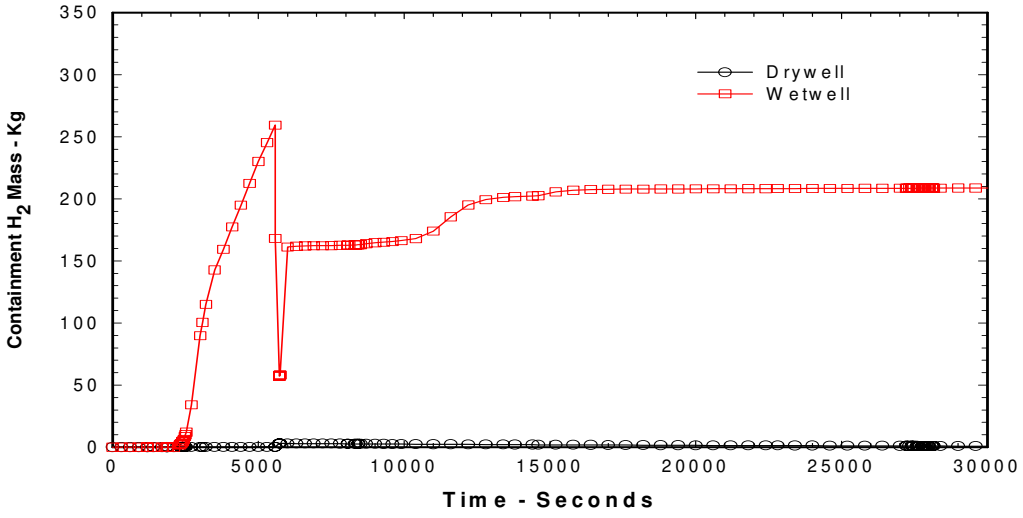

Figure 12-14. Hydrogen in Containment–Version 1.8.4 Calculation

The containment pressure calculated for the two code versions was not significantly different, except for the transient effects of the hydrogen burns, with the long term pressure in both cases being about 1.5 atmospheres with peak burn pressures of above 3.0 (1.8.4) and 3.5 atmospheres (1.8.5). See Figure 12-15 and Figure 12-16 for the containment pressure histories. Containment pressure for the 1.8.5 case exceeded the failure criterion (4.8 atms) during the hydrogen deflagration at 21,500 seconds. Much lower hydrogen production in the 1.8.4 calculation did not yield a peak pressure above the failure criterion and, consequently, no containment failure event took place for that calculation.

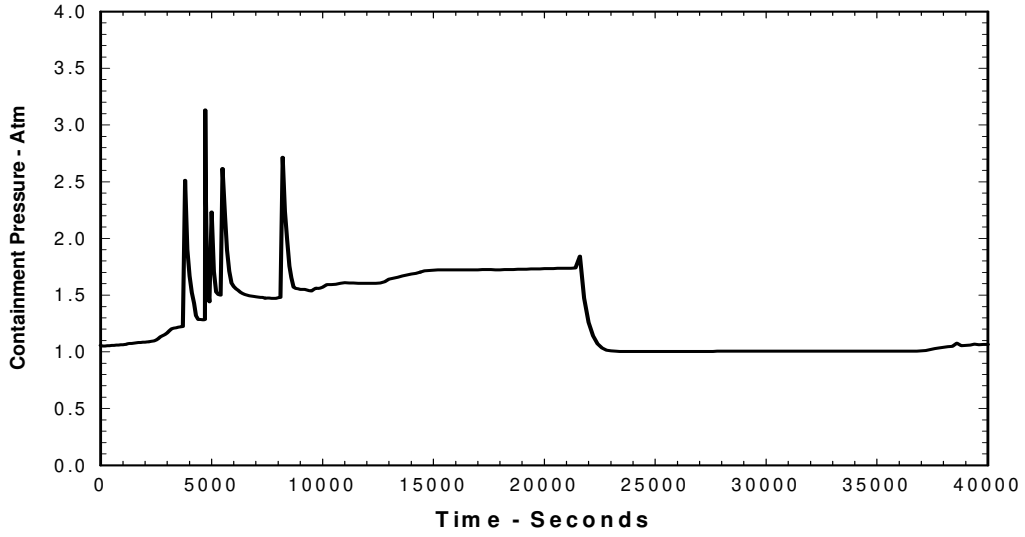

Figure 12-15. Containment Pressure–Version 1.8.5 Calculation

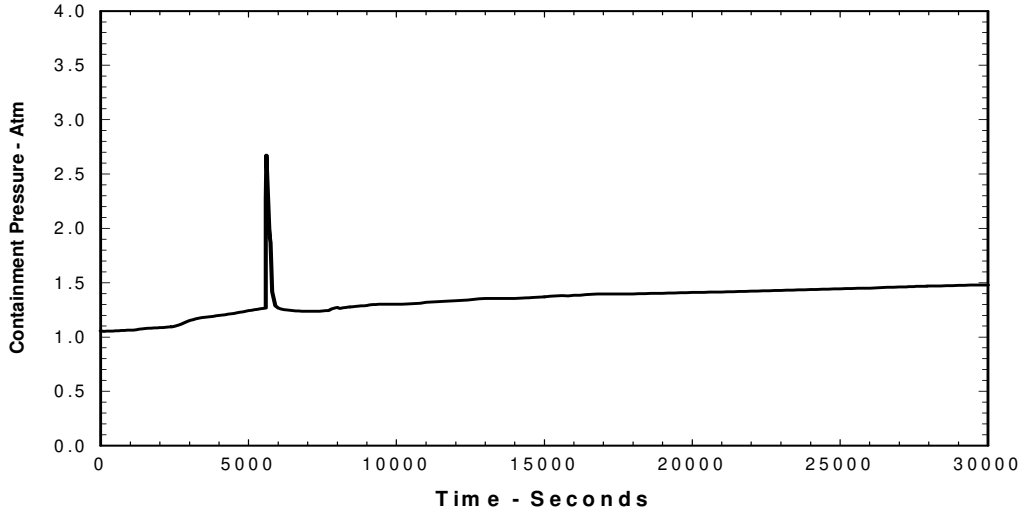

Figure 12-16. Containment Pressure–Version 1.8.4 Calculation

12.4.6 Fission Product Releases and Disposition

Extended holdup of core materials in the core region for 1.8.5 resulted in somewhat higher temperature and longer time-at-temperature. This yielded higher predicted release rates of fission products from the fuel. Figure 12-17 and Figure 12-18 give the fractional releases of the more volatile fission products. Although the long-term releases were essentially the same at nearly 100% of Xe, I, Cs, Te, these fission products were released from the fuel earlier for the 1.8.5 calculation.

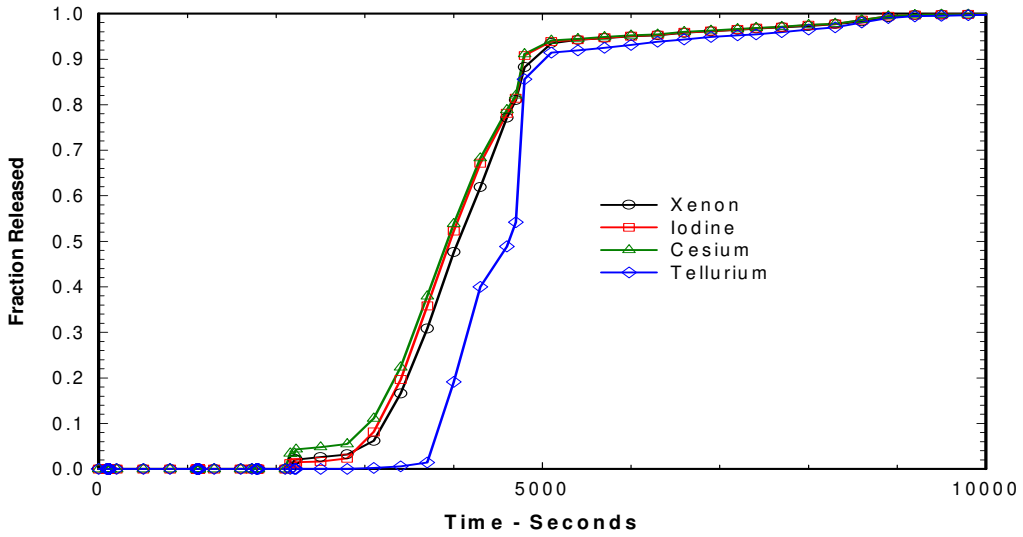

Figure 12-17. Fuel Fission Product Releases–Version 1.8.5 Calculation

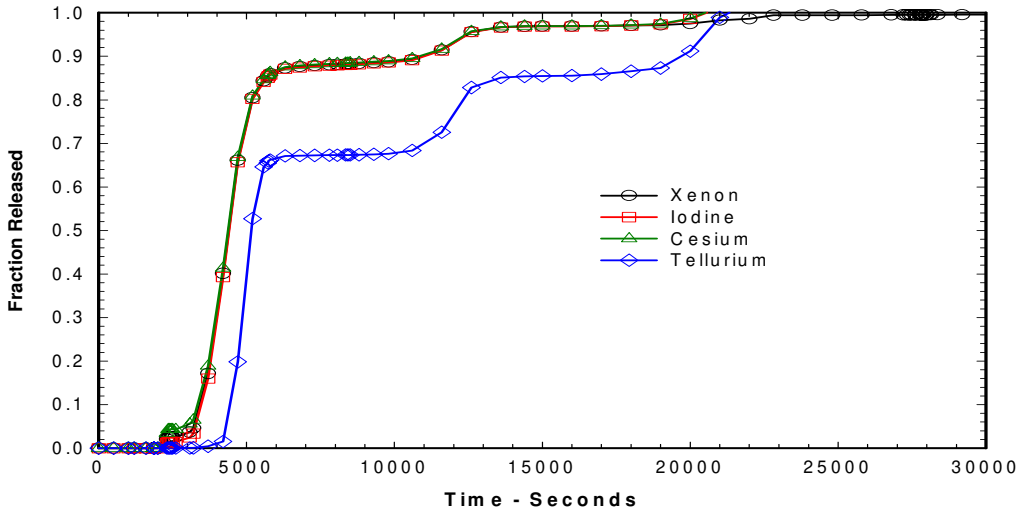

Figure 12-18. Fuel Fission Product Releases–Version 1.8.4 Calculation

In order to relate the disposition in the containment system of the fission products released from the fuel, Figure 12-19 and Figure 12-20 show the fraction of the original inventories located in the containment wetwell. These numbers include fission products in aerosol and vapor form in the atmosphere, pool, and deposited on heat structures in the wetwell. Higher fission product concentrations in the wetwell are observed in the 1.8.5 calculation. This likely is due to the higher temperatures and extended holdup of fuel in the core region and to the more prolonged flow of steam through the core region that carried fission products out into the containment more effectively. It is worth noting, however, that most of the fission product inventory present in the wetwell was retained in the suppression pool and, except for the noble gas Xe, did not experience a large reduction when the containment failed at 21,500 seconds.

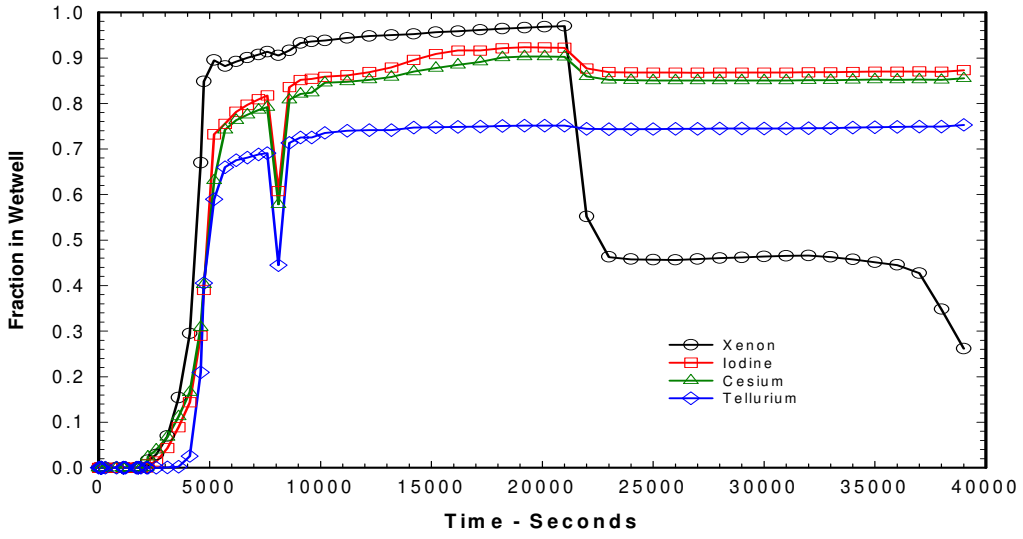

Figure 12-19. Fission Products in Containment–Version 1.8.5 Calculation

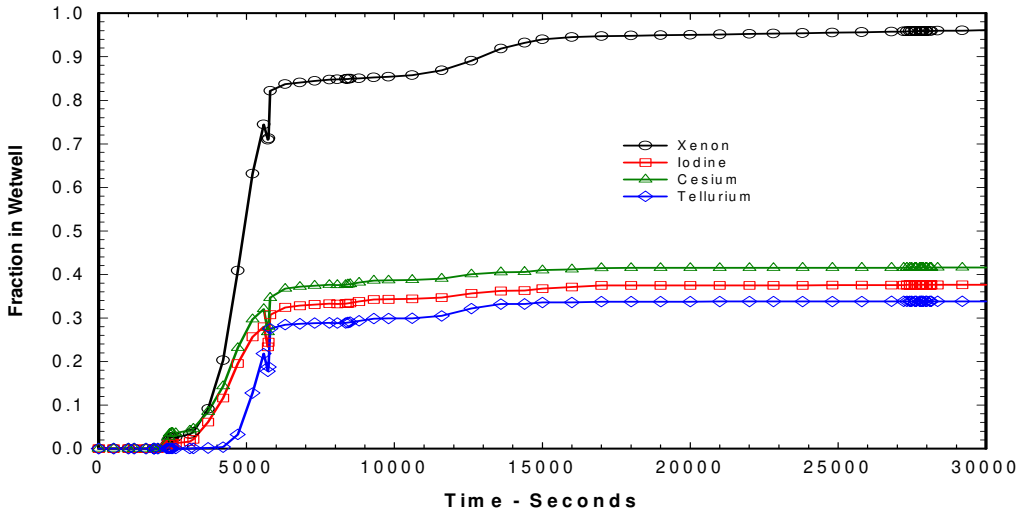

Figure 12-20. Fission Products in Containment–Version 1.8.4 Calculation

Releases to the environment for the 1.8.5 case are shown in Figure 12-21. At the end of the calculation (40,000 seconds) total releases into the environment of iodine and cesium were about 4.5%, while tellurium was 0.7% and Xenon was nearly 80%. Without containment failure in the 1.8.4 calculation and in the absence of an assumed leakage path, there were no calculated releases to the environment for the 1.8.4 case.

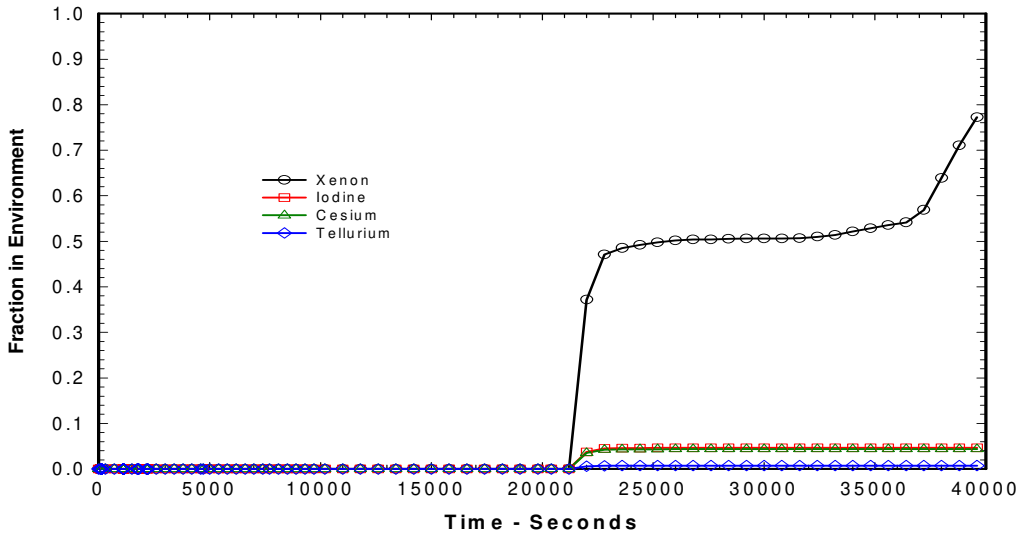

Figure 12-21. Fission Products Released into Environment–Version 1.8.5

A sensitivity calculation was also performed as part of this analysis in which it was assumed that the igniter system was lost along with loss of AC power. There were some changes in the timing of certain events, but the key difference was that the containment did not fail for the case without igniters. In that case, burns that occurred early in the sequence took place at 10% H_2 concentration, and, as in the igniter case, did not fail containment in the early part of the sequence, but did burn off a larger quantity of oxygen. The result was that insufficient O_2 was available to produce the late H_2 burn that failed containment in the igniter case.

12.5 Sensitivity Studies

Subsequent to the official 1.8.5 MELCOR release, considerable experience with the new version has been acquired and several codeing bugs have been identified and eliminated. In addition, as part of a task for developing a consistent set of MELCOR reactor plant decks, the Grand Gulf plant model has been updated and improved. This section, therefore, has been added to update the original analysis to take advantage of the post-release version of MELCOR and the improved plant model.

12.5.1 Plant Deck Improvements and Coding Modifications

The original input model for the Grand Gulf station blackout sequence featured a very simple model of the reactor core region, as described in Section 12.1.1. It included only three control volumes for the core region, one for the channel, one for the BWR flow bypass region, and one for the lower plenum. The COR models included 4 radial rings and 13 axial levels, 6 of which were fueled zones. Thus, a total of 52 COR cells occupied just 3 thermo-hydraulic control volumes. With this model, it was impossible to determine the effects of local channel plugging due to relocation and refreezing of molten core materials in the lower extremities of the core region. One problem with this model was the large quantity of hydrogen produced due to the inability to prevent steam flow through plugged channels. Thus, there was a failure to cut off steam sources to metallic components. These components continued to produce hydrogen under conditions in which they would normally be steam-starved.

This problem was addressed by subdividing the core and bypassing each CVH control volume into 20 separate volumes. An additional ring was added for a total of five rings. Other than the addition of an extra ring, the axial COR nodalization was retained, but the CVH nodalization was changed to include a set of control volumes that included 13 axial levels for each of the 5 rings. This was done for both the channel and bypass regions. Thus, there are now 4 control volumes for each ring in the fueled core region and steam flow can detour around plugged regions limiting metal/water reactions in those locations. The net effect on core region CVH nodalization is an increase from 3 hydro control volumes to 41 control volumes, and an increase from 4x13=52 to 5x13=65 COR cells.

Elaborate flow path connections were provided between adjacent control volumes in the expanded CVH nodalization scheme. For example, where there were originally two flow paths between the lower plenum and the core region (one to the channel and one to the bypass), there are now 10 flow paths (5 to the channel control volumes and five to the bypass). A similar set of flow paths connects one axial level to the next higher level in each ring. Thus, there are a total of 50 vertical flow paths into, within, and out of the core region. In addition, there are 16 new horizontal flow paths that connect bypass control volumes on the same axial level in one ring to bypass control volumes in adjacent rings. These are open continuously. A second set of 20 horizontal flow paths from channel control volumes in each axial level to the adjacent bypass control volume in the same ring was added that open only when the canister wall at a given location has failed.

Plugging in flow channels was activated in the new model by using the FLnnnBk input in the flow path definition cards to allow the CVH/FL flow modeling to adjust flow between control volumes using input conditions from other packages. Currently, the information used can come only from the COR package, and flow constriction through a given path can be calculated as a function of the open volume fraction in a given set of specified COR cells.

A second important change to the Grand Gulf input deck consisted of incorporating a more realistic configuration for the suppression pool. The older model used just two control

volumes to model the drywell/wetwell/weir configuration characteristic of the Mark-III containment system. The seal between the wetwell and the drywell provided by the pool of water that resides between the weir wall and the drywell wall was modeled by assuming that water to be a pool within the drywell. Although this arrangement could adequately simulate the function of the suppression pool vents, it resulted in the presence of a pool in the drywell compartment. Upon vessel head failure, the ejected debris was quenched by this bogus pool, thus preventing the expected debris/concrete interactions.

The problem was solved by adding a third control volume to the containment system consisting of the weir volume. A large flow path was added to connect the weir to the drywell, and the old set of vent paths that connected the drywell to the wetwell were redefined to connect the weir to the wetwell. Thus, the drywell in the new model is actually dry, the water in the weir being confined to the weir volume. This does not mean, however, that water cannot enter the drywell from the wetwell through the weir. Hydrogen burns in the wetwell, for example, may pressurize the wetwell fast enough, despite the action of vacuum breakers, to force significant quantities of water into the weir and over the weir wall into the drywell compartment.

The bugs that were fixed in the post-release version of MELCOR 1.8.5 were mostly functional rather than significant with regard to code accuracy. The most troublesome bug that came to light in the application of the 1.8.5 version to the finely noded Grand Gulf station blackout was one having to do with the disposition of decay heat from aerosols and fission product vapor phase components. When control volumes have been voided of solid components such as rods, structures, and debris, the existing models simply put the decay heat into the cell atmosphere. The decay heat from this source can be significant and this together with the limited heat capacity of steam can result in the cell gas temperature being elevated to extremely high levels (in excess of 10,000 K). This situation will usually be trapped as an unrealistically high temperature automatically terminating the run or it can feed into a properties function that will overrun a table, producing an error, and again terminating the run.

This problem seems to have manifested here due to the juxtaposition of two modeling practices incorporated into the new Grand Gulf model. These were the fine CVH nodalization of the core region in which an entire control volume within the core could become completely voided, and the flow path blockage model that can result in essentially zero convective flow rates through a control volume due to plugging. With no solid material to absorb the decay heat and no convective cooling or convective flow to sweep fission products out of the control volume, the result can be unrealistic gas phase temperatures. In reality, the decay heat is primarily in the form of gamma and beta radiation that are not absorbed by the atmosphere in any case, because of low absorption cross sections of gas phase components. This energy would be absorbed on whatever surfaces it might encounter along the beam path. The solution was to provide a mechanism by which the code searches for the appropriate surfaces in adjacent control volumes if the source control volume is voided of material or lacks surfaces for absorption.

12.5.2 Sensitivity Case Descriptions

As part of the sensitivity studies performed with the improved plant model and the updated code version, two additional calculations have been performed and are reported here. Of particular concern was the apparent increase in hydrogen production between the 1.8.4 version and the original 1.8.5 calculation as discussed in Section 12.4.4. (See Figure 12-11 and Figure 12-12.) In order to explore the causes of the additional hydrogen source and its apparent association with the BH model and, in particular, the early transition to BH, the improved Grand Gulf deck was run both with BH activated and without BH activated. In the first case the BH model input was left intact except for those BH input that were affected by the new plant models (such as the addition of a fifth radial ring). For the case without BH, the BH input was simply removed and the COR package was allowed to handle the heatup of debris and its thermal interaction with water in the lower plenum. All other MELCOR input parameters were identical between the two cases. What follows is a brief discussion of the most significant aspects of the results from these two cases.

12.5.3 Results of Sensitivity Calculations

The sequence of events that occurred during the calculations for the sensitivity cases are summarized in Table 12-2 and Table 12-3. The data are divided into two separate tables because the failure modes were significantly different and for the most part could not be compared one-to-one. For example, the case with BH on (Table 12-2) shows that the CSP failures occurred by overheating of the plate (PLATE-B failure mode). On the other hand, for the NO-BH case (BH inactive, Table 12-3), both the PLATE-B failure mode and the CRGT column failure mode contributed to CSP failure.

By way of explanation, the PLATE-B model consists of a horizontal flat edge-supported plate, which has a failure mode based either on a fixed plate temperature or a logical control function that provides a signal when a user-specified condition has been met. When this failure mechanism has been activated, only particulate debris above the plate location can relocate downward. Intact structure and rods cannot relocate. The COLUMN support model assumes that the support of overlying structures remains in place due to the presence of CRGT columns. These columns, while remaining in place, support overlying structure until a specified temperature or logical control function signals a loss of ability to support overlying material. When such a signal is indicated, all structure or debris including intact rods lose support and are relocated downward.

Table 12-2 and Table 12-3 show that PLATE-B CSP failure in radial rings 1, 2, and 3 occurred at essentially the same times, between about 4650 and 5480 seconds. Thus, particulate debris in these three rings that was present on or above the CSP began moving into the lower plenum during this period for both cases. These are not significantly different from the failure times in Table 12-1 for the inner three rings. Note that the new rings 1 and 2 together constitute the old ring 1. (Ring 1 was divided into two equal area rings.)

A key difference between the two sensitivity cases is that for the NO-BH case, debris that has entered the lower plenum via the PLATE-B mechanism begins heating up the CRGT columns, resulting in failure of these columns, starting with ring 3 at about 5600 seconds. The failure criterion was defaulted at 1273 K. Failure of the CRGTs in the COLUMN failure mode results in the remaining intact rods and structure being dumped into the lower plenum fairly early in the NO-BH case. This does not occur in the case with BH activated because BH subsumes the CRGTs and the debris, thus bypassing the COLUMN failure logic in the COR package. Instead, BH has its own internal logic that sends a signal to COR when it decides that the CRGTs have failed or that the core boundary heat structure (core shroud) has overheated. In this case, that signal was sent at about 19,100 seconds based on the attainment of a core shroud failure temperature of 850 K. At this user specified temperature, the core boundary is assumed to fail and the entire core slumps into the lower plenum. Note that the failure of the shroud occurred soon after dryout of the downcomer. This resulted in gross failure of the CSP and the addition of all remaining fuel and core materials into the lower plenum. Thus, the timing of material relocation from the core into the lower plenum is somewhat different between the two cases.

The second major difference between the two cases is the timing of vessel head failure. Table 12-2 shows that the vessel head failed due to creep rupture at 23,591 seconds. BH has two mechanisms for vessel head failure: gross failure of the head by creep rupture and failure of the welds at the vessel penetrations (CRGT and instrumentation penetrations). The criterion for vessel head failure is hard-coded in the BH model and is based on a Larson-Miller creep rupture model. The weld failure model is also a creep rupture model based on user input failure temperatures of 1672 K for failure at 6 minutes and 1560 K for failure at 60 minutes. In the present case, the former mechanism failed the vessel head. Inspection of Table 12-3 will show that in the NO-BH calculation, the vessel head did not fail in the creep rupture mode, but rather through the vessel penetration failure mode. The COR model has its own Larson-Miller parameter creep failure mode, but it also has a simple temperature-driven penetration failure model. The failure criterion for this model was set at 1700 K in the NO-BH case and this is the mechanism that caused vessel breach in this case. Table 12-3 shows that the vessel was breached due to failure of CRGT tube penetrations in ring 1 starting at about 15,238 seconds. Consequently, vessel head failure occurred 8350 seconds earlier in the NO-BH case.

The penetration failure models in both COR and BH are at best semi-mechanistic and depend on user-supplied parameters such as failure criterion, heat transfer areas and heat transfer coefficients. Judicious trial and error selection of these parameters could bring vessel head failure timing into better agreement. An interesting approach for follow-on model testing would be to turn off the penetration failure models in both cases (with and without BH) and compare the differences in the creep rupture failure timing.

Table 12-2. Sequence of Events for Grand Gulf Sensitivity Case with BH

Event	Time(Seconds)
Accident Initiation	0.0
ADS Actuation	1416

Event	Time(Seconds)
Accident Initiation	0.0
Gap Release in Ring 1	2492
Gap Release in Ring 2	2495
Gap Release in Ring 3	2568
Gap Release in Ring 4	2842
First H2 Burn in Wetwell	3571
Gap Release in Ring 5	3797
PLATE-B Failure of Ring 1 CSP	4641
PLATE-B Failure of Ring 2 CSP	4692
Initiation of BH Package	4733
Second H2 Burn in Wetwell	4963
Third H2 Burn in Wetwell	5305
PLATE-B Failure of Ring 3 CSP	5470
Fourth H2 Burn in Wetwell	5940
PLATE-B Failure of Ring 5 CSP	9320
PLATE-B Failure of Ring 4 CSP	12,708
Fifth H2 Burn in Wetwell	14,834
Core Shroud Failed	19096
CSP Failed by BH Signal–Core Slumps	19096
Vessel Head Failure by Creep Rupture	23,591
End of Calculation	40,000

Table 12-3. Sequence of Events for Grand Gulf Sensitivity Case without BH

Event	Time (Seconds)
Accident Initiation	0.0
ADS Actuation	1443
Gap Release in Ring 1	2520
Gap Release in Ring 2	2522
Gap Release in Ring 3	2596
Gap Release in Ring 4	2870
First H2 Burn in Wetwell	3601
Gap Release in Ring 5	3822
PLATE-B Failure of CSP in Ring 2	4707
PLATE-B Failure of CSP in Ring 1	4873
PLATE-B Failure of CSP in Ring 3	5475
COLUMN Failure of CSP in Ring 3	5592
COLUMN Failure of CSP in Ring 1	6116
COLUMN Failure of CSP in Ring 2	7415
Second H2 Burn in Wetwell	7614
COLUMN Failure of CSP in Ring 4	7672

Event	Time (Seconds)
PLATE-B Failure of CSP in Ring 4	8593
COLUMN Failure of CSP in Ring 5	8974
Lower Head Penetration Failure in Ring 1	15,238
First H2 Burn in Drywell	15,516
Second H2 Burn in Drywell	15,671
Lower Head Penetration Failure in Ring 2	18,040
Third H2 Burn in Drywell	18,910
Fourth H2 Burn in Drywell	18,913
Third H2 Burn in Wetwell	19,456
Fifth H2 Burn in Drywell	19,578
Lower Head Penetration Failure in Ring 3	21,545
Lower Head Penetration Failure in Ring 4	22,611
PLATE-B Failure of CSP in Ring 5	23,556
PLATE-B Failure of CSP in Ring 2	24,775
Lower Head Penetration Failure in Ring 1	25,118
PLATE-B Failure of CSP in Ring 1	28,176
PLATE-B Failure of CSP in Ring 4	29,674
PLATE-B Failure of CSP in Ring 3	30,734
PLATE-B Failure of CSP in Ring 5	33,973
Sixth H_2 Burn in Drywell	33,973
End of Calculation	40,000

A new technique was developed to illustrate the progression of material relocation and thermal response predicted by MELCOR for the sensitivity calculations. The method uses the EDF capability to write output files in an XYZ format that can be used by many plotting packages to calculate and plot two-dimensional contour graphs at selected times during the calculated accident progression. The sequence of events associated with core heatup, melt/rubblization, and downward relocation was similar for both the sensitivity calculates, so the results will be shown here for only the NO-BH case. This case was selected because the contours can be shown for both the core and lower plenum regions in this case. In the other case, when BH takes over the lower plenum calculations, COR output parameters are lost and corresponding BH output is not available.

The disposition of core material for the NO-BH case is shown here in Figure 12-22 to Figure 12-26. These figures show the solid volume fraction in the core and lower plenum. More accurately, it is the fraction of the total volume that is occupied by non-CVH components (core materials). Figure 12-22 represents the distribution of core materials at the beginning of the calculation prior to any relocation. Note that the bottom of the lower plenum is at an axial location of 0.0 m. The bottom of the core corresponds to the locations of the CSP, which is seen here as the horizontal 0.4 contour (5.25 m). The top of the core is at about 9.66 m (top of active core is 9.16 m). The original solid volume fraction is about 0.33 in the core region, except in the outer ring which includes the core shroud, and therefore has a volume fraction of about 0.45, similar to that in the CSP.

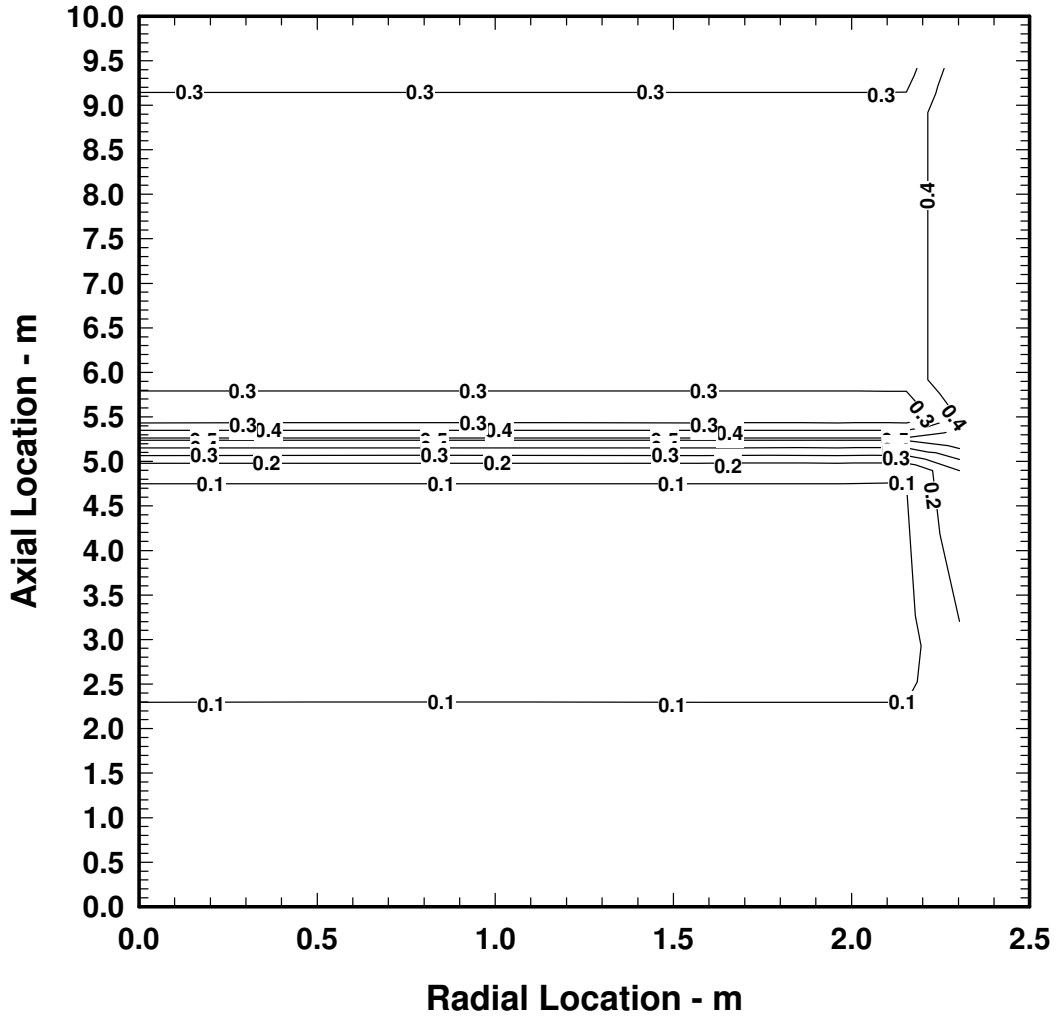

Figure 12-22. Core Material Volume Fraction at 0.0 Seconds

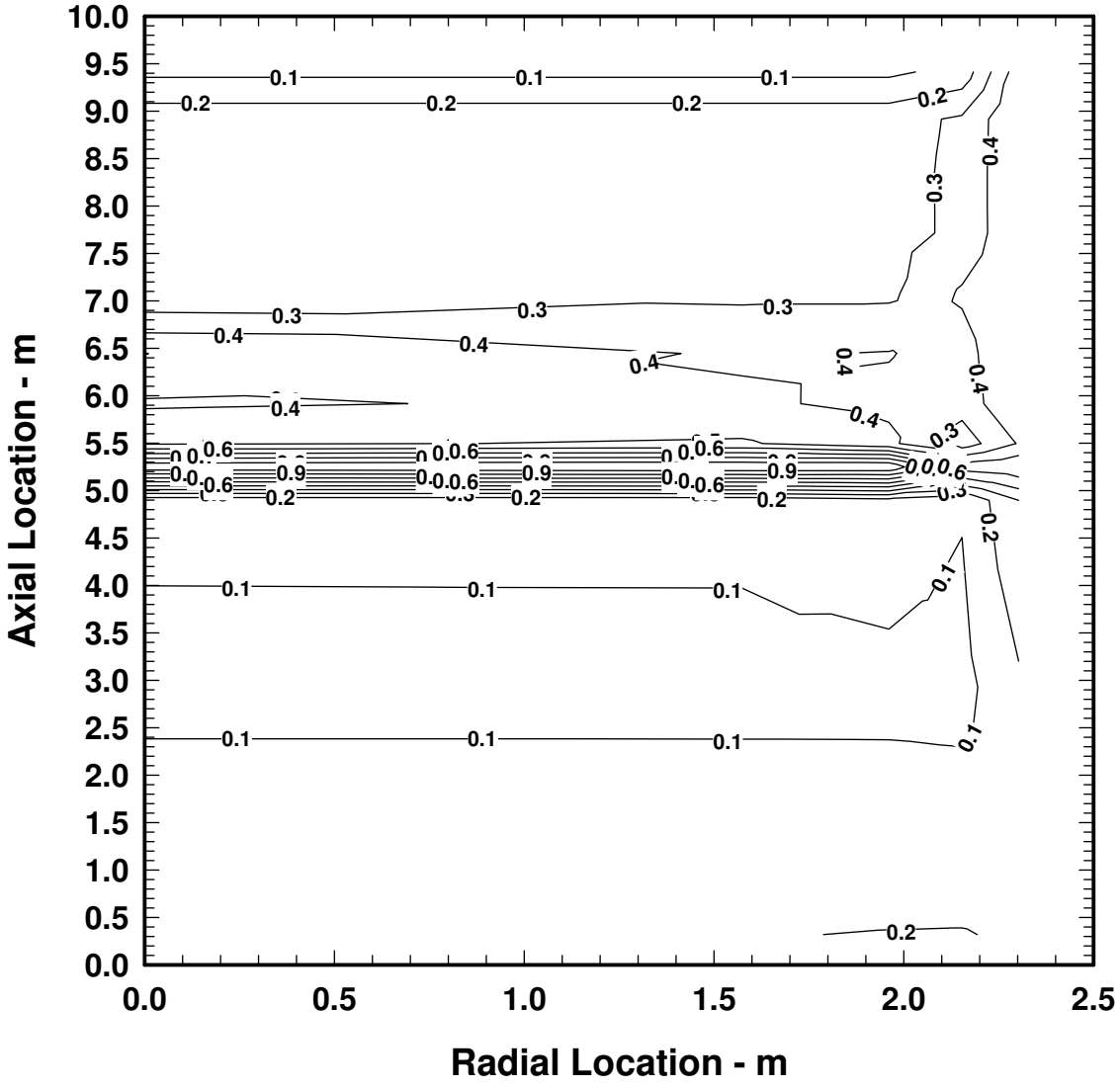

Figure 12-23. Core Material Volume Fraction at 4000 Seconds

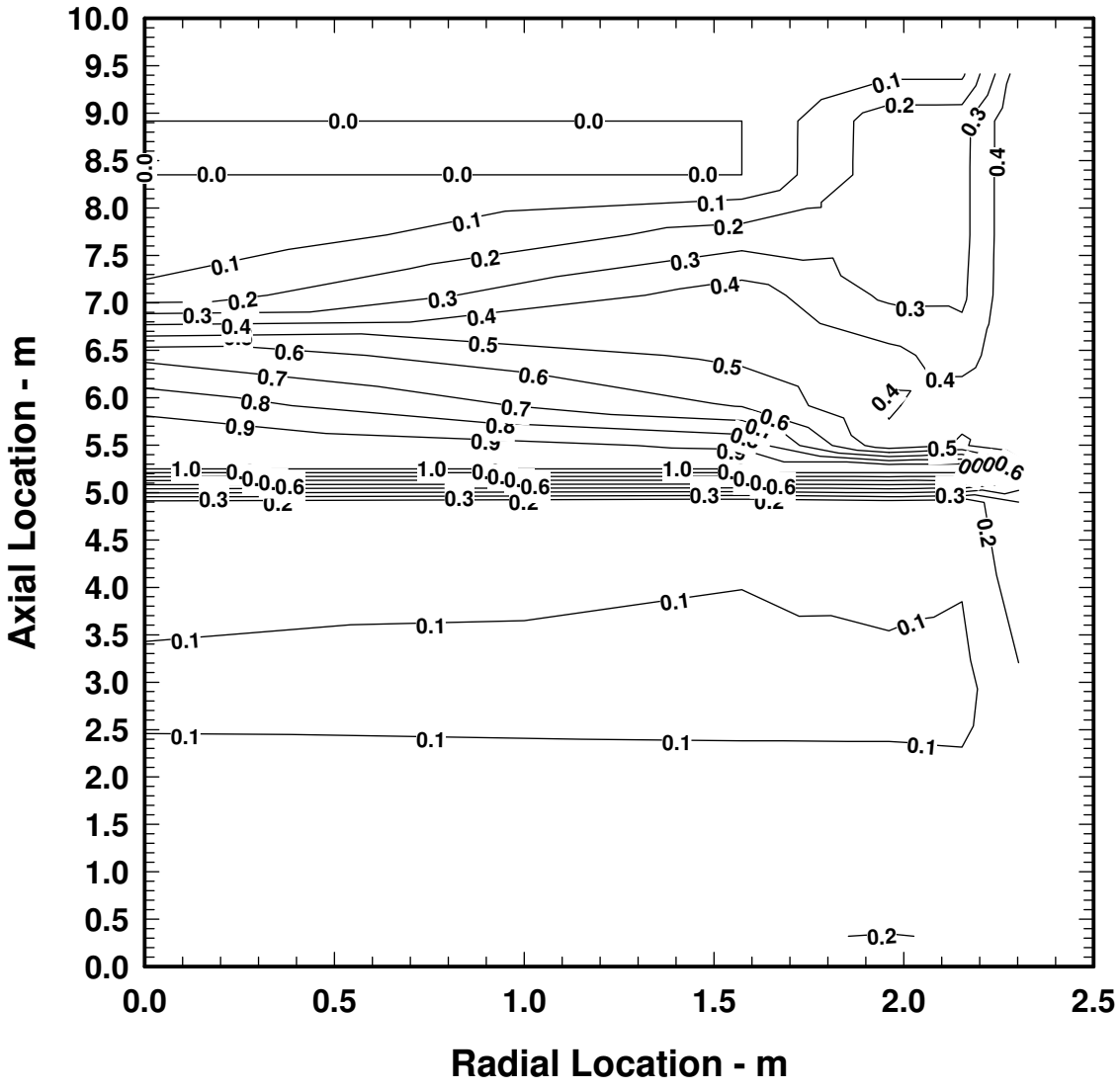

Figure 12-24. Core Material Volume Fraction at 4500 Seconds

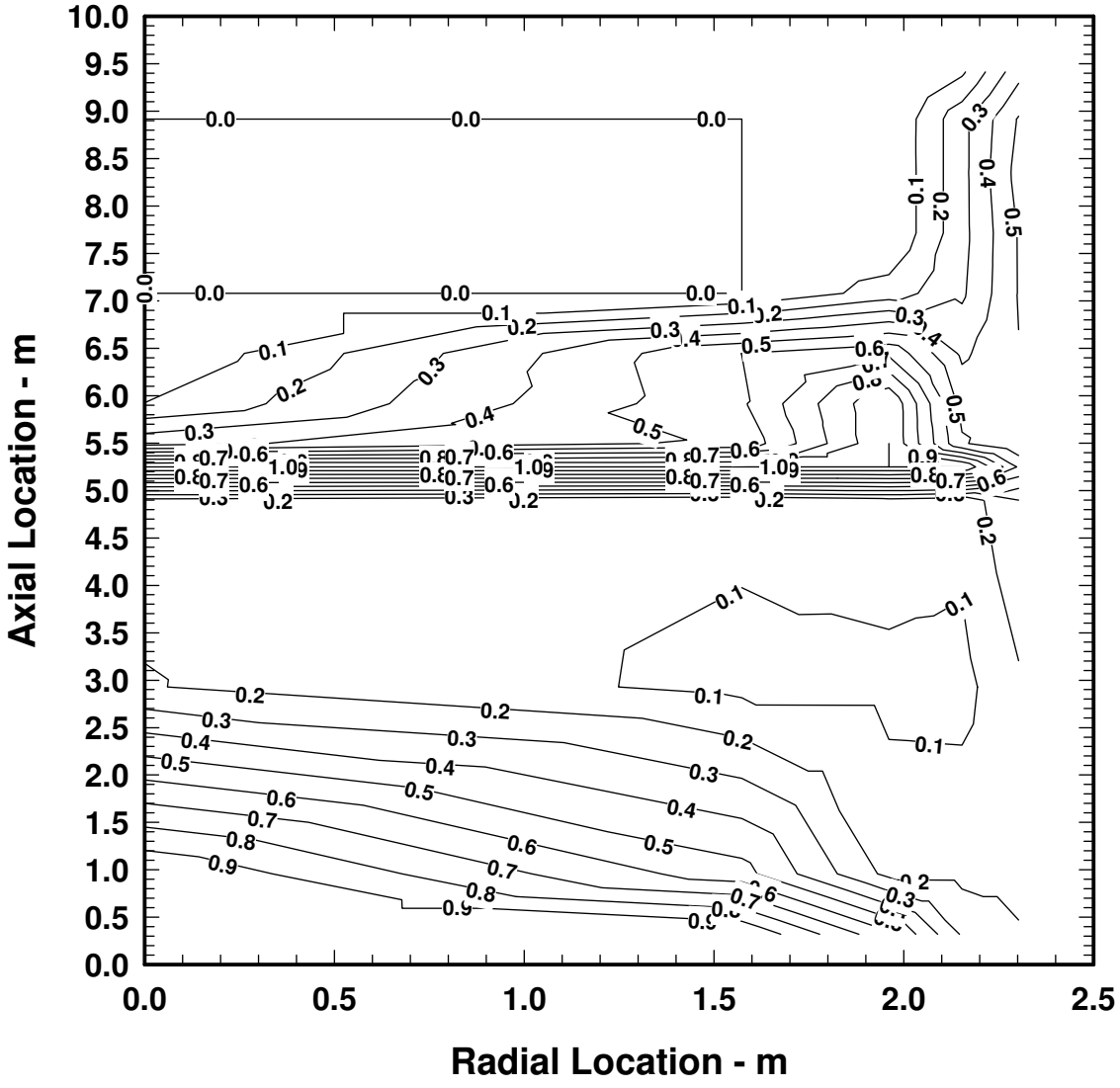

Figure 12-25. Core Material Volume Fraction at 5000 Seconds

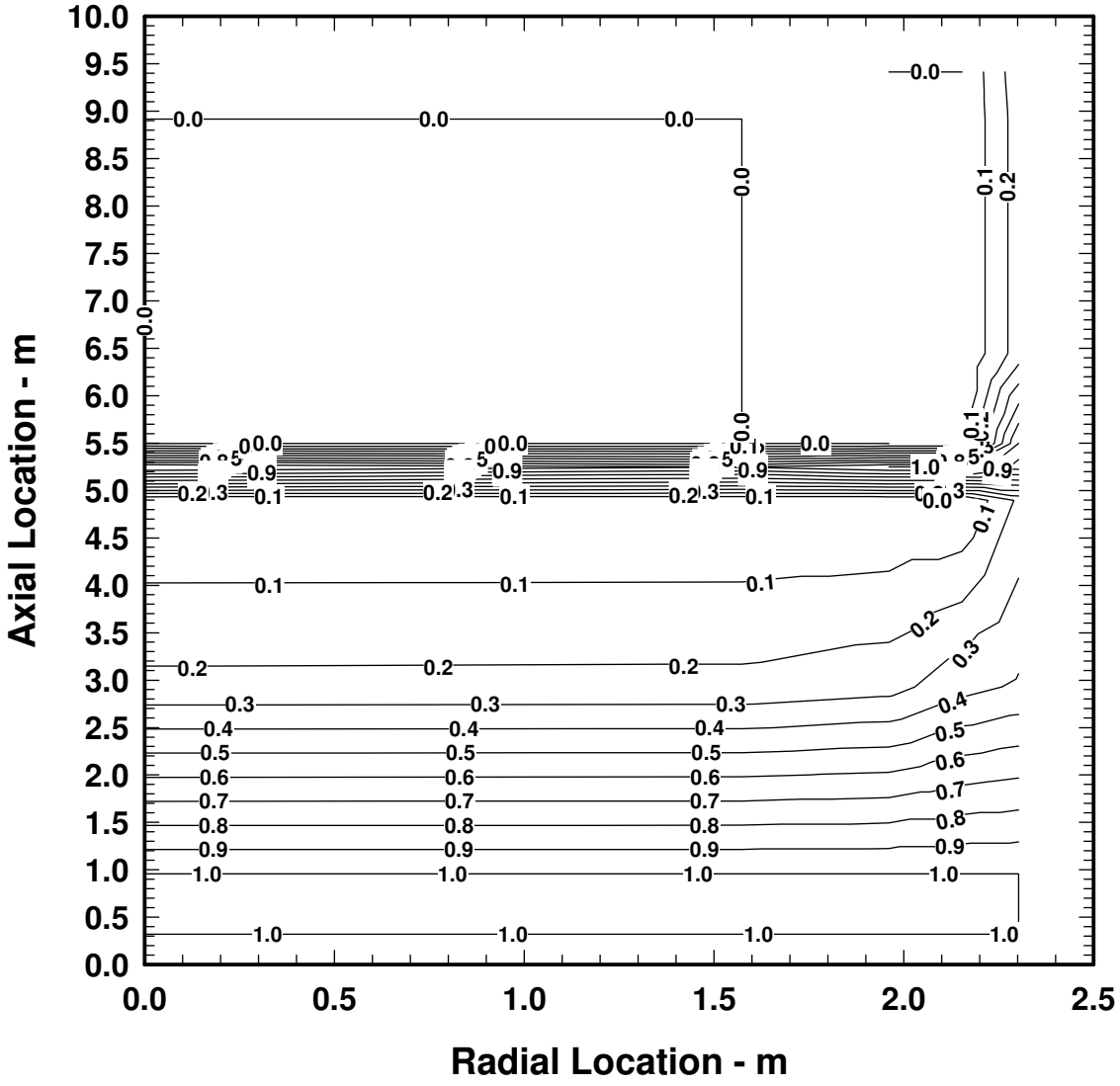

Figure 12-26. Core Material Volume Fraction at 10,000 Seconds

The distribution of core material at 4000 seconds is given in Figure 12-23. This time slice is prior to CSP failure and shows incipient slumping of material from the upper half of the core into the lower half and the accumulation of resolidified metallic components in the vicinity of the CSP.

At 4500 seconds, just prior to the first CSP failure, Figure 12-24 shows that the upper third of the core region is essentially void, and a great deal of core material has accumulated on the CSP.

By 5000 seconds (Figure 12-25), the CSP has failed in radial rings 1 and 2, dumping the particulate debris in the core region in those two rings into the lower plenum where it resides on the bottom of the reactor vessel head. Note that rings 3, 4, and 5 still retain considerable core material on the CSP.

The entire core region is essentially void at 10,000 seconds due to the COLUMN failure of all five rings beginning at 5592 seconds and finishing at 8974 seconds (see Table 12-3) when ring 5 CSP failed. The COLUMN failure results in all the remaining intact components losing their support and slumping into the lower plenum. This condition is depicted in Figure 12-26.

The calculated thermal response of the core and lower plenum regions is given in Figure 12-27 to Figure 12-29. The data from which these plots were made were extracted from the COR package output through control functions that selected the maximum of all the component temperatures including fuel, structures, particulate, conglomerate, and gas phase. For example, where a region is voided, the corresponding temperature is the atmospheric temperature.

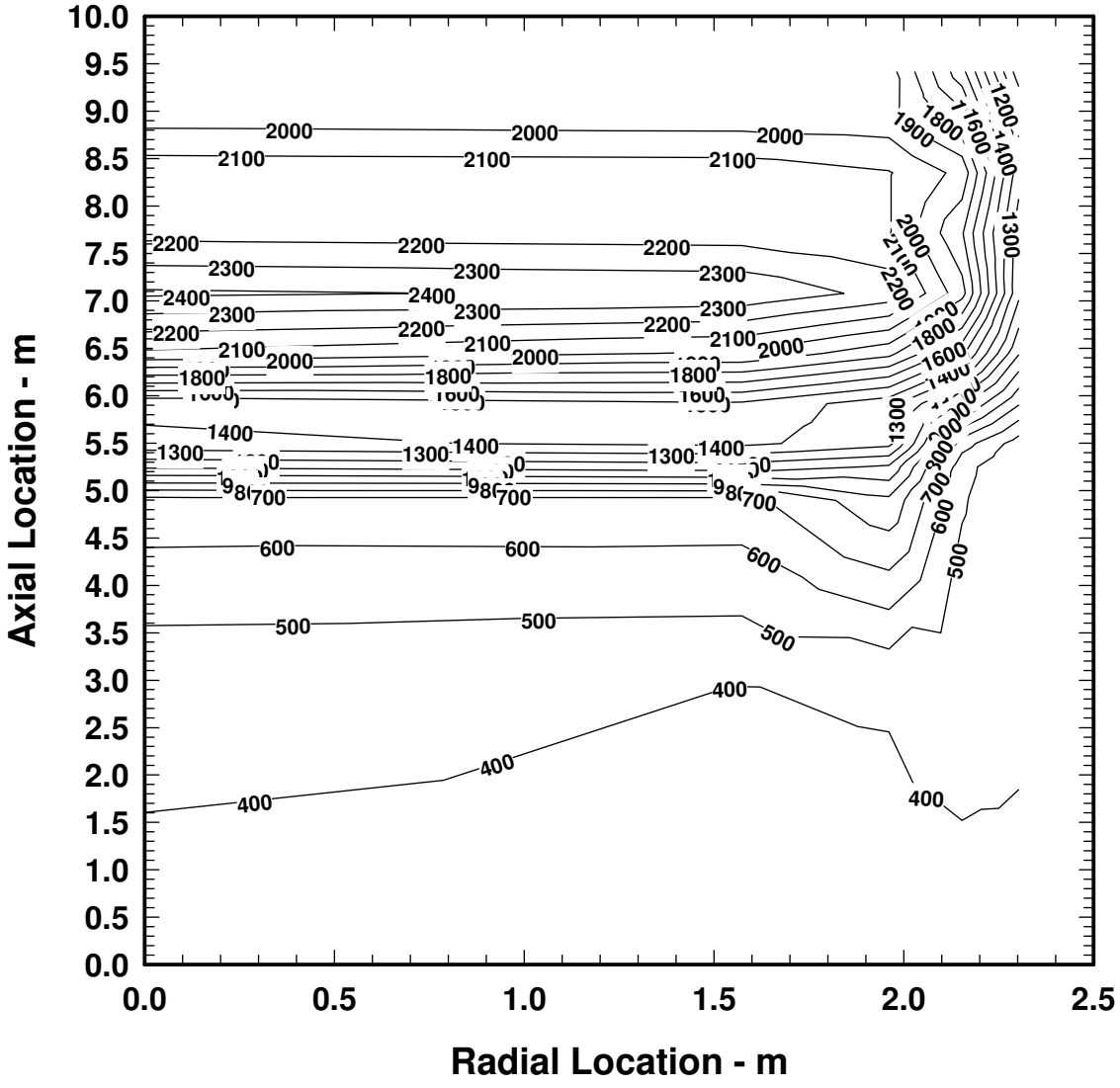

Figure 12-27. Core Temperature Profile at 4000 Seconds

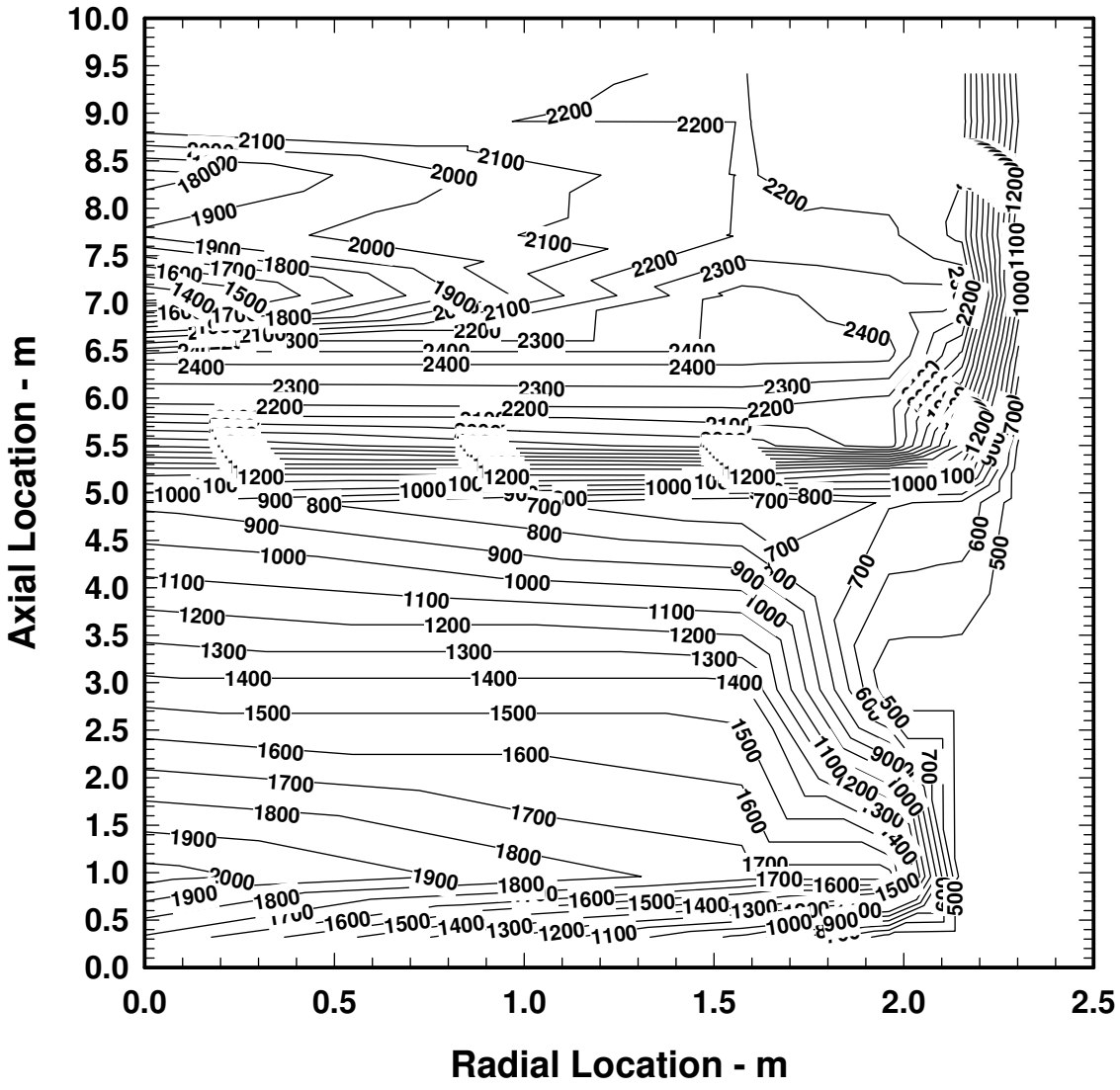

Figure 12-28. Core Temperature Profile at 5000 Seconds

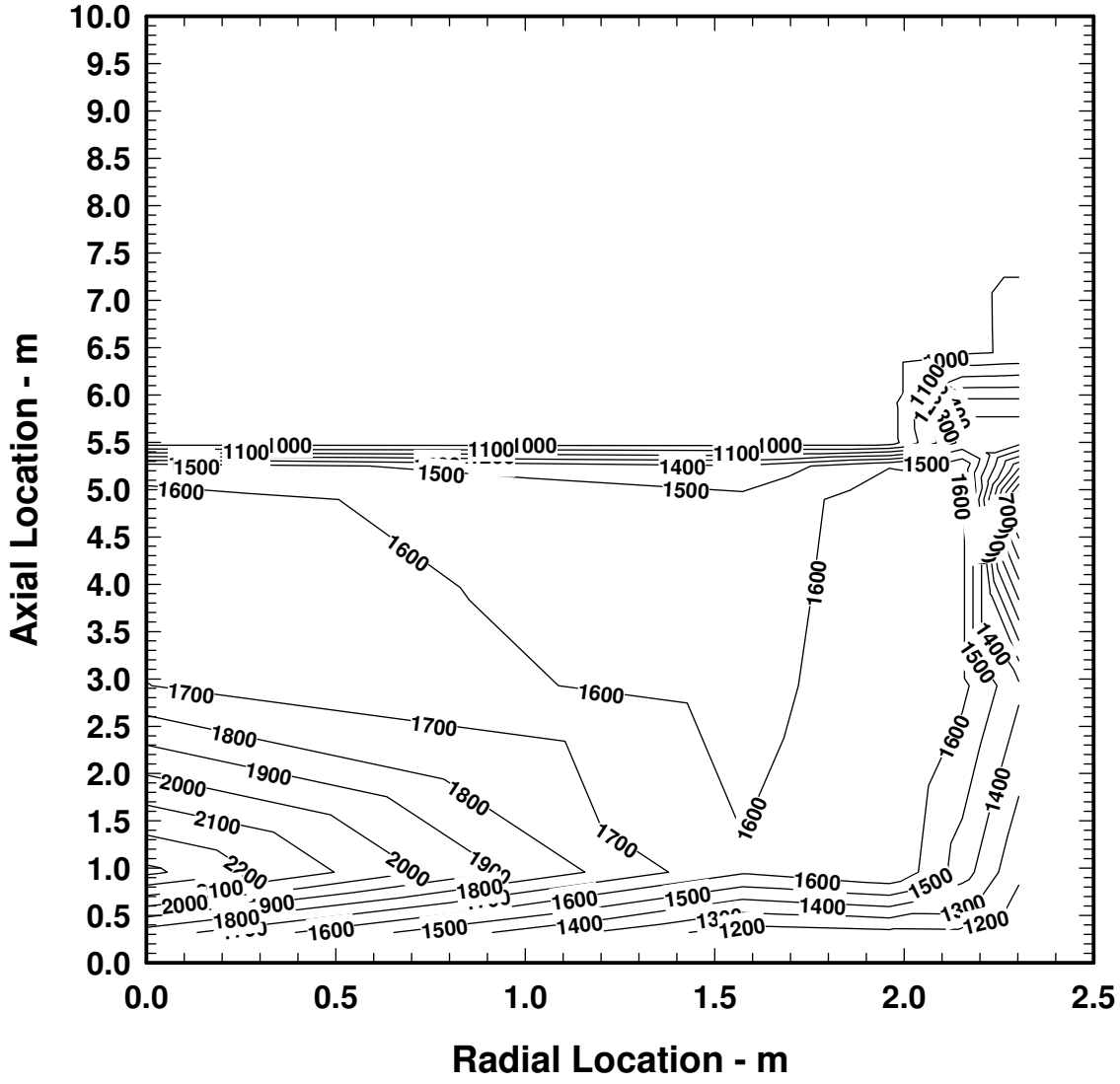

Figure 12-29. Core Temperature Profile at 10,000 Seconds

Figure 12-27 shows the temperature contours at the 4000-second time slice. The peak temperature of about 2400 K appears at about the 7-meter elevation at the top of the pile of debris that is accumulating above the CSP (see Figure 12-23).

At 5000 seconds, the CSP has failed in rings 1 and 2, and the debris from those rings has relocated to the lower plenum. The temperature distribution (Figure 12-28) reflects this

redistribution of core materials. The temperature peak in the core region has shifted somewhat radially outward due to the loss of core material in the inner rings, and axially downward due to slumping of core material. The temperature distribution in the lower plenum is characterized by high temperatures on the vessel head increasing from the bottom to top of the debris bed while decreasing from bottom to top of the gas space above the debris bed. This indicates heat transfer from the bottom of the debris bed to the vessel head and convective heat transfer upward from the top of the debris bed.

By 10,000 seconds (Figure 12-29), all the core debris is in the lower plenum and the water has completely boiled off, somewhat cooling the debris. The temperature profile along the bottom of the debris bed has not changed much from the 4,000 second time slice, but the debris bed is considerably deeper and hotter in its upper levels. Heatup of this debris bed ultimately leads to vessel head penetration failure and transfer of core debris to the reactor cavity at about 15,000 seconds.

A final graph in this section (Figure 12-30) shows a comparison of the total hydrogen produced for the four calculations considered in this report. Differences in hydrogen production between MELCOR 1.8.4 and the original release version of 1.8.5, the QX version, has been viewed as problematic. Early transition to the BH package, as discussed in Section 12.4.4, leads to increased hydrogen production by the COR package as seen in comparing Figure 12-11 and Figure 12-12. The situation is even worse when, the total hydrogen produced is shown by adding that generated by the BH package and that produced by the CAV package (core/concrete interactions). Figure 12-30 shows the total hydrogen. It is immediately obvious that the 1.8.5 QX version actually produced 1700 Kg of H_2 versus only 420 Kg in the 1.8.4 QL version of the code. As noted in Section 12.4.4, an extended period of coolant boiloff in the lower plenum produced about twice as much hydrogen by the COR package, but BH itself has a metal/water reaction model which produced an additional 600 Kg. This is apparent in Figure 12-30, which shows 1700 Kg for the QX calculation.

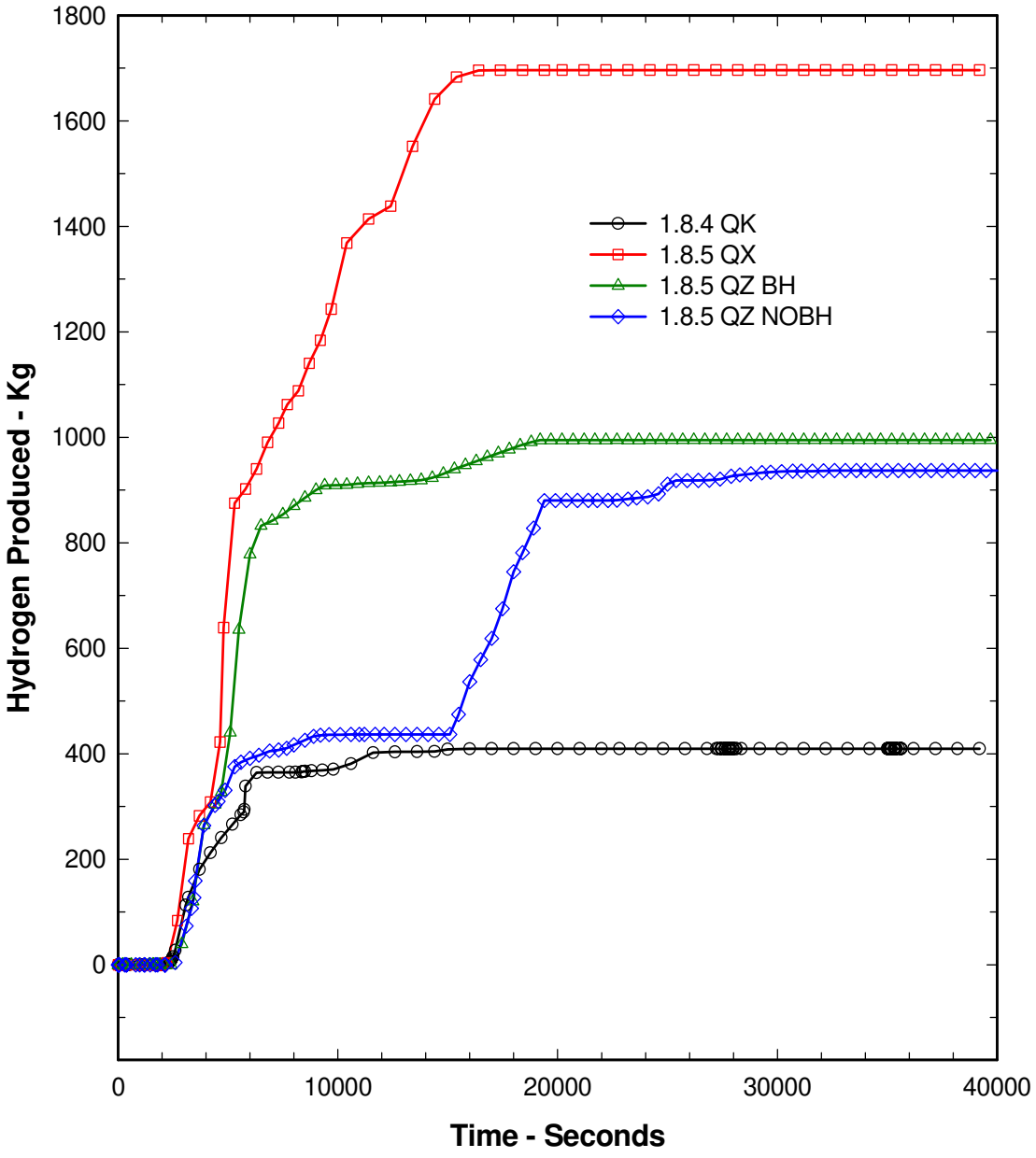

Figure 12-30 Comparison of Total H_2 Production

It was proposed that the COR package production of hydrogen was being significantly overestimated by the code because of the single control volume representation of the core and its associated inability to plug and restrict steam flow through blocked channels. The

primary purpose of the two sensitivity calculations reported in this section was: first, to more finely nodalize the control volumes in the core region and to add the flow blockage model to restrict flow in blocked regions; and second, to determine the differences between hydrogen production when the COR package was allowed to perform the heatup of debris in the lower plenum versus that generated by the BH package treatment of that process.

The results of the first effect, fine nodalization and local channel blockage, is seen in Figure 12-30. The total hydrogen was reduced from 1700 Kg in the QX case to only 1000 Kg in the QZ version run with BH active. This difference can be directly attributed to denying or limiting steam access to metallic components in core zones that have been blocked or the flow significantly restricted.

The second effect that is due to differences in the COR and BH metal/water reaction models for particulate debris is seen by comparing the last two curves in Figure 12-30. The QZ code version, run without the BH package activated (the NOBH case), generates quantities of hydrogen that are much more consistent with those seen in the 1.8.4 QL version of MELCOR. For this case, hydrogen was only 20 or 30 Kg higher than the QL version until about 15,000 seconds when the vessel head failed and the core debris was deposited in the reactor cavity. The subsequent production of hydrogen was then due to core/concrete interactions produced by the CAV package.

It is apparent that the COR metal/water reaction model for particulate debris in the lower plenum produces very small quantities of hydrogen compared to the BH models. On the surface, the models appear to be similar. It may require a detailed examination of the models to determine the differences and decide which model is the more accurate. Such an assessment is nontrivial because it not only involves the differences in the way COR and BH model the metal/water reaction but also the disposition of the debris/molten pool that forms in the lower plenum. For example, when BH takes possession of the lower plenum and its debris components, it reconfigures the bed into three axial levels and three radial zones in the lower axial level and five radial levels in each of the other two layers. What goes into these layers depends on what is in the lower plenum at the time that BH takes over. In general, the lowest level is assumed to be metallic components that candled into the lower plenum early in the sequence. There is a hierarchy in the model for depositing the remaining debris in the other two layers. Where the molten debris resides determines to some extent how available it is for oxidation. A reflood model is used in both packages and those models determine the availability of steam at various locations in the bed.

Both packages use a parabolic diffusion limited oxidation rate model for calculating the oxidation rate. However, BH allows for the periodic sloughing and removal of the oxide layer from the metallic surface and, although it is not clear from the model description, it may commence the calculation with a zero initial oxide layer thickness. The COR package, on the other hand, calculates an oxide layer thickness from the start, based on the assumption that the entire zirconium oxide inventory in the debris forms a layer on the metallic particle surfaces. This oxide layer apparently is not allowed to slough off. These

differences alone, aside from the question of steam/water/metal proximity, would seem to indicate that the COR package should generate less hydrogen than the BH package.

12.6 Discussion

The comparisons presented here for the Grand Gulf station blackout sequence analysis using the MELCOR versions 1.8.4 and 1.8.5 did not produce unexpected surprises given the significant modeling changes that have been incorporated in the new release version. The changes in the OS modeling were anticipated to result in the extended retention of core material in the core region, especially for BWR-type reactors in which the CRGTs are expected to continue to support the fuel assemblies even after failure of the CSP. This feature could not be properly modeled in earlier code versions. The holdup of fuel in the core was also expected to produce higher temperatures and more in-vessel fission product releases. These effects were clearly observed.

Early transition into the BH package was expected to produce earlier boiloff of coolant inventory from the lower plenum. In combination with the extended fuel holdup in the core, however, this effect was not seen. In fact, the boiloff of coolant inventory was extended far beyond that seen in the 1.8.4 version due to limited core debris transfer into the lower plenum. In retrospect, this is not a surprise.

Enhanced hydrogen production, more numerous hydrogen deflagrations, more rapid fission product releases, and enhanced transport of fission products into the containment building are all predictable results, given the effects that were produced by the OS and BH modeling changes. However, the increase in hydrogen production was perceived to be excessive and beyond what might be expected. Sensitivity calculations were performed and the case was made that care must be taken in nodalizing the core and lower plenum regions in order to take advantage of blockage models. When this was done, hydrogen production was reduced to more defensible quantities. An issue still remains unresolved, however, regarding the oxidation of metallic debris in the BH and COR packages. A possible future task may involve a merging of the COR and BH models to eliminate the discontinuities that currently exist between these two models.

It can be concluded that the version 1.8.5 calculation of the Grand Gulf station blackout sequence did not reveal any anomalous behavior in the new code version. In fact, itproduced results that were consistent with those anticipated given the nature and extent of the associated modeling improvements.

13. Simulation of the TMI-2 Accident

The accident that occurred at Three Mile Island Unit 2 (TMI-2) Nuclear Power Plant on March 28, 1979, is a well-established benchmark for analytical models of in-vessel core damage progression. The accident has been studied using many previous versions of MELCOR, including 1.7.0 [1], 1.8.3 [2] and 1.8.4 [3].

A standard framework for studying the TMI-2 accident divides the accident progression into four sequential time periods, where each is governed by different phenomena. Because the focus of the current analysis is on in-vessel core damage progression, the calculation described here is limited to Phase 2 of the TMI-2 accident, the period in which core uncovery, heatup, clad oxidation, and initial material melting occurred.

Phase 1 of the TMI-2 accident begins with a loss of main feedwater to the steam generators (SGs), which induces a turbine trip. Steam generator inventories decrease, degrading heat rejection from the RCS. The resulting increase in RCS pressure causes the pressurizer PORV to lift and stick in the open position. Misinterpretation of pressurizer water level indications caused the operators to reduce emergency coolant injection, initiating a small-break LOCA with inadequate coolant makeup. For analysis purposes, the transition from Phase 1 to Phase 2 occurs 100 minutes after accident initiation, when the final RCP is tripped due to excess vibration. Phase 2 lasts for 74 minutes and ends when RCP 2B is restarted.

13.1 Background

The TMI-2 nuclear station was a B&W PWR with a large-dry containment and a 2x4 loop reactor RCS, i.e., primary coolant emerged from the reactor vessel through two horizontally opposed hot legs, and returned to the vessel through a total of four cold legs (two from each loop). Heat transfer from the primary to secondary coolant circuits is achieved through two once-through SGs. The reactor vessel is a typical PWR cylindrical pressure vessel with hemispherical ends. As shown in Figure 13-1, major reactor vessel internal structures include the core barrel, thermal shield, and fuel assemblies in the active core region; control rod guide tubes and drive assemblies in the upper plenum region; and a flow distributor and in-core instrumentation tubes in the lower head region. The TMI-2 reactor was fueled with 177 fuel assemblies and generated 2772 MW at rated conditions.

13.2 Nodalization

The hydrodynamic nodalization scheme applied to the reactor vessel is illustrated in Figure 13-2. Distinct control volumes are defined to represent coolant in the downcomer, lower plenum, active core region, core bypass areas, upper plenum and upper dome. Within the active core, fuel behavior is modeled by subdividing the core into three radial rings and 12 axial levels. This pattern is also illustrated in Figure 13-2. Ring 1 represents the central 25 fuel assemblies. Ring 2 represents the surrounding 72 fuel assemblies. The remaining 80

assemblies are represented by ring 3. The twelve axial levels are equal in height, representing roughly 1-foot increments of the core. Two additional axial levels are defined to represent the volume below the active core, where damaged fuel can relocate.

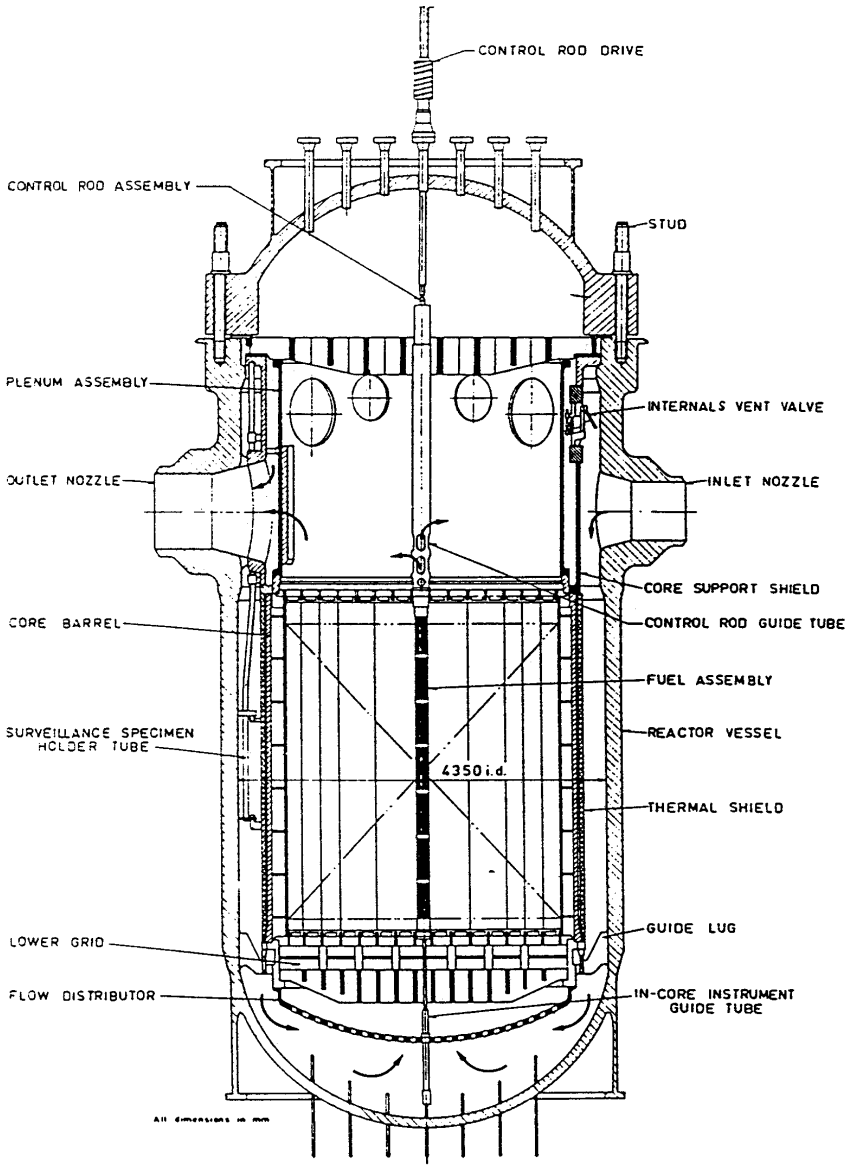

Figure 13-1. Cross-Section of the TMI-2 Reactor Vessel

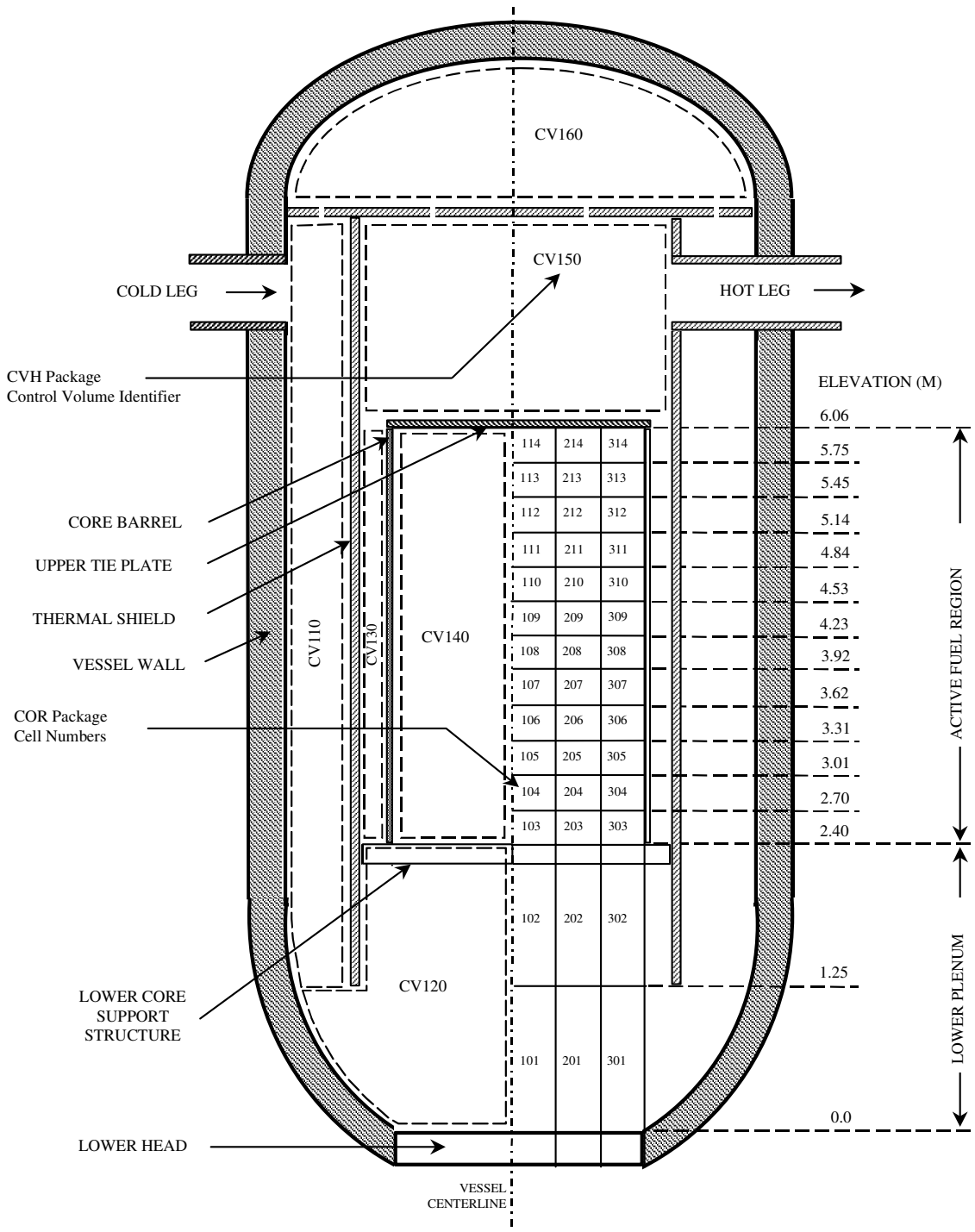

Figure 13-2. MELCOR Nodalization of the TMI-2 Reactor Vessel

The hydrodynamic nodalization scheme for the TMI-2 RCS and SG secondary is shown in Figure 13-3. The coolant flow and heat transfer through the A and B loops are represented

as distinct flow circuits. However, the division of primary coolant flow at the exit of each SG into two parallel cold leg piping systems is neglected, and the pair of RCPs in each loop are represented as a single composite pump.

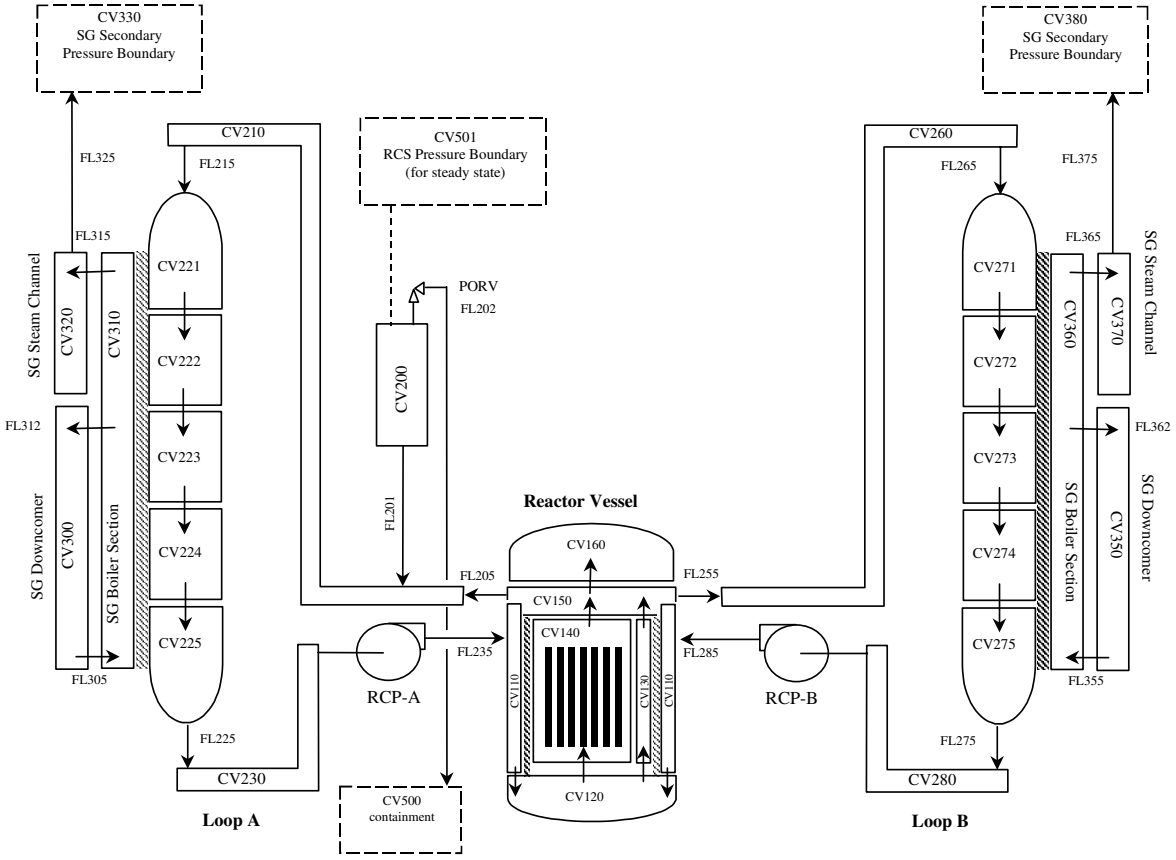

Figure 13-3. Hydrodynamic Nodalization of the TMI-2 RCS

Heat transfer across the SG tubes is modeled using 10 vertically stacked heat structures. The temperature gradient on the primary coolant side of the tubes is represented by a series of 5 control volumes. The boiler section of the SG secondary is represented by a single control volume. The downcomer and annular steam channel are represented with separate control volumes.

With the release of MELCOR 1.8.5, much has been learned of the importance of natural circulation phenomena in high pressure accident sequences. The present TMI-2 analysis, which builds on earlier work using a very similar vessel/RCS nodalization, uses a simplified nodalization for the core and upper plenum region. In doing so, it is not capable of capturing any important circulation patterns between the core and upper vessel head

region. Further analyses of this accident will make use of a more detailed CVH nodalization in the core and upper plenum region. The simplified nodalization is retained for the present MELCOR 1.8.5 analysis in order to facilitate comparison to an earlier MELCOR 1.8.4 analysis.

13.3 MELCOR Input Specifications

Ideally, the calculation of Phase 2 of the TMI-2 accident would follow directly from results of a Phase 1 calculation. In the current analysis, as with past MELCOR simulations of the TMI-2 accident, calculations of each phase of the accident are performed independently. That is, the Phase 2 calculation was performed without reading data directly from a restart file generated by a Phase 1 calculation. Rather, initial conditions for the Phase 2 calculation were specified as part of MELGEN input data. This approach is used to reduce the influence of potential errors in the Phase 1 calculation from propagating to Phase 2.

Many of the initial conditions for the Phase 2 MELCOR model were derived from results of an earlier Phase 1 calculation. For example, local fluid velocities in flow paths were initialized to values calculated at the end of a MELCOR 1.8.3 analysis of Phase 1 [2]. Values for many other parameters, however, were taken directly from the TMI-2 Initial and Boundary Conditions (ICBC) data base [4] or TMI-2 standard problem guidelines [5]. Examples of the latter include HPI and RCS letdown flow rates, hot and cold leg fluid temperatures, RCS and SG secondary pressure, and water levels in the pressurizer and SG secondary.

SG secondary system behavior was modeled in a more indirect manner. Control functions were defined to monitor SG boiler liquid level. Coolant was automatically added or removed as necessary to follow the water level signature reported in the ICBC data base. SG secondary pressure was controlled directly by attaching a time-dependent (i.e., pressure-specified) volume to the steam line.

Because this calculation was performed strictly as an assessment of in-vessel core damage modeling capabilities, containment response was not modeled, and the RN package was not activated.

In general, the TMI-2 MELCOR model was developed using standard default modeling parameters. This was particularly true for parameters governing core degradation, where nonstandard input was required in earlier MELCOR simulations of the accident to generate a reasonably accurate representation of material damage.

Plant data and accident boundary conditions were specified in two MELGEN input files for this calculation. Filename “tmi2-p2.gen” contains all input data except that required for the COR package. Filename “cor.gen” contains COR package input.

The MELCOR input file for this calculation is “tmi2-p2.cor.”

13.4 Results of Analysis

The loss of primary coolant through the stuck-open PORV results in a gradual decrease in reactor water level as shown in Figure 13-4. Results from the MELCOR 1.8.5 calculation are shown in comparison to those from MELCOR 1.8.4. Data are not available for reactor water level, but results from an earlier analysis performed with SCDAP/RELAP5 [6] are shown as a useful reference. Elevations of the top and bottom of the active fuel are shown as solid horizontal lines (0.0 and ~3.6 m).

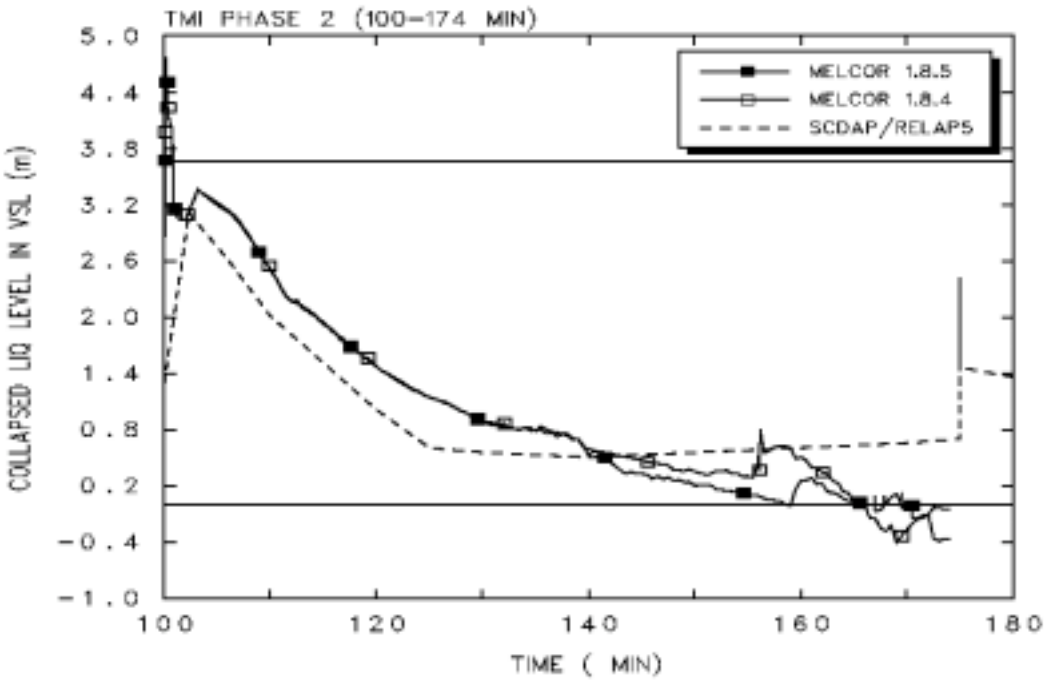

Figure 13-4. Reactor Vessel Water Level

Results from the two MELCOR calculations are virtually identical for the first 40 minutes of the calculation (140 minutes into the accident), and diverge only slightly after that point in time. The small differences in calculated water levels late in the Phase 2 calculation are due to differences in coolant evaporation caused by core material relocation, which is calculated to begin approximately 135 minutes into the accident. These differences are discussed further below. Both calculations compare well with the SCDAP/RELAP5 result prior to the onset of material relocation. However, they each depart from the stable water level predicted by SCDAP/RELAP5 late in Phase 2, eventually decreasing below the bottom of active fuel. The sharp increase in water level shown at 174 minutes in the SCDAP/RELAP5 calculation is caused by the restart of RCPs, which is not modeled in the MELCOR calculations.

The calculated RCS pressure is shown in Figure 13-5 with comparisons to measured data and the SCDAP/RELAP5 result. The MELCOR 1.8.5 result is greatly improved from the MELCOR 1.8.4 result, which exhibits a sudden increase in pressure at approximately 155 minutes. This increase is not due to steam generation accompanying RCP restart (which is the reason for the late pressure rise in the SCDAP/RELAP5 result and plant data) but rather to approximately 100 kg of core debris (particulate) which is calculated to fall into the reactor vessel lower head in the MELCOR 1.8.4 calculation at approximately 155 minutes. The event is not observed in the MELCOR 1.8.5 results, nor is it generally believed to have occurred in the actual accident.

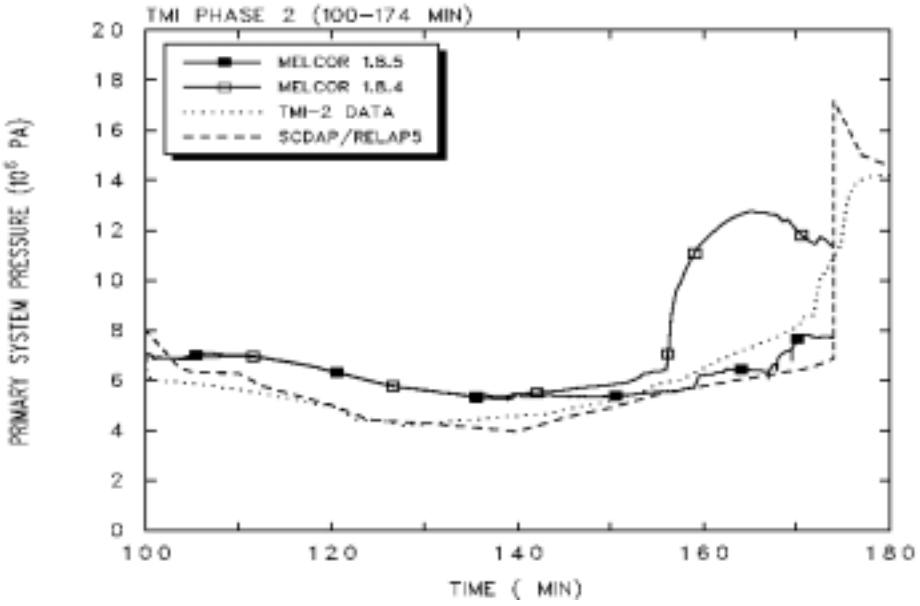

Figure 13-5. Reactor Coolant System Pressure

A summary of calculated fuel cladding temperature histories is shown in Figure 13-6. This figure displays the maximum and minimum core temperatures along the core center line (i.e., the central ring of the MELCOR model), at three elevations: the upper third of the core, the central third, and the lower third.

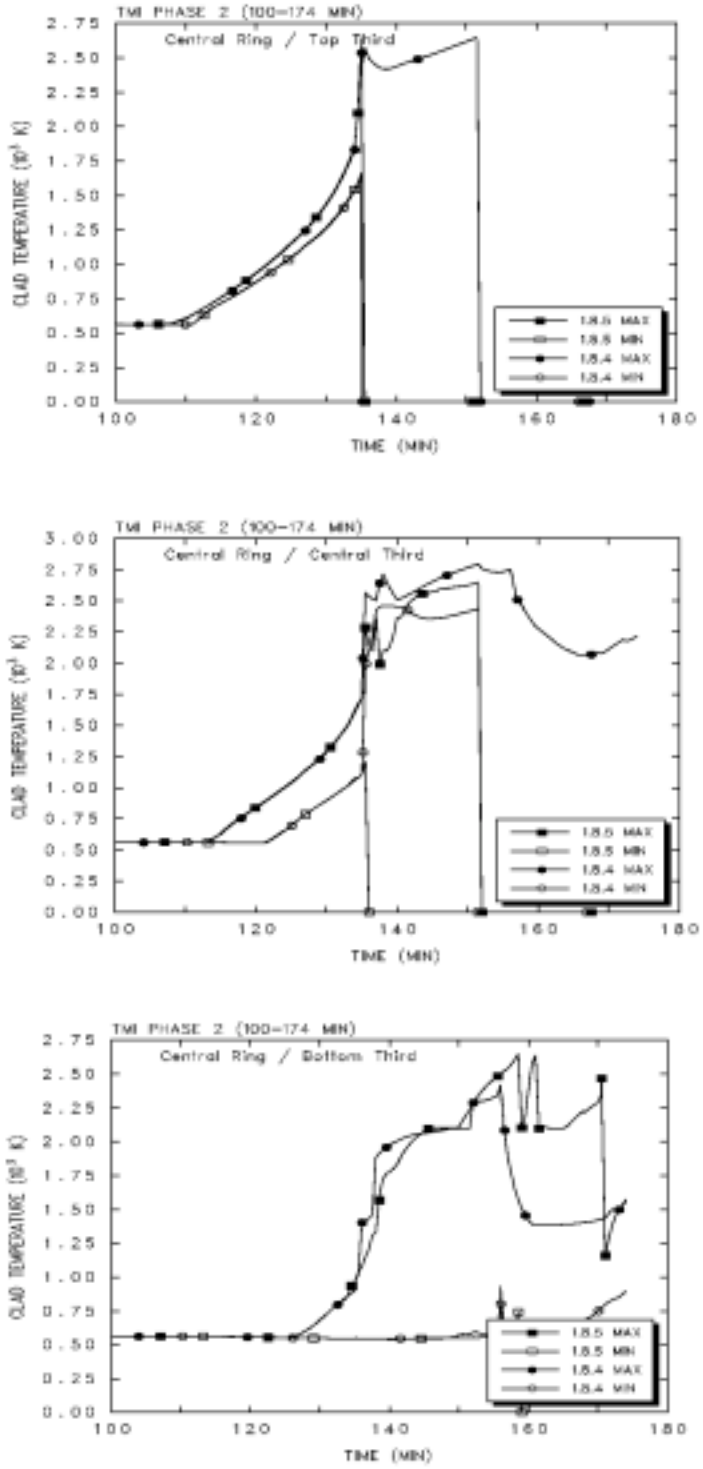

Figure 13-6. Cladding Temperatures

The temperature histories calculated by these two versions of the code are qualitatively similar with one noticeable exception. The maximum temperature at the upper two-thirds of

the core decreases to zero (indicating a total loss of intact material at those locations) much sooner in the MELCOR 1.8.5 calculation than in the MELCOR 1.8.4 case. This difference is primarily due to the change in default values for COR package sensitivity coefficient 1132(1), the temperature at which fuel rods collapse in the absence of unoxidized cladding. If this temperature is manually changed back to the value used in MELCOR 1.8.4 (i.e., from 2500K to 2800K), fuel rods remain intact longer, and the temperature signatures resemble those shown in Figure 13-6 for the older version of the code.

The calculated total (integral) quantity of hydrogen generated during Phase 2 of the accident is shown in Figure 13-7, with comparisons to results from an earlier SCDAP/RELAP5 calculation. Both MELCOR results have very similar signatures, and the final amount of hydrogen generated is 300–325 kg. However, the target value for this phase of the accident is ~400 kg [5], and clad oxidation is shown to begin 10–15 minutes sooner than estimated by the SCDAP/RELAP5 calculations. Additional work is required to resolve these deficiencies.

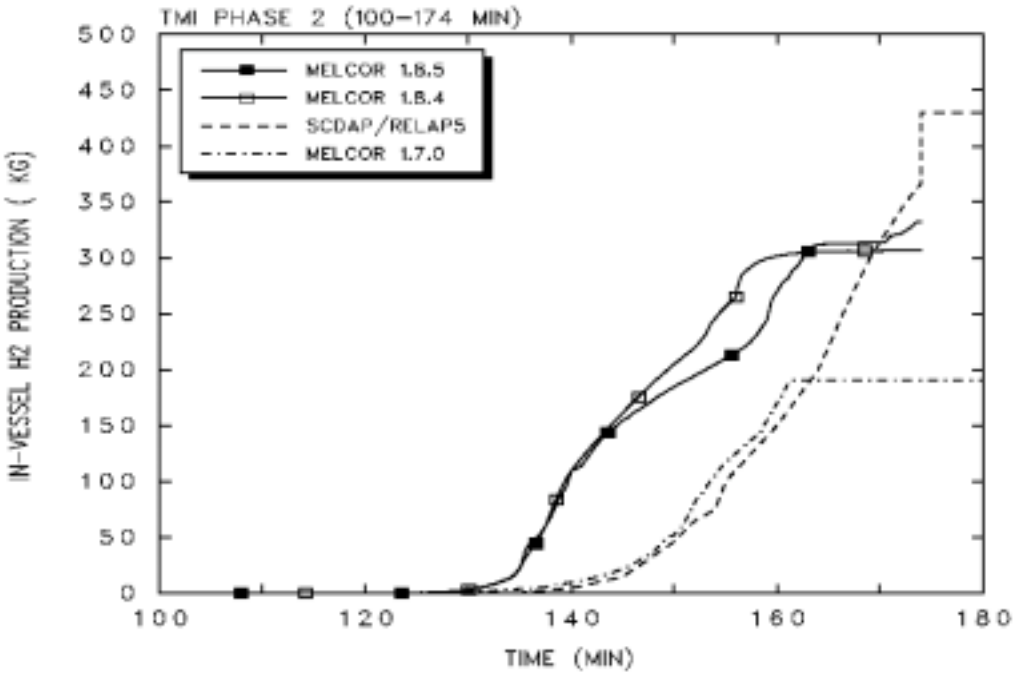

Figure 13-7. Total Hydrogen Produced from Cladding Oxidation

One area where MELCOR 1.8.5 results exhibit different characteristics from those obtained from MELCOR 1.8.4 is core material relocation. Only a few examples are described here, but the general trend observed in these calculations can be described as follows. In MELCOR 1.8.4, molten material was only allowed to candle downward and refreeze on the surfaces of core components of the same kind. For example, melting Zr cladding could

flow downward on lower level cladding, where it could refreeze as conglomerate material. In MELCOR 1.8.5, melting material can candle and refreeze as before, but it is also allowed to associate with particulate material at the same elevation.

The effects of this subtle change in material relocation modeling are observed in the TMI-2 calculation in at least two places. One of them is the reactor vessel lower head. During Phase 2 of the TMI-2 accident, a relatively small amount of particulate debris is calculated to pass into the lower head in the MELCOR 1.8.4 calculation but not in the MELCOR 1.8.5 calculation. The consequence of this difference is subtle but noticeable. (See Figure 13-5.) The increase in RCS pressure at ~155 minutes in the MELCOR 1.8.4 calculation is due to a sudden release of approximately 100 kg of particulate debris into the lower head. This does not occur in the MELCOR 1.8.5 calculation, and RCS pressure remains relatively stable during core degradation in conformance with measured data.

Particulate debris is generated in the MELCOR 1.8.5 calculation but does not travel to the bottom of the core. Molten (unoxidized) Zr cladding from the upper third of the core partially candles down intact cladding but relocates in greater quantities as conglomerate material associated with particulate debris. This is evident in Figure 13-8, which shows temporal changes in the mass of unoxidized Zr in various physical forms: intact cladding and refrozen conglomerate (clad), particulate debris (part), and conglomerate material attached to particulate debris (cngl-pd). The total mass of unoxidized Zr is also shown as ‘total zr’. A clear difference is observed between the MELCOR 1.8.5 result and the MELCOR 1.8.4 result at this mid-core Level 6 elevation. Conglomerate Zr in the MELCOR 1.8.4 calculation is associated solely with intact cladding as particulate material passes through this elevation and migrates to the bottom of the core. In the MELCOR 1.8.5 calculation, however, conglomerate Zr at mid-core elevations is associated primarily with particulate debris. The additional material mass associated with particulate debris occupies a larger fraction of the interstitial volume inhibiting particulate migration to lower elevations in the core.

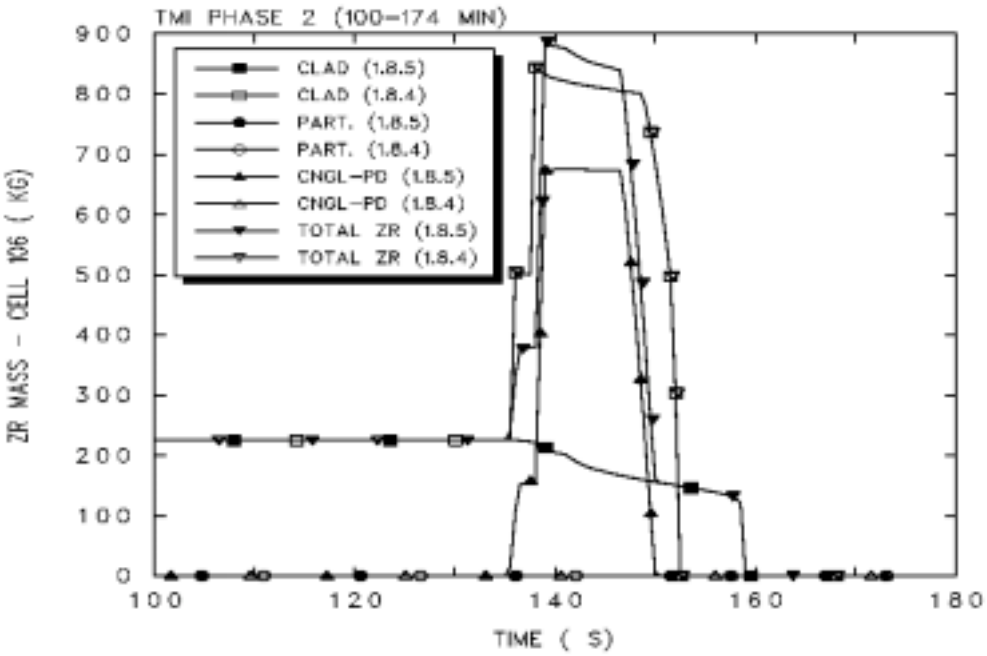

Figure 13-8. Zircaloy Mass in Various Physical Forms–Central Ring/Level 6

13.5 Discussion

Overall the results of the TMI-2 (Phase 2) calculations performed with MELCOR 1.8.5 are quite similar to those from MELCOR 1.8.4. The differences described above do not appear to significantly alter the overall results of the TMI-2 calculation. However, the details of the MELCOR 1.8.5 calculation appear more physically realistic than those generated by MELCOR 1.8.4. Recent changes to core material relocation modeling greatly inhibit the nonphysical downward migration of particulate debris, and allowed molten materials to interact with neighboring structures. These changes do not appear to have altered the calculation of major figures of merit for this accident, for example, the total level of clad oxidation or hydrogen generation.

13.6 References

1. E.A. Boucheron and J.E. Kelly, “MELCOR Analysis of the Three Mile Island Unit-2 Accident,” *Nuclear Technology*, 87, pp 1050-1057, December 1989.

2. I.K. Madni and S. Wang, “TMI-2 Analysis Using MELCOR 1.8.3,” A-3281, Brookhaven National Laboratory, October 1996.

3. I.K. Madni and S. Wang, “TMI-2 Analysis Using MELCOR 1.8.3,” A-3281, Brookhaven National Laboratory, October 1996.

4. R.W. Brower, et al., “ICBC Version 3.1, TMI-2 Initial and Boundary Conditions Data Base,” GEND-INF-078, January 1988.

5. D.W. Golden, et al., “TMI-2 Standard Problem Package,” EFF-TMI-7382, September 1986.

6. J.K. Hohorst, et al, “TMI-2 Analysis Using SCDAP/RELAP5/MOD3.1,” INEL-94-0157, November 1994